Exploring the Indium Phosphide Landscape: Precursor and Solvent Effects on Nanocrystal Size, Morphology, and Crystallization Temperature

Helen Larson

A dissertation

submitted in partial fulfillment of the

requirements for the degree of

Doctor of Philosophy

University of Washington

2025

Reading Committee:

Brandi Cossairt, Chair

Alexandra Velian

Dianne Xiao

Program Authorized to Offer Degree:

Chemistry

© Copyright 2025

Helen Larson

University of Washington

Abstract

Exploring the Indium Phosphide Landscape: Precursor and Solvent Effects on Nanocrystal Size, Morphology, and Crystallization Temperature

Helen Larson

Chair of the Supervisory Committee:
Brandi Cossairt
Department of Chemistry

Understanding the synthesis of colloidal quantum dots (QDs) allows for precise control over desired properties such as emission wavelength, morphology, phase, or monodispersity. InP is a crucial QD material due to its direct bandgap tunable across the visible and near-infrared wavelengths, strong absorbance coefficient, and lack of restricted heavy metals. Important developments in colloidal InP synthesis include size control through secondary injections, high photoluminescence quantum yield through surface passivation, and discovery of atomically-precise clusters. However, challenges remain including the lack of mechanisms for precursor reactivity-based size control, minimal routes to anisotropic morphologies, and high temperatures required for crystallization. The studies presented herein address these challenges by taking

inspiration from how nature controls ionic strength for facile crystallization, nucleation with organized cation-binding moieties, and crystallization with confined spaces.

Chapter 1 introduces colloidal nanocrystal nucleation and growth, and details how biomineralization can inspire solutions for outstanding InP synthetic challenges. Chapter 2 explores InP QD synthesis in polar solvent environments. Polar solvents are hypothesized to lower the crystallization temperature of InP by imparting ionicity or stabilizing charged reaction species. High-throughput experimentation identifies key factors for low temperature growth as increased percentage of polar solvent, carboxylic acid choice, and inclusion of polar additives. Guided by these insights, high-quality, crystalline InP QDs were synthesized at 60 °C using a toluene-dimethylformamide mixture, and exhibited a photoluminescence quantum yield of 25% after HF treatment. Chapter 3 demonstrates indium precursor reactivity-based size control for InP QDs using aminophosphine chemistry. Increasing the equivalents of metal-chelating aminopolycarboxylic acid EDTA ([CH2N(CH2CO2H)2]2) was found to decrease the final diameter of InP QDs from 4.5 to 2.3 nm by lowering the initial InP growth rate. This size trend was rationalized by invoking a continuous nucleation model in which suppressed initial growth rates are attributed to a competitive decrease in reactivity caused by indium-EDTA complexation and a lower effective concentration. Chapter 4 presents the synthesis of zinc blende InP nanowires made using indium tris(trifluoroacetate) and tris(diethylaminophosphine). Transmission electron microscopy and nuclear magnetic resonance spectroscopy identified a solution-liquid-solid growth mechanism using *in situ*-formed indium metal nanoparticles with the aminophosphine as the reducing agent.

TABLE OF CONTENTS

List of Figures vi

List of Supplementary Figures vii

List of Schemes x

List of Tables x

Chapter 1. Introduction 1

1.1 Colloidal Nanocrystal Nucleation and Growth 1

1.1.1 Complexities in Nanocrystal Nucleation 2

1.1.2 Impact of Nucleation and Growth on Nanocrystal Size 3

1.2 Landscape of InP Nucleation and Growth 5

1.2.1 Applications and Current Landscape 5

1.2.2 InP Nanocrystal Synthetic Methods 7

1.2.3 Nuances in InP Quantum Dot Nucleation and Growth 10

1.3 Inspiration from Nature to Solve Challenges in Nanocrystal Synthesis 12

1.3.1 Mechanisms of Control in Biomineralization Applied to Nanocrystal Synthesis 13

1.3.2 Addressing Challenges in InP Synthesis Inspired by Biomineralization 15

1.4 References 16

Chapter 2. Expanding Parameter Space to Enable Low Temperature Synthesis of Crystalline Indium Phosphide Quantum Dots 27

2.1 Introduction 27

2.2 Results and Discussion 30
2.2.1 High Throughput Colloidal InP QD Synthesis 31
2.2.2 Optimized Low Temperature Synthesis of InP QDs 38
2.3 Conclusions 46
2.4 Experimental Methods 47
2.4.1 General Practices 47
2.4.2 High-Throughput Experimentation 48
2.4.3 Synthesis of InP QDs at 60°C (heat-up) 49
2.4.4 Optimization of Synthesis of InP QDs at 60 °C 50
2.4.5 Synthesis of Zinc Oleate [$Zn(OA)_2$] Powder 51
2.4.6 Preparation of 2.0 M HF in Acetone 51
2.4.7 Zinc Exchange and HF Treatment of InP Cores 51
2.4.8 UV-Vis Absorbance Spectroscopy 52
2.4.9 Photoluminescence Spectroscopy 52
2.4.10 Time Resolved Photoluminescence (TRPL) and Photoluminescent Quantum Yield (PLQY) 53
2.4.11 Transmission Electron Microscopy (TEM) 53
2.4.12 Powder X-ray Diffraction (PXRD) 54
2.4.13 Raman Spectroscopy 54
2.4.14 Supplementary Figures 55
2.4.15 Experimental Conditions for High-Throughput Experiments 64
2.4.16 UV-visible Absorbance Spectra of Time points for High-Throughput Experiments 72

2.5 References 92

Chapter 3. Indium–Poly(carboxylic acid) Ligand Interactions Modify Indium Phosphide Quantum Dot Nucleation and Growth 97

3.1 Introduction 97

3.2 Results and Discussion 100

3.2.1 EDTA-Dependent Size Control 100

3.2.2 Impact of Precursor Reactivity on Nucleation and Growth 103

3.2.3 Formation and Study of In-EDTA Complex 110

3.3 Conclusions 114

3.4 Experimental Methods 115

3.4.1 General Practices 115

3.4.2 Synthesis of InP QDs using $InCl_3$ 116

3.4.3 Synthesis of InP QDs using InI_3 117

3.4.4 Post-synthetic addition of EDTA to InP QDs 117

3.4.5 ^1H NMR Studies of $InCl_3$ and EDTA 117

3.4.6 Transmission electron microscopy (TEM) 117

3.4.7 Powder X-ray Diffraction (XRD) 118

3.4.8 NMR spectroscopy 118

3.4.9 Supplementary Figures 119

3.5 References 133

Chapter 4. Alternate Indium Phosphide Synthesis with Aminophosphines: Solution-Liquid-Solid Nanowire Growth 137

4.1 Introduction 137
4.2 Results and Discussion 140
4.2.1 Synthesis of InP Nanowires 140
4.2.2 Mechanism of Indium Reduction 145
4.2.3 Morphology Control 149
4.3 Conclusions 154
4.4 Experimental Methods 155
4.4.1 General Practices 155
4.4.2 Synthesis of In(trifluoroacetate)$_3$ 156
4.4.3 Synthesis of InP Nanowires using In(trifluoroacetate)$_3$ 157
4.4.4 Synthesis of InP Nanowires using In(trifluoromethanesulfonate)$_3$ 158
4.4.5 Synthesis of InP Nanowires using External In^0 Nanoparticles 158
4.4.6 Control Synthesis without Aminophosphine 158
4.4.7 Control Synthesis with Diethylamine 159
4.4.8 Synthesis of Tris(oleylamino)phosphine oxide 159
4.4.9 ^{19}F NMR Study of Trifluoroacetic Anhydride 160
4.4.10 Synthesis of InP Quantum Dots from InI$_3$ or InCl$_3$ 160
4.4.11 Transmission Electron Microscopy (TEM) 160
4.4.12 Scanning Electron Microscopy (SEM) 160
4.4.13 Atomic Force Microscopy (AFM) 161
4.4.14 Powder X-ray Diffraction (PXRD) 161
4.4.15 NMR Spectroscopy 161
4.4.16 Mass Spectrometry 161

4.4.17 Cyclic Voltammetry 161
4.4.18 Supplementary Figures 162
4.5 References 183
Appendix A: Collaborative Efforts 189

LIST OF FIGURES

Figure 1.1 Molecular and nonmolecular components of colloidal nanocrystal synthesis. 2
Figure 1.2 Mass balance of solutes towards nucleation or growth. 4
Figure 2.1 High throughput experimentation enabled the discovery of low temperature synthesis of high-quality, crystalline InP QDs..... 30
Figure 2.2 High throughput experimentation of 60 °C InP QD synthesis 34
Figure 2.3 Characterization of optimized synthesis of oleate-capped InP QDs at 60 °C 40
Figure 2.4 Optimizing oleate-capped InP QD synthesis at 60 °C..... 43
Figure 2.5 Characterization of myristate- and benzoate-capped InP QDs synthesized at 60 °C 45
Figure 3.1 Optical, crystallographic, and morphological characterization of InP QDs. 102
Figure 3.2 Nucleation and growth data and interpretation..... 106
Figure 3.3 Comparing EDTA-based size control to indium stoichiometry-based size control 107
Figure 3.4 Temperature-dependent initial rate kinetics of InP QD synthesis with EDTA108
Figure 3.5 Phosphorus speciation over time of InP QD synthesis with EDTA..... 109
Figure 3.6 Proton NMR of the indium EDTA complex 111
Figure 4.1 Morphological and crystallographic characterization of the InP nanowires 142
Figure 4.2 Evidence for a mechanism of indium reduction by aminophosphine 147
Figure 4.3 TEM images of variations on the InP nanowires 151
Figure 4.4 Morphological and crystallographic characterization of bulk InP nanowires synthesized using $In(OTf)_3$ 152

LIST OF SUPPLEMENTARY FIGURES

Figure S 2.1 High-throughput experimentation absorbance spectra 55
Figure S 2.2 UV-visible absorbance spectrum fit to a gaussian 56
Figure S 2.3 Raman spectra 57
Figure S 2.4 UV-visible absorbance and photoluminescence of InP QDs synthesized at 60 °C 58
Figure S 2.5 Temporal evolution of the absorbance and emission profiles of InP QDs grown at 60 ºC when subjected to zinc exchange and fluorination by HF at 180 ºC 59
Figure S 2.6 Optical characteristics of InP/Zn-F QDs plotted on an energy scale 60
Figure S 2.7 Time-resolved photoluminescence decay of InP/Zn-F QDs 60
Figure S 2.8 Photoluminescence excitation spectra of InP/Zn-F QDs made at 60 °C..... 61
Figure S 2.9 UV-visible absorbance spectra showing reproducibility of optimized InP QD synthesis 62
Figure S 2.10 UV-visible absorbance spectra comparing QD products with and without ethyl acetate and NMP additives 62
Figure S 2.11 Characterization of InP QDs synthesized using acid-free indium(III) myristate 63
Figure S 3.1 Absorbance spectra for syntheses at 190 and 220 °C 119
Figure S 3.2 TEM images of InP QDs 120
Figure S 3.3 Comparison of final InP QD size 121
Figure S 3.4 Fits of the pXRD patterns of the EDTA series InP QDs 122
Figure S 3.5 Proton NMR spectra InP QD series and indium EDTA complex 123
Figure S 3.6 IR spectroscopy of InP QD series 124
Figure S 3.7 Tracking the full width at half maximum (FWHM) of the lowest energy electronic transitions of aliquots from synthesis of InP QDs with 0.25 equivalents of EDTA 125
Figure S 3.8 Comparison of InP yield between lower $InCl_3$ concentration and equivalents of EDTA additive 126

Figure S 3.9 Comparison of initial rates of InP growth between lower $InCl_3$ concentration and equivalents of EDTA additive 126
Figure S 3.10 Proton NMR spectra of heated indium-EDTA amine complex 127
Figure S 3.11 ^{31}P NMR spectra of the crude reaction before purification of InP QDs made using 0, 0.25, and 0.5 eq. EDTA and reaction time of overnight 128
Figure S 3.12 ^{1}H NMR spectrum comparing the reaction of indium chloride with oleylamine to the reaction of $InCl_3$, EDTA, and oleylamine 129
Figure S 3.13 Absorbance spectra and initial rate of InP QDs made with 1 eq. EDTA 130
Figure S 3.14 Absorbance spectra of aliquots from the control reaction of 1eq. $InCl_3$, 1 eq. EDTA in oleylamine subjected to the InP synthesis conditions without injection of aminophosphine 130
Figure S 3.15 EDTA-based size control for InP QDs made using InI_3 131
Figure S 3.16 Absorbance spectra and TEM image of QDs with a post-synthetic addition of EDTA 132
Figure S 4.1 Characterization of $In(TFA)_3$ 165
Figure S 4.2 TEM images of buckled nanoribbon 165
Figure S 4.3 Additional AFM of InP NWs 166
Figure S 4.4 TEM images of NWs made using pre-made indium nanoparticles..... 166
Figure S 4.5 Absorbance spectra over the course of a nanowire synthesis, and photoluminescence measurement 167
Figure S 4.6 TEM images and absorbance spectra of control syntheses varying the 120 °C evacuation step 168
Figure S 4.7 ^{19}F Diffusion-Ordered Spectra 170
Figure S 4.8 TEM of diameter dispersity increases with lower precursor concentration171
Figure S 4.9 TEM images and powder X-ray diffraction patterns of oleylamine and diethylamine control syntheses 172
Figure S 4.10 Proton and phosphorus NMR spectra of $O=P(NEt_2)_3$ 173
Figure S 4.11 ^{31}P NMR spectrum of transaminated $O=P(NHR)_3$ 174
Figure S 4.12 Phosphorus NMR spectra of crude nanowire solution spiked with tris(oleylamine)phosphine oxide 175

Figure S 4.13 ^{1}H NMR spectra of $In(TFA)_3$, trifluoroacetic acid, and trifluoroacetic anhydride in oleylamine 176
Figure S 4.14 ^{19}F NMR spectra of the crude nanowire reaction solution compared to aliquots of a control reaction between trifluoroacetic anhydride and oleylamine 177
Figure S 4.15 UV-vis absorbance spectra of aliquots from control syntheses with $InCl_3$ and InI_3 178
Figure S 4.16 Cyclic voltammetry data of indium salts 178
Figure S 4.17 TEM images of multipod products 179
Figure S 4.18 Additional TEM images showing reproducibility over three replicate InP nanowire syntheses 180
Figure S 4.19 Absorbance spectra, powder X-ray diffraction patterns, and TEM images of InP QDs made using $In(TFA)_3$ and $In(OTf)_3$ 181
Figure S 4.20 Proton and fluorine NMR spectra of InP QDs made using $In(OTf)_3$ 182
Figure S 4.21 Characterization from the heat-up nanowire synthesis from $In(TFA)_3$ and $P(NEt_2)_3$ 182

LIST OF SCHEMES

Scheme 1.1 Precursor chemistry for InP nanocrystal synthesis 8
Scheme 2.1 Air- and water-free microplate set up 32
Scheme 3.1 Aminophosphine-based InP QD synthesis with ethylenediaminetetraacetic acid (EDTA) additive 100
Scheme 3.2 Formation and transformation of the octahedral indium EDTA complex .. 112
Scheme 3.3 Proposed reaction scheme showing the influence of EDTA chelation on indium precursor reactivity 114
Scheme 4.1 InP nanowire synthesis from indium tris(trifluoroacetate) and tris(diethylamino)phosphine in oleylamine, proceeding through the Solution-Liquid-Solid growth mechanism 140
Scheme 4.2 Options for the reduction of indium. (R = $C_{18}H_{35}$, R' = $C_{17}H_{33}$)..... 146

LIST OF TABLES

Table 2.1 Stock Solutions used in High-Throughput Experiments..... 64
Table 2.2 Conditions for High-Throughput Experiments 66
Table 2.3 UV-visible Absorbance Spectra of Time points for High-Throughput Experiments 72

ACKNOWLEDGEMENTS

A PhD is an individual effort but it would not have been possible without a strong community to support and guide me along the way. I would like to acknowledge and thank the important community of family, friends, and lab mates that have supported me through graduate school. First, I want to thank my family, for supporting me through all the steps of my education and for taking me out of the graduate school grind to go on adventures, whether around Seattle, back home in Minnesota, or abroad. Thank you to my mom and dad for everything, and for listening to my wild rambling stories. I would not be where I am without my sister, Virginia, who has always been a role model to me and paved the way for what life could look like, and I am grateful for her friendship and our many adventures over the last five years. To my family in Seattle, thank you for welcoming me into the family dinners for holidays and birthdays, and thank you to Lisa for all the coffee chats and support over the years.

Graduate school would not have been the same without my incredible lab mates over the years. Even starting in the pandemic, I felt welcomed by the Cossairt lab especially by Nayon as she rallied the troops for dinners out and karaoke nights. Thank you to my mentor Madison, for teaching me how to be a graduate student and instilling a love of electron microscopy in me. I am grateful for the left office crew over the years for always being game for a chat whether about science or otherwise. I was lucky to find incredible friends within the lab, thank you to Micaela for your friendship and all the good times and good chats we had, to Soren for being an excellent climbing partner, to Grant for the good long conversations, and to Ezra for bringing joy. I am thankful for my mentees, for teaching me while I taught them. To my cohort, Eden, and especially the Cossairt lab cohort Emily, Hao, and Chris, I am grateful for the community we formed through

the duress of starting graduate school in a pandemic, and for being alongside me for the whole journey. I am also grateful for CSSAS and the Clean Energy Institute, for supporting me scientifically and for being a source of community on campus outside of the chemistry department.

Thank you to my friends, both in Seattle and elsewhere, who brought much needed joy, fun, and adventure to my time in graduate school. Mercie, I was so lucky to have met you and your friendship has been invaluable. To my housemates, thank you for all the wild times and for making a house a home over the past three years. Thank you to my college friends for your continued and constant love and support, and thank you to my friends from Minnesota, for growing with me and adventuring with me.

Last and most importantly, I would like to thank my advisor Brandi Cossairt for her scientific guidance and mentorship. Her enthusiasm about science was continuously inspiring. Thank you for all of the insightful one on one walks around campus, and for leading by example by being a brilliant scientist and a kind person. Brandi showed all of us in the lab how to be creative, rigorous scientists while maintaining an atmosphere of respect and inclusion. Thank you for fostering a welcoming, fun, exciting lab. I could not have imagined a better combination of advisor, science, and lab mates for my PhD.

Chapter 1. INTRODUCTION

1.1 Colloidal Nanocrystal Nucleation and Growth

Colloidal nanocrystal nucleation and growth involves two components, the molecular component, precursor chemistry, and the non-molecular component, crystallization (**Figure 1.1**). The molecular component comprises of the generation of solutes as ions in solution or from bond-forming reactions between the initial molecular reagents. The solutes go on to be the building blocks for crystallization, starting with solute build-up leading to nucleation of the crystalline phase, and then the nuclei undergo growth to a larger crystal. Colloquially, the nucleation process is a transition from disparate, unordered solutes that come together, with increasing concentration and structure, in the initial emergence of a crystalline phase, the nucleus. Classical Nucleation Theory defines nucleation as formation of a critical crystal size, the nucleus, that is the largest size where it does not dissolve and the smallest size where it can grow larger.[1] Critical crystal size is thermodynamically determined by a balance of unfavorable surface energy and favorable free energy loss due to higher chemical potential of the solute in solution than as a component in the crystal.[1] After nucleation, the new nanocrystal undergoes growth. Common models for nanocrystal growth include diffusion-limited growth, where the growth rate depends on the diffusion rate of solutes to the surface, and reaction-limited growth, where the reactivity of solutes at the nanocrystal surface controls the growth rate.[2,3]

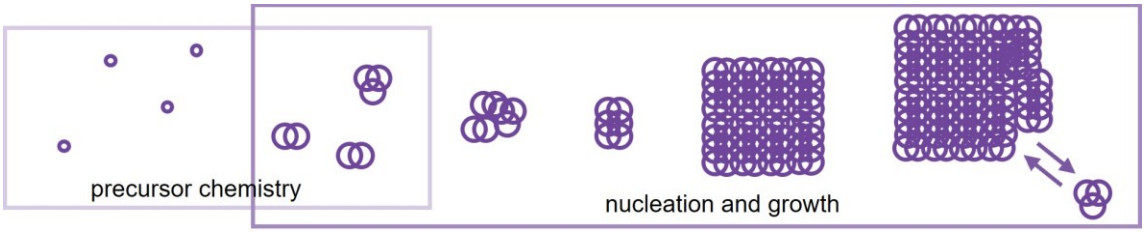


Figure 1.1 Molecular and nonmolecular components of colloidal nanocrystal synthesis.

1.1.1 *Complexities in Nanocrystal Nucleation*

However, few systems can be fully explained by classical nucleation theory or simple growth models. Crystallization occurs in systems with varying degrees of complexity of the free energy landscape and influence of dynamics.[4] From conventional nucleation, increasing complexity can arise in the form of thermodynamically metastable particles, metastable phases, or modulation by templates or mineralizing agents.[4] One example of metastable phases observed in the nucleation process of some systems including in proteins, polymers, biominerals, and molecular organic materials, is that nucleation goes through a 'two-step' phase change process by increasing concentration and structure sequentially rather than simultaneously.[1,5,6] This creates an intermediate dense liquid phase within which the nuclei forms.[1,7] Complexity is also introduced through dynamics by changing supersaturation or temperature and this induces crystallization through particle attachment or non-equilibrium material.[4,6] For example, many natural systems exhibit crystallization through particle attachment such as bone, and are discussed further in the following section on biomineralization. Another example of dynamics affecting nucleation is found in experimental studies for iridium nanoparticles which have demonstrated a low-molecularity kinetically-limited nucleus that differs from the thermodynamic nucleus of classical nucleation theory.[8–10]

Another type of complexity in nanocrystal nucleation arises when the supersaturated solution where nucleation occurs is confined on the order of the nanocrystal size. This results in a limitation of the crystallization front to the size of the confined solution. Vapor-liquid-solid, and the analogous solution-liquid-solid (SLS) nanowire growth use this principle to force a growing crystal into a one dimensional morphology.[11] In the SLS mechanism, the precursors are introduced in the solution along with a liquid metal nanoparticles, then as precursors dissolve in the liquid nanoparticle, supersaturation is reached and nucleation occurs. Because the liquid nanoparticle acts as a nanoreactor and facilitates localized high precursor concentration, the crystallization only occurs within the nanoparticle leading to extrusion of a one-dimensional nanowire.

1.1.2 *Impact of Nucleation and Growth on Nanocrystal Size*

Even within conventional nucleation that is invoked for colloidal nanocrystal synthesis, variations in the precursor chemistry, material system, temperature, and free energy landscape can cause complexities in the crystallization pathway.[12–21] **Figure 1.2** describes general nanocrystal nucleation and growth from precursors, where first precursors react to form solutes, which then can either form new nanocrystals, nucleation, or add to existing nanocrystals, growth. The balance between nucleation and growth affects the final nanocrystal size and size dispersity, which is a crucial property in determining the applications of semiconductor nanocrystals. A model proposed by LaMer and further developed by Sugimoto proposes that monodisperse nanocrystals form by temporally separated nucleation and growth, and the size can be controlled by the rate of solute production, in turn controlled by precursor reactivity.[22,23] In the LaMer model, nucleation was assumed to be instantaneous to support the development of a diffusion-controlled growth model to explain monodisperse particle formation.[2,23,24] First, solutes build in concentration until above a critical supersaturation concentration, then after ‘instantaneous’ nucleation, the solute

concentration drops and the remaining solutes add to existing nuclei through diffusion-limited growth.[23] By increasing the precursor reactivity rate and therefore the rate of solute production, more nuclei form during the nucleation burst and grow to smaller nanocrystal size due to less solute left in solution, and the opposite with high precursor reactivity rates forming larger nanocrystals. This concept been demonstrated extensively by Owen and coworkers in II-VI and IV-VI nanocrystal systems, where thio- or selenoureas with varying reactivities control the nanocrystal size as described by the burst nucleation model.[17] However, there are limitations to systems that can be described with the LaMer nucleation and growth model. Specifically, the system must follow mass balance between solute supply and consumption by nucleation and growth processes, the precursor to solute reaction must be rate-determining for crystallization, and nucleation rate must not be influenced by external templates or seeds.[22]

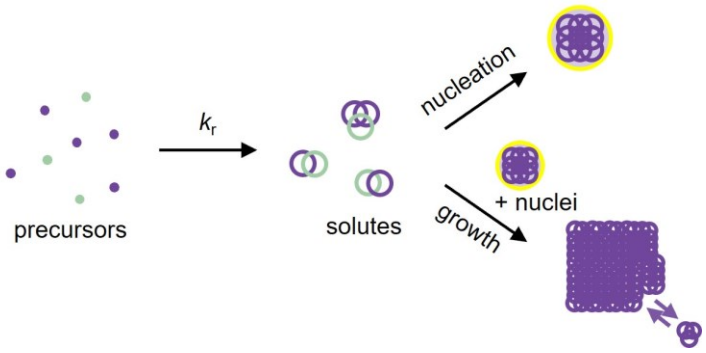


Figure 1.2 Mass balance of solutes towards nucleation or growth.

Considering the complexity of crystallization, it is not surprising that many nanoparticle systems cannot be accurately described by the LaMer model.[10,13,25–28] In fact, experimental studies in 2019 demonstrated that the original sulfur sol system mentioned in the proposal of the LaMer model does not fit a burst nucleation model and instead undergoes continuous nucleation.[2] Continuous nucleation was proposed in a 2-step nucleation and growth model from Finke and

Watzky based off fitting experimental iridium nanoparticle kinetics data to two simple kinetic equations.[25] The first was a slow, continuous nucleation event from precursor (A) to a nanoparticle (B), then fast autocatalytic surface growth where A + B → 2B. This model was updated based on mechanism-enabled population balance modeling, where the particle-size distribution is fit using a minimal number of pseudoelementary steps.[10] The best fit for the iridium nanoparticle size distribution was found through a one-step extension of the previous model that replaced the A + B → 2B step with two steps A + B → C and A + C → 1.5C. The former implies a constant growth rate for all particles, where in the latter case the rate of the first reaction was larger than that of the second implying that smaller particles experience faster growth rates by monomer addition than larger particles. Continuous nucleation and growth has been identified in other nanocrystalline systems, including binary semiconductor nanocrystals, and has been supported with data-driven kinetic models, absorbance spectroscopy, and x-ray scattering data.[18,29–32] A notable example from Owens, Peters, and coworkers developed with a population balance model for lead chalcogenide nanocrystals demonstrated that nucleation events continued for up to 20% of the reaction time and size-dependent growth was necessary to fit the data.[30,31] Size-dependent growth rates allow for systems with continuous nucleation to produce monodisperse nanoparticle populations, and revokes the idea that temporally separated nucleation and growth is necessary to achieve monodispersity.[10,13,31]

1.2 Landscape of InP Nucleation and Growth

1.2.1 *Applications and Current Landscape*

The study of colloidal quantum dot (QD) nucleation and growth is imperative due to their applications in optoelectronics, high-speed electronics, bioimaging, photovoltaics, photocatalysis,

and quantum information science.[33–45] The discovery and synthesis of QDs won the Nobel prize in 2023, highlighting the large impact of the tiny materials on science and technology.[46] Confining a semiconductor to the nanoscale accesses emergent properties due to the quantum confinement effect.[33] When the QD size is decreased below the material-specific Bohr exciton diameter, the electronic wavefunctions experience quantum confinement that leads to the widening of QD bandgap and discretization of the band edge states. The resulting size-dependent bandgap and isolation of the band-edge energy states allows for tunable color-pure emission that can span the color gamut for displays and lighting, and controllable charge transport for electronic or photocatalysis applications.[33] The QD size, monodispersity, and concentration can also be evaluated as a function of the size-dependent absorbance and photoluminescence during and after synthesis which allows for detailed studies on nucleation and growth.

Indium phosphide QDs are spectrally-tunable visible and near-infrared light emitters used industrially for optoelectronic applications[47–49] and are also promising candidates for emerging applications such as electroluminescent light-emitting diodes (LEDs) and near-infrared emission for bioimaging.[50–54] The relatively large, direct bulk bandgap of 1.35 eV, strong absorption coefficient, and lack of restricted heavy metals place InP as a crucial QD material.[47] The synthesis of red-emitting InP QDs in particular has been optimized for unity photoluminescence quantum yield (PL QY) and applied industrially as a down-converting material for LEDs.[55–57] In addition to isotropic QDs, InP nanowires are unique building blocks for electronic and optoelectronic devices due to retention of high carrier mobilities prized in bulk InP and emergent properties such as confined carrier transport in one dimension, large polarization sensitivity, amenity to hybrid structures, and a tunable band gap.[35,36,39,58–64] Because InP QDs are successfully integrated in

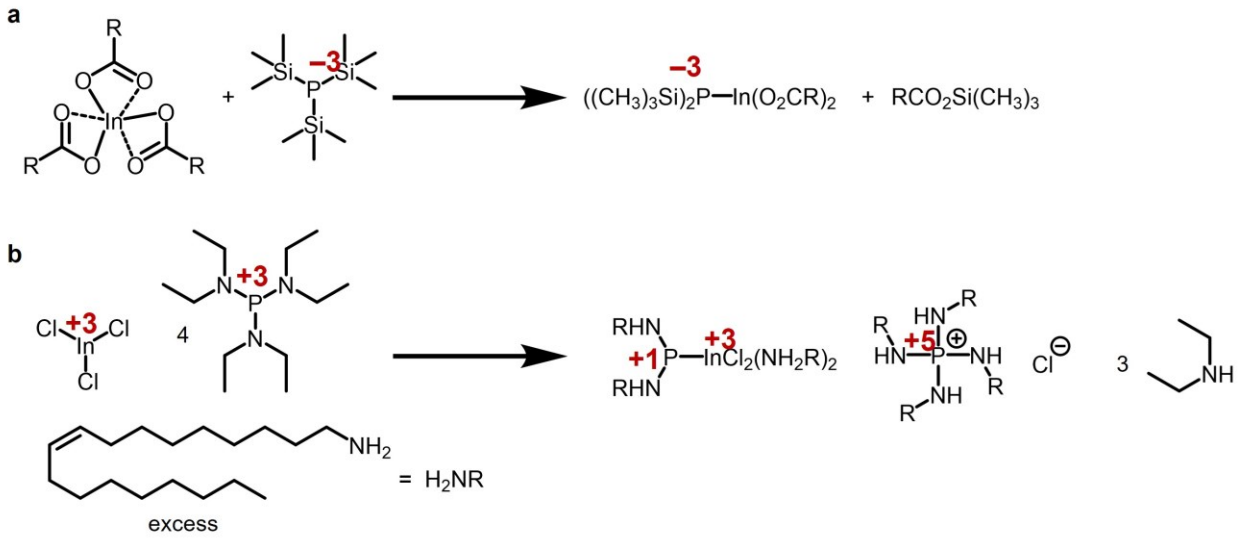
commercial technologies, it is important fundamentally understand and optimize the synthetic process.

Currently, the colloidal InP synthetic landscape contains routes to InP QDs, atomically-precise nanoclusters, nanowires, and nanorods. InP QDs and clusters are typically produced through hot-injection syntheses using high-boiling point nonpolar organic solvents, and the anisotropic nanocrystals through SLS growth methods. The specific chemistries, methods, and nucleation and growth mechanisms are reviewed in detail below. Direct colloidal nucleation of anisotropic InP is elusive and it has been proposed that successful methods to form nanoplatelets and nanorods of II-VI semiconductors are not transferrable to III-V semiconductors due to difficulties in balancing the charge of the cation-rich surface facets required for elongated nanocrystals.[65] Synthetic control is an outstanding challenge in InP nanocrystals, specifically in the limited range of precursor reactivity-based size control, the lack of routes to make anisotropic nanocrystals, and the high temperatures required to nucleate and grow crystalline InP. Additional challenges with InP are its low native PL QY understood to be limited by structural defect-caused electronic traps, and the propensity to oxidation.[47] These challenges related to photophysical properties and stability are not the focus of this thesis and have been studied extensively elsewhere.[47,51,55,56,66–72]

1.2.2 *InP Nanocrystal Synthetic Methods*

There are two main chemistries for colloidal InP QD synthesis based on the phosphorus precursor choice. The most commonly used chemistry employs indium alkanoates as the In^{3+} source, and tris(trimethylsilyl)phosphine for P^{3-}. The first bond forming reaction is shown in **Scheme 1.1a**, where the In–P bond is formed through elimination of a silyl ester.[12] Successful syntheses with this chemistry use hot-injection of the silylphosphine or of pre-formed InP clusters

into a bath of indium carboxylate or pre-formed InP seeds and solvent at high temperatures (260-400 °C), although heat-up methods producing monodisperse InP QDs have also been demonstrated.[16,55,73–75] The addition of tertiary phosphines has been demonstrated to assist in the solubility and reactivity of the indium carboxylate, and secondary injections of small InP clusters can be employed to increase the size while maintaining monodispersity.[73,74] The resulting QDs possess a zinc-blende crystal structure and can range from quasi-spherical particles to tetrahedra.[76] This chemistry is responsible of high-quality InP QDs used in the display industry, however the silylphosphine precursor is extremely pyrophoric and produces toxic phosphine gas upon exposure to air or water.[55] Another challenge, and also an opportunity, in this chemistry is the presence of kinetically persistent InP cluster intermediates, which preclude size control through precursor reactivity but offer an atomically precise platform to study surface properties and can act as a single source precursor for monodisperse synthesis of InP QDs.[16,77–80]



Scheme 1.1 Precursor chemistry for InP nanocrystal synthesis. First bond-forming reactions for (**a**) the silylphosphine-based chemistry and (**b**) the aminophosphine-based chemistry.

Due to hazards associated with the silylphosphine-based InP synthesis, an alternate chemistry was developed in 2015 based on a less hazardous, more stable aminophosphine as the phosphorus source.[81–84] The synthesis typically proceeds first through degassing the hydroscopic indium halide precursor in a bath of primary amine as the solvent, then hot-injection of the aminophosphine at reaction temperatures between 180 – 270 °C. The aminophosphine, typically tris(diethylamino)phosphine or tris(dimethylamino)phosphine, contains phosphorus in a +III oxidation state which must undergo a six electron reduction to phosphide (-III) in InP. The aminophosphine has been proposed to reduce itself during the In–P bond forming reaction, based on detailed ^{31}P nuclear magnetic resonance (NMR) spectroscopy, mass spectrometry, and density functional theory studies.[83,84] Specifically, the aminophosphine complexes to the indium halide, and undergoes acid-base and redox reactions with another equivalent of aminophosphine supported by the primary amine solvent to form a complex of In(+III)–P(+I) and an oxidized $P(NHR)_4Cl$ phosphonium salt (**Scheme 1.1b**). The phosphonium salt has been observed by ^{31}P NMR spectroscopy and mass spectrometry as $P(NHR)_4$, where R is $C_{18}H_{35}$ and originated due to transamination of the aminophosphine with oleylamine, the primary amine used as the solvent.

Current colloidal methods for anisotropic InP nanocrystals are limited to the SLS mechanism, in addition to sparse examples of anisotropy accessed through cation exchange.[85–87] To the best of the author's knowledge, there are only 15 unique reports of InP nanowire synthesis using SLS growth.[11,88–94,61,95–100] SLS was discovered by Buhro and coworkers in 1995 while using organometallic reactions to form InP at temperatures lower than vapor-phase deposition, and mechanistic studies using a single-source InP precursor followed in 1997.[11,88] Control over nanowire diameter was established by varying the metal nanoparticle diameter, along with length control based on precursor to metal nanoparticle ratios.[89–94] Diameter- and length-dependent

optical properties of InP quantum wires and rods were determined through precise SLS-based synthesis and etching.[61,95] A handful of reports studied optimization of self-seeded SLS for InP nanowires, where the an *in-situ* formed indium metal nanoparticle catalyzes nanowire growth. It is noteworthy that all the previously described syntheses either use single source InP precursors or tris(trimethylsilyl)phosphine. Innovation in the phosphorus precursor used for InP SLS is limited to two reports, one using solid $(PH)_x$[99], and the other using aminophosphine with electrically-controlled reduction and anchored metal nanoparticles[98]. This further highlights the need for further studies on anisotropic InP nanocrystal synthesis, especially using the less hazardous, less toxic aminophosphine precursor.

1.2.3 *Nuances in InP Quantum Dot Nucleation and Growth*

For InP QDs, the nucleation and growth pathways depend heavily on the chemistry of the precursors, the solvent, and the temperature. The 'InP' solutes used in crystallization are not simple In^{+3} and P^{-3} ions but likely species containing at least one In–P bond and additional ligands for solubility. InP nucleation and growth in the system using aminophosphine-based chemistry has been shown to have temperature-dependent nucleation fractions.[13] At lower temperatures (180 °C), nucleation occurs over a significant fraction of the reaction, while at higher temperatures, such as 250 °C and above, there is a more 'burst-like' nucleation event.[13] Size-control was achieved based on aminophosphine reactivity at higher temperatures within the 'burst' nucleation regime, but aminophosphines of different reactivities had little effect on the size under the continuous nucleation regime.[13] Despite this result, other studies have shown that varying the indium halide[82] or using diamine additives to modify aminophosphine reactivity[101] does control QD size at temperatures within the continuous nucleation regime. Notably, Chapter 3 describes the use of a

polycarboxylic acid additive to modify the indium precursor reactivity which controls size under the regime of continuous nucleation.[26]

The impact of precursor reactivity on nanocrystal size within a continuous nucleation regime is more difficult to predict than when nucleation and growth are temporally separated with 'burst' nucleation. Higher precursor reactivity leads to faster production of solute which can be directly correlated to the number of nuclei produced in a 'burst' nucleation event, but when nucleation is continuous, the solutes can either participate in nucleation or in growth on existing nuclei. Therefore, it is not surprising that there are different trends for how precursor reactivity affects nanocrystal size in systems with continuous nucleation. As mentioned previously, continuous nucleation has been measured for lead chalcogenides, and perhaps also cadmium chalcogenides, and higher precursor reactivities still lead to smaller nanoparticles as predicted by the traditional LaMer model of nucleation and growth.[30,102] Conversely, the studies controlling precursor reactivity for InP under the continuous nucleation regime display the opposite trend, where higher lead to larger nanoparticles.[26,101] A possible explanation for this is comes from comparing the extent of the nucleation fraction for aminophosphine-based InP and lead chalcogenides, reported each for several precursor reactivities by the Owen lab[13,30], and noting that InP has longer nucleation fractions than lead chalcogenides. Chapter 3 of this thesis will further explore the topic of precursor reactivity-based size control in aminophosphine-based InP synthesis.

InP nucleation and growth through the silylphosphine-based chemistry occurs through a two-step reaction pathway which also complicates synthetic control through precursor reactivity.[16] Cossairt and coworkers identified an atomically-precise InP magic-sized cluster (MSC) as a metastable intermediate on the route to InP QDs when using indium carboxylates and tris(trimethylsilyl)phosphine.[16,19,77] The MSC was demonstrated as a single-source precursor for

InP QDs, and likely undergoes dissolution into fragments unique from the original solutes before proceeding through a second nucleation event to directly form QDs.[16,103] These kinetically-persistent MSCs preclude controlling the InP QD size by varying precursor reactivity. However, a computational study has suggested that the activation energy for In – P bond formation between a model indium carboxylate and PH_3 is highly dependent on In – O bond cleavage, therefore resulting in a reactivity dependence on the conjugate carboxylic acid pKa.[104] Outside of precursor reactivity, the size of InP QDs can be controlled through reaction time, temperature, and secondary injections.[55,76,105,106] Secondary injections of additional indium and phosphorus precursors have been successfully implemented to control the size of monodisperse InP QDs.[55,73] An example at the intersection of precursor reactivity and controlled growth demonstrated that varying the ratio of two silylphosphine precursors of different reactivities controlled the size of InP QDs by introducing solute both quickly, resulting in nucleation, and slowly, for growth.[107] An underexplored region of the InP landscape is the nucleation and growth in polar solvents. Chapter 2 will discuss the particular considerations of covalency and lattice stability of InP in the context of inducing crystallization at lower temperatures using polar solvents.

1.3 Inspiration from Nature to Solve Challenges in Nanocrystal Synthesis

Nature has evolved exquisite control over crystal growth both at the nanoscale and for hierarchical inorganic-organic structures such as shells and bone. The study of biomineralization reveals how systems enact detailed control over mineral nucleation, growth, shape, phase, and assembly.[108] Despite similar objectives in the field of colloidal nanocrystal synthesis, the connection between mechanisms of synthetic control found in nature and opportunities for use in colloidal QD synthesis is underexplored, especially for highly covalent materials like InP. Here,

the lessons to be gained from nature on crystal growth are summarized with examples bridging the study of biomineralization and colloidal nanocrystal synthesis. Then, the lessons from nature are applied as inspiration in addressing outstanding issues in InP nanocrystal synthesis.

1.3.1 *Mechanisms of Control in Biomineralization Applied to Nanocrystal Synthesis*

Biomineralization is the how nature controls complex mineralization. A review from Nudelman and Sommerdijk outlines the five generalized elements of control over mineralization as chemical, spatial, structural, morphological, and constructional.[108] Chemical control involves modulating the parameters responsible for nucleation and crystal growth such as supersaturation, solubility, and ionic composition through controlled matrices and biomolecules that promote or inhibit nucleation. For example, particular facets are favored for calcite mineralization in mollusk shells based on the acidic content of proteins in the mineralization environment.[109,110] For a biomimetic example, varying hydrophobicity of peptoids has been shown to tune the nanocrystal morphology of the wide band-gap semiconductor zinc oxide.[111] The chemical control offered by mineralization inhibitors plays a key role in directing the formation of bone, and it has also been shown that polypeptides with disordered metal-binding groups slow nucleation of calcium sulfate from sea water by a structural incompatibility with the lattice.[112,113] Spatial control is related to chemical control and details the selective transport of species such as mineral precursors or inhibitors. An elegant example is found in bone where expression or destruction of a calcium phosphate inhibitor controls the location of bone formation.[113] Controlled crystallization based of transport of mineral precursors was successfully mimicked through an artificial precursor flux to modulate mineralized titania structures.[114]

Structural, morphological, and constructional control describe the influence of macromolecular templates or enclosures on the crystallographic structure, general morphology,

and assembly, respectively. An organic template can be used to direct the nucleation of biominerals, as observed in the teeth of a limpet where chitin fibrils template needle-like nanocrystals.[115] The concept of templating minerals using designed biomolecules is particularly valuable for colloidal nanocrystal synthesis as it promises exceptional size and phase control through heterogeneous nucleation. For example, designer proteins with regularly-spaced negatively charged functional groups were shown to template non-natural phases of calcite[116] and specific ordering of metal-binding groups on a protein were shown to direct the phase of titania[117]. Morphological control in biomineralization is often accessed by collecting amorphous nanoparticles in a defined enclosure which then undergo crystallization through an amorphous phase or by particle attachment.[4,108] A striking example are the porous spines of sea urchins where a closely entangled macromolecular framework has been observed to direct the secondary crystallization of amorphous calcium carbonate to calcite.[118,119] Mesophases are also known to play roles in templating nanocrystal formation and assembly, for example with QD-organic superlattices templated by liquid crystals, or MSCs formed and assembled within a mesophase.[120–122] Additionally, nanocrystal growth within structured environments is also observed in microemulsion-based growth methods or within protein cages, among other methods, including SLS growth.[123,124] Finally, nature controls the construction of biominerals into complex hierarchical materials with organic and inorganic building blocks, exemplified by the intricate bundles of collogen and calcium phosphate in bone.[4,113,125] Inorganic-organic hybrid assembly is a rich field and while it is outside of the scope of this review of biomineralization for inspiring nanocrystal nucleation and growth, Appendix A discusses several electron microscopy studies of hybrid inorganic-organic assembly.[126–128]

1.3.2 *Addressing Challenges in InP Synthesis Inspired by Biomineralization*

Exploratory synthesis efforts are driven by thinking outside-of-the-box to access new regions of a synthetic landscape. In this thesis, paradigms from biomineralization are applied to address outstanding challenges in InP nanocrystal nucleation and growth. The studies presented here demonstrate that biomineralization strategies for crystallization control are applicable regardless of drastic differences in synthesis conditions between ambient, aqueous, ionic biomineral systems and high-temperature, nonpolar, covalent InP synthesis.

First, InP QD synthesis requires high temperatures at or above 180°C to achieve crystallinity likely due in part to the high covalency and resulting high lattice stability of InP. A low temperature synthesis of high-quality InP QDs would both be industrially useful to lower energy costs, and fundamentally interesting to break the colloquial paradigm of 'hard to make, hard to break' materials. Nature has many strategies to induce nucleation and phase-specific growth at ambient, biological conditions and temperatures. Specifically, increasing ionic strength can induce nucleation in calcite and certain proteins.[129–132] The high ionicity of biominerals and precise control of solution environments as key predictors for facile crystallization lead to the hypothesis of lowering InP nucleation or growth barriers with a polar solvent environment. Chapter 2 explores expanding the parameter space of InP QD synthesis by exploring the low temperature crystallization accessed by a polar solvent environment.

The second outstanding challenge for InP QD synthesis is the lack of breadth of precursor reactivity control over size, particularly through the indium precursor. Biomineralization often controls crystallization through interactions of negatively charged templates with the cationic components of a mineral. Translating the concept of deterministically positioned negatively charged side chains from natural mineralization into InP QD nucleation and growth can lead to a

novel form of reaction control through modulating the indium precursor reactivity. Chapter 3 demonstrates that a polycarboxylic acid acts as a mineralization inhibitor by decreasing the reactivity of the indium precursor to afford QD size control.

The last challenge in InP nanocrystal synthesis addressed here is the limited routes to anisotropic InP nanocrystals. Typical methods of facet control used to make II-VI nanoplatelets and nanorods are not transferrable to InP, proposed to be due to the difficulty of charge passivating required facets.[65] However, anisotropic growth has been induced in colloidal InP synthesis through the SLS growth mechanism, as discussed above. There are parallels between the spatially confined nucleation inside the liquid metal particle for SLS and morphological control of biomineralization in a confined space. Disfavored morphologies can be achieved by imposing spatial restrictions on the growing crystallization front, by the macromolecular framework in biomineralization or by the liquid metal particle in the SLS mechanism. Inspired by the importance of tuning cation-ligand interactions in biomineralization, an indium precursor with a weakly binding carboxylate was chosen to access SLS nanowire growth in the aminophosphine-based chemistry.

1.4 REFERENCES

(1) Vekilov, P. G. Nucleation. *Crystal Growth & Design* **2010**, *10* (12), 5007–5019. https://doi.org/10.1021/cg1011633.
(2) Whitehead, C. B.; Özkar, S.; Finke, R. G. LaMer's 1950 Model for Particle Formation of Instantaneous Nucleation and Diffusion-Controlled Growth: A Historical Look at the Model's Origins, Assumptions, Equations, and Underlying Sulfur Sol Formation Kinetics Data. *Chem. Mater.* **2019**, *31* (18), 7116–7132. https://doi.org/10.1021/acs.chemmater.9b01273.
(3) Rempel, J. Y.; Bawendi, M. G.; Jensen, K. F. Insights into the Kinetics of Semiconductor Nanocrystal Nucleation and Growth. *J. Am. Chem. Soc.* **2009**, *131* (12), 4479–4489. https://doi.org/10.1021/ja809156t.
(4) De Yoreo, J. J.; Gilbert, P. U. P. A.; Sommerdijk, N. A. J. M.; Penn, R. L.; Whitelam, S.; Joester, D.; Zhang, H.; Rimer, J. D.; Navrotsky, A.; Banfield, J. F.; Wallace, A. F.; Michel, F. M.; Meldrum, F. C.; Cölfen, H.; Dove, P. M. Crystallization by Particle Attachment in Synthetic, Biogenic, and Geologic Environments. *Science* **2015**, *349* (6247), aaa6760. https://doi.org/10.1126/science.aaa6760.

(5) Anderson, M. W.; Bennett, M.; Cedeno, R.; Cölfen, H.; Cox, S. J.; Cruz-Cabeza, A. J.; Yoreo, J. J. D.; Drummond-Brydson, R.; Dudek, M. K.; Fichthorn, K. A.; Finney, A. R.; Ford, I.; Galloway, J. M.; Gebauer, D.; Grossier, R.; Harding, J. H.; Hare, A.; Horváth, D.; Hunter, L.; Kim, J.; Kimura, Y.; Kirschhock, C. E. A.; Kiselev, A. A.; Kras, W.; Kuttner, C.; Lee, A. Y.; Liao, Z.; Maini, L.; Lill, S. O. N.; Pellens, N.; Price, S. L.; Rietveld, I. B.; Rimer, J. D.; Roberts, K. J.; Rogal, J.; Salvalaglio, M.; Sandei, I.; Schuszter, G.; Sefcik, J.; Sun, W.; Horst, J. H. ter; Ukrainczyk, M.; Driessche, A. E. S. V.; Veesler, S.; Vekilov, P. G.; Verma, V.; Whale, T.; Wheatcroft, H. P.; Zeglinski, J. Understanding Crystal Nucleation Mechanisms: Where Do We Stand? General Discussion. *Faraday Discuss.* **2022**, *235* (0), 219–272. https://doi.org/10.1039/D2FD90021A.

(6) Du, J. S.; Bae, Y.; De Yoreo, J. J. Non-Classical Crystallization in Soft and Organic Materials. *Nat Rev Mater* **2024**, *9* (4), 229–248. https://doi.org/10.1038/s41578-023-00637-y.

(7) Jin, B.; Chen, Y.; Pyles, H.; Baer, M. D.; Legg, B. A.; Wang, Z.; Washton, N. M.; Mueller, K. T.; Baker, D.; Schenter, G. K.; Mundy, C. J.; De Yoreo, J. J. Formation, Chemical Evolution and Solidification of the Dense Liquid Phase of Calcium (Bi)Carbonate. *Nat. Mater.* **2025**, *24* (1), 125–132. https://doi.org/10.1038/s41563-024-02025-5.

(8) Özkar, S.; Finke, R. G. Nanoparticle Nucleation Is Termolecular in Metal and Involves Hydrogen: Evidence for a Kinetically Effective Nucleus of Three {Ir3H2x·P2W15Nb3O62}6– in Ir(0)n Nanoparticle Formation From [(1,5-COD)IrI·P2W15Nb3O62]8– Plus Dihydrogen. *J. Am. Chem. Soc.* **2017**, *139* (15), 5444–5457. https://doi.org/10.1021/jacs.7b00958.

(9) Laxson, W. W.; Finke, R. G. Nucleation Is Second Order: An Apparent Kinetically Effective Nucleus of Two for Ir(0)n Nanoparticle Formation from [(1,5-COD)IrI·P2W15Nb3O62]8– Plus Hydrogen. *J. Am. Chem. Soc.* **2014**, *136* (50), 17601–17615. https://doi.org/10.1021/ja510263s.

(10) Handwerk, D. R.; Shipman, P. D.; Whitehead, C. B.; Özkar, S.; Finke, R. G. Mechanism-Enabled Population Balance Modeling of Particle Formation En Route to Particle Average Size and Size Distribution Understanding and Control. *J. Am. Chem. Soc.* **2019**, *141* (40), 15827–15839. https://doi.org/10.1021/jacs.9b06364.

(11) Trentler, T. J.; Goel, S. C.; Hickman, K. M.; Viano, A. M.; Chiang, M. Y.; Beatty, A. M.; Gibbons, P. C.; Buhro, W. E. Solution−Liquid−Solid Growth of Indium Phosphide Fibers from Organometallic Precursors: Elucidation of Molecular and Nonmolecular Components of the Pathway. *J. Am. Chem. Soc.* **1997**, *119* (9), 2172–2181. https://doi.org/10.1021/ja9640859.

(12) Gary, D. C.; Cossairt, B. M. Role of Acid in Precursor Conversion During InP Quantum Dot Synthesis. *Chem. Mater.* **2013**, *25* (12), 2463–2469. https://doi.org/10.1021/cm401289j.

(13) McMurtry, B. M.; Qian, K.; Teglasi, J. K.; Swarnakar, A. K.; De Roo, J.; Owen, J. S. Continuous Nucleation and Size Dependent Growth Kinetics of Indium Phosphide Nanocrystals. *Chem. Mater.* **2020**, *32* (10), 4358–4368. https://doi.org/10.1021/acs.chemmater.0c01561.

(14) Cho, W.; Zhou, Z.; Lin, R.; Ondry, J. C.; Talapin, D. V. Synthesis of Colloidal GaN and AlN Nanocrystals in Biphasic Molten Salt/Organic Solvent Mixtures under High-Pressure Ammonia. *ACS Nano* **2023**, *17* (2), 1315–1326. https://doi.org/10.1021/acsnano.2c09552.

(15) Bénas, J.-S.; Liang, F.-C.; Huang, Y.-H.; Liu, F.-C.; Ou, C.-H.; Oikawa, R.; Kobayashi, R.; Mizoguchi, S.; Igarashi, Y.; Chiba, T.; Kido, J.; Kuo, C.-C. Room-Temperature Synthesis

of Triple-Cation Green Perovskite Quantum Dots for Optoelectronic Applications. *Mater. Horiz.* **2025**, *12* (4), 1334–1345. https://doi.org/10.1039/D4MH01270D.
(16) Gary, D. C.; Terban, M. W.; Billinge, S. J. L.; Cossairt, B. M. Two-Step Nucleation and Growth of InP Quantum Dots via Magic-Sized Cluster Intermediates. *Chem. Mater.* **2015**, *27* (4), 1432–1441. https://doi.org/10.1021/acs.chemmater.5b00286.
(17) Hendricks, M. P.; Campos, M. P.; Cleveland, G. T.; Jen-La Plante, I.; Owen, J. S. A Tunable Library of Substituted Thiourea Precursors to Metal Sulfide Nanocrystals. *Science* **2015**, *348* (6240), 1226–1230. https://doi.org/10.1126/science.aaa2951.
(18) Prins, P. T.; Montanarella, F.; Dümbgen, K.; Justo, Y.; van der Bok, J. C.; Hinterding, S. O. M.; Geuchies, J. J.; Maes, J.; De Nolf, K.; Deelen, S.; Meijer, H.; Zinn, T.; Petukhov, A. V.; Rabouw, F. T.; De Mello Donega, C.; Vanmaekelbergh, D.; Hens, Z. Extended Nucleation and Superfocusing in Colloidal Semiconductor Nanocrystal Synthesis. *Nano Lett.* **2021**, *21* (6), 2487–2496. https://doi.org/10.1021/acs.nanolett.0c04813.
(19) Cossairt, B. M. Shining Light on Indium Phosphide Quantum Dots: Understanding the Interplay among Precursor Conversion, Nucleation, and Growth. *Chem. Mater.* **2016**, *28* (20), 7181–7189. https://doi.org/10.1021/acs.chemmater.6b03408.
(20) Franke, D.; Harris, D. K.; Xie, L.; Jensen, K. F.; Bawendi, M. G. The Unexpected Influence of Precursor Conversion Rate in the Synthesis of III–V Quantum Dots. *Angewandte Chemie* **2015**, *127* (48), 14507–14511. https://doi.org/10.1002/ange.201505972.
(21) Xie, R.; Li, Z.; Peng, X. Nucleation Kinetics vs Chemical Kinetics in the Initial Formation of Semiconductor Nanocrystals. *J. Am. Chem. Soc.* **2009**, *131* (42), 15457–15466. https://doi.org/10.1021/ja9063102.
(22) Sugimoto, T. Underlying Mechanisms in Size Control of Uniform Nanoparticles. *Journal of Colloid and Interface Science* **2007**, *309* (1), 106–118. https://doi.org/10.1016/j.jcis.2007.01.036.
(23) LaMer, V. K.; Dinegar, R. H. Theory, Production and Mechanism of Formation of Monodispersed Hydrosols. *J. Am. Chem. Soc.* **1950**, *72* (11), 4847–4854. https://doi.org/10.1021/ja01167a001.
(24) Abécassis, B.; Bouet, C.; Garnero, C.; Constantin, D.; Lequeux, N.; Ithurria, S.; Dubertret, B.; Pauw, B. R.; Pontoni, D. Real-Time in Situ Probing of High-Temperature Quantum Dots Solution Synthesis. *Nano Lett.* **2015**, *15* (4), 2620–2626. https://doi.org/10.1021/acs.nanolett.5b00199.
(25) Watzky, M. A.; Finke, R. G. Transition Metal Nanocluster Formation Kinetic and Mechanistic Studies. A New Mechanism When Hydrogen Is the Reductant: Slow, Continuous Nucleation and Fast Autocatalytic Surface Growth. *J. Am. Chem. Soc.* **1997**, *119* (43), 10382–10400. https://doi.org/10.1021/ja9705102.
(26) Larson, H.; Cossairt, B. M. Indium–Poly(Carboxylic Acid) Ligand Interactions Modify InP Quantum Dot Nucleation and Growth. *Chem. Mater.* **2023**, *35* (15), 6152–6160. https://doi.org/10.1021/acs.chemmater.3c01309.
(27) Whitehead, C. B.; Watzky, M. A.; Finke, R. G. "Burst Nucleation" vs Autocatalytic, "Burst" Growth in Near-Monodisperse Particle-Formation Reactions. *J. Phys. Chem. C* **2020**, *124* (45), 24543–24554. https://doi.org/10.1021/acs.jpcc.0c06875.
(28) Jean, J. H.; Ring, T. A. Nucleation and Growth of Monosized Titania Powders from Alcohol Solution. *Langmuir* **1986**, *2* (2), 251–255. https://doi.org/10.1021/la00068a025.
(29) Pokratath, R.; Lermusiaux, L.; Checchia, S.; Mathew, J. P.; Cooper, S. R.; Mathiesen, J. K.; Landaburu, G.; Banerjee, S.; Tao, S.; Reichholf, N.; Billinge, S. J. L.; Abécassis, B.;

Jensen, K. M. Ø.; De Roo, J. An Amorphous Phase Precedes Crystallization: Unraveling the Colloidal Synthesis of Zirconium Oxide Nanocrystals. *ACS Nano* **2023**. https://doi.org/10.1021/acsnano.3c02149.

(30) Campos, M. P.; Roo, J. D.; Greenberg, M. W.; McMurtry, B. M.; Hendricks, M. P.; Bennett, E.; Saenz, N.; Sfeir, M. Y.; Abécassis, B.; Ghose, S. K.; Owen, J. S. Growth Kinetics Determine the Polydispersity and Size of PbS and PbSe Nanocrystals. *Chem. Sci.* **2022**, *13* (16), 4555–4565. https://doi.org/10.1039/D1SC06098H.

(31) Abécassis, B.; W. Greenberg, M.; Bal, V.; M. McMurtry, B.; P. Campos, M.; Guillemeney, L.; Mahler, B.; Prevost, S.; Sharpnack, L.; P. Hendricks, M.; DeRosha, D.; Bennett, E.; Saenz, N.; Peters, B.; S. Owen, J. Persistent Nucleation and Size Dependent Attachment Kinetics Produce Monodisperse PbS Nanocrystals. *Chemical Science* **2022**, *13* (17), 4977–4983. https://doi.org/10.1039/D1SC06134H.

(32) Mozaffari, S.; Li, W.; Thompson, C.; Ivanov, S.; Seifert, S.; Lee, B.; Kovarik, L.; Karim, A. M. Colloidal Nanoparticle Size Control: Experimental and Kinetic Modeling Investigation of the Ligand–Metal Binding Role in Controlling the Nucleation and Growth Kinetics. *Nanoscale* **2017**, *9* (36), 13772–13785. https://doi.org/10.1039/C7NR04101B.

(33) García de Arquer, F. P.; Talapin, D. V.; Klimov, V. I.; Arakawa, Y.; Bayer, M.; Sargent, E. H. Semiconductor Quantum Dots: Technological Progress and Future Challenges. *Science* **2021**, *373* (6555), eaaz8541. https://doi.org/10.1126/science.aaz8541.

(34) C. Osypiw, A. R.; Lee, S.; Jung, S.-M.; Leoni, S.; M. Smowton, P.; Hou, B.; Min Kim, J.; J. Amaratunga, G. A. Solution-Processed Colloidal Quantum Dots for Light Emission. *Materials Advances* **2022**, *3* (17), 6773–6790. https://doi.org/10.1039/D2MA00375A.

(35) Yue, L.-Q.; Shi, Y.-L.; Sun, N.-F.; Qiang, S.; Qin, J.-K.; Zhen, L.; Xu, C.-Y. InP Low-Dimensional Nanomaterials for Electronic and Optoelectronic Device Applications: A Review. *Advanced Sensor Research* **2023**, *2* (10), 2200101. https://doi.org/10.1002/adsr.202200101.

(36) Zafar, F.; Iqbal, A. Indium Phosphide Nanowires and Their Applications in Optoelectronic Devices. *Proceedings of the Royal Society A: Mathematical, Physical and Engineering Sciences* **2016**, *472* (2187), 20150804. https://doi.org/10.1098/rspa.2015.0804.

(37) Abdellatif, A. A.; Younis ,Mahmoud A; Alsharidah ,Mansour; Al Rugaie ,Osamah; and Tawfeek, H. M. Biomedical Applications of Quantum Dots: Overview, Challenges, and Clinical Potential. *International Journal of Nanomedicine* **2022**, *17*, 1951–1970. https://doi.org/10.2147/IJN.S357980.

(38) Pandey, S.; Bodas, D. High-Quality Quantum Dots for Multiplexed Bioimaging: A Critical Review. *Advances in Colloid and Interface Science* **2020**, *278*, 102137. https://doi.org/10.1016/j.cis.2020.102137.

(39) Chee, A. K.-W. On Current Technology for Light Absorber Materials Used in Highly Efficient Industrial Solar Cells. *Renewable and Sustainable Energy Reviews* **2023**, *173*, 113027. https://doi.org/10.1016/j.rser.2022.113027.

(40) Shih, J.-A.; Yang, S.-J.; Chen, C.-Y.; Sone, M.; Chang, T.-F. M.; Pu, Y.-C.; Hsu, Y.-J. Near-Infrared-Responsive Semiconductor Quantum Dots for Solar Photocatalysis. *ACS Appl. Nano Mater.* **2025**. https://doi.org/10.1021/acsanm.5c00629.

(41) Kagan, C. R.; Lifshitz, E.; Sargent, E. H.; Talapin, D. V. Building Devices from Colloidal Quantum Dots. *Science* **2016**, *353* (6302), aac5523. https://doi.org/10.1126/science.aac5523.

(42) Ding, P.; Chen, D.; Ko, P. K.; Qammar, M.; Geng, P.; Guo, L.; Halpert, J. E. Nanomaterials for Spin-Based Quantum Information. *Nanoscale* **2024**. https://doi.org/10.1039/D4NR04012K.
(43) Cao, Q.; Feng, J.; Chang, K. T.; Liang, W.; Lu, H. Emerging Opportunities of Colloidal Quantum Dots for Photocatalytic Organic Transformations. *Advanced Materials n/a* (n/a), 2409096. https://doi.org/10.1002/adma.202409096.
(44) Jang, E.; Jang, H. Review: Quantum Dot Light-Emitting Diodes. *Chem. Rev.* **2023**. https://doi.org/10.1021/acs.chemrev.2c00695.
(45) Lin, S.; Peng, X. Current Status and Challenges of Solar Cells Based on Semiconductor Nanocrystals. *Energy Fuels* **2021**, *35* (23), 18928–18941. https://doi.org/10.1021/acs.energyfuels.1c02423.
(46) Liz-Marzán, L. M.; Artzi, N.; Bals, S.; Buriak, J. M.; Chan, W. C. W.; Chen, X.; Hersam, M. C.; Kim, I.-D.; Millstone, J. E.; Mulvaney, P.; Parak, W. J.; Rogach, A.; Schaak, R. E. Celebrating a Nobel Prize to the "Discovery of Quantum Dots, an Essential Milestone in Nanoscience." *ACS Nano* **2023**, *17* (20), 19474–19475. https://doi.org/10.1021/acsnano.3c09671.
(47) Almeida, G.; Ubbink, R. F.; Stam, M.; du Fossé, I.; Houtepen, A. J. InP Colloidal Quantum Dots for Visible and Near-Infrared Photonics. *Nat Rev Mater* **2023**, *8* (11), 742–758. https://doi.org/10.1038/s41578-023-00596-4.
(48) Ramasamy, P.; Kim, N.; Kang, Y.-S.; Ramirez, O.; Lee, J.-S. Tunable, Bright, and Narrow-Band Luminescence from Colloidal Indium Phosphide Quantum Dots. *Chem. Mater.* **2017**, *29* (16), 6893–6899. https://doi.org/10.1021/acs.chemmater.7b02204.
(49) A. Gazis, T.; J. Cartlidge, A.; D. Matthews, P. Colloidal III–V Quantum Dots: A Synthetic Perspective. *Journal of Materials Chemistry C* **2023**, *11* (12), 3926–3935. https://doi.org/10.1039/D2TC05234B.
(50) Saeboe, A. M.; Nikiforov, A. Yu.; Toufanian, R.; Kays, J. C.; Chern, M.; Casas, J. P.; Han, K.; Piryatinski, A.; Jones, D.; Dennis, A. M. Extending the Near-Infrared Emission Range of Indium Phosphide Quantum Dots for Multiplexed In Vivo Imaging. *Nano Lett.* **2021**, *21* (7), 3271–3279. https://doi.org/10.1021/acs.nanolett.1c00600.
(51) Zhang, W.; Duan, X.; Chen, L.; Wang, K.; Song, Y.; Wang, W.; Sun, X. W. Synthesis of Deep Blue InP Quantum Dots via HF Etching for Light-Emitting Diodes. *ACS Appl. Electron. Mater.* **2025**. https://doi.org/10.1021/acsaelm.5c00503.
(52) Zhang, W.; Tan, Y.; Duan, X.; Zhao, F.; Liu, H.; Chen, W.; Liu, P.; Liu, X.; Wang, K.; Zhang, Z.; Sun, X. W. High Quantum Yield Blue InP/ZnS/ZnS Quantum Dots Based on Bromine Passivation for Efficient Blue Light-Emitting Diodes. *Advanced Optical Materials* **2022**, *n/a* (n/a), 2200685. https://doi.org/10.1002/adom.202200685.
(53) Zhang, W.; Duan, X.; Tan, Y.; Hao, J.; Zhu, H.; Wang, Q.; Yang, H.; Liu, H.; Wang, K.; Wang, Z.; Wang, Y.-L.; Song, Y.; Sun, X. W. Giant Pyramidal Near-Infrared InP/ZnS Quantum Dots with Size Over 15 Nm for Cell Imaging. *Laser & Photonics Reviews* **2024**, *18* (10), 2400367. https://doi.org/10.1002/lpor.202400367.
(54) Cui, Z.; Yang, D.; Qin, S.; Wen, Z.; He, H.; Mei, S.; Zhang, W.; Xing, G.; Liang, C.; Guo, R. Advances, Challenges, and Perspectives for Heavy-Metal-Free Blue-Emitting Indium Phosphide Quantum Dot Light-Emitting Diodes. *Advanced Optical Materials* **2023**, *11* (4), 2202036. https://doi.org/10.1002/adom.202202036.

(55) Won, Y.-H.; Cho, O.; Kim, T.; Chung, D.-Y.; Kim, T.; Chung, H.; Jang, H.; Lee, J.; Kim, D.; Jang, E. Highly Efficient and Stable InP/ZnSe/ZnS Quantum Dot Light-Emitting Diodes. *Nature* **2019**, *575* (7784), 634–638. https://doi.org/10.1038/s41586-019-1771-5.

(56) Van Avermaet, H.; Schiettecatte, P.; Hinz, S.; Giordano, L.; Ferrari, F.; Nayral, C.; Delpech, F.; Maultzsch, J.; Lange, H.; Hens, Z. Full-Spectrum InP-Based Quantum Dots with Near-Unity Photoluminescence Quantum Efficiency. *ACS Nano* **2022**, *16* (6), 9701–9712. https://doi.org/10.1021/acsnano.2c03138.

(57) Wang, S.; Li, Y.; Chen, J.; Lin, O.; Niu, W.; Yang, C.; Tang, A. Development and Challenges of Indium Phosphide-Based Quantum-Dot Light-Emitting Diodes. *Journal of Photochemistry and Photobiology C: Photochemistry Reviews* **2023**, *55*, 100588. https://doi.org/10.1016/j.jphotochemrev.2023.100588.

(58) Mukherjee, C.; Deng, M.; Nodjiadjim, V.; Riet, M.; Mismer, C.; Guendouz, D.; Caillaud, C.; Bertin, H.; Vaissiere, N.; Luisier, M.; Wen, X.; De Matos, M.; Mounaix, P.; Maneux, C. Towards Monolithic Indium Phosphide (InP)-Based Electronic Photonic Technologies for beyond 5G Communication Systems. *Applied Sciences* **2021**, *11* (5), 2393. https://doi.org/10.3390/app11052393.

(59) Markman, B.; Schröter, M. Indium-Phosphide Transistors: A Review of Current State and Suitability for Commercial > 100-GHz Wireless Communication Systems. *IEEE Microwave Magazine* **2024**, *25* (10), 38–53. https://doi.org/10.1109/MMM.2024.3428191.

(60) Mediavilla, I.; Pura, J. L.; Hinojosa, V. G.; Galiana, B.; Hrachowina, L.; Borgström, M. T.; Jimenez, J. Composition, Optical Resonances, and Doping of InP/InGaP Nanowires for Tandem Solar Cells: A Micro-Raman Analysis. *ACS Nano* **2024**. https://doi.org/10.1021/acsnano.3c12973.

(61) Wang, F.; Buhro, W. E. Determination of the Rod−Wire Transition Length in Colloidal Indium Phosphide Quantum Rods. *J. Am. Chem. Soc.* **2007**, *129* (46), 14381–14387. https://doi.org/10.1021/ja075015c.

(62) Wang, J.; Gudiksen, M. S.; Duan, X.; Cui, Y.; Lieber, C. M. Highly Polarized Photoluminescence and Photodetection from Single Indium Phosphide Nanowires. *Science* **2001**, *293* (5534), 1455–1457. https://doi.org/10.1126/science.1062340.

(63) Bucci, G.; Zannier, V.; Rossi, F.; Musiał, A.; Boniecki, J.; Sęk, G.; Sorba, L. Zincblende InAsxP1–x/InP Quantum Dot Nanowires for Telecom Wavelength Emission. *ACS Appl. Mater. Interfaces* **2024**, *16* (20), 26491–26499. https://doi.org/10.1021/acsami.4c00615.

(64) Duan, X.; Huang, Y.; Cui, Y.; Wang, J.; Lieber, C. M. Indium Phosphide Nanowires as Building Blocks for Nanoscale Electronic and Optoelectronic Devices. *Nature* **2001**, *409* (6816), 66–69. https://doi.org/10.1038/35051047.

(65) Dümbgen, K. C.; Zito, J.; Infante, I.; Hens, Z. Shape, Electronic Structure, and Trap States in Indium Phosphide Quantum Dots. *Chem. Mater.* **2021**, *33* (17), 6885–6896. https://doi.org/10.1021/acs.chemmater.1c01795.

(66) Ubbink, R. F.; Almeida, G.; Iziyi, H.; du Fossé, I.; Verkleij, R.; Ganapathy, S.; van Eck, E. R. H.; Houtepen, A. J. A Water-Free In Situ HF Treatment for Ultrabright InP Quantum Dots. *Chem. Mater.* **2022**, *34* (22), 10093–10103. https://doi.org/10.1021/acs.chemmater.2c02800.

(67) Xie, R.; Battaglia, D.; Peng, X. Colloidal InP Nanocrystals as Efficient Emitters Covering Blue to Near-Infrared. *J. Am. Chem. Soc.* **2007**, *129* (50), 15432–15433. https://doi.org/10.1021/ja076363h.

(68) Respekta, D.; Schiettecatte, P.; Giordano, L.; De Vlamynck, N.; Geiregat, P.; Climente, J. I.; Hens, Z. Energy-Level Structure and Band Alignment in InP/ZnSe Core/Shell Quantum Dots. *ACS Nano* **2025**. https://doi.org/10.1021/acsnano.5c02258.
(69) Hens, Z.; Llusar, J.; Infante, I. Fuzzy Band Structure of Quantum Dots by Bloch Orbital Expansion: Unconventional Insights into Geometric-Electronic Structure Relations. *ACS Nano* **2025**. https://doi.org/10.1021/acsnano.4c17941.
(70) Berkinsky, D. B.; Proppe, A. H.; Utzat, H.; Krajewska, C. J.; Sun, W.; Šverko, T.; Yoo, J. J.; Chung, H.; Won, Y.-H.; Kim, T.; Jang, E.; Bawendi, M. G. Narrow Intrinsic Line Widths and Electron–Phonon Coupling of InP Colloidal Quantum Dots. *ACS Nano* **2023**. https://doi.org/10.1021/acsnano.2c10237.
(71) Stam, M.; Almeida, G.; Ubbink, R. F.; van der Poll, L. M.; Vogel, Y. B.; Chen, H.; Giordano, L.; Schiettecatte, P.; Hens, Z.; Houtepen, A. J. Near-Unity Photoluminescence Quantum Yield of Core-Only InP Quantum Dots via a Simple Postsynthetic InF3 Treatment. *ACS Nano* **2024**. https://doi.org/10.1021/acsnano.4c03290.
(72) Park, N.; Beck, R. A.; Hoang, K. K.; Ladd, D. M.; Abramson, J. E.; Rivera-Maldonado, R. A.; Nguyen, H. A.; Monahan, M.; Seidler, G. T.; Toney, M. F.; Li, X.; Cossairt, B. M. Colloidal, Room-Temperature Growth of Metal Oxide Shells on InP Quantum Dots. *Inorg. Chem.* **2023**. https://doi.org/10.1021/acs.inorgchem.3c00161.
(73) Xu, Z.; Li, Y.; Li, J.; Pu, C.; Zhou, J.; Lv, L.; Peng, X. Formation of Size-Tunable and Nearly Monodisperse InP Nanocrystals: Chemical Reactions and Controlled Synthesis. *Chem. Mater.* **2019**, *31* (14), 5331–5341. https://doi.org/10.1021/acs.chemmater.9b02292.
(74) Hu, R.; He, F.; Hou, R.; Wu, Z.; Zhang, X.; Shen, H. The Narrow Synthetic Window for Highly Homogenous InP Quantum Dots toward Narrow Red Emission. *Inorg. Chem.* **2024**. https://doi.org/10.1021/acs.inorgchem.3c04358.
(75) Ramasamy, P.; Ko, K.-J.; Kang, J.-W.; Lee, J.-S. Two-Step "Seed-Mediated" Synthetic Approach to Colloidal Indium Phosphide Quantum Dots with High-Purity Photo- and Electroluminescence. *Chem. Mater.* **2018**, *30* (11), 3643–3647. https://doi.org/10.1021/acs.chemmater.8b02049.
(76) Click, S. M.; Rosenthal, S. J. Synthesis, Surface Chemistry, and Fluorescent Properties of InP Quantum Dots. *Chem. Mater.* **2023**. https://doi.org/10.1021/acs.chemmater.2c03074.
(77) Gary, D. C.; Flowers, S. E.; Kaminsky, W.; Petrone, A.; Li, X.; Cossairt, B. M. Single-Crystal and Electronic Structure of a 1.3 Nm Indium Phosphide Nanocluster. *J. Am. Chem. Soc.* **2016**, *138* (5), 1510–1513. https://doi.org/10.1021/jacs.5b13214.
(78) Sandeno, S. F.; Schnitzenbaumer, K. J.; Krajewski, S. M.; Beck, R. A.; Ladd, D. M.; Levine, K. R.; Dayton, D.; Toney, M. F.; Kaminsky, W.; Li, X.; Cossairt, B. M. Ligand Steric Profile Tunes the Reactivity of Indium Phosphide Clusters. *J. Am. Chem. Soc.* **2024**, *146* (5), 3102–3113. https://doi.org/10.1021/jacs.3c10203.
(79) Ritchhart, A.; Cossairt, B. M. Quantifying Ligand Exchange on InP Using an Atomically Precise Cluster Platform. *Inorg. Chem.* **2019**, *58* (4), 2840–2847. https://doi.org/10.1021/acs.inorgchem.8b03524.
(80) Klein, M. D.; Bisted, C. H.; Dou, F. Y.; Sandwisch, J. W.; Cossairt, B. M.; Khalil, M. Measuring Relative Energies of Ligand Binding Conformations on Nanocluster Surfaces with Temperature-Dependent FTIR Spectroscopy. *J. Phys. Chem. C* **2023**, *127* (34), 16970–16978. https://doi.org/10.1021/acs.jpcc.3c03951.
(81) Song, W.-S.; Lee, H.-S.; Lee, J. C.; Jang, D. S.; Choi, Y.; Choi, M.; Yang, H. Amine-Derived Synthetic Approach to Color-Tunable InP/ZnS Quantum Dots with High

Fluorescent Qualities. *J Nanopart Res* **2013**, *15* (6), 1750. https://doi.org/10.1007/s11051-013-1750-y.

(82) Tessier, M. D.; Dupont, D.; De Nolf, K.; De Roo, J.; Hens, Z. Economic and Size-Tunable Synthesis of InP/ZnE (E = S, Se) Colloidal Quantum Dots. *Chem. Mater.* **2015**, *27* (13), 4893–4898. https://doi.org/10.1021/acs.chemmater.5b02138.

(83) Tessier, M. D.; De Nolf, K.; Dupont, D.; Sinnaeve, D.; De Roo, J.; Hens, Z. Aminophosphines: A Double Role in the Synthesis of Colloidal Indium Phosphide Quantum Dots. *J. Am. Chem. Soc.* **2016**, *138* (18), 5923–5929. https://doi.org/10.1021/jacs.6b01254.

(84) Buffard, A.; Dreyfuss, S.; Nadal, B.; Heuclin, H.; Xu, X.; Patriarche, G.; Mézailles, N.; Dubertret, B. Mechanistic Insight and Optimization of InP Nanocrystals Synthesized with Aminophosphines. *Chem. Mater.* **2016**, *28* (16), 5925–5934. https://doi.org/10.1021/acs.chemmater.6b02456.

(85) Stone, D.; Li, X.; Naor, T.; Dai, J.; Remennik, S.; Banin, U. Size and Emission Control of Wurtzite InP Nanocrystals Synthesized from Cu3–xP by Cation Exchange. *Chem. Mater.* **2023**. https://doi.org/10.1021/acs.chemmater.3c02226.

(86) Liu, L.; Bai, B.; Yang, X.; Du, Z.; Jia, G. Anisotropic Heavy-Metal-Free Semiconductor Nanocrystals: Synthesis, Properties, and Applications. *Chem. Rev.* **2023**. https://doi.org/10.1021/acs.chemrev.2c00688.

(87) Chen, S.; Riedinger, A. Anisotropic and Hyperbranched InP Nanocrystals via Chemical Transformation of in Situ Produced In2O3. *Chem. Commun.* **2022**. https://doi.org/10.1039/D2CC03456E.

(88) Trentler, T. J.; Hickman, K. M.; Goel, S. C.; Viano, A. M.; Gibbons, P. C.; Buhro, W. E. Solution-Liquid-Solid Growth of Crystalline III-V Semiconductors: An Analogy to Vapor-Liquid-Solid Growth. *Science* **1995**, *270* (5243), 1791–1794. https://doi.org/10.1126/science.270.5243.1791.

(89) Kan, S.; Aharoni, A.; Mokari, T.; Banin, U. Shape Control of III–V Semiconductor Nanocrystals: Synthesis and Properties of InAs Quantum Rods. *Faraday Discuss.* **2003**, *125* (0), 23–38. https://doi.org/10.1039/B302898D.

(90) Ahrenkiel, S. P.; Mićić, O. I.; Miedaner, A.; Curtis, C. J.; Nedeljković, J. M.; Nozik, A. J. Synthesis and Characterization of Colloidal InP Quantum Rods. *Nano Lett.* **2003**, *3* (6), 833–837. https://doi.org/10.1021/nl034152e.

(91) Yu, H.; Li, J.; Loomis, R. A.; Wang, L.-W.; Buhro, W. E. Two- versus Three-Dimensional Quantum Confinement in Indium Phosphide Wires and Dots. *Nature Mater* **2003**, *2* (8), 517–520. https://doi.org/10.1038/nmat942.

(92) Nedeljković, J. M.; Mićić, O. I.; Ahrenkiel, S. P.; Miedaner, A.; Nozik, A. J. Growth of InP Nanostructures via Reaction of Indium Droplets with Phosphide Ions: Synthesis of InP Quantum Rods and InP−TiO2 Composites. *J. Am. Chem. Soc.* **2004**, *126* (8), 2632–2639. https://doi.org/10.1021/ja039311a.

(93) Fanfair, D. D.; Korgel, B. A. Bismuth Nanocrystal-Seeded III-V Semiconductor Nanowire Synthesis. *Crystal Growth & Design* **2005**, *5* (5), 1971–1976. https://doi.org/10.1021/cg0502587.

(94) Shweky, I.; Aharoni, A.; Mokari, T.; Rothenberg, E.; Nadler, M.; Popov, I.; Banin, U. Seeded Growth of InP and InAs Quantum Rods Using Indium Acetate and Myristic Acid. *Materials Science and Engineering: C* **2006**, *26* (5), 788–794. https://doi.org/10.1016/j.msec.2005.09.040.

(95) Wang, F.; Yu, H.; Li, J.; Hang, Q.; Zemlyanov, D.; Gibbons, P. C.; Wang; Janes, D. B.; Buhro, W. E. Spectroscopic Properties of Colloidal Indium Phosphide Quantum Wires. *J. Am. Chem. Soc.* **2007**, *129* (46), 14327–14335. https://doi.org/10.1021/ja074049h.
(96) Strupeit, T.; Klinke, C.; Kornowski, A.; Weller, H. Synthesis of InP Nanoneedles and Their Use as Schottky Devices. *ACS Nano* **2009**, *3* (3), 668–672. https://doi.org/10.1021/nn800846d.
(97) Liu, Z.; Sun, K.; Jian, W.-B.; Xu, D.; Lin, Y.-F.; Fang, J. Soluble InP and GaP Nanowires: Self-Seeded, Solution–Liquid–Solid Synthesis and Electrical Properties. *Chemistry – A European Journal* **2009**, *15* (18), 4546–4552. https://doi.org/10.1002/chem.200900190.
(98) Dorn, A.; Allen, P. M.; Bawendi, M. G. Electrically Controlling and Monitoring InP Nanowire Growth from Solution. *ACS Nano* **2009**, *3* (10), 3260–3265. https://doi.org/10.1021/nn900820h.
(99) H. Lim, T.; Ravi, S.; W. Bumby, C.; G. Etchegoin, P.; D. Tilley, R. Synthesis, Characterization and Photoconductivity of Highly Crystalline InP Nanowires Prepared from Solid Hydrogen Phosphide. *Journal of Materials Chemistry* **2009**, *19* (27), 4852–4856. https://doi.org/10.1039/B902474C.
(100) Banerjee, C.; L. Hughes, D.; Bochmann, M.; Nann, T. InP Nanowires from Surfactant - Free Thermolysis of Single Molecule Precursors. *Dalton Transactions* **2012**, *41* (24), 7244–7248. https://doi.org/10.1039/C2DT30283G.
(101) Valleix, R.; Cisnetti, F.; Okuno, H.; Boutinaud, P.; Chadeyron, G.; Boyer, D. Size-Controlled Indium Phosphide Quantum Dots for Bright and Tunable Light Emission by Simple Hindered Diamine Addition. *ACS Appl. Nano Mater.* **2021**, *4* (10), 11105–11114. https://doi.org/10.1021/acsanm.1c02577.
(102) Hamachi, L. S.; Yang, H.; Plante, I. J.-L.; Saenz, N.; Qian, K.; Campos, M. P.; Cleveland, G. T.; Rreza, I.; Oza, A.; Walravens, W.; Chan, E. M.; Hens, Z.; Crowther, A. C.; Owen, J. S. Precursor Reaction Kinetics Control Compositional Grading and Size of CdSe1−xSx Nanocrystal Heterostructures. *Chem. Sci.* **2019**, *10* (26), 6539–6552. https://doi.org/10.1039/C9SC00989B.
(103) Friedfeld, M. R.; Stein, J. L.; Ritchhart, A.; Cossairt, B. M. Conversion Reactions of Atomically Precise Semiconductor Clusters. *Acc. Chem. Res.* **2018**, *51* (11), 2803–2810. https://doi.org/10.1021/acs.accounts.8b00365.
(104) Kim, J. Y.; Steeves, A. H.; Kulik, H. J. Harnessing Organic Ligand Libraries for First-Principles Inorganic Discovery: Indium Phosphide Quantum Dot Precursor Design Strategies. *Chem. Mater.* **2017**, *29* (8), 3632–3643. https://doi.org/10.1021/acs.chemmater.7b00472.
(105) Xu, S.; Ziegler, J.; Nann, T. Rapid Synthesis of Highly Luminescent InP and InP/ZnS Nanocrystals. *J. Mater. Chem.* **2008**, *18* (23), 2653–2656. https://doi.org/10.1039/B803263G.
(106) Zhang, X.; Lv, H.; Xing, W.; Li, Y.; Geng, C.; Xu, S. Trioctylphosphine Accelerated Growth of InP Quantum Dots at Low Temperature. *Nanotechnology* **2021**, *33* (5), 055602. https://doi.org/10.1088/1361-6528/ac3180.
(107) Gary, D. C.; Glassy, B. A.; Cossairt, B. M. Investigation of Indium Phosphide Quantum Dot Nucleation and Growth Utilizing Triarylsilylphosphine Precursors. *Chem. Mater.* **2014**, *26* (4), 1734–1744. https://doi.org/10.1021/cm500102q.

(108) Nudelman, F.; Sommerdijk, N. A. J. M. Biomineralization as an Inspiration for Materials Chemistry. *Angewandte Chemie International Edition* **2012**, *51* (27), 6582–6596. https://doi.org/10.1002/anie.201106715.
(109) Albeck, S.; Aizenberg, J.; Addadi, L.; Weiner, S. Interactions of Various Skeletal Intracrystalline Components with Calcite Crystals. *J. Am. Chem. Soc.* **1993**, *115* (25), 11691–11697. https://doi.org/10.1021/ja00078a005.
(110) Addadi, L.; Weiner, S. Control and Design Principles in Biological Mineralization. *Angewandte Chemie International Edition in English* **1992**, *31* (2), 153–169. https://doi.org/10.1002/anie.199201531.
(111) Yang, W.; Cai, B.; Lachowski, K. J.; Yin, Q.; De Yoreo, J. J.; Pozzo, L. D.; Chen, C.-L. Insights into the Biomimetic Synthesis of 2D ZnO Nanomaterials through Peptoid Engineering. *J. Phys. Chem. Lett.* **2023**, *14* (43), 9732–9739. https://doi.org/10.1021/acs.jpclett.3c01882.
(112) Sarig, S.; Kahana, F.; Leshem, R. Selection of Threshold Agents for Calcium Sulfate Scale Control on the Basis of Chemical Structure. *Desalination* **1975**, *17* (2), 215–229. https://doi.org/10.1016/S0011-9164(00)84057-6.
(113) Murshed, M. Mechanism of Bone Mineralization. *Cold Spring Harb Perspect Med* **2018**, *8* (12), a031229. https://doi.org/10.1101/cshperspect.a031229.
(114) Pushpavanam, K.; Hellner, B.; Baneyx, F. Interrogating Biomineralization One Amino Acid at a Time: Amplification of Mutational Effects in Protein-Aided Titania Morphogenesis through Reaction-Diffusion Control. *Chem. Commun.* **2021**, *57* (39), 4803–4806. https://doi.org/10.1039/D1CC01521D.
(115) Weiner, S.; Nudelman, F.; Sone, E.; Zaslansky, P.; Addadi, L. Mineralized Biological Materials: A Perspective on Interfaces and Interphases Designed over Millions of Years. *Biointerphases* **2006**, *1* (2), P12–P14. https://doi.org/10.1116/1.2207607.
(116) Davila-Hernandez, F. A.; Jin, B.; Pyles, H.; Zhang, S.; Wang, Z.; Huddy, T. F.; Bera, A. K.; Kang, A.; Chen, C.-L.; De Yoreo, J. J.; Baker, D. Directing Polymorph Specific Calcium Carbonate Formation with de Novo Protein Templates. *Nat Commun* **2023**, *14* (1), 8191. https://doi.org/10.1038/s41467-023-43608-1.
(117) Hellner, B.; Stegmann, A. E.; Pushpavanam, K.; Bailey, M. J.; Baneyx, F. Phase Control of Nanocrystalline Inclusions in Bioprecipitated Titania with a Panel of Mutant Silica-Binding Proteins. *Langmuir* **2020**, *36* (29), 8503–8510. https://doi.org/10.1021/acs.langmuir.0c01108.
(118) Beniash, E.; Addadi, L.; Weiner, S. Cellular Control Over Spicule Formation in Sea Urchin Embryos: A Structural Approach. *Journal of Structural Biology* **1999**, *125* (1), 50–62. https://doi.org/10.1006/jsbi.1998.4081.
(119) Politi, Y.; Arad, T.; Klein, E.; Weiner, S.; Addadi, L. Sea Urchin Spine Calcite Forms via a Transient Amorphous Calcium Carbonate Phase. *Science* **2004**, *306* (5699), 1161–1164. https://doi.org/10.1126/science.1102289.
(120) Braun, P. V.; Osenar, P.; Stupp, S. I. Semiconducting Superlattices Templated by Molecular Assemblies. *Nature* **1996**, *380* (6572), 325–328. https://doi.org/10.1038/380325a0.
(121) Liu, Y.-H.; Wang, F.; Wang, Y.; Gibbons, P. C.; Buhro, W. E. Lamellar Assembly of Cadmium Selenide Nanoclusters into Quantum Belts. *J. Am. Chem. Soc.* **2011**, *133* (42), 17005–17013. https://doi.org/10.1021/ja206776g.

(122) Nevers, D. R.; Williamson, C. B.; Savitzky, B. H.; Hadar, I.; Banin, U.; Kourkoutis, L. F.; Hanrath, T.; Robinson, R. D. Mesophase Formation Stabilizes High-Purity Magic-Sized Clusters. *J. Am. Chem. Soc.* **2018**, *140* (10), 3652–3662. https://doi.org/10.1021/jacs.7b12175.

(123) Nguyen, H. A.; Sharp, D.; Fröch, J. E.; Cai, Y.-Y.; Wu, S.; Monahan, M.; Munley, C.; Manna, A.; Majumdar, A.; Kagan, C. R.; Cossairt, B. M. Deterministic Quantum Light Arrays from Giant Silica-Shelled Quantum Dots. *ACS Appl. Mater. Interfaces* **2023**, *15* (3), 4294–4302. https://doi.org/10.1021/acsami.2c18475.

(124) Han, Z.; Guo, A. X.; Luo, T.; Cai, T.; Mirkin, C. A. Biomineralization of Semiconductor Quantum Dots Using DNA-Functionalized Protein Nanoreactors. *Science Advances* **2025**, *11* (19), eadv6906. https://doi.org/10.1126/sciadv.adv6906.

(125) Bala, Y.; Farlay, D.; Boivin, G. Bone Mineralization: From Tissue to Crystal in Normal and Pathological Contexts. *Osteoporos Int* **2013**, *24* (8), 2153–2166. https://doi.org/10.1007/s00198-012-2228-y.

(126) Qi, X.; Helland, S.; Lowe, C. D.; Larson, H.; Cui, J.; Zheng, R.; Monahan, M.; Chen, C.-L.; De Yoreo, J.; Pfaendtner, J.; Cossairt, B. Toward Computation-Guided Design of Tunable Organic–Inorganic CdS Quantum Dot Binary Superlattices. *Nano Lett.* **2025**, *25* (10), 3989–3996. https://doi.org/10.1021/acs.nanolett.5c00024.

(127) Naser, N. Y.; Wixson, W. C.; Larson, H.; Cossairt, B. M.; Pozzo, L. D.; Baneyx, F. Biomimetic Mineralization of Positively Charged Silica Nanoparticles Templated by Thermoresponsive Protein Micelles: Applications to Electrostatic Assembly of Hierarchical and Composite Superstructures. *Soft Matter* **2025**, *21* (2), 166–178. https://doi.org/10.1039/D4SM00907J.

(128) Lowe, C. D.; Larson, H. C.; Cai, Y.; Chiang, H. T.; Pozzo, L. D.; Baneyx, F.; Cossairt, B. M. Induced Chirality in QDs Using Thermoresponsive Elastin-like Polypeptides. *Langmuir* **2024**. https://doi.org/10.1021/acs.langmuir.4c04339.

(129) Möller, J.; Schroer, M. A.; Erlkamp, M.; Grobelny, S.; Paulus, M.; Tiemeyer, S.; Wirkert, F. J.; Tolan, M.; Winter, R. The Effect of Ionic Strength, Temperature, and Pressure on the Interaction Potential of Dense Protein Solutions: From Nonlinear Pressure Response to Protein Crystallization. *Biophysical Journal* **2012**, *102* (11), 2641–2648. https://doi.org/10.1016/j.bpj.2012.04.043.

(130) Zuddas, P.; Mucci, A. Kinetics of Calcite Precipitation from Seawater: II. The Influence of the Ionic Strength. *Geochimica et Cosmochimica Acta* **1998**, *62* (5), 757–766. https://doi.org/10.1016/S0016-7037(98)00026-X.

(131) McPherson, A.; Gavira, J. A. Introduction to Protein Crystallization. *Acta Cryst F* **2014**, *70* (1), 2–20. https://doi.org/10.1107/S2053230X13033141.

(132) Baird, J. K.; Scott, S. C.; Kim, Y. W. Theory of the Effect of pH and Ionic Strength on the Nucleation of Protein Crystals. *Journal of Crystal Growth* **2001**, *232* (1), 50–62. https://doi.org/10.1016/S0022-0248(01)01059-4.

Chapter 2. EXPANDING PARAMETER SPACE TO ENABLE LOW TEMPERATURE SYNTHESIS OF CRYSTALLINE INDIUM PHOSPHIDE QUANTUM DOTS

2.1 INTRODUCTION

Covalent crystalline materials, such as InP, are colloquially termed ‘hard to make, hard to break’. This is in comparison to ionic materials, which have much softer, reversible bonding, and refers to the high temperatures necessary for crystallization, contrasted with the resulting lattice stability. One way this is understood is through microscopic reversibility of monomer attachment during crystallization, which requires reversible bond breaking and forming.[1] Comparing InP, CdS, $CsPbCl_3$, and NaCl, the predicted formation energies are -0.358, -0.774, -1.874, and -2.038 eV/atom,[2,3] and the electronegativity differences are 0.41, 0.89, 0.83 (Pb–Cl) and 2.37 (Cs–Cl), and 2.23, respectively. There is a clear trend between more favorable formation energies and the increased ionicity of the lattice. Additionally, when choosing available precursor chemistries to access more covalent materials, such as InP, we typically consider combining a source of In^{3+} and P^{3-}, but elemental trianions are extremely reactive and are not typically liberated as free species from precursors like $P(SiMe_3)_3$, in contrast to dianions and monoanions like S^{2-} and Cl^-.[4] Therefore, P^{3-} for InP is typically harvested from molecular phosphines through chemical reactions. Appropriately, reports of low or room temperature crystallization of cadmium chalcogenides and perovskites are common, and leverage polar solvents such as water, alcohols, or polar organic solvents to stabilize the ionic species.[5–10] If InP could be made to behave more like an ionic material, the crystallization would likely be more energetically favorable. An

additional source of inspiration was taken from nature, where a variety of biomineralization mechanisms induce the crystallization of many different minerals in ambient conditions. This is achieved through highly evolved control over supersaturation, nucleation, growth, and phase transformation by structural templates, mineralizers, and solution ionic composition.[11,12] For example, higher ionic strength has been observed to drastically increase the precipitation rate of calcite, and ionic strength plays an important role in protein crystallization.[13–16] These examples highlight ionicity and solvent environments as key predictors for ambient crystallization, which points towards exploring InP nucleation and growth in polar solvents.

Established methods for synthesizing high-quality InP quantum dots (QDs) proceed in anhydrous low-polarity solvents and require temperatures at or above 180 °C to achieve crystallinity. This is the case across both silylphosphine- and aminophosphine-based chemistries used for InP synthesis. For example, InP QDs with unity photoluminescence quantum yield (PL QY) used in red light-emitting diodes were synthesized at 280 °C using silylphosphine, and InP QDs with near unity PL QY made with the aminophosphine-based chemistry were synthesized at 180 °C.[17,18] In contrast, colloidal InP QD synthesis in polar solvents is severely understudied. In a 2022 study, Nguyen and coworkers collected a comprehensive dataset of previously reported InP synthetic conditions for machine learning.[19] Out of 220 different synthetic conditions, only two used polar solvents (dielectric constants >10), and the rest used one of 8 nonpolar solvents. The existing polar solvent syntheses used dimethylformamide or 4-ethylpyridine, sodium phosphide as a phosphorus precursor, and required multiple-day reaction times at 120-160 °C.[20,21] More recently, Talapin and coworkers demonstrated the synthesis of III-V nanocrystals in molten salts.[22] Specifically, the ionic molten salt solvent was able to facilitate the microscopic reversibility necessary for crystallization that is energetically difficult in strongly bonded materials.[1] For

applications requiring QDs in polar solvents, post-synthetic methods have been developed, such as ligand exchange or shelling.[23–29] There is a clear gap in the InP QD synthesis literature on exploring nucleation and growth in polar solvents.

In this work, we present the low-temperature synthesis of crystalline InP at 60 °C in a solvent mixture of nonpolar and polar aprotic solvents. Successful conditions were selected based on an initial screen of the parameter space using high-throughput synthesis in a microplate reader, modified for this study for air-free colloidal synthesis in a range of solvents. Scaled-up oleate-capped InP QDs made using optimized low-temperature conditions were characterized for crystallinity and emissive properties using powder X-ray diffraction (XRD), transmission electron microscopy (TEM), Raman spectroscopy, and absorbance and PL spectroscopies. Established hydrofluoric acid surface treatment enhanced the PL QY of the core-only InP QDs to 25%, demonstrating the high quality of the QDs despite a low-temperature synthesis (**Figure 1.1**). Extension of the method to other surface chemistries is also presented, producing myristate- and benzoate-capped QDs.

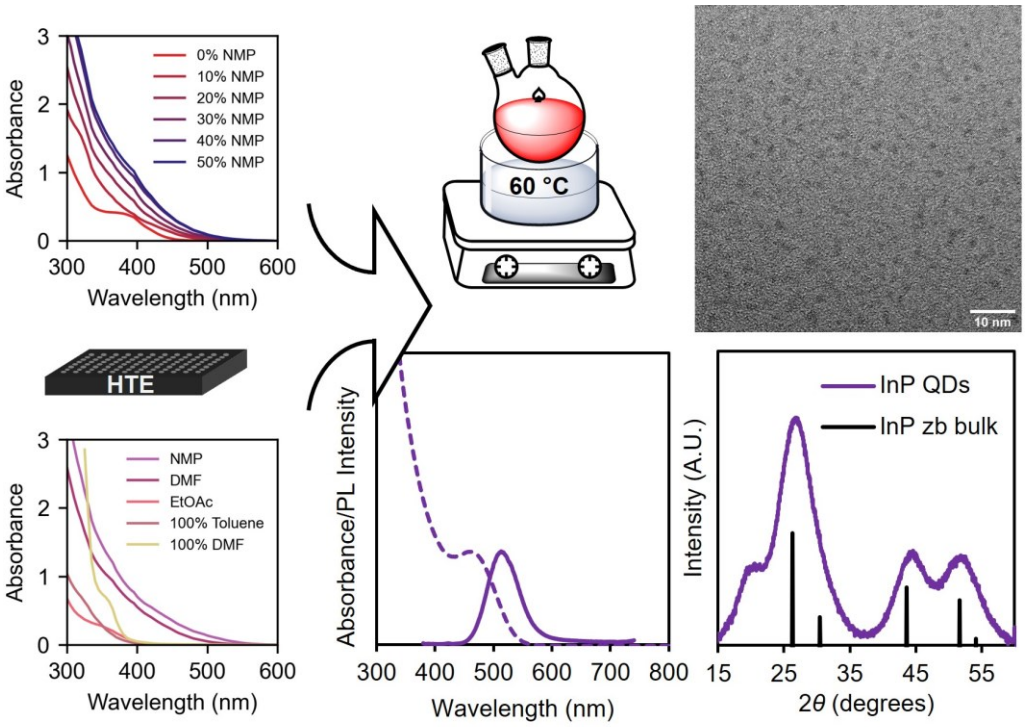


Figure 2.1 High throughput experimentation enabled the discovery of low temperature synthesis of high-quality, crystalline InP QDs. After surface treatment, the photoluminescent quantum yield of the resulting InP cores is 25%.

2.2 Results and Discussion

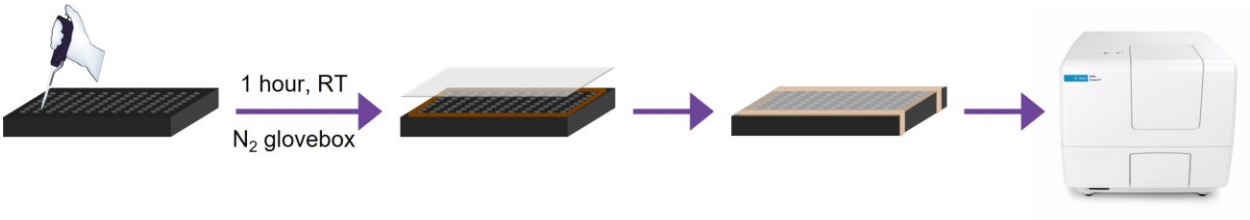
We hypothesized that crystallization of InP in polar solvents is more energetically favorable than in traditional nonpolar solvents due to two main considerations. First, we drew inspiration from the natural crystallization of ionic minerals and the behavior of ionic semiconductors such as halide perovskites. In these systems, the high dipole moment of polar solvents can enhance ionic character by polarizing constituent atoms, in our case, indium and phosphorus, thereby promoting crystallization. Second, we considered organic reaction mechanisms, where polar solvents are known to accelerate substitution reactions by stabilizing

charged transition states.[30] In light of these considerations and considering the case of InP, polar solvents would thereby lower the activation energy required for In–P bond formation. Supporting this view, a computational study by Kulik and coworkers identified the energetics of In–O bond cleavage as a key determinant of the energy barrier to In–P bond formation.[31] Specifically, they found that indium precursors bearing one monodentate and two bidentate carboxylate ligands exhibited a significantly lower activation barrier compared to precursors with fully bidentate ligands. This difference arises from the need to stabilize the partial negative charge on the dangling oxygen atom. We propose that polar solvents may facilitate this stabilization, either by favoring monodentate coordination or by lowering the transition state energy through solvation of partial charges. Together, these effects could reduce the energy barrier for InP crystallization in polar environments.

2.2.1 *High Throughput Colloidal InP QD Synthesis*

High-throughput experimentation (HTE) was chosen as an efficient method to explore the parameter space of InP QD synthesis in polar solvents. HTE has been employed in a variety of fields, including drug discovery in the pharmaceutical industry,[32–34] as well as materials science.[35–37] Exploring the parameter space for the low temperature synthesis of InP QDs presents an intriguing scenario for HTE using a multi-well microplate absorbance reader. The microplate reader controls temperature up to 70 °C and automatically monitors the absorbance of many reactions in the well plate over time. Microplate readers are typically used for biological systems in air- and water-containing environments. However, InP is highly oxygen sensitive and makes use of a pyrophoric phosphorus precursor, so the microplate was modified to ensure a rigorously air- and water-free internal environment. Starting with a chemically resistant quartz 96-well microplate, the HTE setup was optimized using a ketyl solution to monitor oxidation.[38] The

optimized setup was as follows: the microplate was prepared in a nitrogen glovebox, then sealed with high-temperature vacuum grease and a custom-sized quartz cover slip, with rubber bands to hold tension (illustrated in **Scheme 1.1**). Then, the microplate was transferred into the microplate reader, which maintained a low oxygen environment through a gas control system supplying argon gas. Additional details and safety information can be found in the SI.



Scheme 2.1 Air- and water-free microplate set up. A 96-well quartz microplate was prepared in a nitrogen glovebox, followed by 1 hour of reaction to allow for any protonolysis of $P(SiMe_3)_3$ in a controlled atmosphere, then high-temperature vacuum grease was added to seal a custom quartz coverslip compressed by rubber bands. The plate was then removed from the glovebox and loaded into an argon-filled plate reader for absorbance measurements.

We investigated a range of polar aprotic solvents, including ethyl acetate, N-methyl-2-pyrrolidone (NMP), dimethylformamide (DMF), and dimethylacetamide (DMA) with dielectric constants of 6.08, 32.6, 37, and 37.8, respectively.[39–41] Polar aprotic solvents were chosen specifically over protic solvents due to the hazardous reactivity of the phosphorus precursor, tris(trimethylsilyl)phosphine ($P(SiMe_3)_3$), with proton sources. Typical nonpolar solvents such as octadecene or toluene used for InP QD and nanocluster synthesis have dielectric constants around 2 - 2.5.[40,42] The other parameters explored were the ratio of polar to nonpolar solvent, carboxylic acid, reactant concentration, equivalents of excess carboxylic acid, amine or amide additives, indium precursors, and additional polar solvents.

The HTE workflow began with hypothesis-driven identification of parameter scopes, typically involving 20 unique reaction conditions, each run in triplicate per microplate. Triplicate reactions for each condition allowed for monitoring and minimizing the effect of non-uniform reactivity in the microplate. Stock solutions of the solvents, molecular additives, indium carboxylate precursor, and phosphorus precursor were prepared and added to the microplate in that order (**Table 2.1**, **Table 2.2**). Due to the absorbance detector sensitivity of the microplate reader, the reactions were run at a low concentration of 2 mM indium. For the preliminary parameter scope, the indium and phosphorus precursors were prepared in toluene, allowing for the addition of up to 50% polar solvent additives. Additional controls were designed to look at the impact of preparing indium and phosphorus stock solutions in toluene versus polar solvents. After 1 hour of room temperature reaction in the glovebox to allow for any protonolysis of $P(SiMe_3)_3$ in a contained environment, the microplate was loaded into the argon-filled plate reader and heated to 60 °C, where absorbance was monitored over a two-hour reaction period (**Table 2.3**). The results were interpreted based on the absorbance intensity of the reaction after two hours at 350 and 500 nm wavelengths. Absorbance at higher energy (350 nm) indicated the formation of InP semiconducting material, and absorbance at lower energy (500 nm) indicated the formation of larger QDs as opposed to high-energy absorbing clusters.[43,44]

Figure 2.2a shows a scatter plot mapping each of the HTE reactions by its absorbance intensity at 350 nm and at 500 nm. The data was considered based on the three possible outcomes for the reaction. First, conditions with low (<1.0) or zero absorbance intensity at 350 nm were reactions that failed to produce InP at 60 °C (**Figure 2.2a, gray**). Second, conditions with high (>1.0) absorbance intensity at 350 nm and low (<0.12) intensity at 500 nm were reactions that successfully produced In–P bonds but were not conducive to significant nanocrystal growth; for

example, a nanocluster would fall in this category (**Figure 2.2a, yellow**). Third, and of most interest, were conditions exhibiting high absorbance intensity at both 350 nm (>1.0) and 500 nm (>0.12), indicating that the reactions successfully produced semiconductor InP and induced QD growth (**Figure 2.2a red**). The following analysis discusses the different parameters that lead to a reaction producing results in one of these three categories.

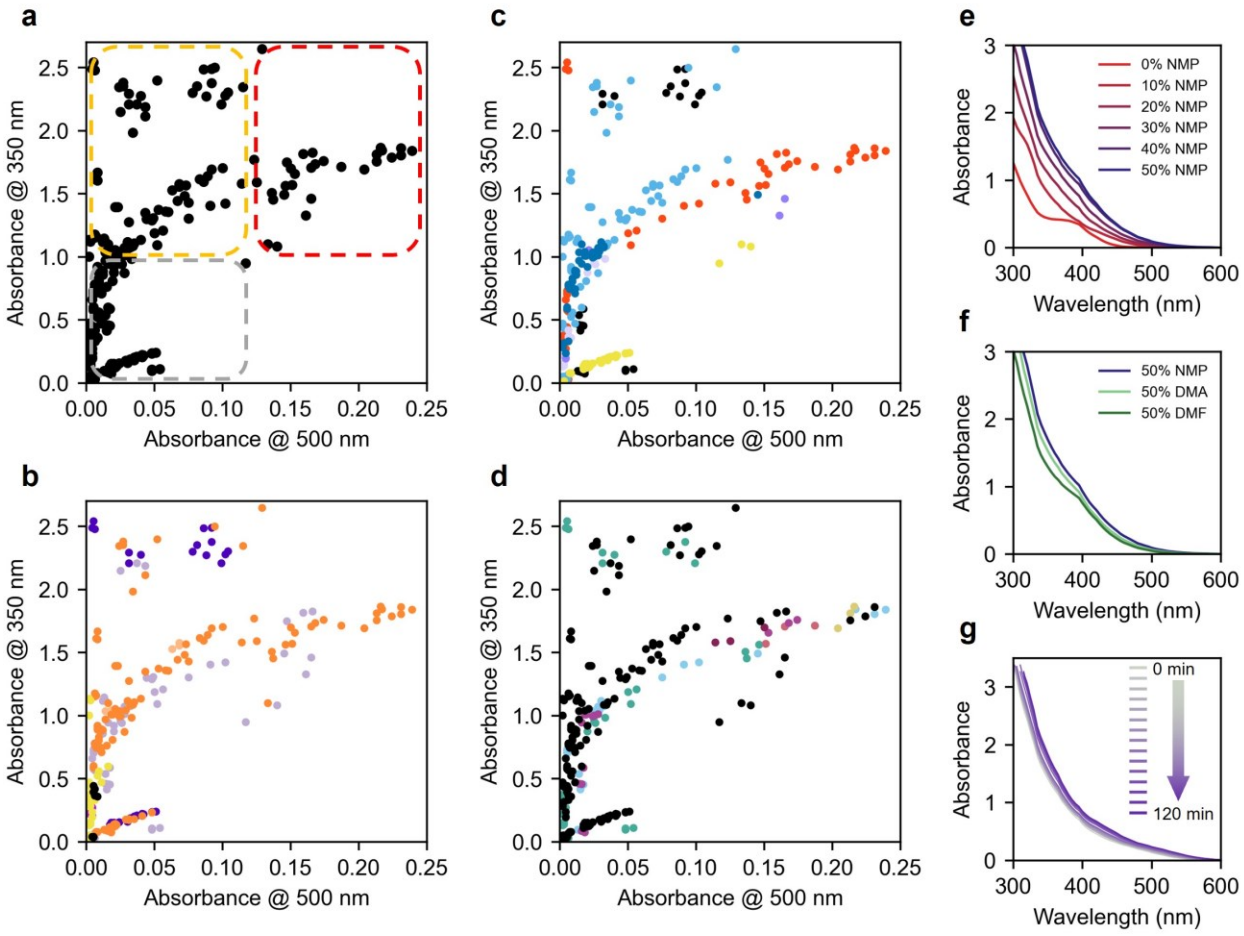


Figure 2.2 High throughput experimentation of 60 °C InP QD synthesis. (**a**) Scatter plot summarizing microplate experiment results with options of minimal or no reaction (gray), nanocluster (yellow), and QD (red). (**b**) Comparing ligand choice of oleic acid (light blue), technical grade oleic acid (dark blue), stearate (purple), technical grade oleic acid/benzoic acid mixture (light purple), phenylacetic acid (yellow), and aspartic acid (black). (**c**) Comparing solvent

choice of 100% toluene (yellow), NMP/toluene mixture (orange), DMA/toluene mixture (light orange), DMF/toluene mixture (light purple), ethyl acetate/toluene mixture (pink), toluene/DMF/NMP/ethyl acetate mixture (black), and 100% polar solvent (dark purple). (**d**) Comparing polar additive equivalents of 10 eq. (magenta), 100 eq. (pink), 200 eq. (yellow), 400 eq. (blue), 600 eq. (teal), 800 eq. (dark green) added or no extra polar additives added (black). (**e, f**) Comparing endpoints of InP QD synthesis using oleic acid ligands across varying percentages of polar solvent in toluene. (**g**) Absorbance traces during the reaction for the most successful HTE hit, synthesis using indium(benzoate)$_3$ with ethyl acetate and DMF as polar additives in a 50% toluene, 50% NMP solvent.

The main factor that led to productive InP QD crystallization at 60 °C was a partially polar solvent environment. The range of solvent conditions explored is displayed in **Figure 2.2b**, where the successful QD-producing reactions included 50% DMF or NMP and 50% toluene. Comparing absorbance spectra from conditions with increasing percentages of NMP in toluene, a clear trend emerged for more InP produced with increasing amounts of polar solvent (**Figure 2.2e**). Similar absorbance profiles were observed for conditions using 50% DMF or DMA in toluene (**Figure 2.2f**). This foundational result, which showed significant InP production from a partially polar solvent environment, validated the hypotheses discussed above that a more polar environment facilitates the formation of InP at low temperatures.

Another key parameter in the synthesis of InP at 60 °C was the choice of carboxylic acid, which acted as a ligand for the indium precursor and the growing nanocrystals. The two main carboxylic acids explored were oleic acid and benzoic acid because oleic acid is a common ligand for InP QDs with high solubility in nonpolar solvents, and benzoic acid is soluble in polar aprotic

solvents. Other carboxylic acids investigated were stearic acid, phenylacetic acid, aspartic acid, and mixtures. **Figure 2.2c** displays the HTE data labeled by carboxylic acid. The ligands used in conditions producing QDs were primarily benzoic acid, as well as oleic and stearic acid. For oleic acid, both 99% purity and technical grade oleic acid were used and achieved high absorbance in polar solvents, albeit slightly less so for technical grade oleic acid (**Figure S 3.1a-d**).[45,46] Stearic acid behaved similarly to oleic acid, as expected due to its similar solubility and acidity (**Figure S 3.1e**). A mixture of benzoic acid and oleic acid was also explored to investigate whether entropic ligand effects could contribute to the formation of InP at low temperatures. A mix of ligand chain lengths has been shown to increase nanoparticle solubility and play a role in surface accessibility and therefore growth.[47–49] However, the mixture of carboxylic acids did not lead to synergistic effects; instead, it appeared to induce InP formation to an extent between the two ligands (**Figure 2.2c (light purple), Figure S 3.1f,g**).

Within the reactions that achieved high InP concentration and QD growth, the inclusion of additional polar solvents was seen to extend growth to larger sizes. Stoichiometric amounts of polar aprotic additives were explored to drive InP crystallization, inspired by the complexity of natural mineralization systems. Ethyl acetate, DMF, and NMP have functional groups such as esters and amides that complement the carboxylic acids introduced with the indium precursor. For example, if the solvent were half toluene, half DMF, the polar additives would be ethyl acetate and NMP. Varied equivalents of polar additives within the QD-forming conditions tuned the extent of growth, and intermediate amounts of polar additives (10 – 400 eq.) were most successful (**Figure 2.2d**). Within a specific solvent environment and ligand choice, polar additives were observed to increase the InP concentration and size more with oleic acid than with benzoic acid (**Figure S 3.1h-n**).

Investigation into the conditions that failed to produce InP revealed that low or no polar solvent, insoluble ligands, high amine amounts, or majority NMP solvent environments were detrimental to InP formation. Ethyl acetate as the partial solvent, even with DMF and NMP additives, was unable to promote growth, likely due to the much lower polarity (**Figure S 3.1o**). Similarly, a solvent environment of 100% toluene, even with polar additives in stoichiometric amounts, did not promote InP formation (**Figure S 3.1p**). Among the various carboxylic acids explored, phenylacetic acid and aspartic acid lead to poor InP nucleation and growth (**Figure 2.2c, Figure S 3.1q**). This was likely due to limited solubility in toluene or apolar protic solvents at room temperature. Finally, a nanocluster product was observed, particularly in conditions with a solvent composition of 100% DMF, which indicated that polar solvents induced In–P bond formation, while a mix of polar and nonpolar solvents was beneficial for growth (**Figure 2.2b**). Other conditions found in the same region were conditions with reactant concentrations set at 4 mM indium.

In addition to impactful parameters, HTE enabled the elimination of various factors with minimal impact on low-temperature InP synthesis. The remaining parameters to be discussed only slightly affected InP nucleation and growth in polar solvents. Lowering the excess carboxylic acid to 13% and 3% induced slightly more InP formation than with 20%, but the effect is not large (**Figure S 3.1r**). This was rationalized because less acid destabilizes the InP magic-sized cluster, minimizing this kinetic trap, but also slows In–P bond formation for slower solute production, which detrimentally impacts crystallization.[50,51] Adding amines in conditions with partially polar solvents led to the formation of InP nanoclusters rather than the desired effect of destabilizing nanocluster species for InP growth.[52] We also tested whether polar solvents could induce growth

of pre-synthesized InP QDs, including both carboxylate- and oleylamine-capped QDs, however, this was unsuccessful under the conditions explored.

From HTE, the optimal reaction conditions for InP formation and growth at 60 °C were identified to be a solvent mixture of 50/50 toluene and NMP, ethyl acetate and DMF as polar additives, and benzoic, oleic, or myristic acid as the carboxylate ligand (**Figure 2.2g**). It is worth noting that the absorbance spectra of QD-forming reactions from HTE had no defined lowest energy electronic transition (LEET) as expected for the absorbance of monodisperse, crystalline quantum dots. This was likely due to polydispersity or low crystallinity, which could be caused by the low reagent concentration. Doubling the reaction concentration for HTE induces a slight shoulder in the absorbance (**Figure S 3.1s**), hinting at improved monodispersity with increasing concentration.

2.2.2 *Optimized Low Temperature Synthesis of InP QDs*

A successful synthesis for InP QDs should yield a monodisperse, crystalline product that can be modified through surface treatments or shelling for high PL QY. With these goals in mind, the optimal reaction conditions identified through HTE were applied to a synthesis with scaled-up solvent volumes and reactant concentrations (2-5 mL solvent and 0.11 M indium compared to 200 μL and 2.2 mM indium for the microplate reactions). Here, we present synthetic methods at 60 °C to access crystalline InP QDs capped with oleate, benzoate, or myristate ligands, with details on the optimization of the scaled-up syntheses discussed below.

First, in a nitrogen glovebox, the indium carboxylate precursor was prepared in toluene from trimethylindium and the carboxylic acid, with 20% excess carboxylic acid. Then, an equal amount of DMF to toluene was added along with one equivalent per indium of ethyl acetate and NMP. With 60 rpm stirring, $P(SiMe_3)_3$ (0.25 eq. per indium) was quickly added, and a yellow color

was observed, indicating nucleation or formation of In–P bonds. After one minute, the stir bar was removed, and the reaction was allowed to proceed in a 60 °C silicone oil bath for 3 hours.

InP QDs capped with oleic acid were synthesized at 60 °C, with a LEET at 456 nm (**Figure 2.3a, Figure S 2.2**). The crystallinity was measured using powder X-ray diffraction (XRD), which showed agreement with a zinc blende crystal structure and revealed an average crystallite size of 1.4 ± 0.1 nm, as determined by Scherrer analysis (**Figure 2.3b**). TEM imaging revealed quasi-spherical QDs with an average diameter of 2.0 ± 0.3 nm. Comparing the QD diameter to the crystallite size indicated a partially amorphous surface, although diameter measurements of small InP QDs are subject to error based on low contrast (**Figure 2.3c**). The InP QDs were also characterized by Raman spectroscopy to investigate more subtle perturbations to crystallinity (such as point defects) that do not show up in XRD or TEM measurements. The Raman spectrum exhibits a predominant peak centered at 303 cm^{-1} and a broad, lower-intensity feature centered around 345 cm^{-1} (**Figure S 2.3 purple**). These peak positions are consistent with bulk InP TO (306 cm^{-1}) and LO (348.5 cm^{-1}) modes, with some size-dependent line broadening and an increase in the TO mode intensity relative to the LO mode.[53,54]

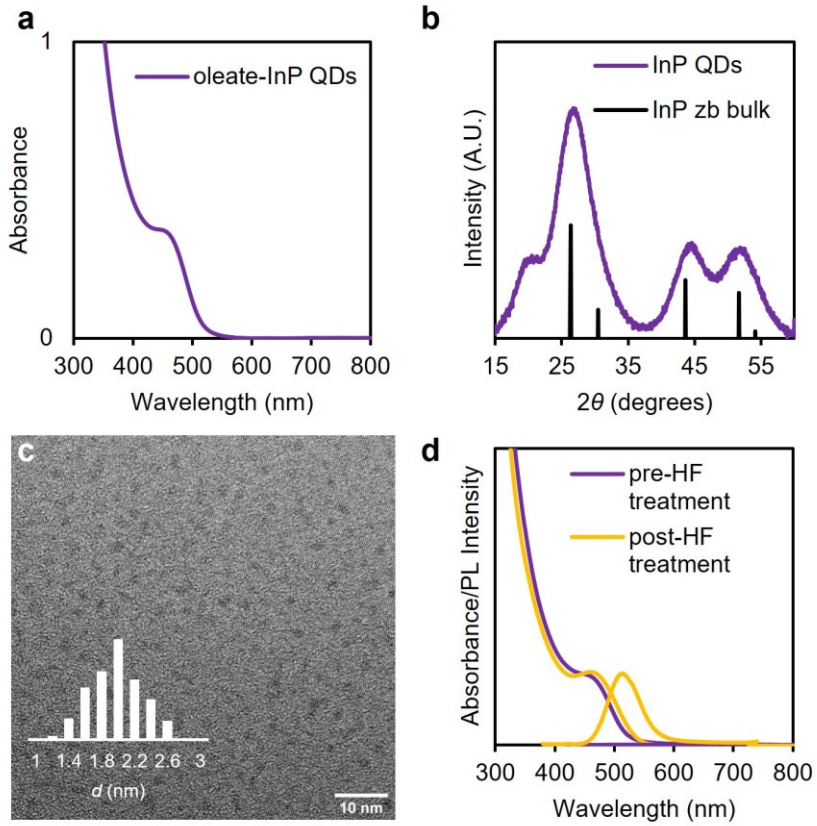


Figure 2.3 Characterization of optimized synthesis of oleate-capped InP QDs at 60 °C, including (**a**) the UV-visible absorbance spectrum with a lowest energy electronic transition at 456 nm, (**b**) the powder XRD pattern showing a zinc blende crystal structure with a crystallite size of 1.4 ± 0.1 nm, (**c**) transmission electron microscope image showing 2.0 ± 0.3 nm diameter QDs, and (**d**) UV-visible absorbance and photoluminescence spectra before (purple) and after (gold) surface treatment.

Next, the oleate-capped InP QDs were subjected to surface treatment to improve the PL QY. The native QDs have a PL QY below 1% with significant emission lower in energy of the band edge (**Figure S 2.4**). Typically, the PL QY of native InP QDs is enhanced either through hydrofluoric acid (HF) surface treatment or shelling, or both.[17,55] HF is proposed to break up

polyphosphates on the surface and passivate P dangling bonds with z-type InF_3.[55] For this study, we employed an HF surface treatment to demonstrate that the InP QDs synthesized at 60 °C can be modified similarly to traditional high-temperature synthesized QDs. The HF treatment proceeded by the addition of purified QDs into a bath of hexadecane with a mixture of zinc acetate and zinc oleate, followed by heating to 180 °C to facilitate zinc exchange on the InP surface. The HF was injected at 120 °C, and the reaction was held at 180 °C until the PL stopped increasing (**Figure S 2.5**). After HF treatment, a slight blueshift of the lowest energy electronic transition was observed along with a drastic increase in PL intensity. The InP/Zn-F QDs exhibited PL with a peak maximum at 518 nm (2.39 eV), a full width at half maximum of 63 nm (292 meV), and a PL QY of 25% (**Figure 2.3d, Figure S 2.6**). Time-resolved photoluminescence decay of the InP/Zn-F QDs was fit to a biexponential function with lifetimes of 21.8 and 61.8 ns, and an average intensity weighted lifetime of 52.3 ns (**Figure S 2.7**). These lifetimes fall within a typical range for HF-treated InP QDs, and the lack of a fast component indicates limited issues with trap-assisted recombination.[56] The identification of two components with similar lifetimes could indicate multiple QD populations within the ensemble. Photoluminescence excitation spectra collected with excitations spanning the photoluminescence signal revealed multiple emissive populations (**Figure S 2.8**). The luminescent InP/Zn-F QDs show a substantial reduction in the observed LO phonon intensity in the Raman spectrum (**Figure S 2.3, gold**). This phenomenon was previously observed in both zinc- and HF-treated QDs by Talapin and coworkers, who demonstrated that these common surface treatments likely introduce a degree of lattice disorder via point defects, which have a more pronounced effect on the observed Raman spectra than size trends alone.[57] Because the size of these quantum dots is on the order of the InP lattice constant (0.587 nm), the

effects of breaking translational symmetry on the observed Raman spectrum become more pronounced.

The synthesis of oleate-capped InP QDs presented above was optimized for scaled-up synthesis from the conditions identified by HTE through careful consideration of volume and stir rate. First, hot injection synthesis was attempted by injecting 0.5 eq. $P(SiMe_3)_3$ into a Schlenk flask containing 1 eq. indium oleate, 0.6 eq. oleic acid, and solvents (2 mL) at 60 °C with 550 rpm stirring. This resulted in a polydisperse QD product with a similar absorbance peak position to the 386-InP magic-sized cluster (accessed under these conditions with only toluene solvent) (**Figure 2.4a, yellow, blue**). However, similar reaction conditions run at a smaller scale (0.5 mL solvent) in an air-free J. Young tube with no stirring produced larger InP QDs with a LEET at 480 nm (**Figure 2.4a, purple**). This suggests that even if the polar environment assists InP formation, hot injection with rapid mixing leads to smaller nanocrystals than if there is no stirring during growth. Therefore, a heat-up synthesis was investigated where the $P(SiMe_3)_3$ is injected into the indium carboxylate solution in a Schlenk flask at room temperature before the reaction is transferred to the 60 °C oil bath. Mixing of the reaction during $P(SiMe_3)_3$ injection was important to control, and was investigated by controlling the stir rate during the addition of $P(SiMe_3)_3$ at room temperature for the heat-up method. Increasing the stir rate from no stirring/uncontrolled mixing to a controlled rate of 60, 125, or 350 rpm caused a red shift of the LEET, and the slowest stir rate of 60 rpm afforded the largest and most monodisperse QDs (**Figure 2.4b**).

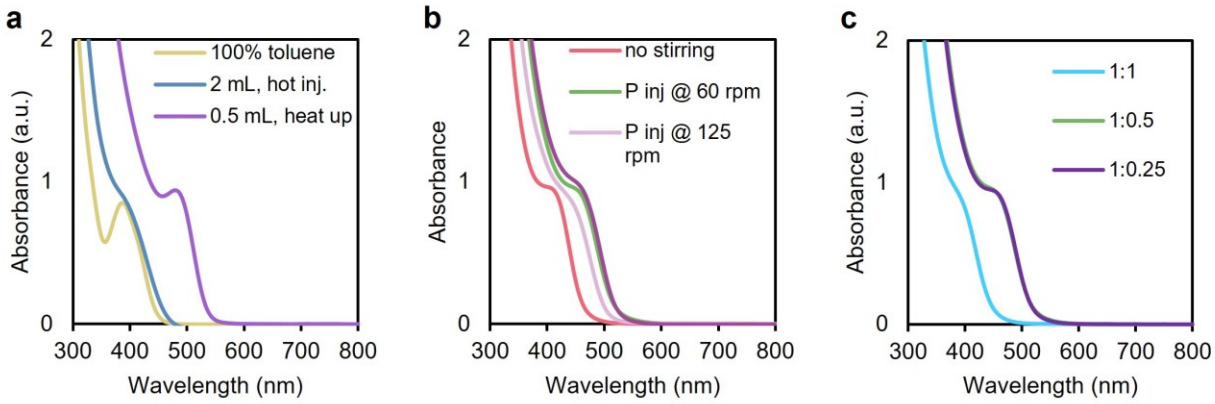


Figure 2.4 Optimizing oleate-capped InP QD synthesis at 60 °C with a toluene NMP solvent mixture and polar additives. UV-visible absorbance spectra of QD product from syntheses comparing (**a**) scale and hot injection versus heat-up methods, (**b**) stir-rate during $P(SiMe_3)_3$ addition for the 2 mL scale heat-up method, and (**c**) In:P stoichiometry for the 2 mL scale heat-up method with 60 rpm stirring for $P(SiMe_3)_3$ addition.

The effects of mixing can be rationalized by invoking a separated nucleation and growth paradigm in which good mixing disperses $P(SiMe_3)_3$ in solution, leading to the formation of many nuclei and less solute left over in solution, leading to smaller QDs. With slow mixing, there are likely locally varying concentrations of P, which would lead to a smaller number of nuclei that would then undergo diffusion-controlled growth with more solute to grow larger QDs. Finally, varying the indium to phosphorus stoichiometry under the optimized heat-up conditions showed that a 1:1 In:P ratio leads to smaller QDs (**Figure 2.4c**). A higher In:P ratio (1:0.25) did not increase the size compared to the QDs made with a 1:0.5 In:P ratio; however, the absorbance peak sharpened slightly, indicating a decrease in polydispersity. The final optimized condition, used for the HF treatment described above, used a toluene and DMF solvent mixture, indium oleate, a 1:0.25 In:P ratio, and 1 eq. NMP and ethyl acetate with 60 rpm stirring for the room temperature

$P(SiMe_3)_3$ injection. The synthesis was highly reproducible, producing nearly identical absorbance profiles across three separate syntheses (**Figure S 2.9**). A control synthesis run without the ethyl acetate or NMP additives resulted in a broader QD absorbance feature, indicating poorer size dispersion (**Figure S 2.10**).

Low-temperature synthesis of InP QDs can be extended to other ligand chemistries beyond oleic acid, consistent with the observations made in the high-throughput experimentation. **Figure 2.5a** shows the absorbance spectra of InP QDs made using myristic acid and benzoic acid, with LEETs at 464 nm and around 400 nm, respectively. Both the myristate- and benzoate-capped QDs crystallized with a zinc blende structure, with average crystallite sizes of 1.5 ± 0.3 and 1.6 ± 0.2 for myristate- and benzoate-capped QDs, respectively (**Figure 2.5b**). Myristic acid behaved similarly to oleic acid, as expected by its similar acidity and solubility, while benzoic acid led to significantly smaller InP QDs. Benzoic acid is more acidic than myristic or oleic acids, with pKa's of 4.2, 4.9, and 5.0, respectively, and is more soluble in polar solvents, both of which could impact the production rate of solutes. It has been shown computationally that indium precursors with carboxylates that are weaker bases have lower activation energies for In–P bond formation.[31] Therefore, in the context of separated nucleation and growth, increased rates of In–P bond formation from indium–benzoate versus indium–oleate (or myristate) can explain the smaller-sized QDs produced. The opposite size dependence was observed in the high-throughput microplate reactions, where benzoic acid led to larger QDs than oleic acid (**Figure S 3.1a**). The high-throughput reactions were run with significantly lower reactant concentrations, which we hypothesize causes a less defined nucleation event due to a slower solute production rate, which removes the clear dependence of QD size on precursor reactivity. The larger QDs produced with

benzoate can be explained by favorable growth due to increased solubility and reactivity of the surface.

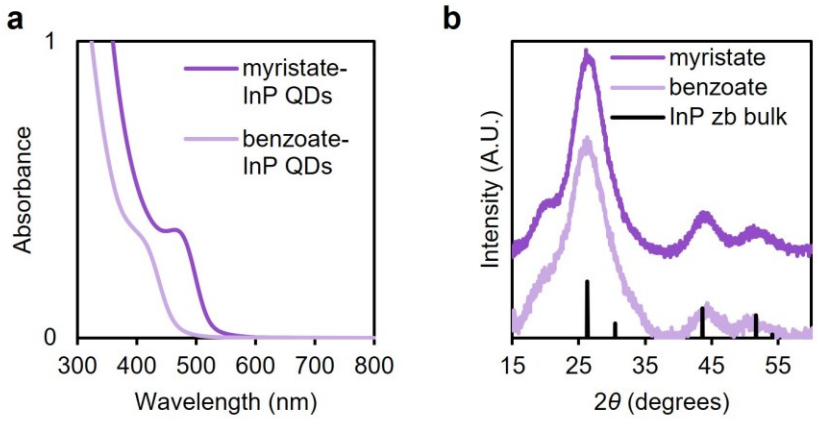


Figure 2.5 Characterization of myristate- and benzoate-capped InP QDs synthesized at 60 °C in toluene NMP solvent mixture with polar additives, including (**a**) UV-visible absorbance spectra and (**b**) powder X-ray diffraction patterns showing a zinc blende crystal structure for both samples.

Interestingly, the synthesis of InP QDs at low temperatures with myristic acid behaved differently depending on the precursor source. The indium carboxylates in the reactions described above were prepared from 1 equivalent of trimethylindium and 3.6 equivalents of carboxylic acid, and led to QD formation times of 2-3 hours at 60 °C. However, when an acid-free indium (III) myristate precursor was used for InP QD synthesis in a mixture of NMP and toluene, with the excess 0.6 equivalents of carboxylic acid added separately, InP QDs with a LEET around 520 nm formed rapidly at room temperature within minutes (**Figure S 2.11a**). TEM imaging revealed a bimodal size distribution with diameters of 2.0 ± 0.5 nm and 4.3 ± 0.6 nm (**Figure S 2.11b, c**). By powder XRD, the QDs exhibited low crystallinity with a quasi-wurtzite crystal structure that has been previously observed in magic-sized InP clusters (**Figure S 2.11d**).[58] Raising the temperature to 60 °C produced QDs with a broader absorbance peak and did not induce growth of InP in the

zinc blende crystal structure, instead producing QDs of similar crystallinity (**Figure S 2.11d, e**). Additionally, the formation of InP QDs under these conditions proceeded at 0 °C, forming smaller QDs with a LEET around 480 nm (**Figure S 2.11e**). This result suggests that the coordination state of the indium carboxylate precursor likely plays a larger role in determining the size and crystallinity of the final InP QD product in reactions run at low temperature, in contrast to what is typically observed at temperatures >180 °C.

2.3 CONCLUSIONS

In summary, we have demonstrated the synthesis of crystalline InP QDs at 60 °C induced by a mixture of polar aprotic and nonpolar solvents. Oleate-capped InP QDs synthesized through this method exhibited a PL QY of 25% after treatment with hydrofluoric acid, demonstrating the QD quality. This discovery was guided by high-throughput experimentation for which we developed a custom air-free microplate system for low-temperature nanocrystal synthesis. High-throughput experimentation allowed for the evaluation of a large parameter space, including studies of how percentage polar solvent, ligand identity and equivalents, reaction concentration, and additional polar additives affected InP formation. This study has revealed a large, uncharted landscape of InP synthesis in polar solvents that contains a wealth of possibilities for future study. Low temperature synthesis of InP in polar solvents opens up a new paradigm of III-V nanocrystal synthesis, from ‘hard to make, hard to break’ to ‘easy to make, hard to break’.

2.4 Experimental Methods

2.4.1 *General Practices*

All glassware was dried in a 160 °C oven overnight prior to use. All syntheses were performed under an inert atmosphere of nitrogen using a glovebox or standard Schlenk techniques, unless otherwise noted. Indium chloride (98%), oleic acid (technical grade, 90%), stearic acid (95%), myristic acid (>99%), phenylacetic acid (99%), L-Aspartic acid (≥98%, HPLC), benzylamine, benzoic acid, and hexadecane (99%) were purchased from MilliporeSigma and dried before being stored in a nitrogen glovebox. Dimethylacetamide (anhydrous, 99.8%), ethyl acetate (anhydrous, 99.8%), acetonitrile (anhydrous, 99.8%), hydrofluoric acid (ACS reagent, 48 wt %), zinc (II) oxide (99.99%), acetone (>99.9%), anhydrous ethanol (>99.5%), and 1-methyl-2-pyrrolidone (NMP) (anhydrous, 99.5%) were purchased from MilliporeSigma and used as received. Oleic acid (99%) was purchased from TCI America and used as received. Indium myristate (acid-free) was purchased from American Research Chemical and used as received. Zinc (II) acetate (*anhydrous,* 99.99%) and acetone (*extra dry*, 99.8%) were purchased from ThermoFisher Scientific and used as received. Deuterated toluene was obtained from Cambridge Isotope Laboratories, dried over CaH2, and distilled before use. Trimethylindium (98+%) was purchased from Strem and used as received. Tris(trimethylsilyl)phosphine ($P(SiMe_3)_3$) was prepared according to literature procedures.[50] *Caution! $P(SiMe_3)_3$ is highly pyrophoric and generates toxic phosphine gas upon exposure to moisture. Handle and quench with care.* Dimethylformamide (DMF) (certified ACS) was purchased from Fisher and dried according to literature procedures, briefly was stirred over molecular sieves for 72 hours, transferred to fresh sieves, then stirred for an additional 72 hours and distilled at reduced pressure to yield the dry solvent that was stored in a nitrogen glovebox in the dark.[59] High-performance liquid chromatography grade toluene was purified and dried using a

solvent still[60], and stored over sodium in a nitrogen glovebox for use as reaction solvent. Toluene (high-performance liquid chromatography grade) was purchased from ThermoFisher and used as purchased for UV-vis absorbance spectroscopy of reaction aliquots.

2.4.2 *High-Throughput Experimentation*

High-throughput experiments were run in a Hellma quartz 96-well microplate using a BioTek Synergy H1 Multimode Reader in UV-Vis Absorbance mode configured with a CO_2/O_2 Gas Controller.

Safety Note! $P(SiMe_3)_3$ is extremely pyrophoric and can produce PH_3 on reaction with protic reagents. PH_3 is extremely toxic, with a safe exposure limit of 0.3 ppm (OSHA, NIOSH). The total amount of $P(SiMe_3)_3$ used in each microplate reaction was such that if all $P(SiMe_3)_3$ converted to PH_3 and expanded to fill about 1 m^3 the concentration would be within the safe exposure limit. Additional safety measures implemented were the one hour 'pre-reaction' in the N_2 glovebox of each microplate experiment.

The quartz microplate and quartz cover plate were dried in a 160 °C oven overnight and brought into a N_2 glovebox. Stock solutions were prepared as noted in **Table S1**. Then, the stock solutions and desired solvents were pipetted in to the microplate as noted in **Table S2** following the general order of solvent, indium precursor, phosphorus precursor.

The microplate was covered and incubated at room temperature for one hour in the glovebox for 'pre-reaction' to to allow for any protonolysis of $P(SiMe_3)_3$ in a contained environment. Then, the microplate was sealed with high temperature vacuum grease and a quartz cover slip, and secured with rubber bands. The plate reader was set up to monitor absorbance at desired timepoints from 300 to 600 or 700 nm in increments of 5 nm with sweep mode, and the gas controller was used to minimize the percent oxygen by addition of argon gas.

2.4.3 *Synthesis of InP QDs at 60°C (heat-up)*

In a nitrogen glovebox, oleic acid (0.792 mmol, 250 μL, 3.6 eq.) and 0.5 mL toluene were added to an oven dried 50 mL Schlenk flask equipped with a stir bar. Separately a trimethylindium solution was prepared from trimethylindium (0.22 mmol, 0.0352 g, 1 eq) and 0.5 mL toluene, and added in dropwise (2 drops/second) to the oleic acid solution with stirring to form indium(oleate)$_3$, and the reaction was stirred for 10 minutes. Next, 1 mL of DMF was added, and then ethyl acetate (0.22 mmol, 21.5 μL, 1 eq.) and 1-methyl-2-pyrrolidone (0.22 mmol, 21.2 μL, 1 eq.) were added. Then, the stirring was set to 60 rpm and P(SiMe$_3$)$_3$ (0.055 mmol, 16.0 μL, 0.25 eq.) was swiftly injected, with one minute of stirring. The stir bar was removed and the reaction was transferred to heat in a 60 °C silicone oil bath for 3 hours. After removal from heat, the red quantum dot product became insoluble in the toluene/DMF and was collected by centrifugation, and redissolved in minimal anhydrous toluene. The quantum dots were flocculated with a ratio of 3:1 acetonitrile to toluene and isolated by centrifugation (7380 rpm, 10 minutes), and this procedure was repeated three times to yield a waxy, red pellet that was stored as a dilute solution in toluene for characterization.

For myristate-capped InP QDs, the procedure above was followed with myristic acid instead of oleic acid. For InP QDs made with acid-free indium myristate, the procedure above was followed except with the use of the acid-free indium myristate with 0.6 eq. myristic acid added to the indium precursor solution, 0.5 eq. P(SiMe$_3$)$_3$, a solvent mixture of equal parts NMP and toluene, and the reaction was run at room temperature with 350 rpm stirring.

For benzoate-capped InP QDs, the procedure above was followed with benzoic acid instead of oleic acid, and NMP instead of DMF, and a 0.5 mL solvent scale. The indium benzoate solution (0.11 M In, 0.25 mL) was added to an oven dried J. Young tube along with 0.25 mL NMP, 1 eq

ethyl acetate, and 1 eq DMF. $P(SiMe_3)_3$ (0.0275 mmol, 8.0 μL, 0.5 eq.) was added to the J. Young tube, the J. Young tube was capped, inverted to mix, and added to the silicone oil bath. The purification also differed from oleate-capped InP QDs due to the solubility of benzoate-capped InP QDs in DMF. The quantum dots were flocculated with a ratio of 2:1:1 anhydrous hexane to reaction mixture to toluene and isolated by centrifugation (7380 rpm, 10 minutes), and this procedure was repeated three times to yield a waxy, yellow pellet that was stored as a dilute solution in DMF for characterization.

2.4.4 *Optimization of Synthesis of InP QDs at 60 °C*

Hot injection: procedure for oleate-capped InP QDs above was followed except 0.4 mL toluene each was used to prepare the oleic acid and trimethylindium solutions, and the reaction was equilibrated in the 60 °C silicone oil bath for 10 minutes, with stirring at 550 rpm, before $P(SiMe_3)_3$ in 0.2 mL toluene was injected.

100% toluene: $In_{37}P_{20}$ magic-sized cluster synthesis, adapted from *Cossairt, et al.*[61] In a nitrogen glovebox, oleic acid (0.197 mmol, 62 μL, 3.4 eq.) and 0.25 mL toluene were added to 20 mL scintillation vial equipped with a stir bar. Separately a trimethylindium solution was prepared from trimethylindium (0.058 mmol, 0.0093 g, 1 eq) and 0.25 mL toluene, and added in dropwise (2 drops/second) to the oleic acid solution with stirring to form indium(oleate)$_3$, and the reaction was stirred for 10 minutes. The indium(oleate)$_3$ solution was transferred to an oven dried J. Young tube, $P(SiMe_3)_3$ (0.0275 mmol, 8.0 μL, 0.5 eq.) was added to the J. Young tube, the J. Young tube was capped, inverted to mix, and added to the silicone oil bath for a reaction time of 3 hours.

Stir-rate dependence: the procedure for oleate-capped InP QDs was followed above except with a 125 or 350 rpm stir rate for $P(SiMe_3)_3$ addition.

Stoichiometry dependence: the procedure for oleate-capped InP QDs was followed above except $P(SiMe_3)_3$ was varied from 0.25, 0.5, and 1 equivalent per indium.

2.4.5 *Synthesis of Zinc Oleate [$Zn(OA)_2$] Powder*

Zinc oleate was synthesized using a modified version of the iron oleate from iron trifluoroacetate synthesis via Hendricks et al.[62] Lead (II) oxide is exchanged for Zinc (II) oxide (7.3 g, 90 mmol). The resulting powder was dried under dynamic vacuum for 24 hours to yield a free-flowing white powder in 93% yield (52.75g). ^{1}H NMR (500 MHz, d8-Tol) δ= 0.96 (t, ^{3}JH-H= 7 Hz, 6H, CH3), 1.15-1.51(m, 40H, (CH2)6 and (CH2)4), 1.59 (m, 4H, COCH2CH2), 2.06-2.18 (m, 8H, =CHCH2), 2.26 (t, ^{3}JH-H =7.6 Hz, 4H, COCH2), 5.50 (m, 4H, =CHCH2).

2.4.6 *Preparation of 2.0 M HF in Acetone*

The HF solutions for surface oxide treatment were prepared immediately before use by diluting 48 wt% HF (145 μL, 8 mmol) with acetone (1855 μL) in a 15 mL PTFE centrifuge tube. *Caution! HF is extremely toxic, corrosive, and should be handled with care.*

2.4.7 *Zinc Exchange and HF Treatment of InP Cores*

A 15 mL, oven-dried 3-neck flask equipped with a stir bar, air condenser, thermowell, and hose adapter was cycled onto the Schlenk line by three sequential evacuation (~50 mtorr) and N_2 backfill cycles. To the flask under a stream of N_2 was added anhydrous hexadecane (3.0 mL), followed by $Zn(OAc)_2$ (0.02 mmol, 3.6 mg) and $Zn(OA)_2$ (0.2 mmol, 63.0 mg). The zinc precursors in hexadecane were subsequently degassed at 80ºC for 30 minutes. Then, 60 nmol of InP QD cores in toluene (0.37 mL, 60nmol) were added to the flask at room temperature under N_2 and volatiles removed under reduced pressure for 20 minutes. The flask was then backfilled and

heated to 180ºC where it was held for 30 minutes to facilitate zinc exchange on the InP surface. Then, the flask was cooled to 120ºC and freshly prepared 2.0M HF in acetone (0.1 mL, 0.2 mmol) was carefully injected under N_2. The temperature was then raised to 180ºC where the reaction proceeded for 80 minutes. Upon completion, the flask was cooled to room temperature where any volatiles were removed under reduced pressure (*Warning! Residual HF can collect in cold traps at this point and the traps should be carefully quenched via a soluble, aqueous source of* Ca^+). The flask was cycled into the box where the nanocrystal solution (~3.5 mL) was flocculated by the addition of 15 mL/ anhydrous ethanol and collected by centrifugation. The resulting pellet was resuspended in ~5.0 mL of anhydrous toluene and subsequently precipitated again by the addition of 20 mL/ anhydrous acetone and collected by centrifugation. The purified QDs were suspended in ~2 mL of anhydrous toluene, passed through a PTFE syringe filter (0.22 uM) and dried to a powder for storage.

2.4.8 *UV-Vis Absorbance Spectroscopy*

Measurements were collected using either an Agilent Cary 60 or Agilent Cary 5000 Spectrophotometer in dual beam mode. Solution concentrations were adjusted to maintain OD<2 within regions of interest. All solution phase absorbance was collected in 1.0 cm fluorescence cuvettes (Spectrocell). HF treatment of cores were monitored by diluting 20 μL aliquots in 3.0 mL of toluene, followed by immediate measurement.

2.4.9 *Photoluminescence Spectroscopy*

Standard emission spectra collected to monitor HF treatment of cores were obtained from 380-740 nm using a Horiba Jobin Yvon FluoroMax-4 Fluorescence spectrophotometer with an excitation

wavelength of 365 nm, both emission and excitation bandwidths set to 1.0 nm, and integrated for 0.1 s with 1.0 nm resolution.

2.4.10 *Time Resolved Photoluminescence (TRPL) and Photoluminescent Quantum Yield (PLQY)*

TRPL and PLQY were measured on an Edinburgh FLS1000 Fluorometer equipped with a visible photomultiplier tube detector. All samples and references were prepared in 1.0 cm quartz fluorescence cuvettes using anhydrous toluene, sealed inside a glovebox atmosphere, and measured within one hour. TRPL (TCSPC) measurements were collected following excitation from an Edinburgh EPL-405 pulsed laser diode (excitation wavelength of 402.4 nm) operating with a pulse period of 2 μs. Signal from the emission at 520 ± 0.5 nm was accumulated to 10k counts across a 1 μs time range (4096 channels). Absolute PLQY measurements were collected in an Edinburgh FLS1000 integrating sphere (N-M01) and excited using a Xenon flash lamp at 385 nm with a slit width of 4.0 nm. All sample concentrations were adjusted to have OD<0.05 at 385 nm. Emission was collected with a 0.35 nm slit width from 365-700 nm and integrated for 0.5s with 0.1 nm resolution. Absolute PLQY integrations of solvent and sample were done using the associated Fluoracle® software, and emission was integrated from 450 nm to 670 nm.

2.4.11 *Transmission Electron Microscopy (TEM)*

All TEM imaging was done on a FEI Tecnai G2 F20 SuperTwin microscope operated at 200 kV using bright field imaging mode. Samples were prepared in a nitrogen glovebox by drop-casting 5 μL of dilute suspensions in toluene or DMF onto a suspended ultrathin carbon film on a lacey carbon support film, 400 mesh, copper grids purchased from Ted Pella Inc, and allowed to dry fully then placed under vacuum overnight. TEM size analysis was performed using manual

analysis in ImageJ based off images from at least two different grid locations and over 300 diameter measurements per sample.

2.4.12 *Powder X-ray Diffraction (PXRD)*

Powder XRD diffraction patterns were collected on solid films drop-cast onto a Si wafer using a Bruker D8 Discover diffractometer. The crystallite size was determined from the Scherrer equation, and used full widths at half maxima from peaks fit with Igor.

2.4.13 *Raman Spectroscopy*

Raman spectra were acquired on a Reinshaw InVia Raman spectrometer equipped with a Lecia DMIRBE inverted optical microscope. The microscope was calibrated to the 520 cm-1 line of an internal silicon standard. All samples were excited by a 785 nm laser source. Samples were prepared in a glovebox by drop-casting concentrated solutions from 1-octane onto clean Si substrates. All measurements were recorded in backscattering geometry within 30 minutes of air exposure. Rising backgrounds were corrected by applying a polynomial fit to the baseline.

2.4.14 *Supplementary Figures*

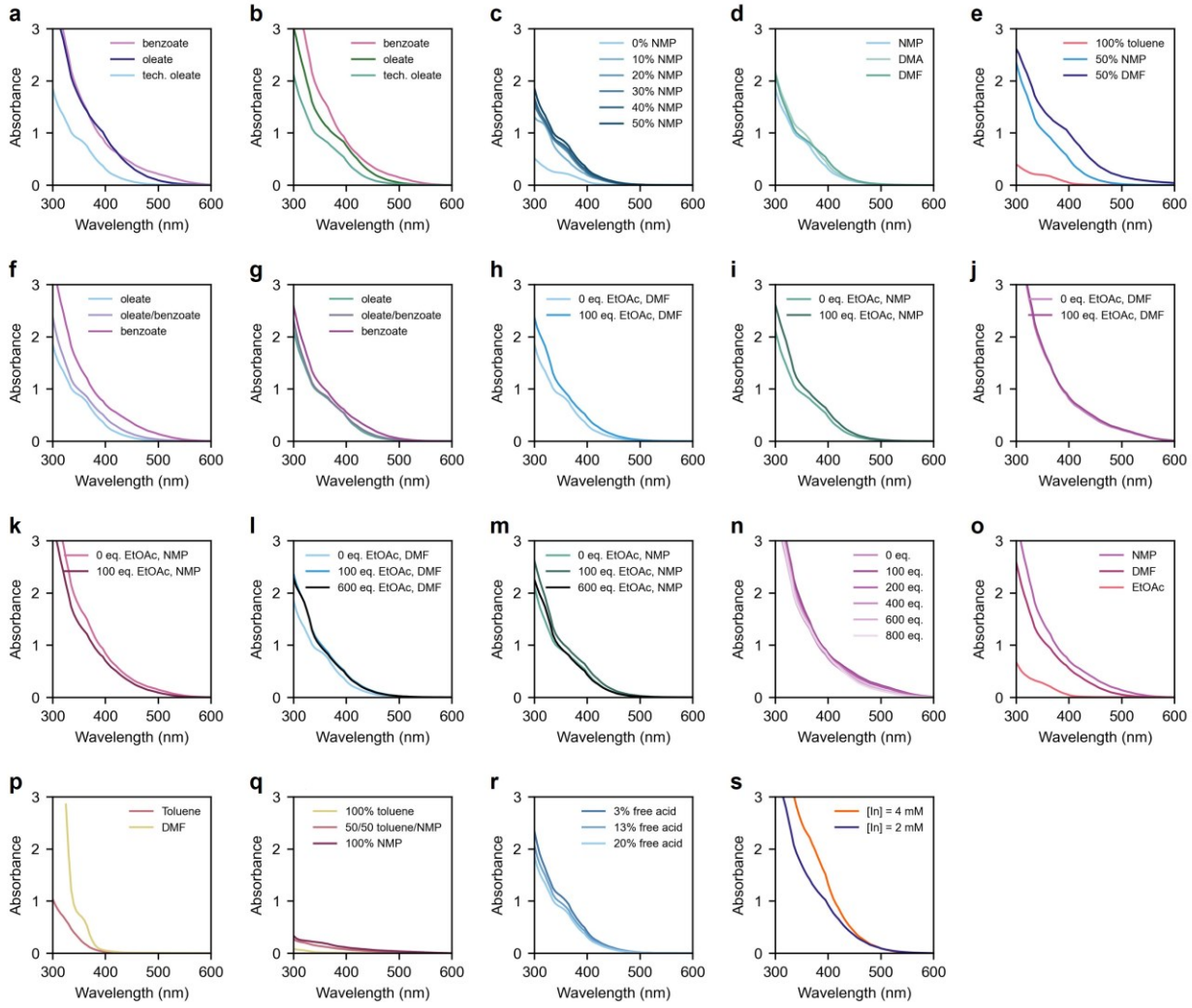


Figure S 2.1 High-throughput experimentation absorbance spectra. Comparing UV-visible absorbance spectra of the final time point across relevant high-throughput conditions. The legends describe the different conditions with shared conditions as follows: (**a**) solvent of toluene/NMP, (**b**) solvent of toluene/DMF, (**c**) technical grade oleic acid and solvent environment of toluene with listed percent NMP, (**d**) technical grade oleic acid and solvent environment of toluene/polar solvent, (**e**) stearic acid and listed solvent environment with toluene, (**f**) solvent of toluene/NMP and 100 eq. ethyl acetate and DMF, (**g**) solvent of toluene/DMF and 100 eq. of ethyl acetate and

NMP, (**h**) oleic acid and solvent of toluene/NMP, (**i**) oleic acid and solvent of toluene/DMF, (**j**) benzoic acid and solvent of toluene/NMP, (**k**) benzoic acid and solvent of toluene/DMF, (**l**) oleic acid and solvent of toluene/NMP, (**m**) oleic acid and solvent of toluene/DMF, (**n**) benzoic acid and solvent of toluene/NMP with ethyl acetate and DMF additives, (**o**) benzoic acid with 10 eq. polar additives and solvent of toluene/listed polar solvent, (**p**) benzoic acid with 10 eq. ethyl acetate, NMP, (and DMF), (**q**) phenylacetic acid, (**r**) technical grade oleic acid and solvent of toluene/NMP, (**s**) oleic acid and solvent of toluene/NMP.

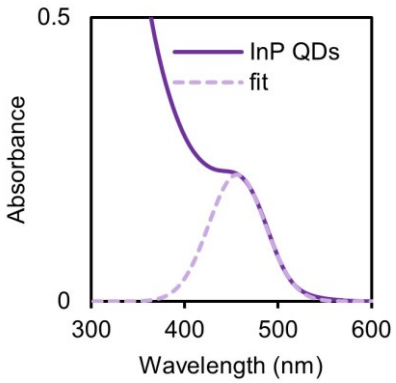


Figure S 2.2 UV-visible absorbance spectrum fit to a gaussian to determine peak maximum of 456 nm.

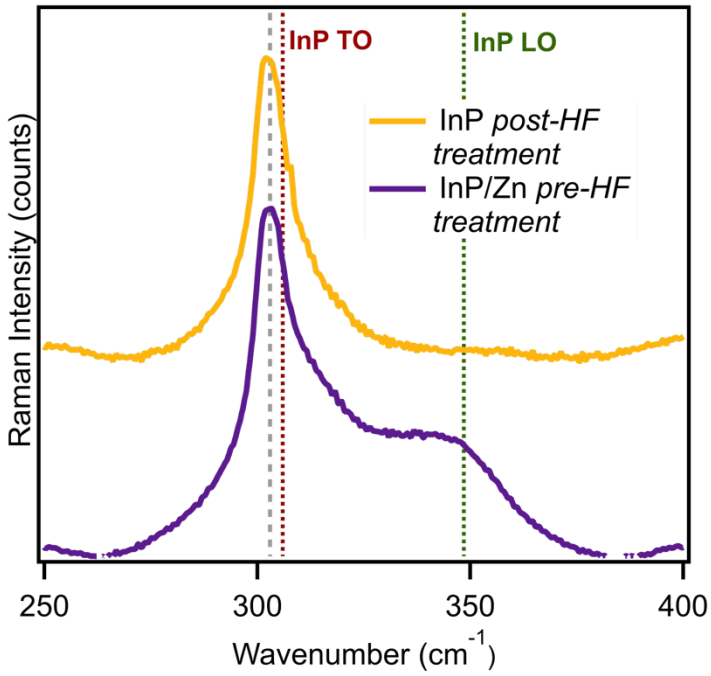


Figure S 2.3 Raman spectra of as-synthesized InP QDs at 60 ºC (purple) and after being treated with zinc carboxylate and HF at 180 ºC (gold) using l_{ex}= 785 nm. The bulk zincblende InP transverse optical (TO) and longitudinal optical (LO) phonon modes are indicated by lines at 306 cm^{-1} (red) and 348.5 cm^{-1} (green).[63] The grey dashed line shows that the measured peak at 303 cm^{-1} does not shift after surface treatment.

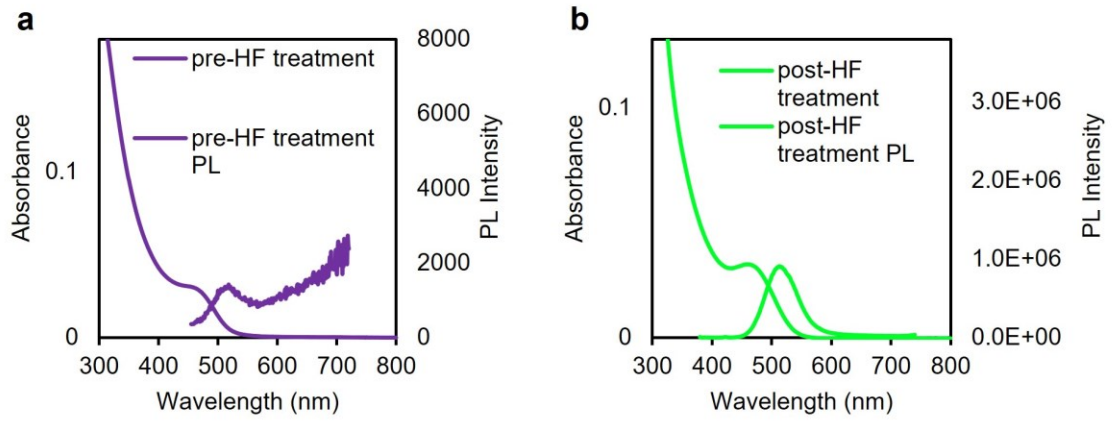


Figure S 2.4 UV-visible absorbance and photoluminescence of InP QDs synthesized at 60 °C **(a)** before surface treatment and **(b)** after surface treatment. Note the drastic increase in PL intensity after surface treatment, indicating a negligible photoluminescence quantum yield before surface treatment.

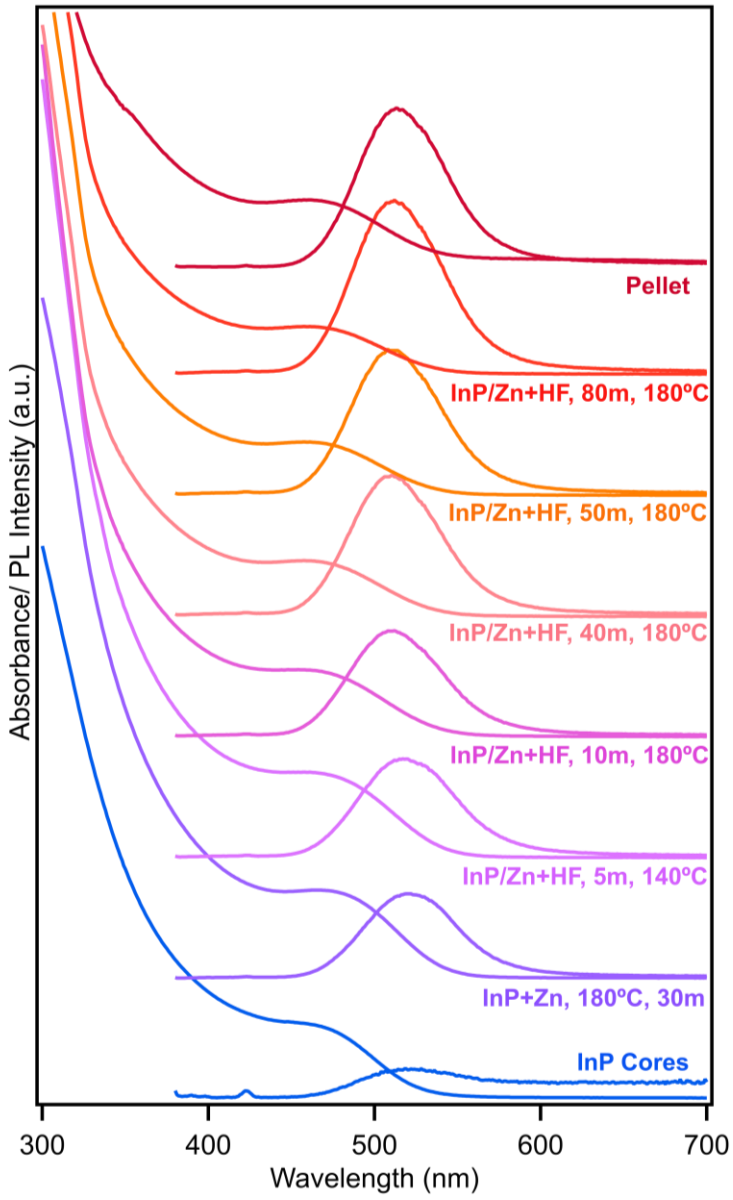


Figure S 2.5 Temporal evolution of the absorbance and emission profiles of InP QDs grown at 60 ºC when subjected to zinc exchange and fluorination by HF at 180 ºC. The gradual blue-shift of the absorbance and PL, along with the monotonic increase in PL intensity is consistent with the zinc-exchange induced reduction in QD diameter and passivation of residual surface traps by HF.

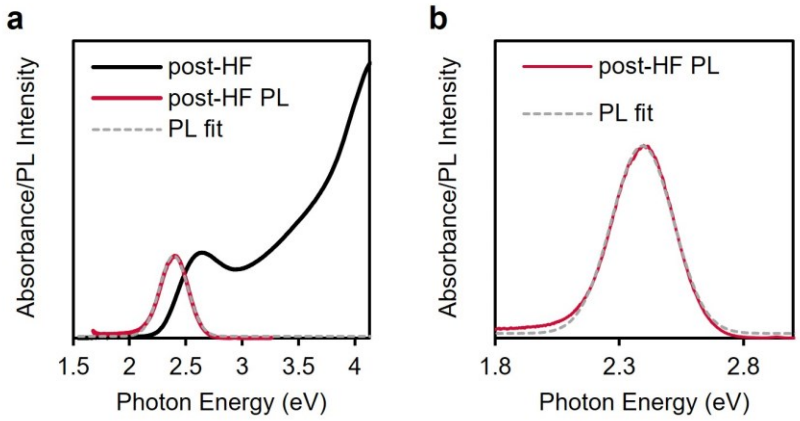


Figure S 2.6 Optical characteristics of InP/Zn-F QDs plotted on an energy scale **(a)**. After applying the conversion factor[64], the PL was fit **(b)** to a single Gaussian function to extract the full width at half maximum. Coefficient values ± one standard deviation as follows: y0 = 4.9233E06 ± 9.1E04, A = 1.8881E08 ± 2.37E05, x0 = 2.3931 ± 0.000173 eV, width = 0.17561 ± 0.000273 eV.

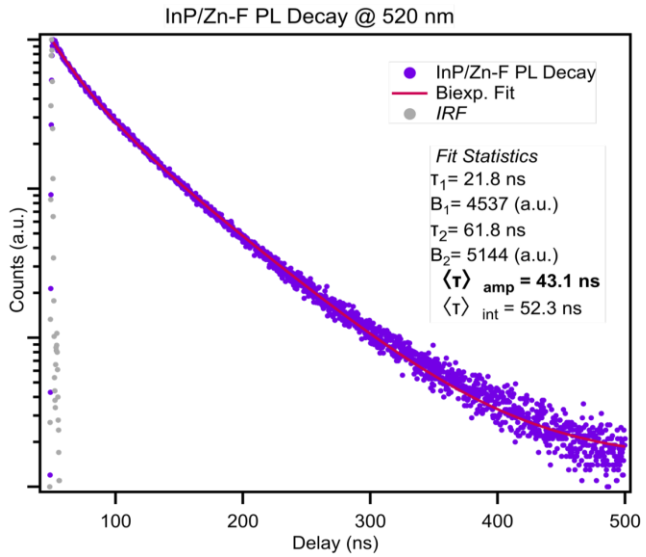


Figure S 2.7 Time-resolved photoluminescence decay of InP/Zn-F QDs, excited by a pulsed laser at 402.5 nm and measured at 520 nm. The decay profile was fit to a biexponential function to extract the intensity weighted lifetime, reported in nanoseconds.

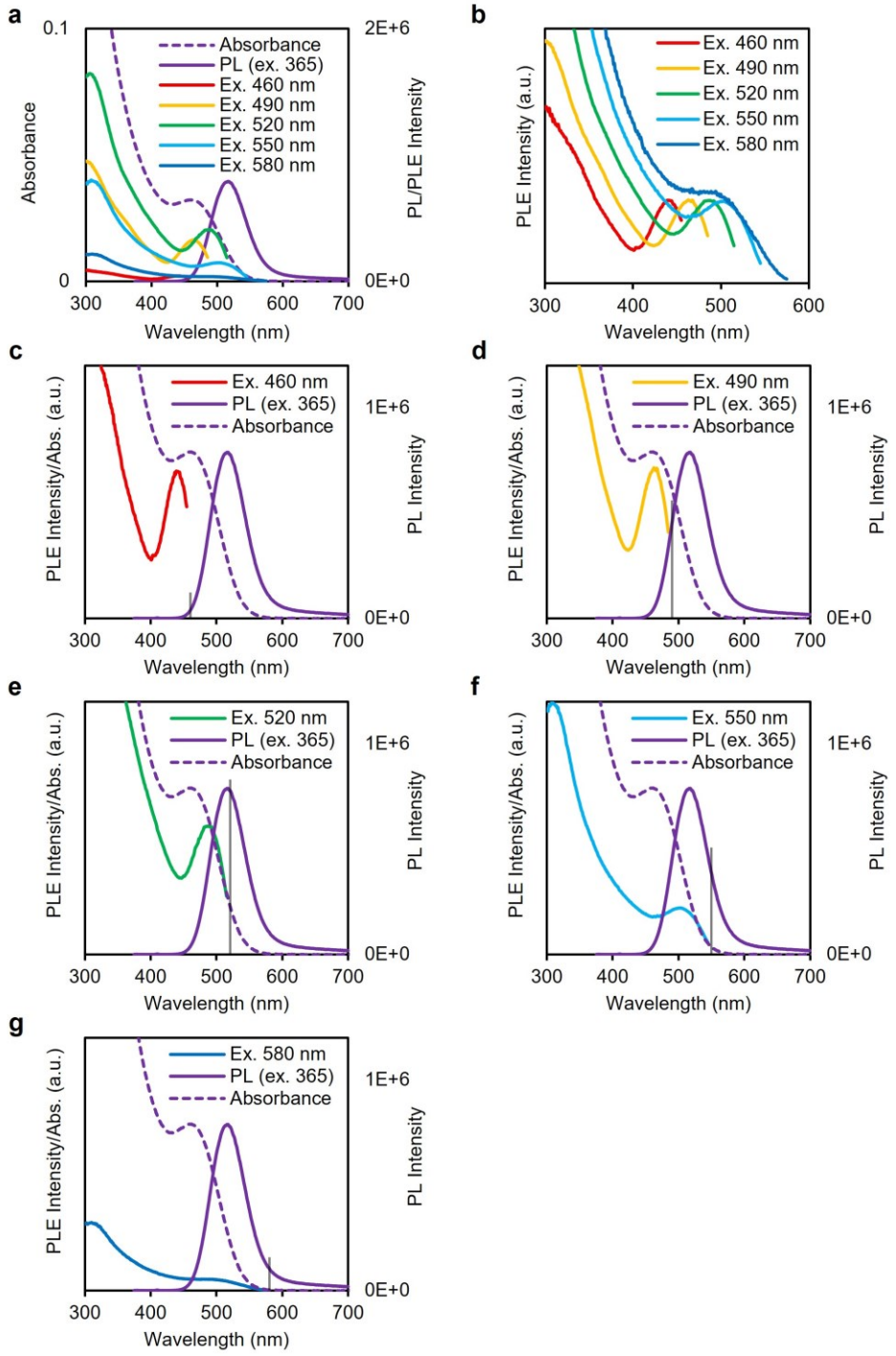


Figure S 2.8 Photoluminescence excitation spectra of InP/Zn-F QDs made at 60 °C. **(a)** Photoluminescence excitation (PLE) spectra excited at 460, 490, 520, 550, and 580 nm plotted with the absorbance and photoluminescence spectra. **(b)** Normalized PLE spectra to demonstrate

peak shift with excitation wavelength, indicating multiple QD populations contributing to the photoluminescence signal. The two populations emitting at 490 and 520 nm have the highest intensity. **(c-g)** Normalized absorbance, PLE, and photoluminescence spectra for each wavelength, with the gray line indicating the excitation wavelength for PLE.

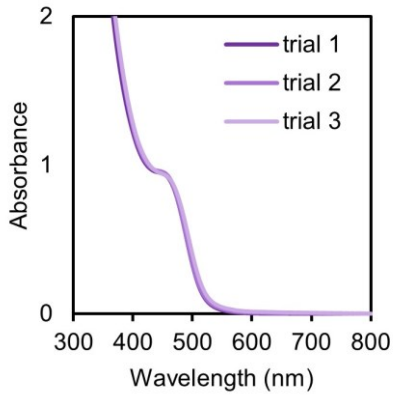


Figure S 2.9 UV-visible absorbance spectra showing reproducibility of optimized InP QD synthesis.

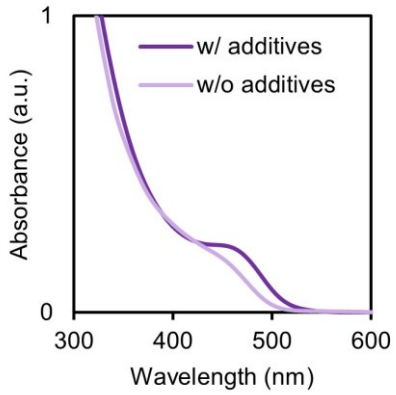


Figure S 2.10 UV-visible absorbance spectra comparing QD products with and without ethyl acetate and NMP additives from a synthesis using oleic acid and a solvent environment of 50/50 toluene/DMF. The broader peak without additives indicates a worse QD size dispersion.

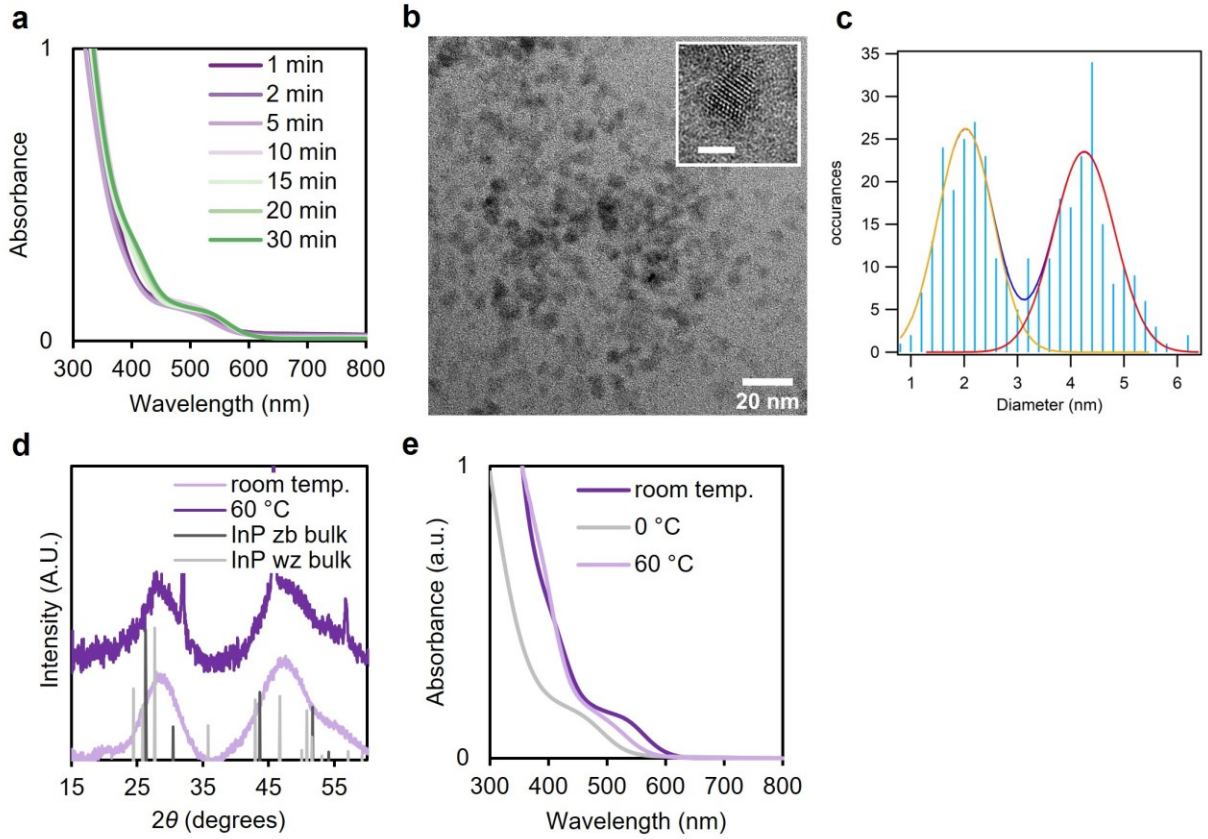


Figure S 2.11 Characterization of InP QDs synthesized using acid-free indium(III) myristate. **(a)** UV-visible absorbance spectra of aliquots of a reaction at room temperature with indium(III) myristate (acid-free, 1 eq.) with 0.6 eq. myristic acid, 0.5 eq. $P(SiMe_3)_3$, and a solvent mixture of equal parts NMP and toluene, **(b)** TEM image of InP QDs from the room temperature synthesis, inset of high resolution image showing a defect-ridden crystal structure with scale bar of 3 nm, **(c)** QD diameter distribution from TEM image analysis fit to two gaussians illustrating the bimodal size distribution, **(d)** powder X-ray diffraction patterns showing a quasi-wurtzite structure for InP QDs made using acid-free indium(III) myristate at both room temperature and 60 °C, and **(e)** UV-visible absorbance spectra of QD products using previously stated conditions at different reaction temperatures.

2.4.15 *Experimental Conditions for High-Throughput Experiments*

Table 2.1 Stock Solutions used in High-Throughput Experiments

Label	Reagent 1	Reagent 1 conc. (mM)	Reagent 2	Reagent 2 conc. (mM)	Solvent	Notes/ extra reagent
In.ol.tol	$In(CH_3)_3$	8.88	oleic acid	32.0	toluene	
In.ol.tol.2x	$In(CH_3)_3$	17.8	oleic acid	63.9	toluene	*a*
In.ol.tol.10x	$In(CH_3)_3$	88.8	oleic acid	320	toluene	
In.13%.ol.tol	$In(CH_3)_3$	8.88	oleic acid	30.2	toluene	*a*
In.13%.ol.tol.2x	$In(CH_3)_3$	17.8	oleic acid	60.4	toluene	*a*
In.13%.ol.tol.10x	$In(CH_3)_3$	88.8	oleic acid	302	toluene	
In.t.ol.tol	$In(CH_3)_3$	8.88	tech. grade oleic acid	32.0	toluene	
In.13%.t.ol.tol	$In(CH_3)_3$	8.88	tech. grade oleic acid	30.2	toluene	
In.3%.t.ol.tol	$In(CH_3)_3$	8.88	tech. grade oleic acid	27.5	toluene	
In.ph.tol	$In(CH_3)_3$	8.88	Phenylacetic acid	32.0	toluene	
In.ph.NMP	$In(CH_3)_3$	8.88	Phenylacetic acid	32.0	NMP	
In.st.tol	$In(CH_3)_3$	8.88	stearic acid	32.0	toluene	
In.bz.tol	$In(CH_3)_3$	8.88	benzoic acid	32.0	toluene	
In.bz.DMF	$In(CH_3)_3$	8.88	benzoic acid	32.0	DMF	
In.bz.NMP	$In(CH_3)_3$	8.88	benzoic acid	32.0	NMP	
In.ol.bz.tol	$In(CH_3)_3$	8.88	tech. grade oleic acid	16.0	toluene	benzoic acid (16.0 mM)
In.ASP.bz.NMP	$In(CH_3)_3$	8.88	L-aspartic acid	16.0	NMP	benzoic acid (16.0 mM)
In.ASP.bz.DMF	$In(CH_3)_3$	8.88	L-aspartic acid	16.0	DMF	benzoic acid (16.0 mM)
InCl3.DMF	InCl3	8.88			DMF	
P.tol	$P(SiMe_3)_3$	4.44			toluene	
P.NMP	$P(SiMe_3)_3$	4.44			NMP	
P.DMF	$P(SiMe_3)_3$	4.44			DMF	
P.tol.2x	$P(SiMe_3)_3$	8.88			toluene	
P.tol.10x	$P(SiMe_3)_3$	44.4			toluene	

Label	Reagent 1	Reagent 1 conc. (mM)	Reagent 2	Reagent 2 conc. (mM)	Solvent	Notes/ extra reagent
ol.tol	oleic acid	32.0			toluene	
bz.tol	benzoic acid	32.0			toluene	
bz.DMF	benzoic acid	32.0			DMF	
ASP.DMF	L-aspartic acid	32.0			DMF	
benzamide.NMP	benzamide	4.44			NMP	*a*
benzylamine.NMP	benzylamine	4.44			NMP	*a*
benzylamine.2eq .NMP	benzylamine	8.88			NMP	
benzylamine.10eq .NMP	benzylamine	44.4			NMP	
benzylamine.tol	benzylamine	4.44			toluene	
benzylamine.DMF	benzylamine	4.44			DMF	
E,N.DMF.10eq	ethyl acetate	44.4	NMP	44.4	DMF	
E,D.NMP.10eq	ethyl acetate	44.4	DMF	44.4	NMP	
D,N.EtOAc.10eq	DMF	44.4	NMP	44.4	ethyl acetate	
E,D,N.tol.10eq	ethyl acetate	44.4	DMF	44.4	toluene	NMP (44.4 mM)
E,N.DMF.10eq.2x	ethyl acetate	88.8	NMP	88.8	DMF	
E,N.DMF.100eq	ethyl acetate	444	NMP	444	DMF	
E,D.NMP.100eq	ethyl acetate	444	DMF	444	NMP	
E,D.tol.100eq	ethyl acetate	444	DMF	444	toluene	
E,N.tol.100eq	ethyl acetate	444	NMP	444	toluene	
E,D.NMP.200eq	ethyl acetate	888	DMF	888	NMP	
E,D.NMP.400eq	ethyl acetate	1780	DMF	1780	NMP	
E,D.NMP.600eq	ethyl acetate	2660	DMF	2660	NMP	
E,N.DMF.600eq	ethyl acetate	2660	NMP	2660	DMF	
E,D.tol.600eq	ethyl acetate	2660	DMF	2660	toluene	
E,N.tol.600eq	ethyl acetate	2660	NMP	2660	toluene	
E,D.NMP.800eq	ethyl acetate	3550	DMF	3550	NMP	

a: prepared using serial dilution

Table 2.2 Conditions for High-Throughput Experiments

Reaction Label	In solution	In solution volume (µL)	P solution	P solution volume (µL)	solvent/ additive #1	solvent/ additive #1 volume (µL)	solvent/ additive #2	solvent/ additive #2 volume (µL)
1.B2,D2,F2	In.ol.tol	50	P.tol	50	toluene	100		
1.B3,D3,F3	In.ol.tol	50	P.tol	50	toluene	80	NMP	20
1.B4,D4,F4	In.ol.tol	50	P.tol	50	toluene	60	NMP	40
1.B5,D5,F5	In.ol.tol	50	P.tol	50	toluene	40	NMP	60
1.B6,D6,F6	In.ol.tol	50	P.tol	50	toluene	20	NMP	80
1.B7,D7,F7	In.ol.tol	50	P.tol	50	NMP	100		
1.B8,D8,F8	In.ol.tol	50	P.tol	50	DMF	100		
1.B9,D9,F9	In.ol.tol	50	P.tol	50	DMA	100		
1.B10,D10,F10	In.ph.NMP	50	P.NMP	50	DMF	100		
1.B11,D11,F11	P.NMP	50	P.NMP	50	DMA	100		
1.C2,E2,G2	In.ph.NMP	50	P.NMP	50	toluene	100		
1.C3,E3,F3	In.ph.NMP	50	P.NMP	50	toluene	80	NMP	20
1.C4,E4,G4	In.ph.NMP	50	P.NMP	50	toluene	60	NMP	40
1.C5,E5,G5	In.ph.NMP	50	P.NMP	50	toluene	40	NMP	60
1.C6,E6,G6	In.ph.NMP	50	P.NMP	50	toluene	20	NMP	80
1.C7,E7,G7	In.ph.NMP	50	P.NMP	50	NMP	100		
1.C8,E8,G8	In.ph.NMP	50	P.NMP	50	benzamide .NMP	100		
1.C9,E9,G9	In.ph.NMP	50	P.NMP	50	benzylamine .NMP	100		
1.C10,E10,G10	In.ol.tol	50	P.tol	50	benzamide .NMP			
1.C11,E11,G11	In.ol.tol	50	P.tol	50	benzylamine .NMP			

Reaction Label	In solution	In solution volume (µL)	P solution	P solution volume (µL)	solvent/ additive #1	solvent/ additive #1 volume (µL)	solvent/ additive #2	solvent/ additive #2 volume (µL)
2.B2,D2,F2	In.ol.tol	50	P.tol	50	benzylamine .tol	100		
2.B3,D3,F3	In.ol.tol	50	P.tol	50	benzylamine .2eq.NMP	100		
2.B4,D4,F4	In.ol.tol	50	P.tol	50	benzylamine .10eq.NMP	100		
2.B5,D5,F5	In.ol.tol	50	P.tol	50	NMP	90	benzylamine	10
2.B6,D6,F6	In.ol.tol	50	P.tol	50	NMP	50	benzylamine	50
2.B7,D7,F7	In.ol.tol	50	P.tol	50	benzylamine	100		
2.B8,D8,F8	In.ol.tol	50	P.tol	50	benzylamine .DMF	100		
2.B9,D9,F9	In.ol.tol	50	P.tol	50	DMF	90	benzylamine	10
2.B10,D10,F10	In.13%.ol.tol	50	P.tol	50	toluene	60	NMP	40
2.B11,D11,F11	In.13%.ol.tol.10x	50	P.tol.10x	50	toluene	60	NMP	40
2.C2,E2,G2	In.ol.tol.2x	50	P.tol.2x	50	toluene	100		
2.C3,E3,F3	In.ol.tol.2x	50	P.tol.2x	50	toluene	60	NMP	40
2.C4,E4,G4	In.ol.tol.2x	50	P.tol.2x	50	NMP	100		
2.C5,E5,G5	In.13%.ol.tol.2x	50	P.tol.2x	50	toluene	60	NMP	40
2.C6,E6,G6	In.ol.tol.2x	50	P.tol.2x	50	benzylamine .NMP	100		
2.C7,E7,G7	In.ol.tol.2x	50	P.tol.2x	50	benzylamine	100		
2.C8,E8,G8	In.ol.tol.2x	50	P.tol.2x	50	DMF	100		
2.C9,E9,G9	In.ol.tol.10x	50	P.tol.10x	50	toluene	100		
2.C10,E10,G10	In.ol.tol.10x	50	P.tol.10x	50	toluene	60	NMP	40
2.C11,E11,G11	In.ol.tol.10x	50	P.tol.10x	50	benzylamine .NMP	100		

Reaction Label	In solution	In solution volume (µL)	P solution	P solution volume (µL)	solvent/ additive #1	solvent/ additive #1 volume (µL)	solvent/ additive #2	solvent/ additive #2 volume (µL)
3.B2,E2	In.t.ol.tol	v	P.tol	50	toluene	100		
3.B3,E3	In.t.ol.tol	50	P.tol	50	toluene	80	NMP	20
3.B4,E4	In.t.ol.tol	50	P.tol	50	toluene	60	NMP	40
3.B5,E5	In.t.ol.tol	50	P.tol	50	toluene	40	NMP	60
3.B6,E6	In.t.ol.tol	50	P.tol	50	toluene	20	NMP	80
3.B7,E7	In.t.ol.tol	50	P.tol	50	NMP	100		
3.B8,E8	In.3%.t.ol.tol	25	P.tol	25	toluene	150		
3.B9,E9	In.t.ol.tol	50	P.tol	50	DMF	100		
3.B10,E10	In.t.ol.tol	50	P.tol	50	DMA	100		
3.B11,E11	In.t.ol.tol	50	P.tol	50	benzylamine .2eq.NMP	100		
3.C2	In.st.tol	50	P.tol	50	toluene	100		
3.C3	In.st.tol	50	P.tol	50	NMP	100		
3.C4,F4	In.st.tol	50	P.tol	50	DMF	100		
3.C5,F5	In.st.tol	50	P.tol	50	benzylamine .2eq.NMP	100		
3.C6	In.ph.tol	50	P.tol	50	toluene	100		
3.C7	In.ph.tol	50	P.tol	50	NMP	100		
3.C8,F8	In.ph.tol	50	P.tol	50	DMF	100		
3.C9,F9	In.ph.tol	50	P.tol	50	benzylamine .2eq.NMP	100		
3.F2	In.3%.t.ol.tol	50	P.tol	50	toluene	60	NMP	40
3.F3	In.13%.t.ol.tol	50	P.tol	50	toluene	60	NMP	40
3.F6	In.3%.t.ol.tol	50	P.tol	50	NMP	100		
3.F7	In.13%.t.ol.tol	50	P.tol	50	NMP	100		

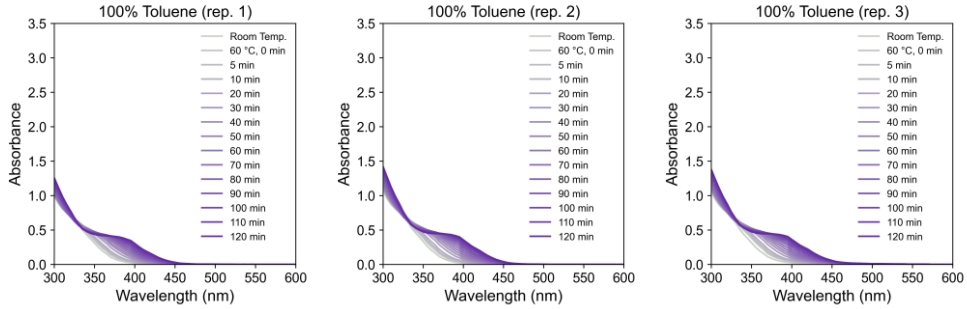
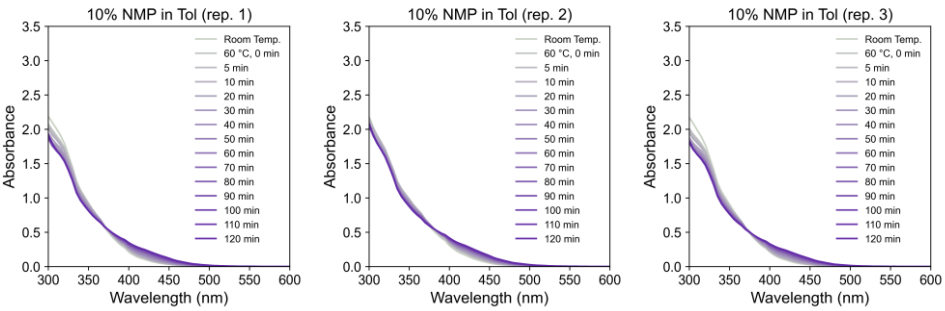
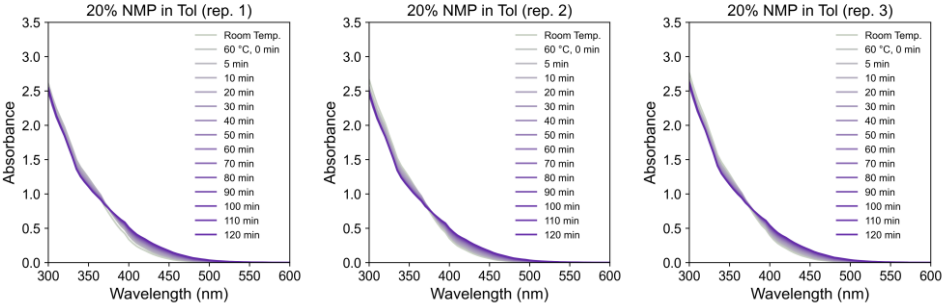
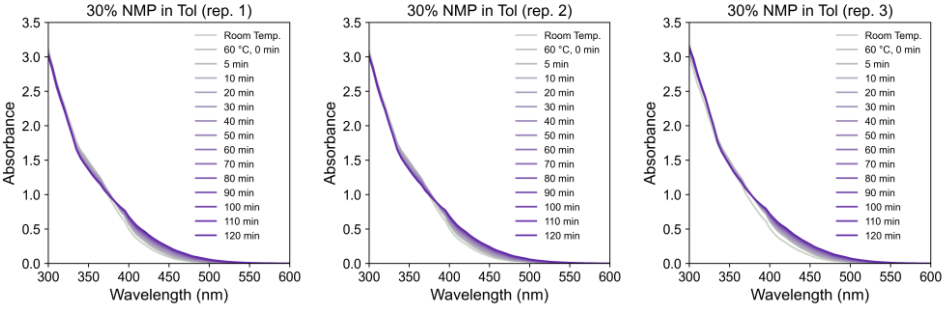
Reaction Label	In solution	In solution volume (µL)	P solution	P solution volume (µL)	solvent/ additive #1	solvent/ additive #1 volume (µL)	solvent/ additive #2	solvent/ additive #2 volume (µL)	solvent/ additive #3	solvent/ additive #3 volume (µL)
4.B2,D2,F2	In.bz.tol	50	P.tol	50	E,N.DMF .10eq	100				
4.B3,D3,F3	In.bz.tol	50	P.tol	50	E,D.NMP .10eq	100				
4.B4,D4,F4	In.bz.tol	50	P.tol	50	D,N.EtOAc .10eq	100				
4.B5,D5,F5	In.bz.DMF	50	P.DMF	50	E,N.DMF .10eq	100				
4.B6,D6,F6	In.bz.tol	50	P.tol	50	E,D,N.tol .10eq	100				
4.B7,D7,F7	In.ol.bz.tol	50	P.tol	50	E,N.DMF .10eq	100				
4.B8,D8,F8	In.ol.bz.tol		P.tol	50	E,D.NMP .10eq	100				
4.B9,D9,F9	In.ol.bz.tol	50	P.tol	50	D,N.EtOAc .10eq	100				
4.B10,D10,F10	In.ol.bz.tol	50	P.tol	50	E,D,N.tol. 10eq	100				
4.B11,D11,F11	In.ol.bz.tol	50	P.DMF	50	ethyl acetate	50	NMP	50		
4.C2,E2,G2	InCl3.DMF	50	P.tol	50	E,N.DMF .10eq.2x	50	ol.tol	50		
4.C3,E3,F3	InCl3.DMF	50	P.tol	50	E,N.DMF .10eq.2x	50	bz.tol	50		
4.C4,E4,G4	InCl3.DMF	50	P.DMF	50	E,N.DMF .10eq.2x	50	bz.DMF	50		
4.C5,E5,G5	InCl3.DMF	50	P.DMF	50	E,N.DMF .10eq.2x	50	ASP.DMF	50		

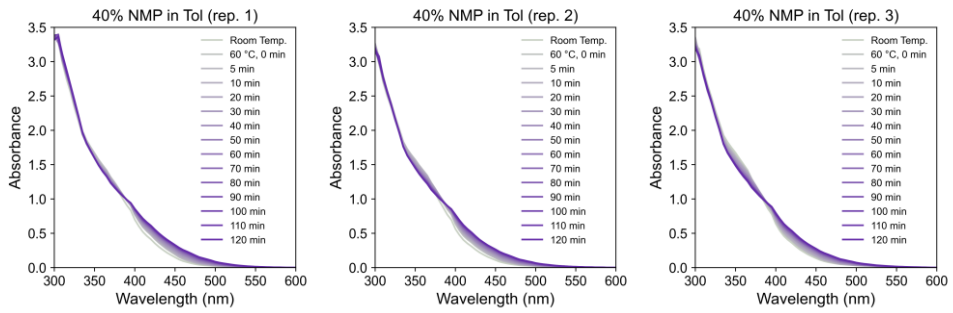
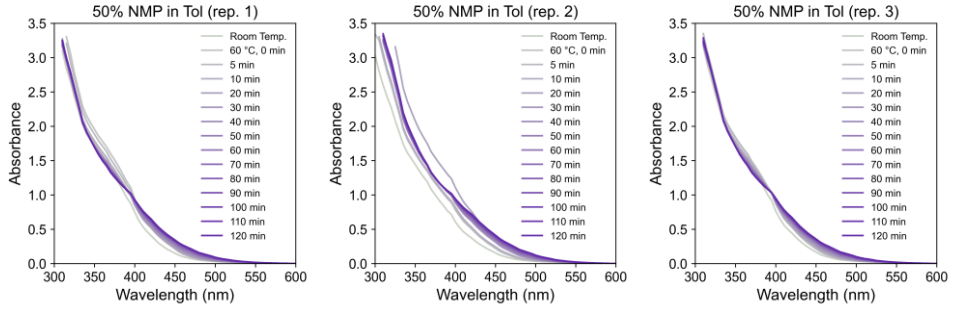
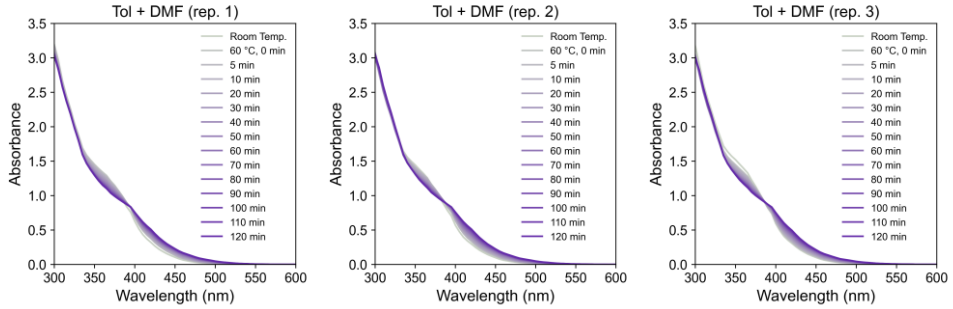
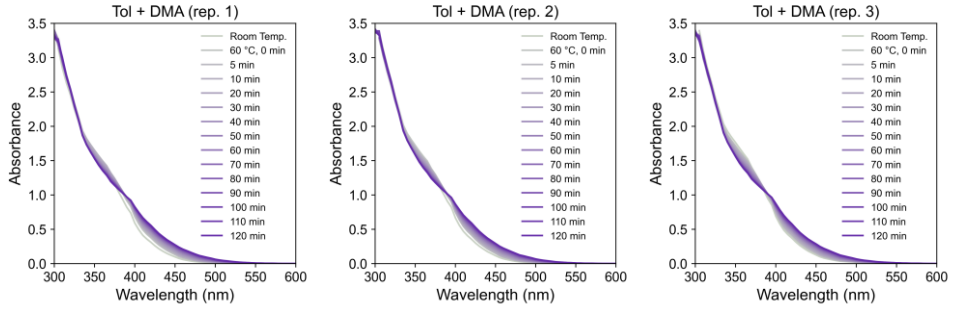
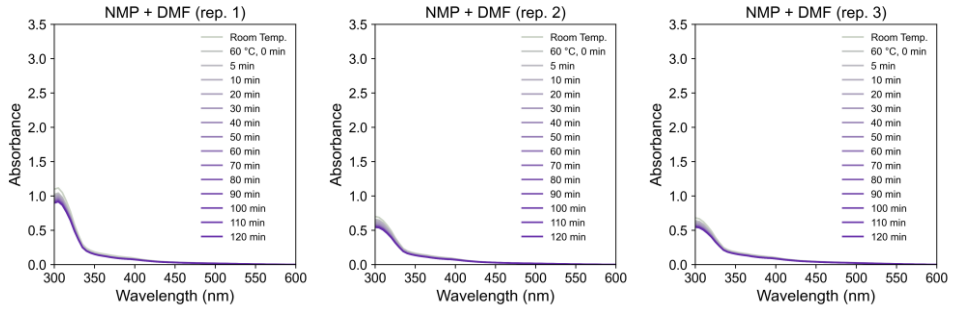
Reaction Label	In solution	In solution volume (μL)	P solution	P solution volume (μL)	solvent/ additive #1	solvent/ additive #1 volume (μL)	solvent/ additive #2	solvent/ additive #2 volume (μL)	solvent/ additive #3	solvent/ additive #3 volume (μL)
4.C6,E6,G6	InCl3.DMF	50	P.DMF	50	E,N.DMF .10eq.2x	50	ASP.DMF	25	bz.DMF	25
4.C7,E7,G7	InCl3.DMF	50	P.tol	50	E,N.DMF .10eq.2x	50	ASP.DMF	25	ol.tol	25
4.C8,E8,G8	InCl3.DMF	50	P.DMF	50	DMF	50	ASP.DMF	50		
4.C9,E9,G9	InCl3.DMF	50	P.DMF	50	ethyl acetate	25	NMP	25	ASP.DMF	50
4.C10,E10,G10	In.bz.tol	50	P.DMF	50	ethyl acetate	50	NMP	50		
4.C11,E11,G11	In.bz.tol	50	P.tol	50	E,N.DMF .100eq	100				
5.B2,D2,F2	In.bz.tol	50	P.tol	50	E,D.NMP .100eq	100				
5.B3,D3,F3	In.bz.tol	50	P.tol	50	E,D.NMP .200eq	100				
5.B4,D4,F4	In.bz.tol	50	P.tol	50	E,D.NMP .400eq	100				
5.B5,D5,F5	In.bz.tol	50	P.tol	50	E,D.NMP .600eq	100				
5.B6,D6,F6	In.bz.tol	50	P.tol	50	E,D.NMP .800eq	100				
5.B7,D7,F7	In.bz.DMF	50	P.tol	50	ethyl acetate	50	NMP	50		
5.B8,D8,F8	In.ol.tol	50	P.tol	50	E,D.NMP .100eq	100				
5.B9,D9,F9	In.ol.tol	50	P.tol	50	E,D.NMP .600eq	100				

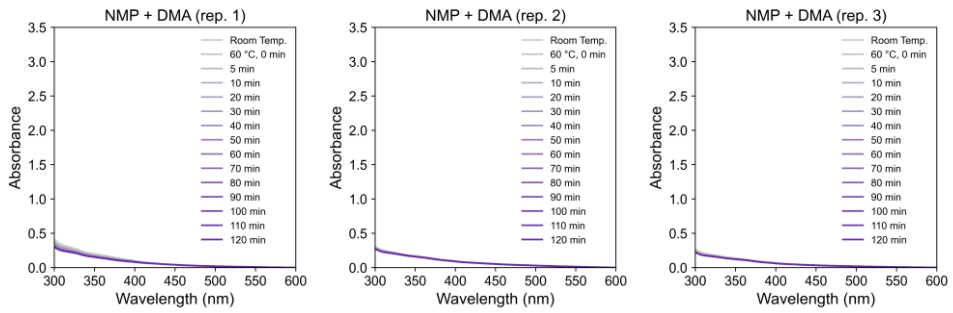
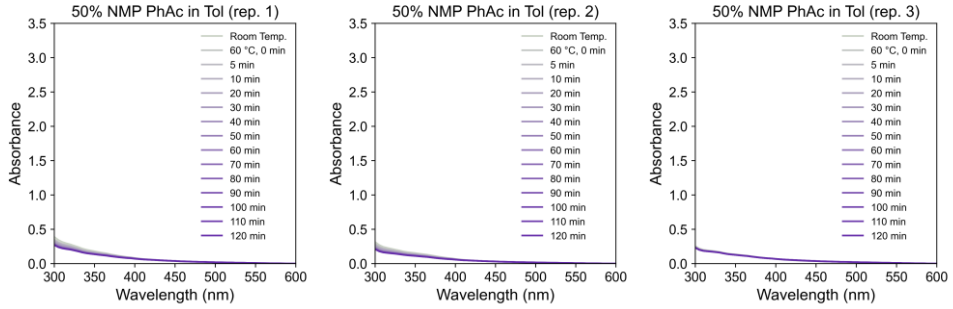
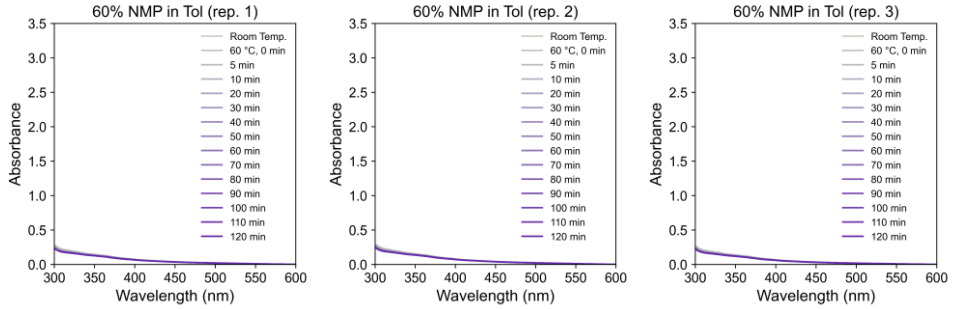
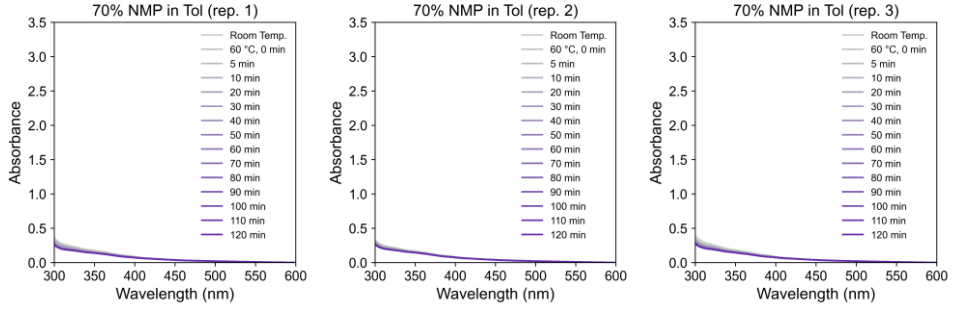
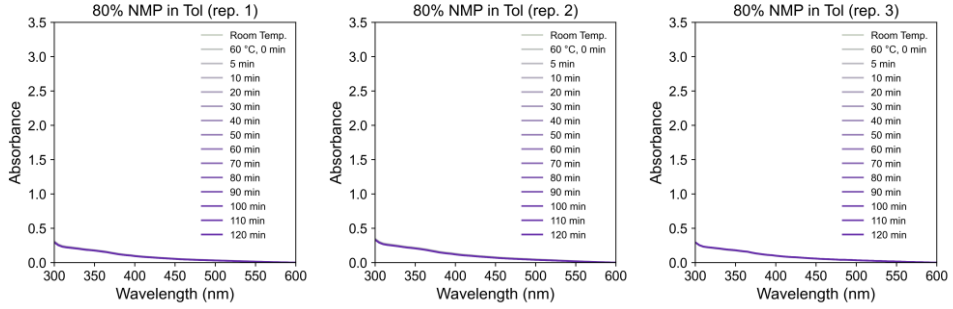
Reaction Label	In solution	In solution volume (μL)	P solution	P solution volume (μL)	solvent/ additive #1	solvent/ additive #1 volume (μL)	solvent/ additive #2	solvent/ additive #2 volume (μL)	solvent/ additive #3	solvent/ additive #3 volume (μL)
5.B10,D10,F10	In.ol.tol	50	P.tol	50	E,N.DMF .100eq	100				
5.B11,D11,F11	In.ol.tol	50	P.tol	50	E,N.DMF .600eq	100				
5.C2,E2,G2	In.bz.tol	50	P.tol	50	NMP	100				
5.C3,E3,F3	In.bz.tol	50	P.tol	50	DMF	100				
5.C4,E4,G4	In.bz.NMP	50	P.NMP	50	toluene	100				
5.C5,E5,G5	In.bz.DMF	50	P.DMF	50	toluene	100				
5.C6,E6,G6	In.bz.NMP	50	P.NMP	50	E,D.tol .100eq	100				
5.C7,E7,G7	In.bz.DMF	50	P.DMF	50	E,N.tol .100eq	100				
5.C8,E8	In.bz.ASP .NMP	50	P.NMP	50	E,D.tol .100eq	100				
5.C9,E9	In.ASP.bz .NMP	50	P.NMP	50	E,D.tol .600eq	100				
5.G10	In.ASP.bz .DMF	50	P.DMF	50	E,N.tol .100eq	100				
5.G11	In.ASP.bz .DMF	50	P.DMF	50	E,N.tol .600eq	100				

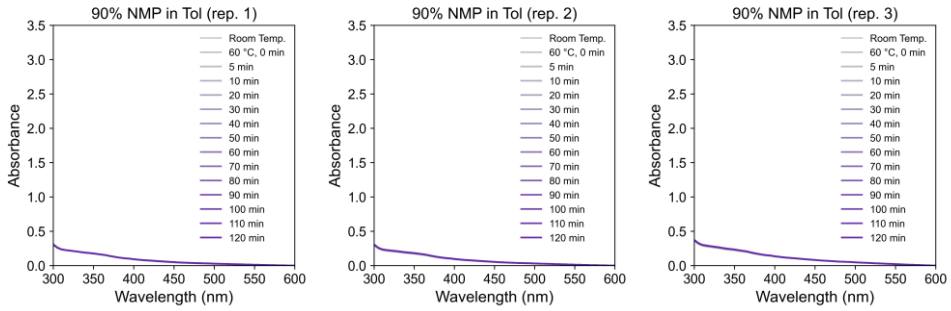
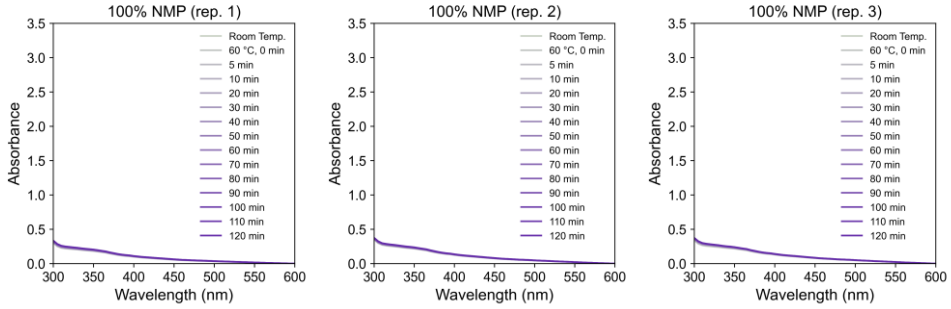
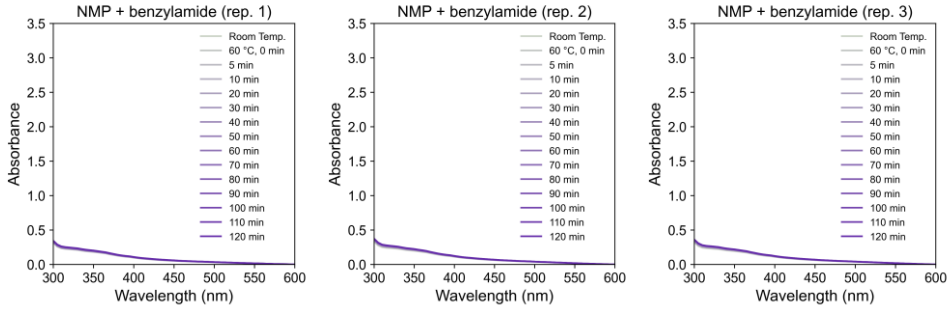
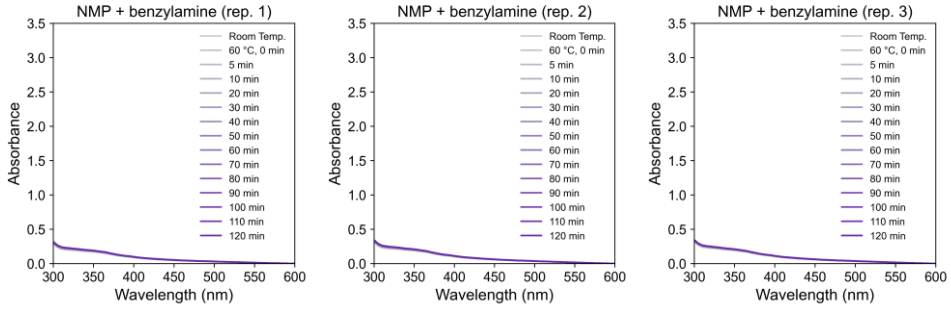
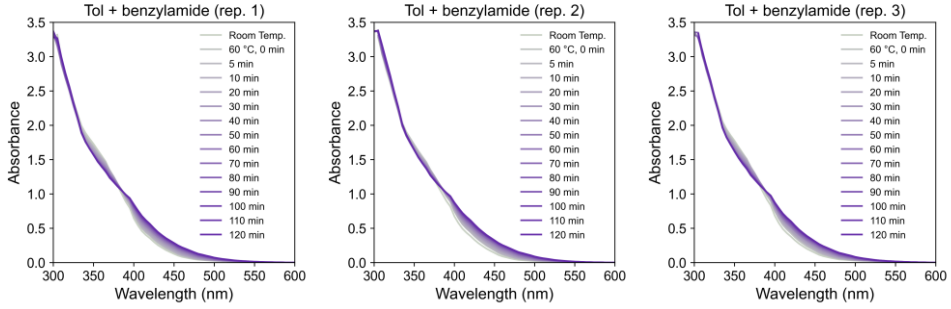
2.4.16 *UV-visible Absorbance Spectra of Time points for High-Throughput Experiments*

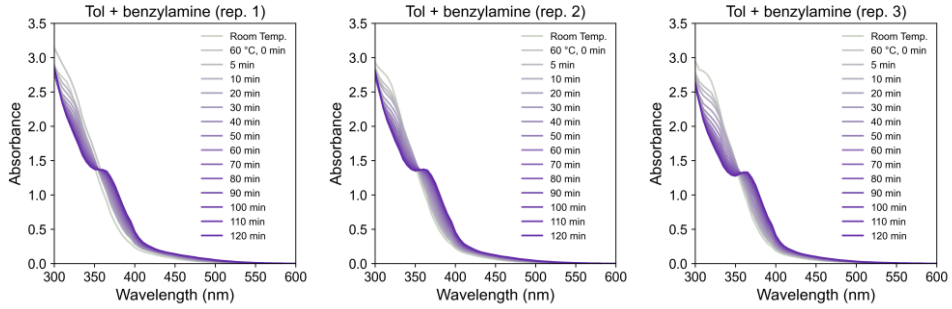
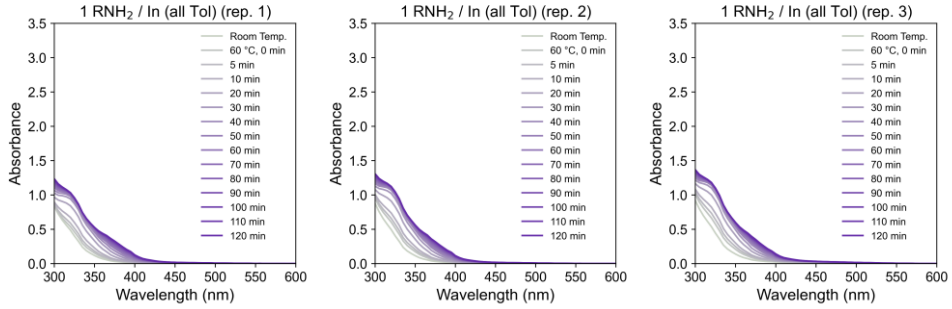
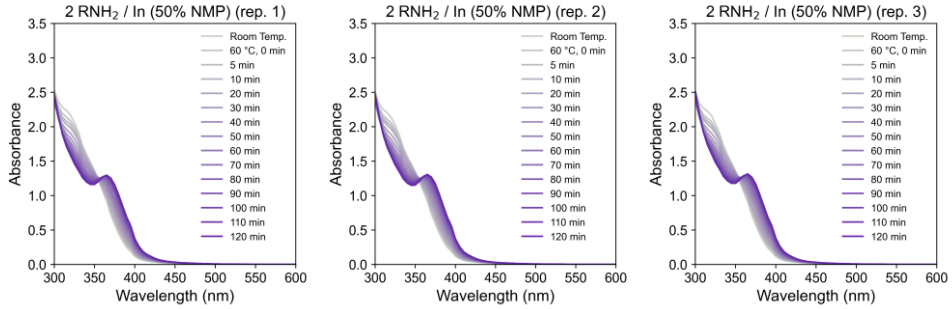
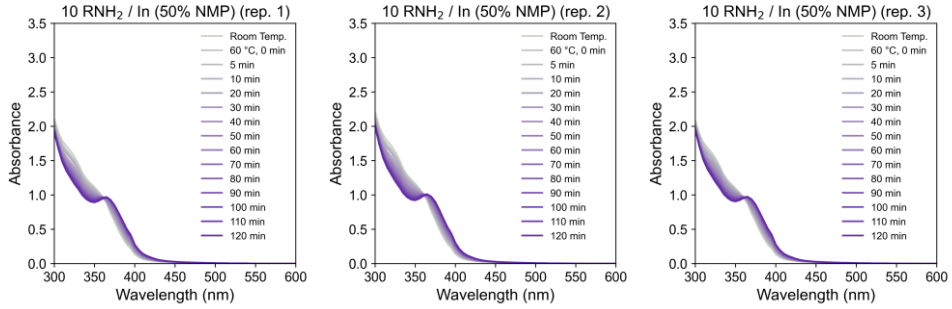
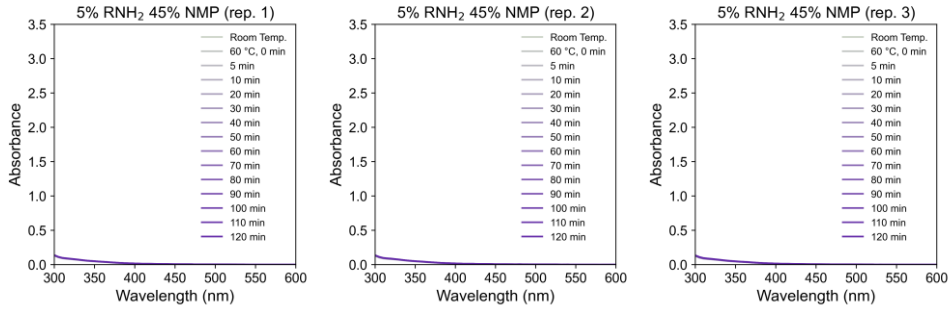
Table 2.3 UV-visible Absorbance Spectra of Time points for High-Throughput Experiments

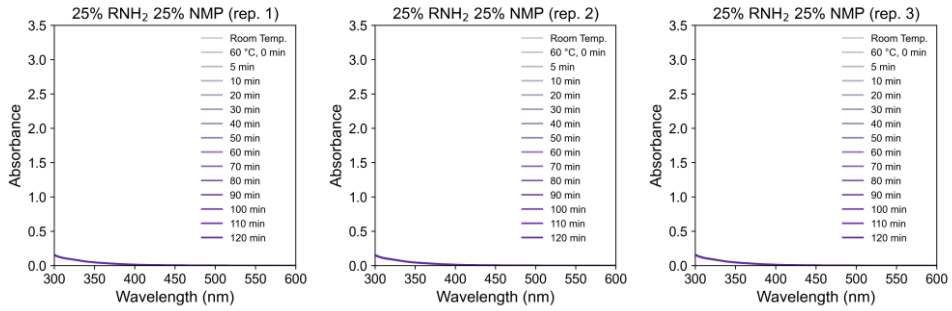
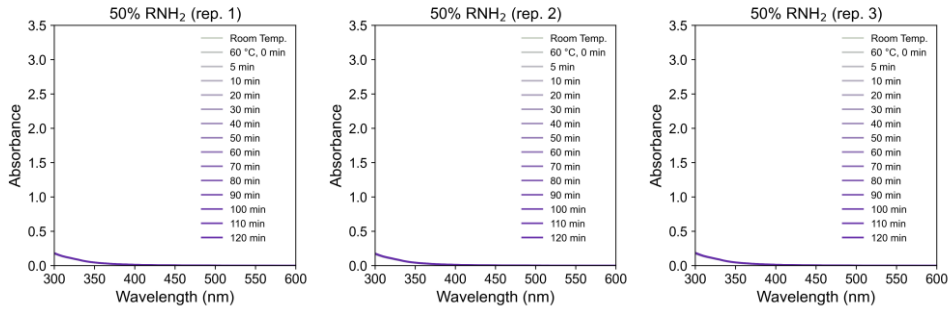
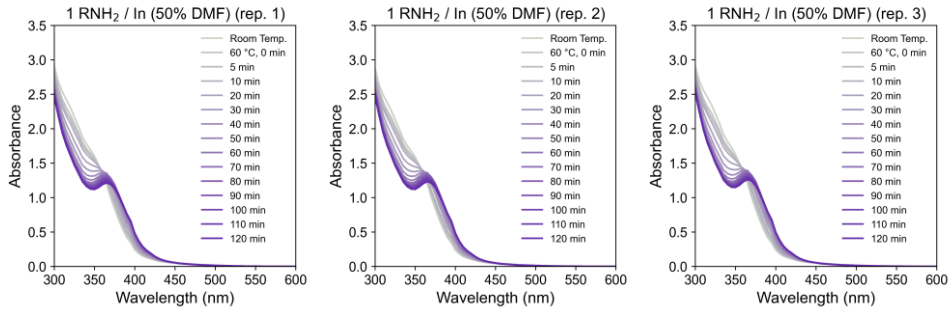
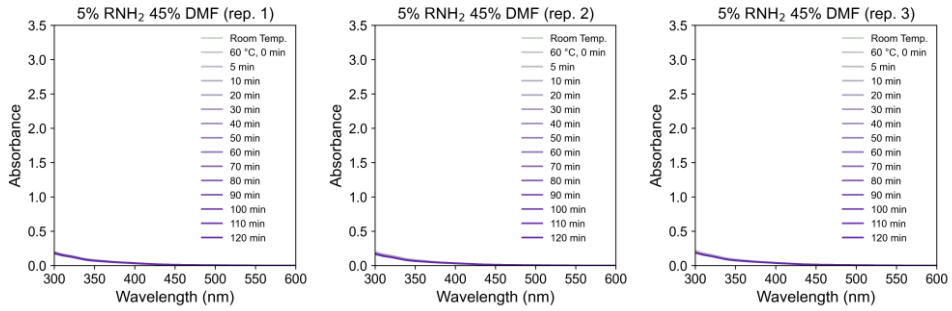
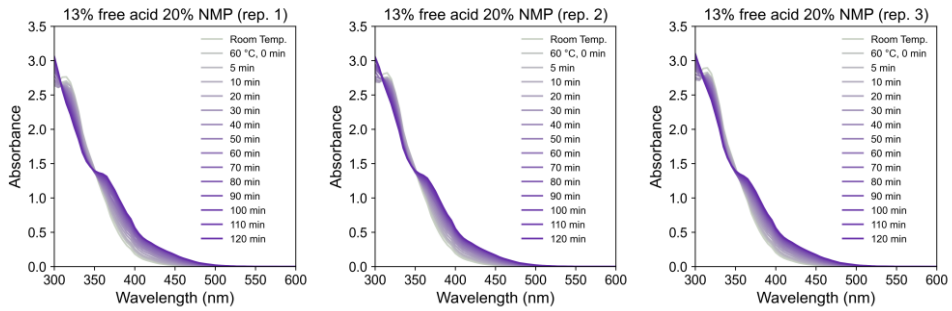
1.B2,D2,F2	
1.B3,D3,F3	
1.B4,D4,F4	
1.B5,D5,F5	

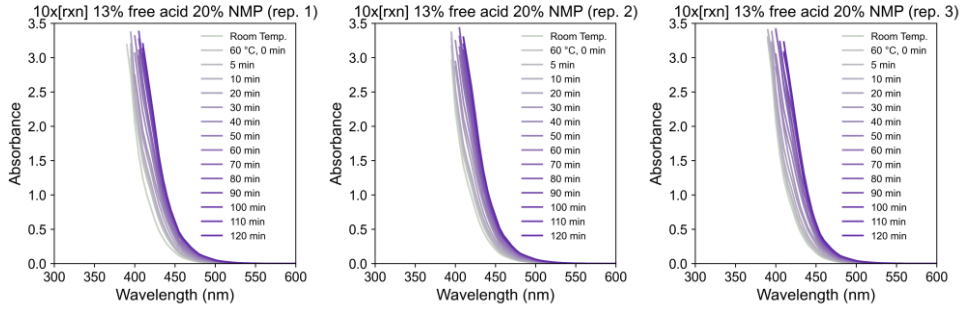
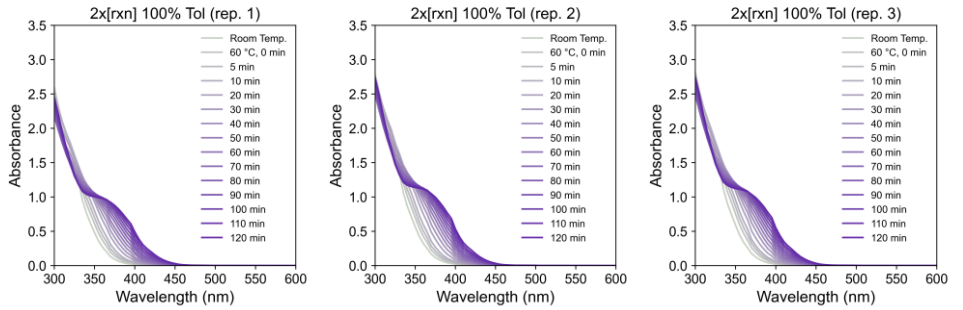
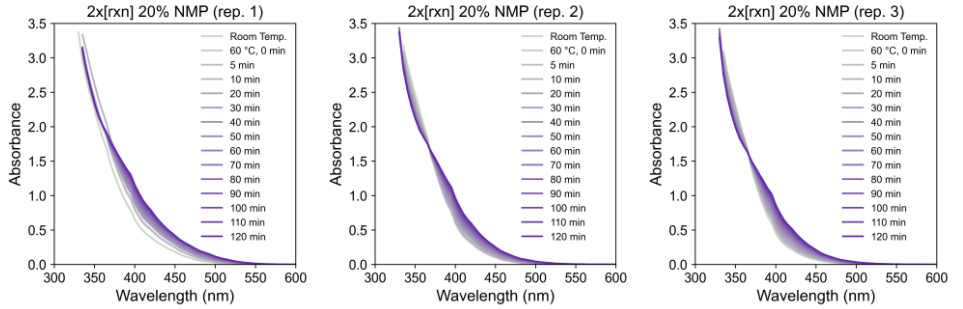
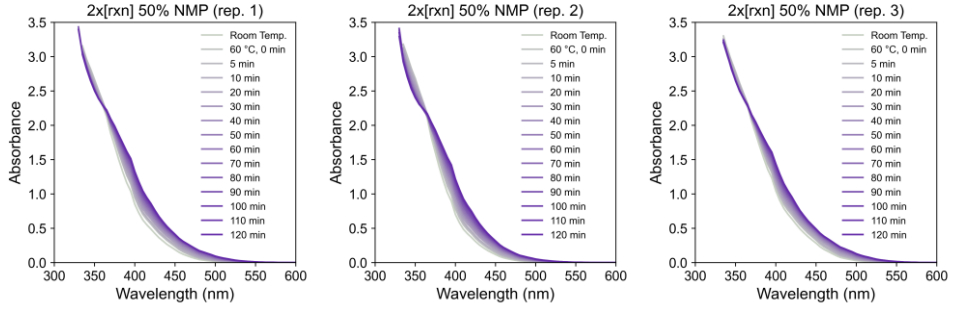
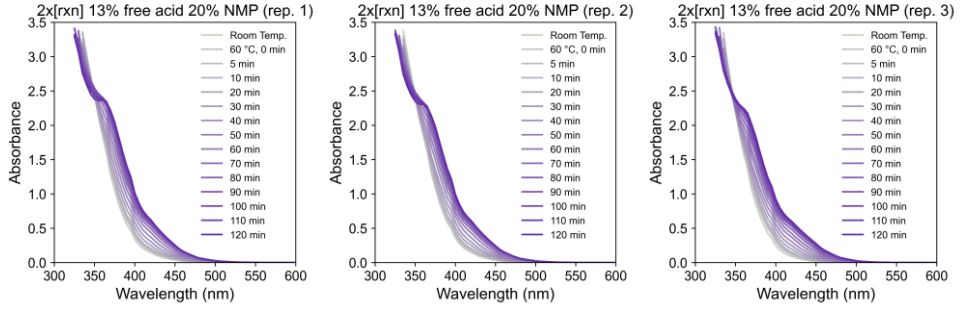
1.B6,D6,F6	
1.B7,D7,F7	
1.B8,D8,F8	
1.B9,D9,F9	
1.B10,D10,F10	

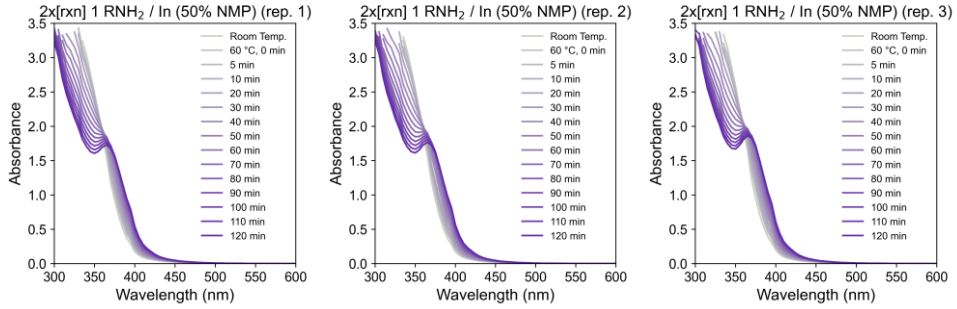
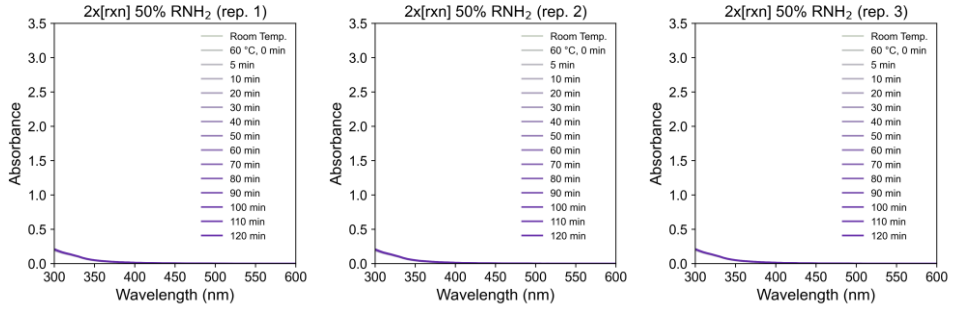
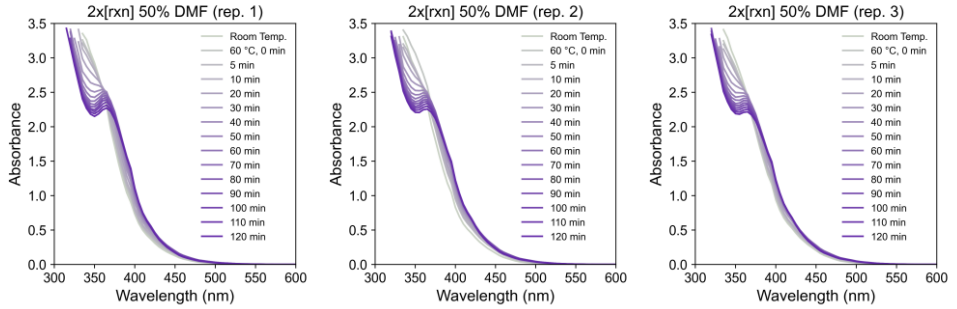
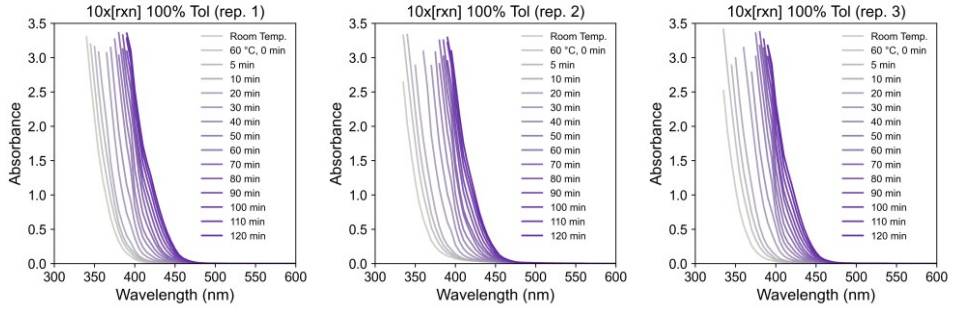
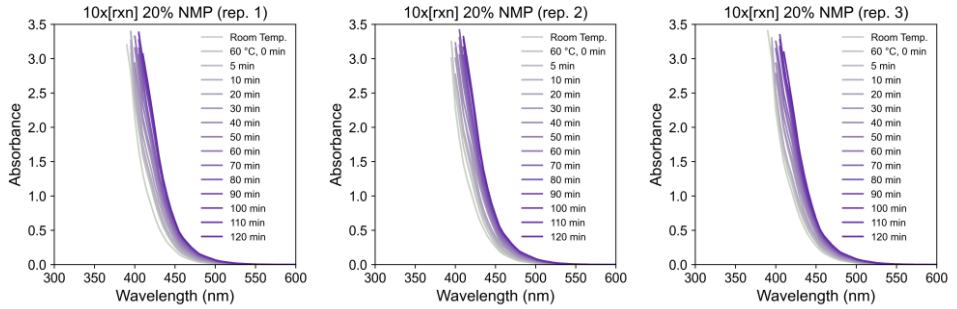
1.B11,D11,F11	
1.C2,E2,G2	
1.C3,E3,F3	
1.C4,E4,G4	
1.C5,E5,G5	

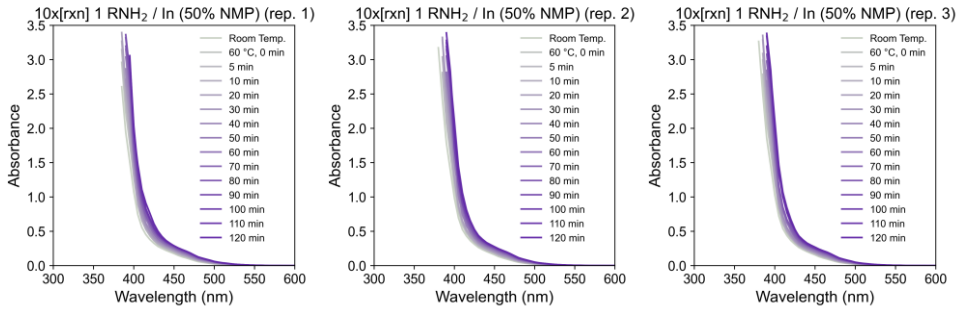
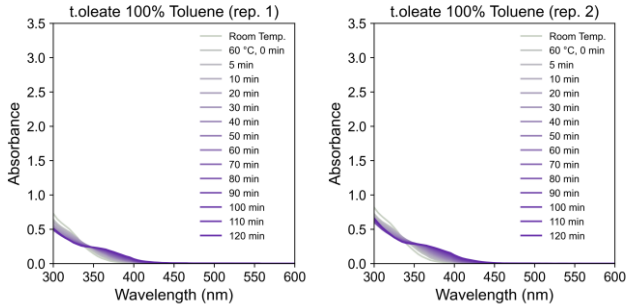
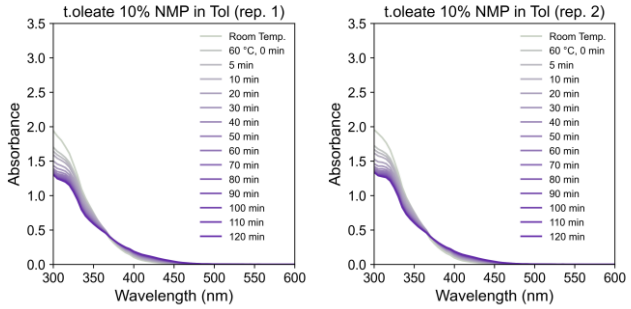
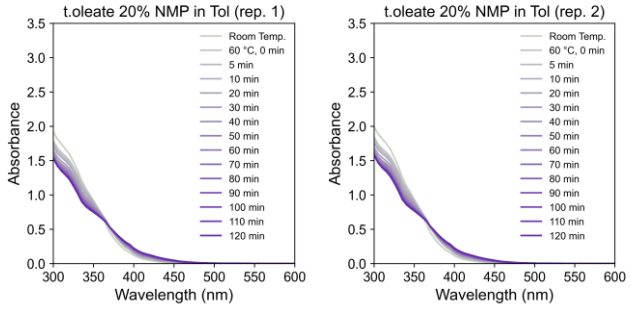
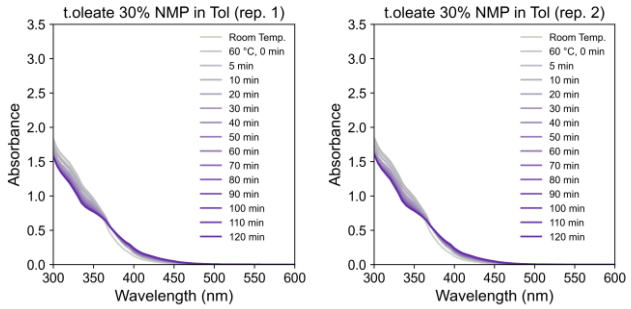
1.C6,E6,G6	
1.C7,E7,G7	
1.C8,E8,G8	
1.C9,E9,G9	
1.C10,E10,G10	

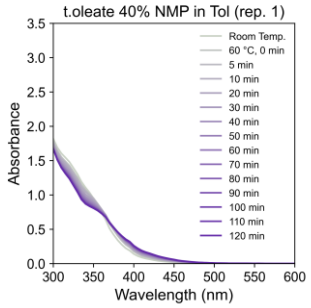
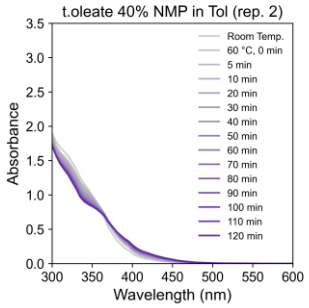
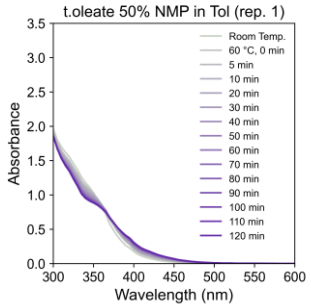
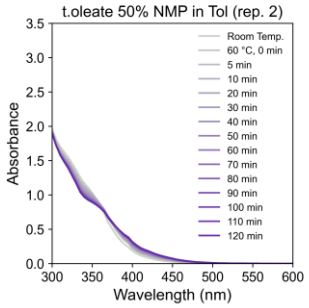
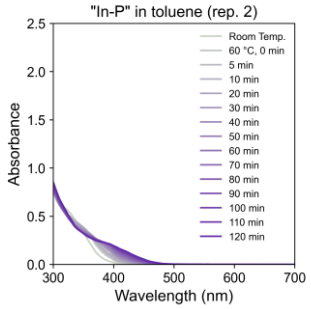
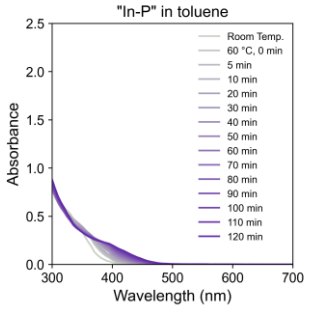
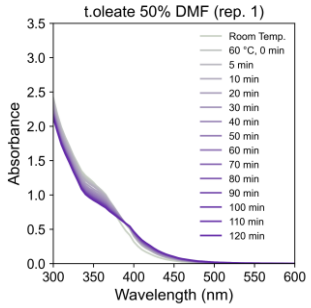
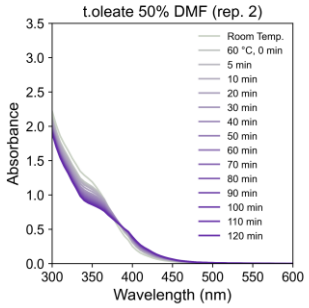
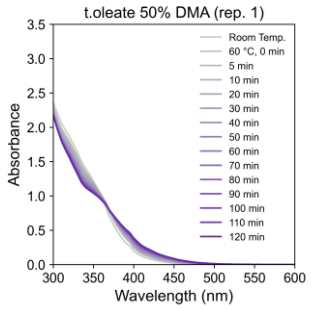
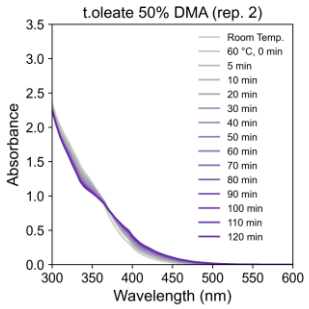
1.C11,E11,G11	
2.B2,D2,F2	
2.B3,D3,F3	
2.B4,D4,F4	
2.B5,D5,F5	

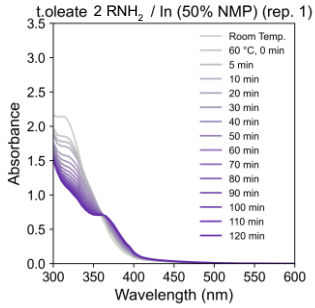
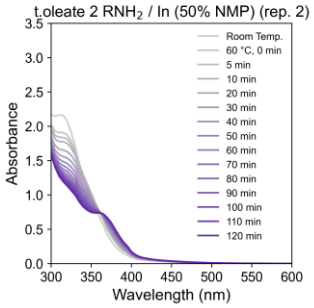
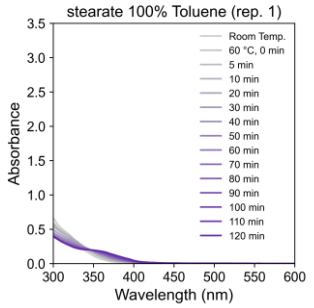
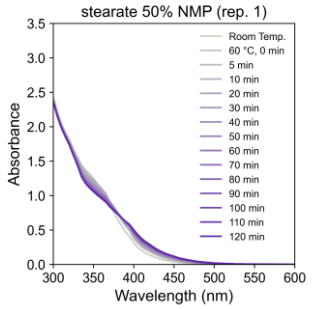
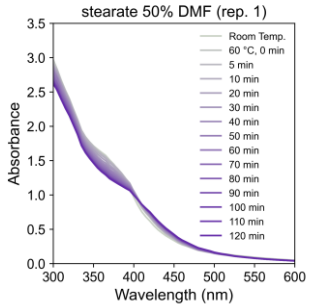
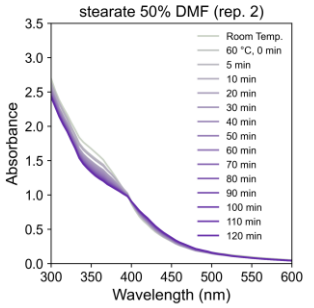
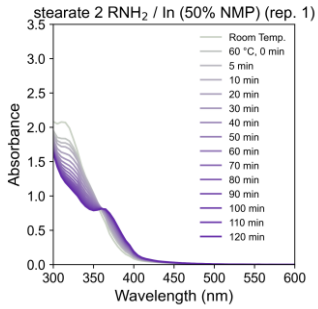
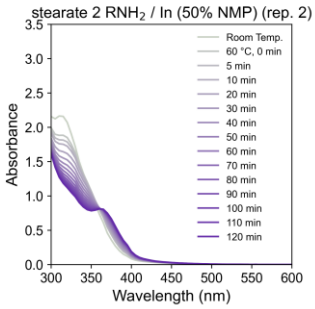
2.B6,D6,F6	
2.B7,D7,F7	
2.B8,D8,F8	
2.B9,D9,F9	
2.B10,D10,F10	

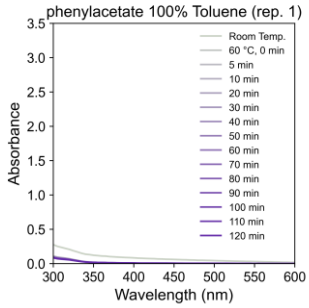
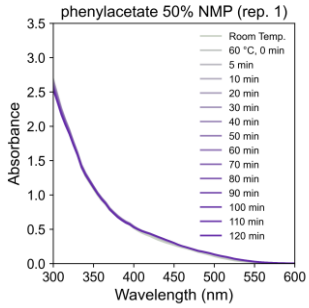
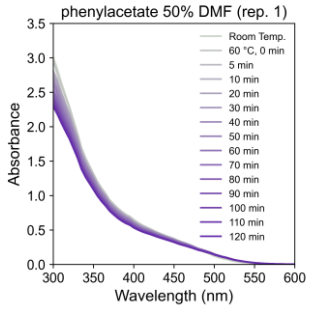
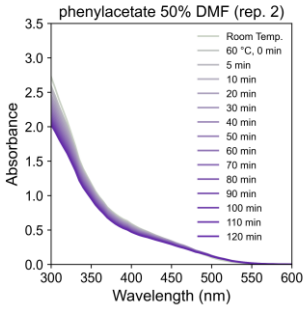
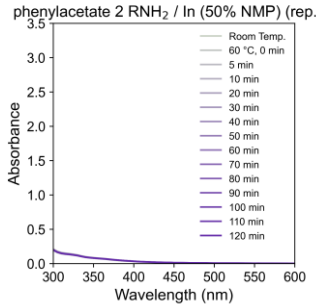
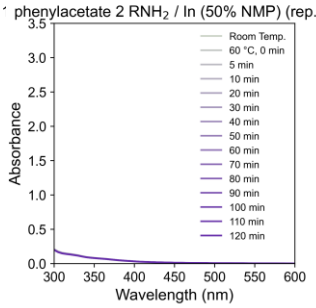
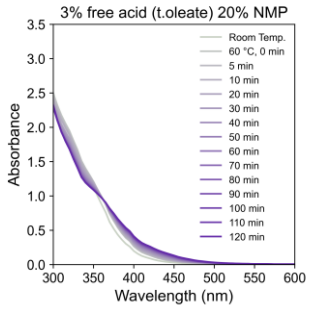
2.B11,D11,F11	
2.C2,E2,G2	
2.C3,E3,F3	
2.C4,E4,G4	
2.C5,E5,G5	

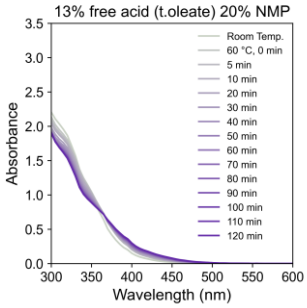
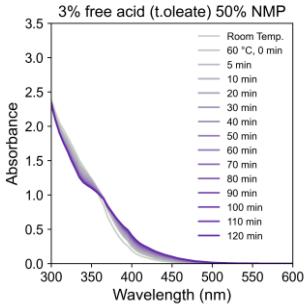
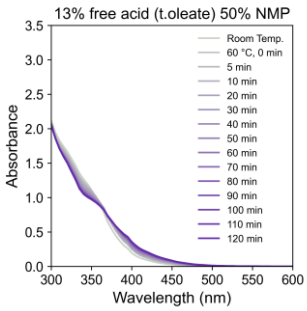
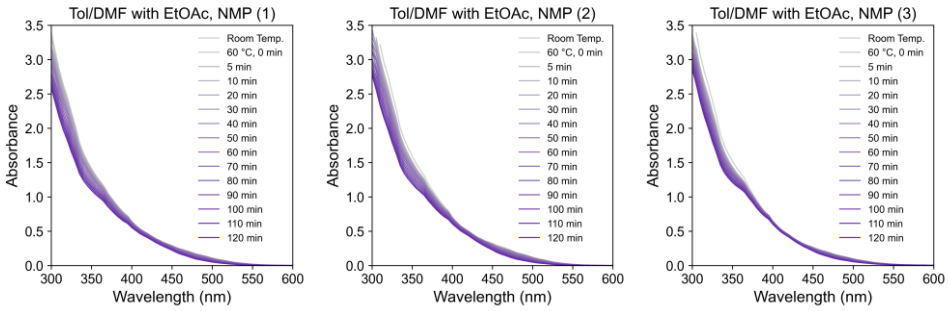
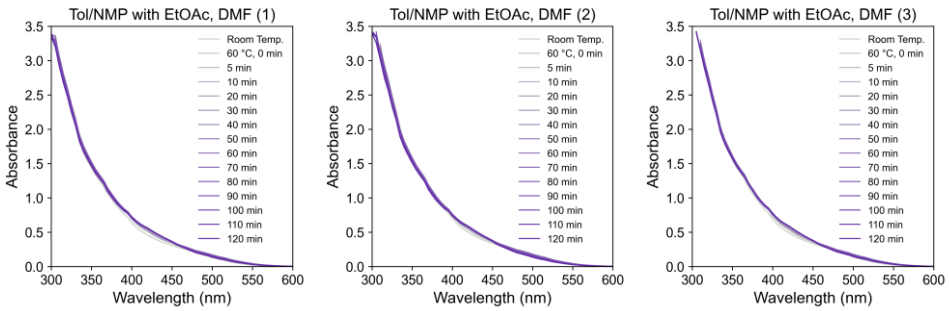
2.C6,E6,G6	
2.C7,E7,G7	
2.C8,E8,G8	
2.C9,E9,G9	
2.C10,E10,G10	

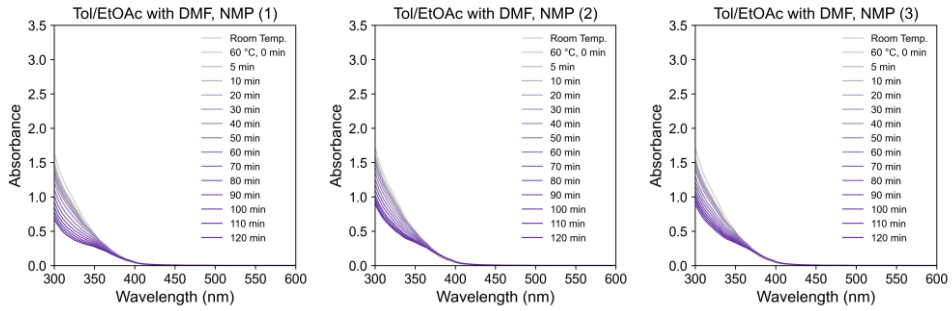
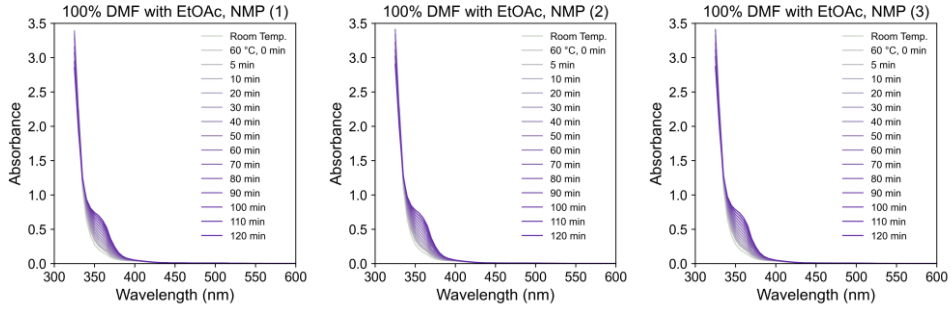
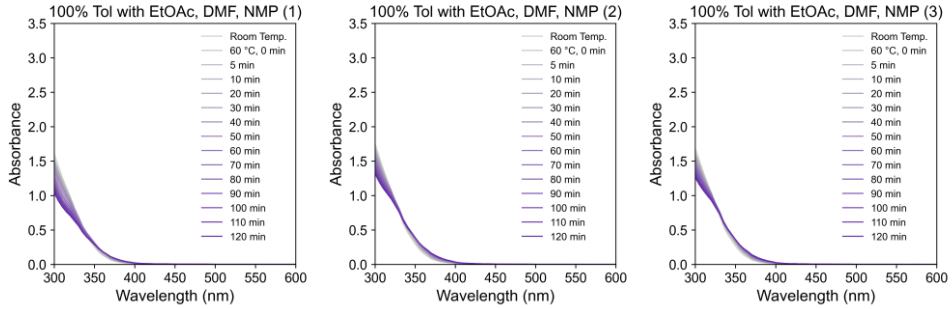
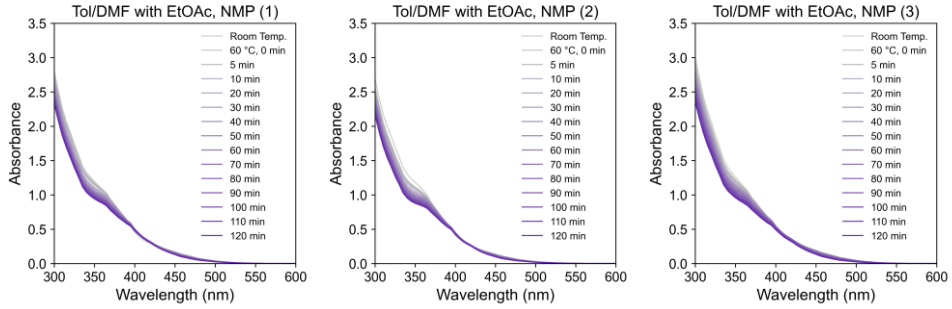
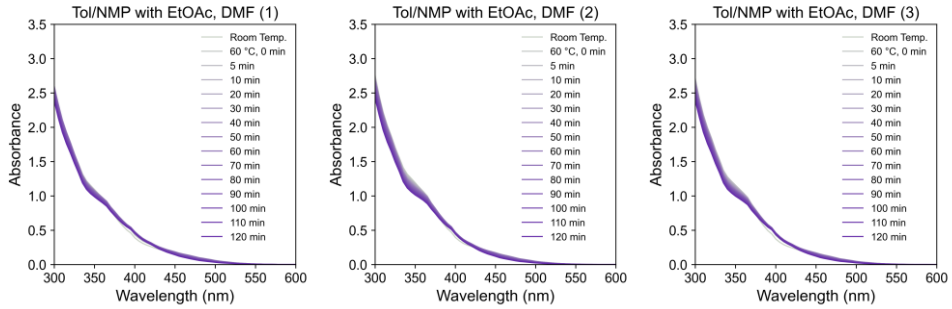
2.C11,E11,G11	
3.B2,E2	
3.B3,E3	
3.B4,E4	
3.B5,E5	

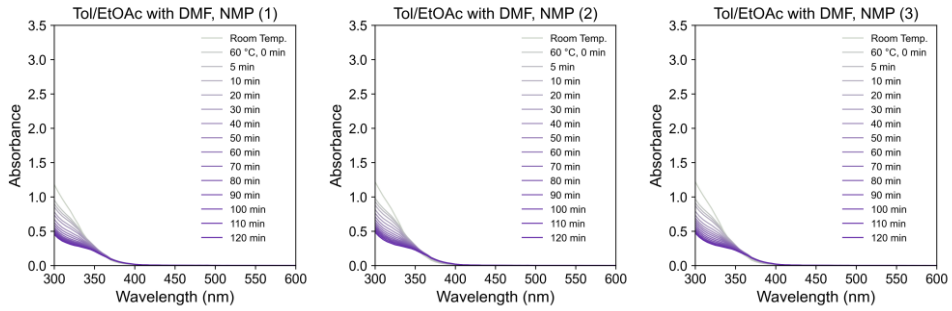
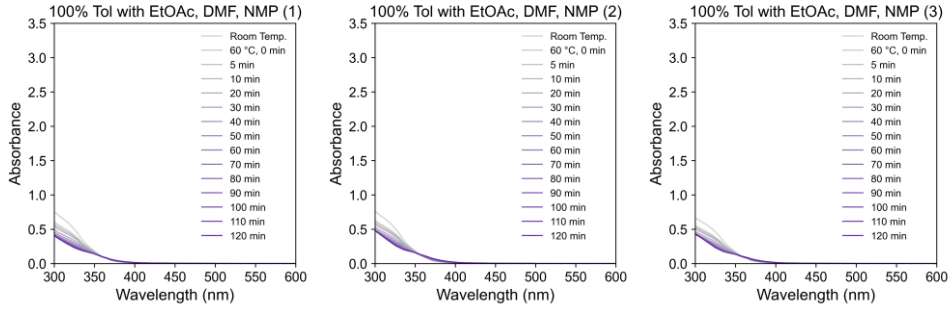
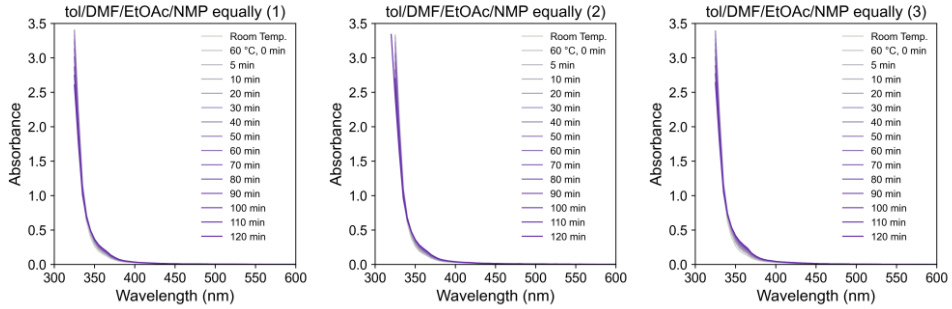
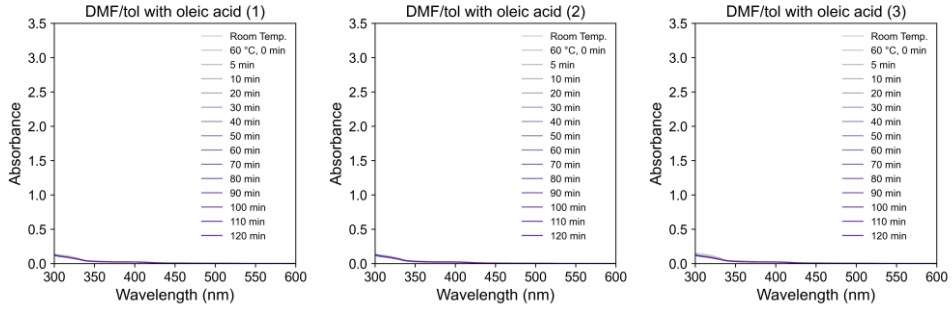
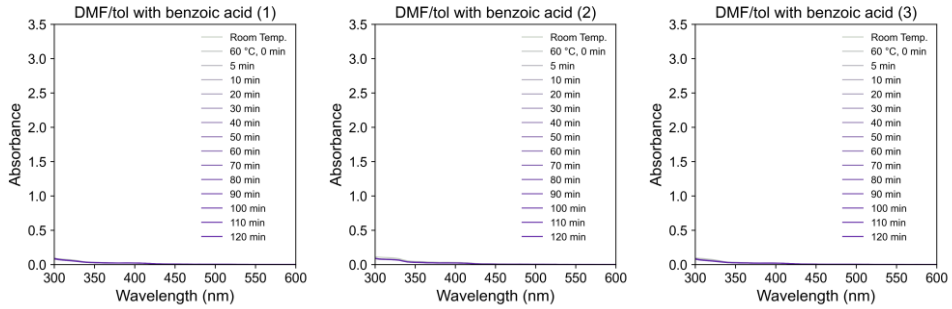
3.B6,E6	 	
3.B7,E7	 	
3.B8,E8	 	
3.B9,E9	 	
3.B10,E10	 	

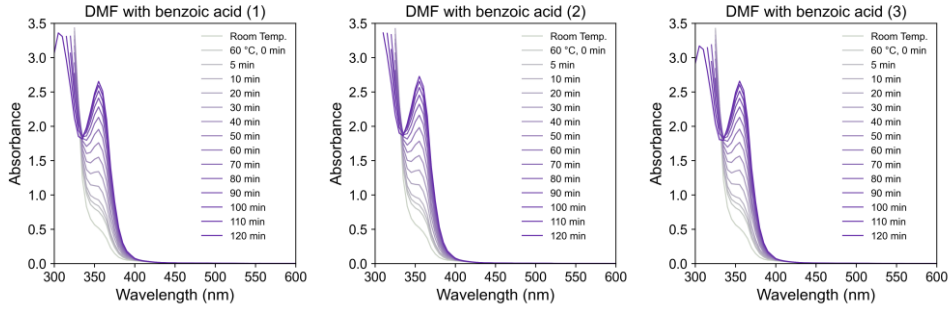
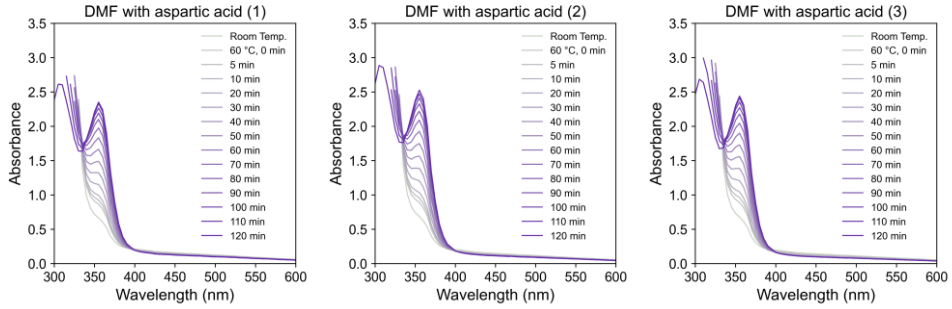
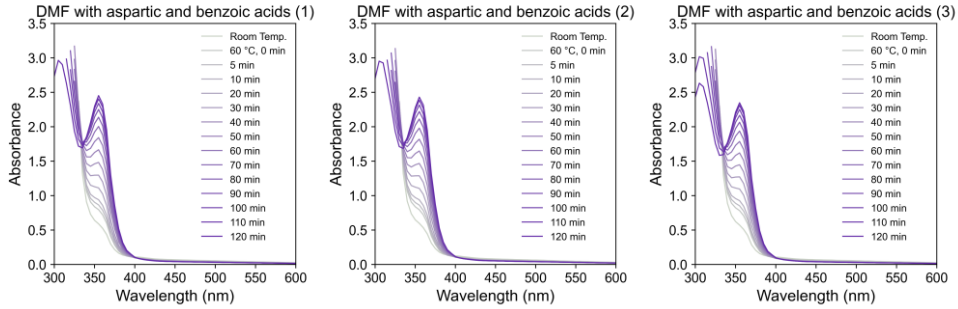
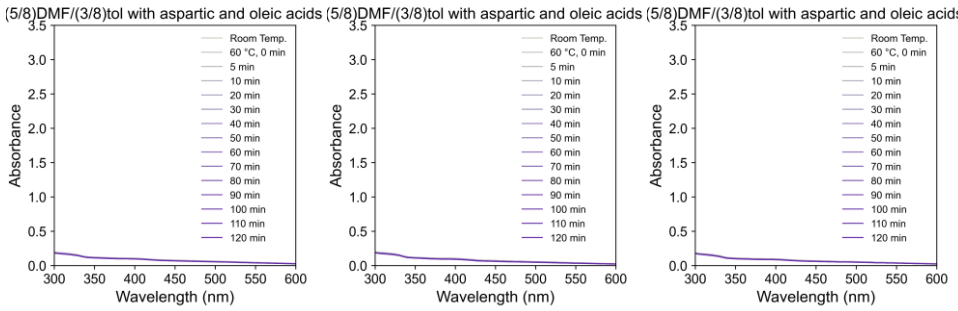
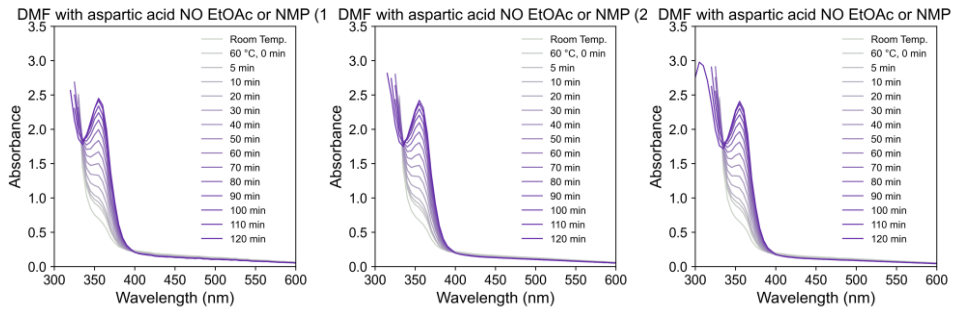
3.B11,E11	 
3.C2	
3.C3	
3.C4,F4	 
3.C5,F5	 

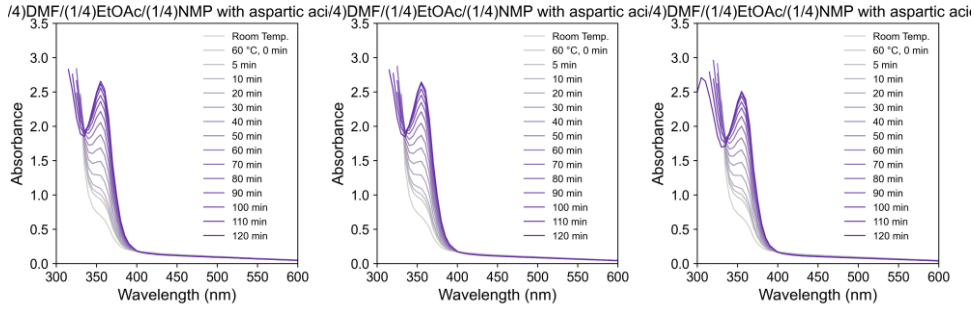
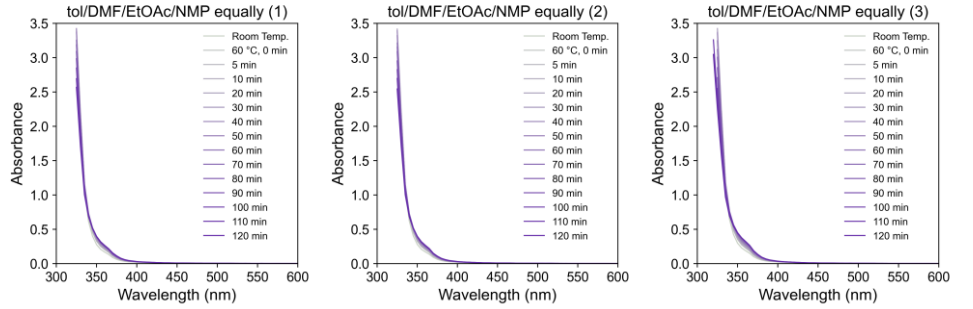
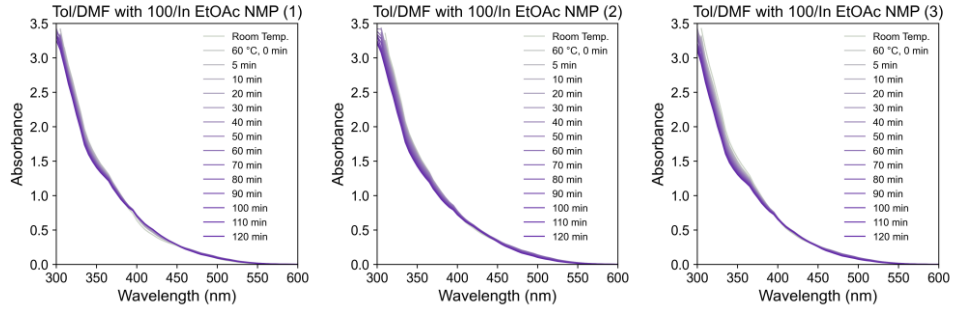
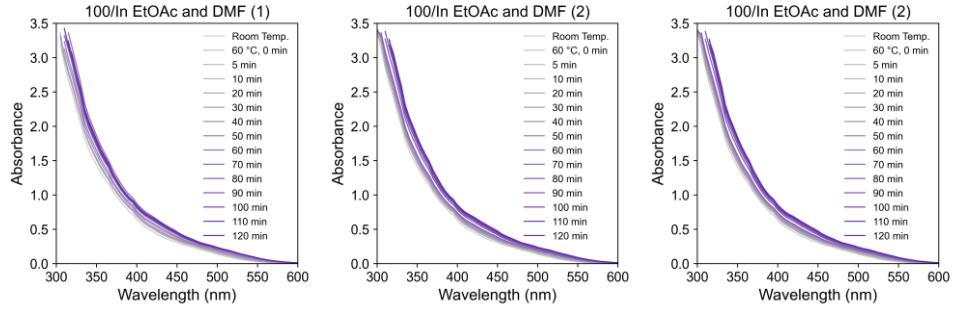
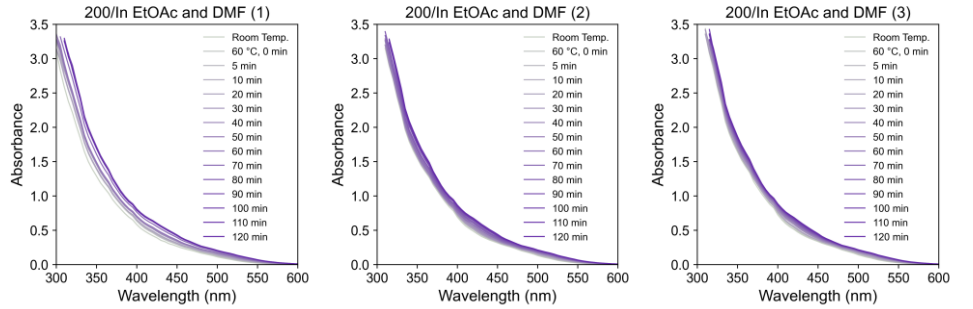
3.C6	
3.C7	
3.C8,F8	 
3.C9,F9	 
3.F2	

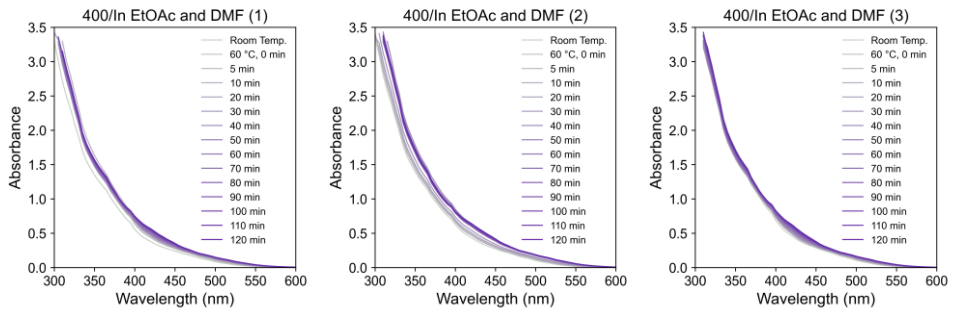
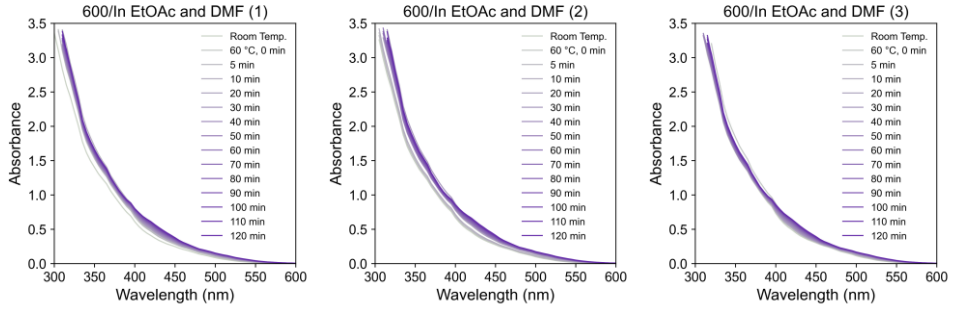
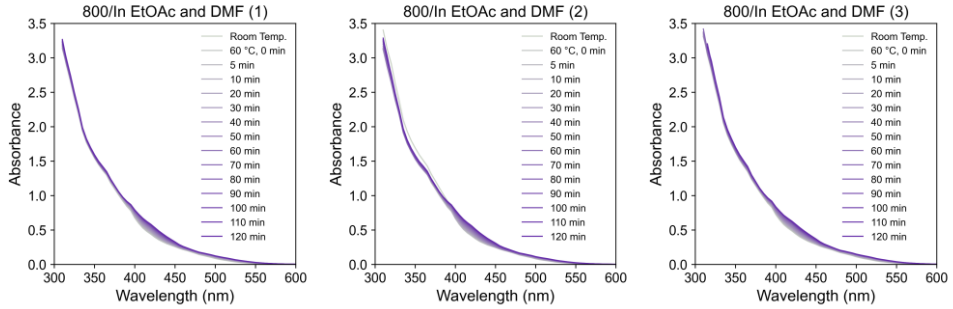
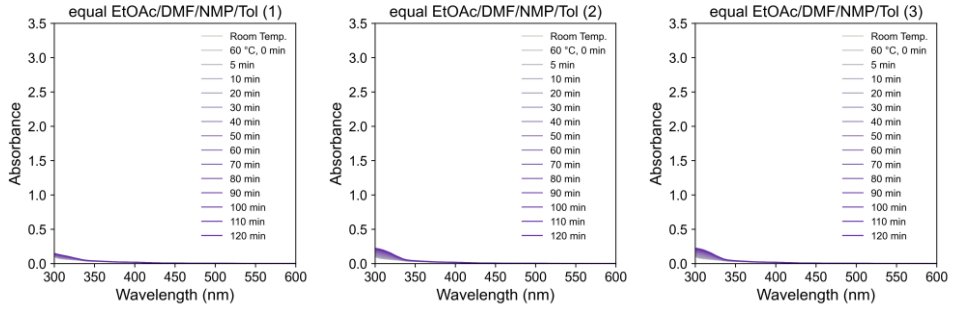
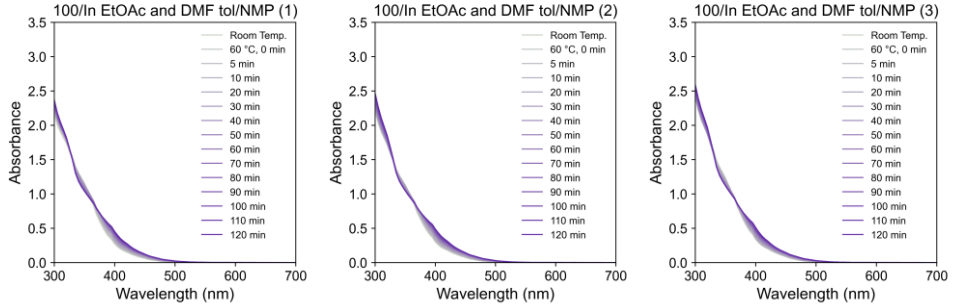
3.F3	
3.F6	
3.F7	
4.B2,D2,F2	
4.B3,D3,F3	

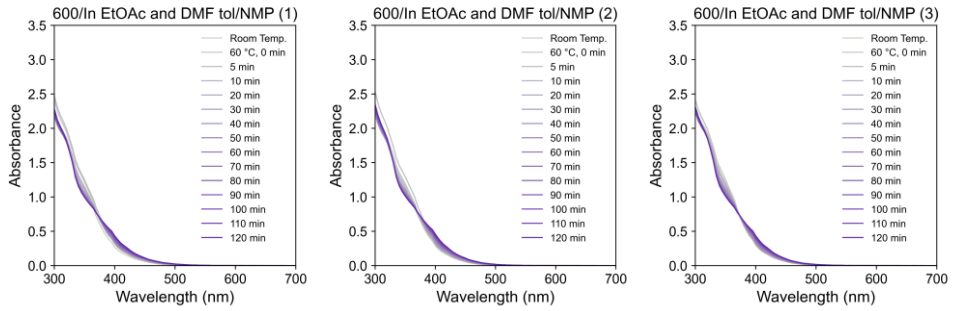
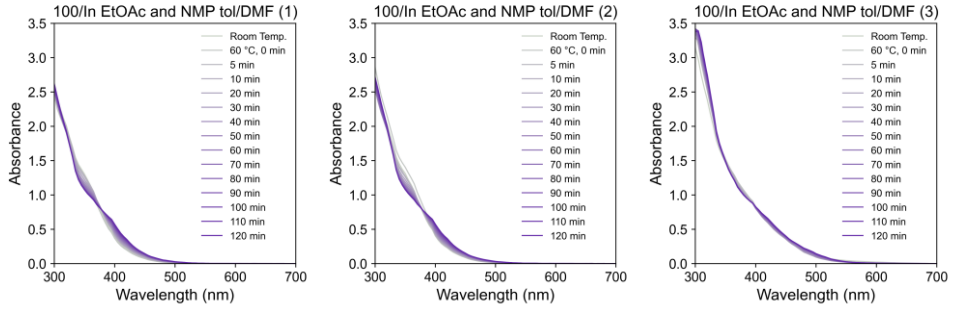
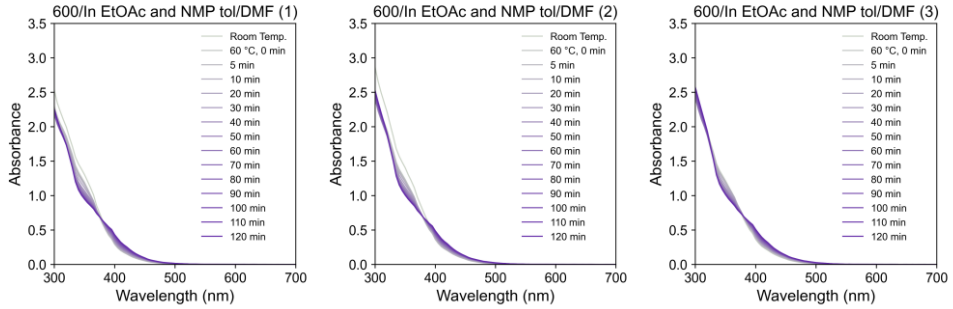
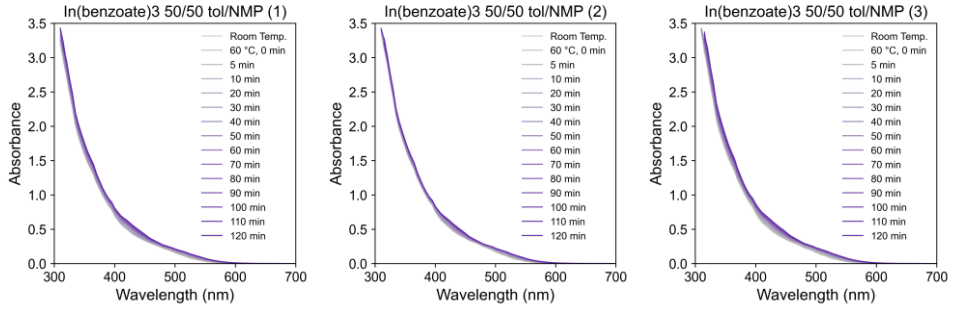
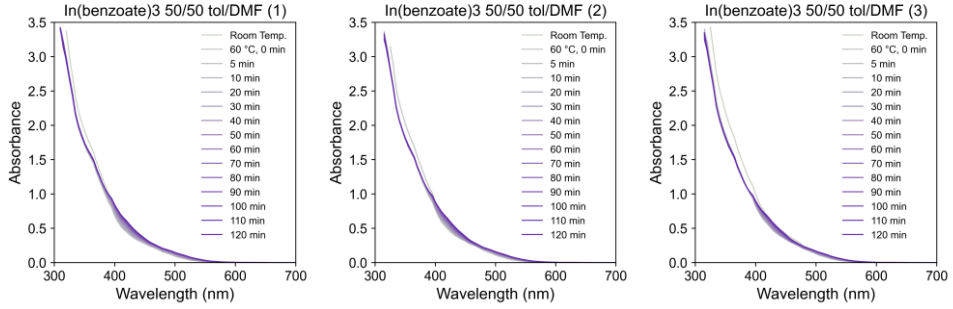
4.B4,D4,F4	
4.B5,D5,F5	
4.B6,D6,F6	
4.B7,D7,F7	
4.B8,D8,F8	

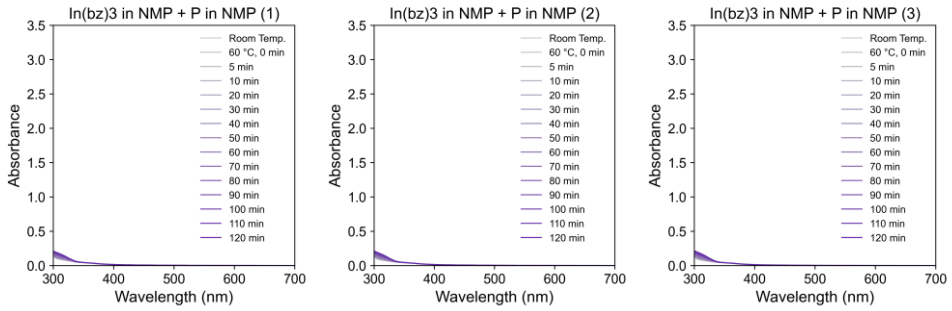
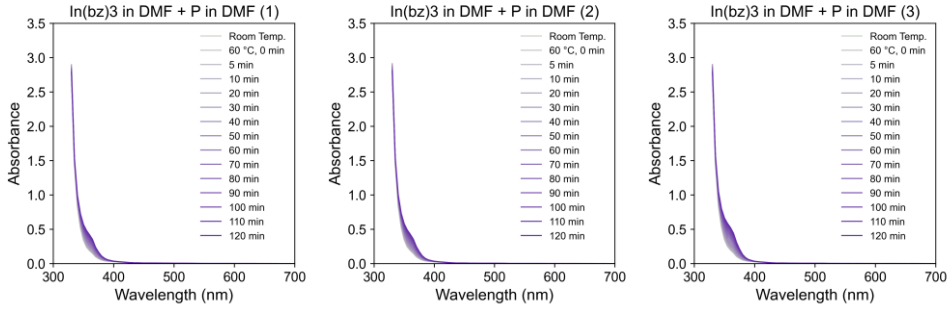
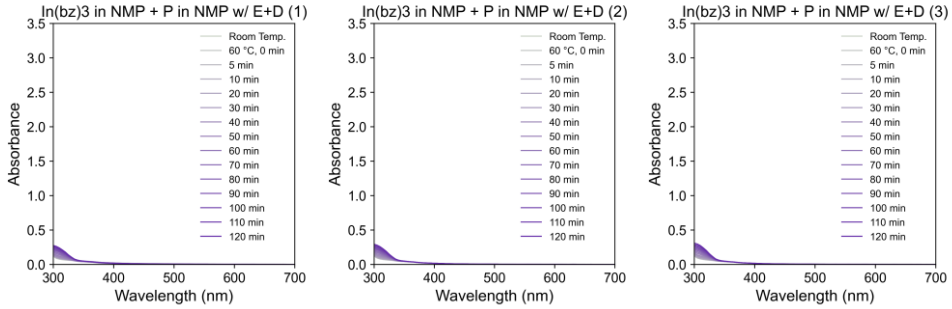
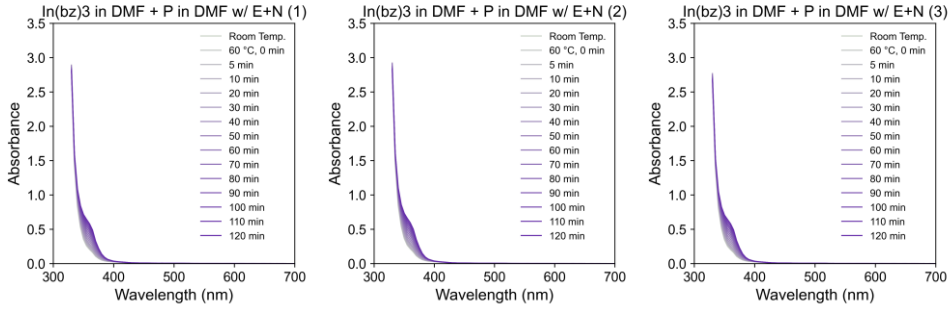
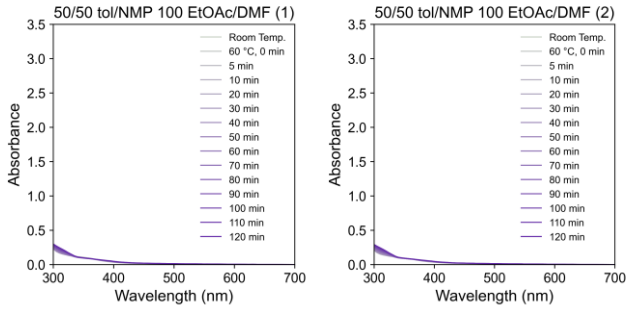
4.B9,D9,F9	
4.B10,D10,F10	
4.B11,D11,F11	
4.C2,E2,G2	
4.C3,E3,F3	

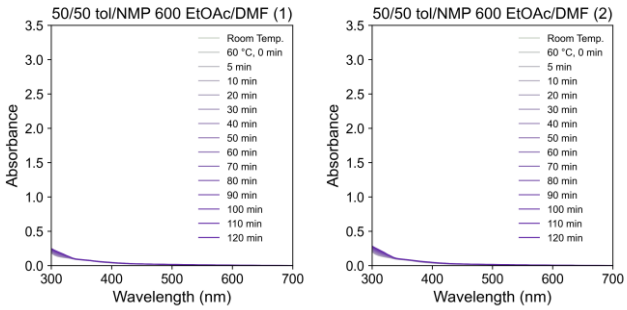
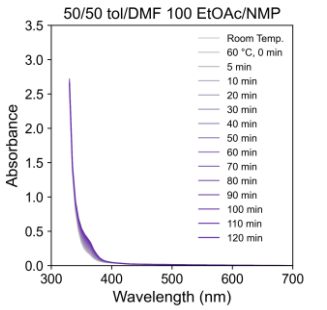
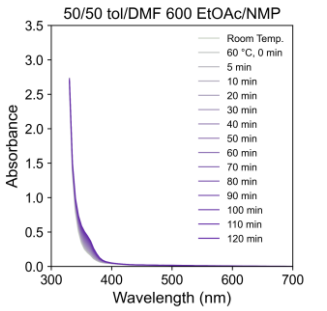
4.C4,E4,G4	
4.C5,E5,G5	
4.C6,E6,G6	
4.C7,E7,G7	
4.C8,E8,G8	

4.C9,E9,G9	
4.C10,E10,G10	
4.C11,E11,G11	
5.B2,D2,F2	
5.B3,D3,F3	

5.B4,D4,F4	
5.B5,D5,F5	
5.B6,D6,F6	
5.B7,D7,F7	
5.B8,D8,F8	

5.B9,D9,F9	
5.B10,D10,F10	
5.B11,D11,F11	
5.C2,E2,G2	
5.C3,E3,F3	

5.C4,E4,G4	
5.C5,E5,G5	
5.C6,E6,G6	
5.C7,E7,G7	
5.C8,E8	

5.C9,E9	
5.G10	
5.G11	

2.5 REFERENCES

(1) Cho, W.; Zhou, Z.; Lin, R.; Ondry, J. C.; Talapin, D. V. Synthesis of Colloidal GaN and AlN Nanocrystals in Biphasic Molten Salt/Organic Solvent Mixtures under High-Pressure Ammonia. *ACS Nano* **2023**, *17* (2), 1315–1326. https://doi.org/10.1021/acsnano.2c09552.

(2) Jain, A.; Ong, S. P.; Hautier, G.; Chen, W.; Richards, W. D.; Dacek, S.; Cholia, S.; Gunter, D.; Skinner, D.; Ceder, G.; Persson, K. A. Commentary: The Materials Project: A Materials Genome Approach to Accelerating Materials Innovation. *APL Materials* **2013**, *1* (1), 011002. https://doi.org/10.1063/1.4812323.

(3) Jain, A.; Hautier, G.; Ong, S. P.; Moore, C. J.; Fischer, C. C.; Persson, K. A.; Ceder, G. Formation Enthalpies by Mixing GGA and GGA $+$ U Calculations. *Phys. Rev. B* **2011**, *84* (4), 045115. https://doi.org/10.1103/PhysRevB.84.045115.

(4) Nag, A.; Kovalenko, M. V.; Lee, J.-S.; Liu, W.; Spokoyny, B.; Talapin, D. V. Metal-Free Inorganic Ligands for Colloidal Nanocrystals: S2–, HS–, Se2–, HSe–, Te2–, HTe–, TeS32–, OH–, and NH2– as Surface Ligands. *J. Am. Chem. Soc.* **2011**, *133* (27), 10612–10620. https://doi.org/10.1021/ja2029415.

(5) Yadav, C.; Surana, K.; Singh, P. K.; Bhattacharya, B. An Ultra-Simple Method for Synthesis of Violet CdS Quantum Dots at Sub-Room Temperature. *Journal of Nanoscience and Nanotechnology* **2020**, *20* (6), 3935–3938. https://doi.org/10.1166/jnn.2020.17496.
(6) Im, J.-H.; Han, M.; Hong, J.; Kim, H.; Oh, K.-S.; Choi, T.; Yusoff, A. R. bin M.; Vasilopoulou, M.; Lee, E.; Hwang, C.-C.; Noh, Y.-Y.; Kim, Y.-K. Controlled Synthesis of Perovskite Nanocrystals at Room Temperature by Liquid Crystalline Templates. *ACS Nano* **2025**, *19* (1), 1177–1189. https://doi.org/10.1021/acsnano.4c13217.
(7) Bénas, J.-S.; Liang, F.-C.; Huang, Y.-H.; Liu, F.-C.; Ou, C.-H.; Oikawa, R.; Kobayashi, R.; Mizoguchi, S.; Igarashi, Y.; Chiba, T.; Kido, J.; Kuo, C.-C. Room-Temperature Synthesis of Triple-Cation Green Perovskite Quantum Dots for Optoelectronic Applications. *Mater. Horiz.* **2025**, *12* (4), 1334–1345. https://doi.org/10.1039/D4MH01270D.
(8) Mi, W.; Tian, J.; Tian, W.; Dai, J.; Wang, X.; Liu, X. Temperature Dependent Synthesis and Optical Properties of CdSe Quantum Dots. *Ceramics International* **2012**, *38* (7), 5575–5583. https://doi.org/10.1016/j.ceramint.2012.03.077.
(9) Wang, W.; Germanenko, I.; El-Shall, M. S. Room-Temperature Synthesis and Characterization of Nanocrystalline CdS, ZnS, and CdxZn1-xS. *Chem. Mater.* **2002**, *14* (7), 3028–3033. https://doi.org/10.1021/cm020040x.
(10) Pratolongo, D.; Campolucci, M.; Vocciante, M.; Pugliesi, L.; Di Giorgio, E.; Lambruschini, C.; Manna, L.; Locardi, F. Lead Halide Perovskites Nanocrystals Synthesized in a Green, Reusable Solvent. *Small n/a* (n/a), 2500535. https://doi.org/10.1002/smll.202500535.
(11) Nudelman, F.; Sommerdijk, N. A. J. M. Biomineralization as an Inspiration for Materials Chemistry. *Angewandte Chemie International Edition* **2012**, *51* (27), 6582–6596. https://doi.org/10.1002/anie.201106715.
(12) Böhm, C. F.; Harris, J.; Schodder, P. I.; Wolf, S. E. Bioinspired Materials: From Living Systems to New Concepts in Materials Chemistry. *Materials* **2019**, *12* (13), 2117. https://doi.org/10.3390/ma12132117.
(13) Möller, J.; Schroer, M. A.; Erlkamp, M.; Grobelny, S.; Paulus, M.; Tiemeyer, S.; Wirkert, F. J.; Tolan, M.; Winter, R. The Effect of Ionic Strength, Temperature, and Pressure on the Interaction Potential of Dense Protein Solutions: From Nonlinear Pressure Response to Protein Crystallization. *Biophysical Journal* **2012**, *102* (11), 2641–2648. https://doi.org/10.1016/j.bpj.2012.04.043.
(14) Zuddas, P.; Mucci, A. Kinetics of Calcite Precipitation from Seawater: II. The Influence of the Ionic Strength. *Geochimica et Cosmochimica Acta* **1998**, *62* (5), 757–766. https://doi.org/10.1016/S0016-7037(98)00026-X.
(15) McPherson, A.; Gavira, J. A. Introduction to Protein Crystallization. *Acta Cryst F* **2014**, *70* (1), 2–20. https://doi.org/10.1107/S2053230X13033141.
(16) Baird, J. K.; Scott, S. C.; Kim, Y. W. Theory of the Effect of pH and Ionic Strength on the Nucleation of Protein Crystals. *Journal of Crystal Growth* **2001**, *232* (1), 50–62. https://doi.org/10.1016/S0022-0248(01)01059-4.
(17) Won, Y.-H.; Cho, O.; Kim, T.; Chung, D.-Y.; Kim, T.; Chung, H.; Jang, H.; Lee, J.; Kim, D.; Jang, E. Highly Efficient and Stable InP/ZnSe/ZnS Quantum Dot Light-Emitting Diodes. *Nature* **2019**, *575* (7784), 634–638. https://doi.org/10.1038/s41586-019-1771-5.
(18) Van Avermaet, H.; Schiettecatte, P.; Hinz, S.; Giordano, L.; Ferrari, F.; Nayral, C.; Delpech, F.; Maultzsch, J.; Lange, H.; Hens, Z. Full-Spectrum InP-Based Quantum Dots

with Near-Unity Photoluminescence Quantum Efficiency. *ACS Nano* **2022**, *16* (6), 9701–9712. https://doi.org/10.1021/acsnano.2c03138.

(19) Nguyen, H. A.; Dou, F. Y.; Park, N.; Wu, S.; Sarsito, H.; Diakubama, B.; Larson, H.; Nishiwaki, E.; Homer, M.; Cash, M.; Cossairt, B. M. Predicting Indium Phosphide Quantum Dot Properties from Synthetic Procedures Using Machine Learning. *Chem. Mater.* **2022**. https://doi.org/10.1021/acs.chemmater.2c00640.

(20) Khanna, P. K.; Eum, M.-S.; Jun, K.-W.; Baeg, J.-O.; Seok, S. I. A Novel Synthesis of Indium Phosphide Nanoparticles. *Materials Letters* **2003**, *57* (30), 4617–4621. https://doi.org/10.1016/S0167-577X(03)00371-9.

(21) Jun, K.-W.; Khanna, P. K.; Hong, K.-B.; Baeg, J.-O.; Suh, Y.-D. Synthesis of InP Nanocrystals from Indium Chloride and Sodium Phosphide by Solution Route. *Materials Chemistry and Physics* **2006**, *96* (2), 494–497. https://doi.org/10.1016/j.matchemphys.2005.07.041.

(22) Ondry, J. C.; Zhou, Z.; Lin, K.; Gupta, A.; Chang, J. H.; Wu, H.; Jeong, A.; Hammel, B. F.; Wang, D.; Fry, H. C.; Yazdi, S.; Dukovic, G.; Schaller, R. D.; Rabani, E.; Talapin, D. V. Reductive Pathways in Molten Inorganic Salts Enable Colloidal Synthesis of III-V Semiconductor Nanocrystals. *Science* **2024**, *386* (6720), 401–407. https://doi.org/10.1126/science.ado7088.

(23) Wang, W.; Zhang, M.; Pan, Z.; Biesold, G. M.; Liang, S.; Rao, H.; Lin, Z.; Zhong, X. Colloidal Inorganic Ligand-Capped Nanocrystals: Fundamentals, Status, and Insights into Advanced Functional Nanodevices. *Chem. Rev.* **2022**, *122* (3), 4091–4162. https://doi.org/10.1021/acs.chemrev.1c00478.

(24) Zhao, T.; Zhao, Q.; Lee, J.; Yang, S.; Wang, H.; Chuang, M.-Y.; He, Y.; Thompson, S. M.; Liu, G.; Oh, N.; Murray, C. B.; Kagan, C. R. Engineering the Surface Chemistry of Colloidal InP Quantum Dots for Charge Transport. *Chem. Mater.* **2022**. https://doi.org/10.1021/acs.chemmater.2c01840.

(25) Liu, W.; Lee, J.-S.; Talapin, D. V. III–V Nanocrystals Capped with Molecular Metal Chalcogenide Ligands: High Electron Mobility and Ambipolar Photoresponse. *J. Am. Chem. Soc.* **2013**, *135* (4), 1349–1357. https://doi.org/10.1021/ja308200f.

(26) Lee, S.; Sagar, L. K.; Li, X.; Dong, Y.; Chen, B.; Gao, Y.; Ma, D.; Levina, L.; Grenville, A.; Hoogland, S.; García de Arquer, F. P.; Sargent, E. H. InP-Quantum-Dot-in-ZnS-Matrix Solids for Thermal and Air Stability. *Chem. Mater.* **2020**, *32* (22), 9584–9590. https://doi.org/10.1021/acs.chemmater.0c02870.

(27) Hai, Y.; Gahlot, K.; Tanchev, M.; Mutalik, S.; Tekelenburg, E. K.; Hong, J.; Ahmadi, M.; Piveteau, L.; Loi, M. A.; Protesescu, L. Metal–Solvent Complex Formation at the Surface of InP Colloidal Quantum Dots. *J. Am. Chem. Soc.* **2024**, *146* (18), 12808–12818. https://doi.org/10.1021/jacs.4c03325.

(28) Liu, Z.; Hou, X.; You, H.; Wang, Z.; Zhu, K.; Hu, X.; Li, P.; Lu, X.; Wang, Q.; Liu, Z.; Hu, D.; Su, J.; Dai, N.; Li, Y. Surface Copassivation Strategy for Developing Water-Soluble InP Colloidal Quantum Dots with High Luminescence and Suppressed Blinking. *J. Am. Chem. Soc.* **2025**, *147* (6), 4778–4789. https://doi.org/10.1021/jacs.4c10731.

(29) Saha, A.; Yadav, R.; Rivaux, C.; Aldakov, D.; Reiss, P. Water-Soluble Alumina-Coated Indium Phosphide Core–Shell Quantum Dots with Efficient Deep-Red Emission Beyond 700 Nm. *Small* **2024**, *20* (45), 2404426. https://doi.org/10.1002/smll.202404426.

(30) Arnaut, L. G.; Formosinho, S. J. The Rates of SN2 Reactions and Their Relation to Molecular and Solvent Properties. *Chemistry – A European Journal* **2007**, *13* (28), 8018–8028. https://doi.org/10.1002/chem.200700276.

(31) Kim, J. Y.; Steeves, A. H.; Kulik, H. J. Harnessing Organic Ligand Libraries for First-Principles Inorganic Discovery: Indium Phosphide Quantum Dot Precursor Design Strategies. *Chem. Mater.* **2017**, *29* (8), 3632–3643. https://doi.org/10.1021/acs.chemmater.7b00472.

(32) Larson, H.; Schultz, D.; Kalyani, D. Ni-Catalyzed C–H Arylation of Oxazoles and Benzoxazoles Using Pharmaceutically Relevant Aryl Chlorides and Bromides. *J. Org. Chem.* **2019**, *84* (20), 13092–13103. https://doi.org/10.1021/acs.joc.9b02094.

(33) Mennen, S. M.; Alhambra, C.; Allen, C. L.; Barberis, M.; Berritt, S.; Brandt, T. A.; Campbell, A. D.; Castañón, J.; Cherney, A. H.; Christensen, M.; Damon, D. B.; Eugenio de Diego, J.; García-Cerrada, S.; García-Losada, P.; Haro, R.; Janey, J.; Leitch, D. C.; Li, L.; Liu, F.; Lobben, P. C.; MacMillan, D. W. C.; Magano, J.; McInturff, E.; Monfette, S.; Post, R. J.; Schultz, D.; Sitter, B. J.; Stevens, J. M.; Strambeanu, I. I.; Twilton, J.; Wang, K.; Zajac, M. A. The Evolution of High-Throughput Experimentation in Pharmaceutical Development and Perspectives on the Future. *Org. Process Res. Dev.* **2019**, *23* (6), 1213–1242. https://doi.org/10.1021/acs.oprd.9b00140.

(34) Mahjour, B.; Zhang, R.; Shen, Y.; McGrath, A.; Zhao, R.; Mohamed, O. G.; Lin, Y.; Zhang, Z.; Douthwaite, J. L.; Tripathi, A.; Cernak, T. Rapid Planning and Analysis of High-Throughput Experiment Arrays for Reaction Discovery. *Nat Commun* **2023**, *14* (1), 3924. https://doi.org/10.1038/s41467-023-39531-0.

(35) Politi, M.; Baum, F.; Vaddi, K.; Antonio, E.; Vasquez, J.; P. Bishop, B.; Peek, N.; C. Holmberg, V.; D. Pozzo, L. A High-Throughput Workflow for the Synthesis of CdSe Nanocrystals Using a Sonochemical Materials Acceleration Platform. *Digital Discovery* **2023**, *2* (4), 1042–1057. https://doi.org/10.1039/D3DD00033H.

(36) Rodriguez, J.; Politi, M.; Adler, S.; Beck, D.; Pozzo, L. High-Throughput and Data Driven Strategies for the Design of Deep-Eutectic Solvent Electrolytes. *Mol. Syst. Des. Eng.* **2022**, *7* (8), 933–949. https://doi.org/10.1039/D2ME00050D.

(37) Shahzad, K.; Mardare ,Andrei Ionut; and Hassel, A. W. Accelerating Materials Discovery: Combinatorial Synthesis, High-Throughput Characterization, and Computational Advances. *Science and Technology of Advanced Materials: Methods* **2024**, *4* (1), 2292486. https://doi.org/10.1080/27660400.2023.2292486.

(38) Carlson, A. W.; Primka, D. A.; Douma, E. D.; Bowring, M. A. Evaluation of Air-Free Glassware Using the Ketyl Test. *Dalton Trans.* **2020**, *49* (43), 15213–15218. https://doi.org/10.1039/D0DT02345K.

(39) Friedfeld, M. R.; Johnson, D. A.; Cossairt, B. M. Conversion of InP Clusters to Quantum Dots. *Inorg. Chem.* **2019**, *58* (1), 803–810. https://doi.org/10.1021/acs.inorgchem.8b02945.

(40) Lang, E. N.; Claridge, S. A. Cow-to-Cow Variation in Nanocrystal Synthesis: Learning from Technical-Grade Oleylamine. *Nanotechnology* **2021**, *33* (8), 082501. https://doi.org/10.1088/1361-6528/ac39cb.

(41) De Roo, J. Chemical Considerations for Colloidal Nanocrystal Synthesis. *Chem. Mater.* **2022**. https://doi.org/10.1021/acs.chemmater.2c01058.

(42) Lee, H.; Yoon, D.-E.; Koh, S.; Sung Kang, M.; Lim, J.; C. Lee, D. Ligands as a Universal Molecular Toolkit in Synthesis and Assembly of Semiconductor Nanocrystals. *Chemical Science* **2020**, *11* (9), 2318–2329. https://doi.org/10.1039/C9SC05200C.

(43) Pang, Z.; Zhang, J.; Cao, W.; Kong, X.; Peng, X. Partitioning Surface Ligands on Nanocrystals for Maximal Solubility. *Nat Commun* **2019**, *10* (1), 2454. https://doi.org/10.1038/s41467-019-10389-5.
(44) Yang, Y.; Qin, H.; Jiang, M.; Lin, L.; Fu, T.; Dai, X.; Zhang, Z.; Niu, Y.; Cao, H.; Jin, Y.; Zhao, F.; Peng, X. Entropic Ligands for Nanocrystals: From Unexpected Solution Properties to Outstanding Processability. *Nano Lett.* **2016**, *16* (4), 2133–2138. https://doi.org/10.1021/acs.nanolett.6b00730.
(45) Gary, D. C.; Cossairt, B. M. Role of Acid in Precursor Conversion During InP Quantum Dot Synthesis. *Chem. Mater.* **2013**, *25* (12), 2463–2469. https://doi.org/10.1021/cm401289j.
(46) Gary, D. C.; Terban, M. W.; Billinge, S. J. L.; Cossairt, B. M. Two-Step Nucleation and Growth of InP Quantum Dots via Magic-Sized Cluster Intermediates. *Chem. Mater.* **2015**, *27* (4), 1432–1441. https://doi.org/10.1021/acs.chemmater.5b00286.
(47) Ning, J.; Banin, U. Magic Size InP and InAs Clusters: Synthesis, Characterization and Shell Growth. *Chem. Commun.* **2017**, *53* (17), 2626–2629. https://doi.org/10.1039/C6CC09778B.
(48) Ubbink, R. F.; Almeida, G.; Iziyi, H.; du Fossé, I.; Verkleij, R.; Ganapathy, S.; van Eck, E. R. H.; Houtepen, A. J. A Water-Free In Situ HF Treatment for Ultrabright InP Quantum Dots. *Chem. Mater.* **2022**, *34* (22), 10093–10103. https://doi.org/10.1021/acs.chemmater.2c02800.

Chapter 3. INDIUM–POLY(CARBOXYLIC ACID) LIGAND INTERACTIONS MODIFY INDIUM PHOSPHIDE QUANTUM DOT NUCLEATION AND GROWTH

Reprinted with permission from *Chem. Mater.* 2023, 35, 15, 6152–6160. Copyright 2023 American Chemical Society.

3.1 INTRODUCTION

Morphological control over nanomaterials by leveraging the interplay of organic and inorganic components is a central focus in the colloidal synthesis community. Nature has also developed exquisite mechanisms for controlling crystal growth at the nanoscale to produce hierarchically structured organic-inorganic composites, like shells and bone. Despite this, the connection between colloidal nanomaterial synthesis and the field of biomineralization is underexplored. A review from Nudelman and Sommerdijk details how the elements of chemical, spatial, structural, morphological, and constructional control in biomineralization systems apply to materials chemistry.[1] Molecular or macromolecular templates with specific binding groups or enclosed spaces regulate the location, reactivity, and concentration of mineral precursors that control nucleation and growth of minerals to impact their shape, size, phase, and assembly. Application of biomineralization design principles has inspired complex synthetic inorganic nanomaterials. Biomimetic macromolecules can template hybrid hierarchical inorganic materials,[2–7] and molecular templates designed to bind certain crystal facets can control the nucleation and growth of inorganic nanomaterials.[8–12] The quantum dot (QD) community can learn from nature's lessons on biomineralization to unlock new synthetic paradigms.

A promising avenue to introduce biomineralization principles to colloidal quantum dot synthesis is to position the capping ligand to take on a more complex cation templating role. Commercially available aminopolycarboxylic acids contain multiple functional groups that mimic the organized binding groups seen in natural mineralization templates such as peptides, and in particular ethylenediaminetetraacetic acid (EDTA) is cheap, low toxicity, and known to chelate metal ions.[13] In the literature, polycarboxylic acids have been shown to control the nucleation and growth of metal oxide and rare-earth fluoride nanomaterials.[14–22] While the use of EDTA as an additive in colloidal semiconductor synthesis is rare, there is precedent for EDTA interacting with metal ions during colloidal synthesis. The strong metal ion chelation of EDTA has been seen to prevent premature nucleation during heating,[15] lower reactivity and prevent undesirable side reactions,[16,18] and sequester metal ions during growth to inhibit excessive nucleation to control particle size.[14] A study of CdS microparticles by Sugimoto and coworkers showed that nucleation was controlled by the molar ratio of EDTA to the cadmium precursor which in turn controls the Cd^{2+} available for nucleation, and then the Cd–EDTA complexes slowly release Cd^{2+} for monodisperse growth.[14]

Precursor identity has been a long standing tool to affect QD synthesis, where precursor reactivities balance nucleation and growth to offer uniform, size-controlled samples.[23,24] This study uses InP QD synthesis to explore the intersections of biomineralization-inspired metal ion control and colloidal QD precursor reactivity. Despite the promise of InP as a leading less toxic, commercially viable semiconductor, realizing precursor conversion reactivity controlled InP QD synthesis has been challenging. For InP QDs made using indium carboxylates and tris(trimethylsilyl)phosphine, kinetically trapped magic sized cluster intermediates complicate control through precursor reactivity, and existing efforts mainly focus on tuning phosphorus

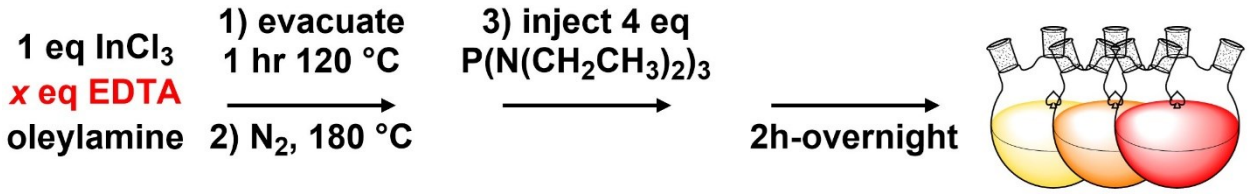
reactivity.[25–27] There have been few examples to date of using indium chemistry to control the synthesis of InP QDs despite a promising theoretical study that highlights the importance of the indium-oxygen bond cleavage energetics in InP bond formation using indium carboxylates.[28,29] Importantly, the advent of indium halides and aminophosphines as precursors for InP QDs opens up new avenues for precursor conversion reactivity control due to the avoidance of kinetic traps like the magic sized cluster.[30–34] Varying the halide in the indium precursor tunes the final size of the QDs,[30,31] and aminophosphines of different reactivities have been employed to effect precursor conversion reactivity control.[32,33] In particular, recent work identifies a continuous nucleation and size-focusing growth mechanism for InP QDs grown using the aminophosphine chemistry, which allows for in depth interpretation of precursor reactivity effects.[32]

Here we investigate the effect of aminopolycarboxylic acid EDTA on the nucleation and growth of InP QDs made using indium chloride and tris(diethyl)aminophosphine. By varying the equivalents of EDTA per indium, we identify an EDTA-dependent trend in the final QD size. Analysis of the initial InP growth rates using UV-vis absorbance spectra of reaction aliquots and rationalization through a continuous nucleation mechanism explains the size trend. Specific indium – EDTA interactions are investigated through ^{1}H NMR spectroscopy and an octahedral indium EDTA complex is identified with low reactivity. We demonstrate how EDTA dose-dependent size control of InP QDs is achieved through a chelation-induced indium sequestration pathway. We present EDTA as an indium precursor modifier that expands the accessible QD size range of a given indium halide precursor.

3.2 Results and Discussion

3.2.1 *EDTA-Dependent Size Control*

Previous studies have optimized the synthesis conditions for making InP QDs using aminophosphines, including indium concentration and equivalents of aminophosphine relative to the indium halide (**Scheme 1.1**).[31] The reaction temperature of 180 °C for this study was chosen to both be comparable to literature precedents and avoid the decomposition of EDTA, which interferes with InP formation at temperatures above 180 °C (**Figure S 3.1**).[35] The indium halide used is indium chloride to offer the largest window for size control, because as the worst leaving group out of the halide series (*i.e.*, chloride, bromide, and iodide) it facilitates the formation of the largest QDs.



Scheme 3.1 Aminophosphine-based InP QD synthesis with ethylenediaminetetraacetic acid (EDTA) additive (x = 0, 0.25, 0.5, 0.75).

Increasing the dose of EDTA from 0 to 0.75 equivalents per indium controls the final size of InP QDs as evidenced by a range of lowest energy electronic transitions (LEET) from ~590 to ~400 nm in UV-vis absorbance data (**Figure 1.1a**). Fitting the low energy tail of each final absorbance spectrum to a gaussian peak to approximate the excitonic absorbance transition gives LEETs at 583, 558, 510 nm for 0, 0.25, and 0.5 equivalents of EDTA per indium, respectively. The approximate LEET for the InP QDs made with 0.75 equivalents of EDTA is estimated using a Tauc plot to be 393 nm (method in SI). Transmission electron microscopy (TEM) images reveal

a slight morphology change from spherical to a truncated tetrahedral nanocrystal shape as well as a size increase as the equivalents of EDTA decrease (**Figure 1.1c-f**). The nanocrystal size can be estimated from the LEET based off electron confinement and effects of shape.[36] Due to stronger confinement in a tetrahedral nanocrystal, the upper size estimate for QDs with LEETs of 583, 558, 510, and 393 nm are edge lengths of 5.9, 5.2, 4.2, and 2.4 nm while assuming a spherical nanocrystal gives diameters of 3.2, 3, 2.6, and 1.8 nm, respectively. The measured diameters from TEM images are 4.5 ± 0.6, 4.2 ± 0.8, 3.9 ± 0.6, and 2.3 ± 0.8 nm for syntheses using 0, 0.25, 0.5, and 0.75 equivalents of EDTA, respectively, agreeing with the identified morphology change from small spheres to larger tetrahedra (**Figure S 3.2**, **Figure S 3.3**).

Powder X-Ray Diffraction (pXRD) data of the purified QDs show zinc blende phase InP (**Figure 1.1b**). Scherrer analysis was performed on the pXRD patterns with defined zinc blende peaks and confirms the size trend with average crystallite sizes of 3.5 ± 0.3 and 2.8 ± 0.4 nm for InP QDs made with 0 and 0.25 equivalents of EDTA, respectively. We note that the smaller QD samples have broad diffraction patterns as is typical of nanocrystals of that size.[37] Additionally, analysis of the peak centered at 20 degrees two theta, which is attributed to the ordering of the surface ligands, offers insight into the size and composition of the QDs. Calvin and coworkers have recently shown through experimental diffraction patterns and theoretical models of different sized InP QDs that the peak from ligand ordering increases in relative intensity compared to the lowest index zinc blende peak as the nanocrystal size decreases.[38] The diffraction patterns were fit to gaussian peaks to confirm that this ratio increases for the size decrease observed across the EDTA series (**Figure S 3.4**).

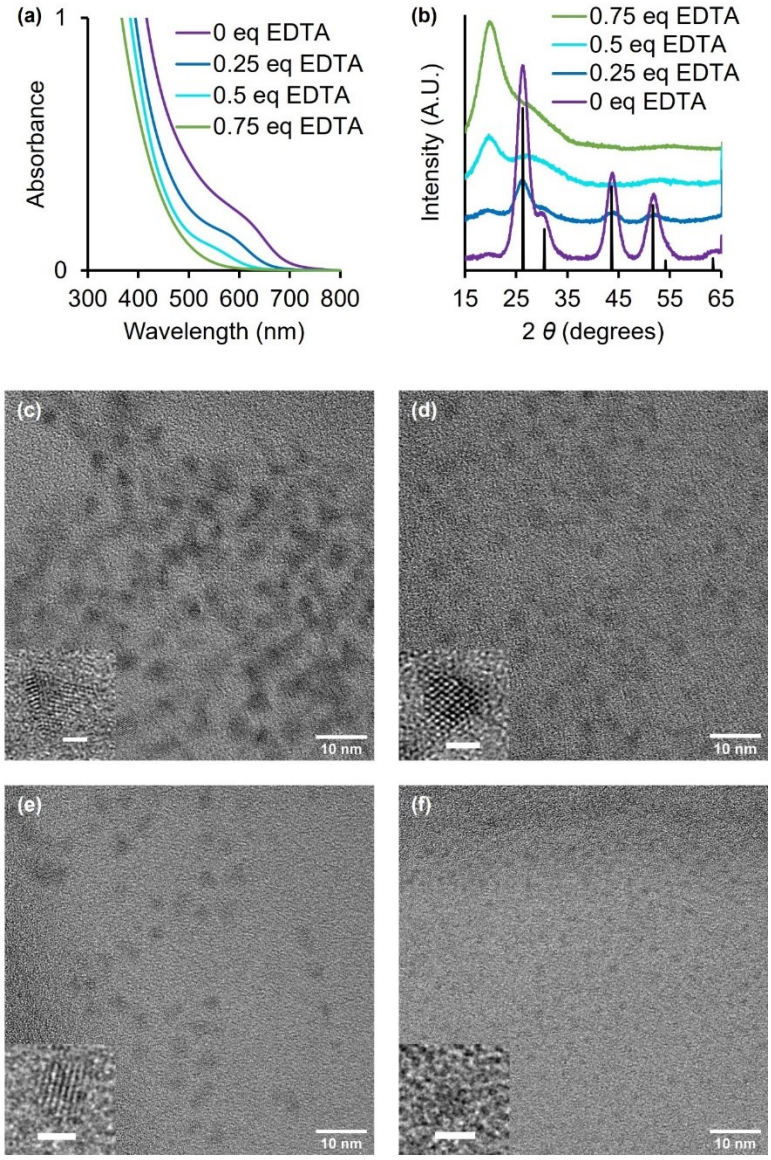


Figure 3.1 Optical, crystallographic, and morphological characterization of InP QDs. (**a**) Overlay of absorbance spectra of final reaction aliquots of InP QDs made using varying equivalents of EDTA per indium. (**b**) XRD pattern of InP QDs after purification to remove excess ligand. TEM images of InP QDs made using (**c**) 0, (**d**) 0.25, (**e**) 0.5, and (**f**) 0.75 equivalents of EDTA, with diameters 4.5 ± 0.6 nm, 4.2 ± 0.8 nm, 3.9 ± 0.6 nm, and 2.3 ± 0.8 nm, respectively. Insets (c-f) show representative QD morphology (scale bars are 2 nm).

3.2.2 *Impact of Precursor Reactivity on Nucleation and Growth*

There are two options for how EDTA could be impacting the nucleation and/or growth processes to cause the size control effect. The first is surface binding, which stabilizes the surface and impedes nanocrystal growth.[21] The second is interference with the precursor conversion reaction affecting the balance between nucleation and growth.[14,32,33] Considering the first option, the observed size trend is consistent with increasing equivalents of EDTA acting as a strong indium chelating ligand, stabilizing the surface and decreasing the QD diameter until growth is prevented entirely. For this hypothesis to be likely, EDTA would be expected to be found on the surface of the QDs after purification as one of the capping ligands. However, by ^{1}H NMR spectroscopy there is no identifiable surface bound EDTA present in the purified QD samples, only the expected oleylamine capping ligands are observed (**Figure S 3.5**).[36,39] The broadening of the ligand resonances as the QD size decreases indicates an increase in ligand disorder caused by the morphology change from tetrahedral to quasi-spherical.[40] The broad resonances centered around 4.2 ppm that increase in intensity with more EDTA in the synthesis can be attributed to species from amine oxidation reactions such as imines and iminiums.[41] IR spectroscopy was taken of purified and dried samples of the QD series and the expected strong carboxylate stretch from EDTA was not identified in any of the spectra (**Figure S 3.6**). Concluding that EDTA is not present on the surface to an extent that adequately explains the observed size control, we turned to the hypothesis that EDTA impacts precursor reactivity.

Recent work on the mechanism of InP nucleation and growth in the aminophosphine system gives great insights on how to interpret the size trend through perturbation of precursor conversion.[32,33] McMurtry and coworkers found that nucleation takes up a sizable fraction of the total reaction time, ranging from a half to less than a tenth of the reaction time.[32] At lower reaction

temperatures, such as 180 °C used in the present study, nucleation of new nanocrystals occurs over about half of the reaction time. For aminophosphines of varying reactivities, the dependence of size on different initial growth rates was found to only become significant at higher temperatures. However, Valleix and coworkers separately observed a decreasing size trend by adding increasing equivalents of a diamine at a reaction temperature of 180 °C.[33] They proposed that a diethylaminophosphine – diamine complex forms from the transaminated oleylaminophosphine, which acts as a competitive reaction to InP production. The crucial point seems to be that the competitive phosphorus precursor reaction both decreases the amount of active phosphorus available to convert to InP *and* decreases the InP production rate. A control done with a lower molar amount of the initial aminophosphine did not decrease QD size, which shows that the lower rate of InP formation is crucial to the size control effect.

In this study, QD size decreases as equivalents of EDTA are increased, which is the same trend seen in the diamine dose-dependent size control study. To probe whether EDTA could be having a similar effect on indium availability as the diamine was found to have on phosphorus availability, we investigated initial rates. The initial rate of InP formation decreases with increasing equivalents of EDTA (**Figure 3.2a**). Initial rates based off absorbance increases in reaction aliquots are sometimes referred to as precursor conversion rates or monomer production rates. However, when the rate is calculated by attributing absorbance at high energy wavelengths to InP units through bulk zinc blende InP parameters, then it should more accurately be thought of as the initial growth rate of crystalline InP and not a measure of monomer production rate. Under the regime of burst nucleation, lower initial rates of monomer production cause less nuclei to form and then those nuclei experience more surface growth due to the mass balance of monomers left over in solution after the nucleation event (**Figure 3.2c**).[23,24,27] In that scenario, low initial InP

formation rates lead to larger QDs but this is the opposite to what is observed with the EDTA series. This can be rationalized by pointing to the evidence that InP made using aminophosphines undergoes continuous nucleation rather than a burst nucleation event.[32] During a longer nucleation period, lower initial InP growth rates could imply slower solute production leading to slower growth on existing nuclei (**Figure 3.2c**). Kinetics of initial InP growth and nucleation are likely affected similarly due to the redox reaction required for InP bond formation, which convolutes the identity of a monomer species and blurs the distinction between nucleation and surface growth. The extended nucleation period allows for many nuclei to form and grow slowly to be small QDs without loss of critical concentration when there are low initial InP formation rates. Similar logic follows that high initial growth rates lead to larger QDs. After the extended nucleation period, the QDs experience size dependent growth allowing for a monodisperse population.[32] This is observed in the current system by the narrowing of the full width at half maximum of the LEET in a representative InP QD synthesis using 0.25 equivalents of EDTA (**Figure S 3.7**). The relative yield of InP is also seen to decrease with increasing equivalents of EDTA, which supports smaller QDs grown with lower initial rates (**Figure 3.2b**). Additionally, lower yields raise the option of precursor loss to some nonproductive route. With potential for initial rates to cause the observed size trend, we next examine the role of EDTA in perturbing the initial InP formation rates.

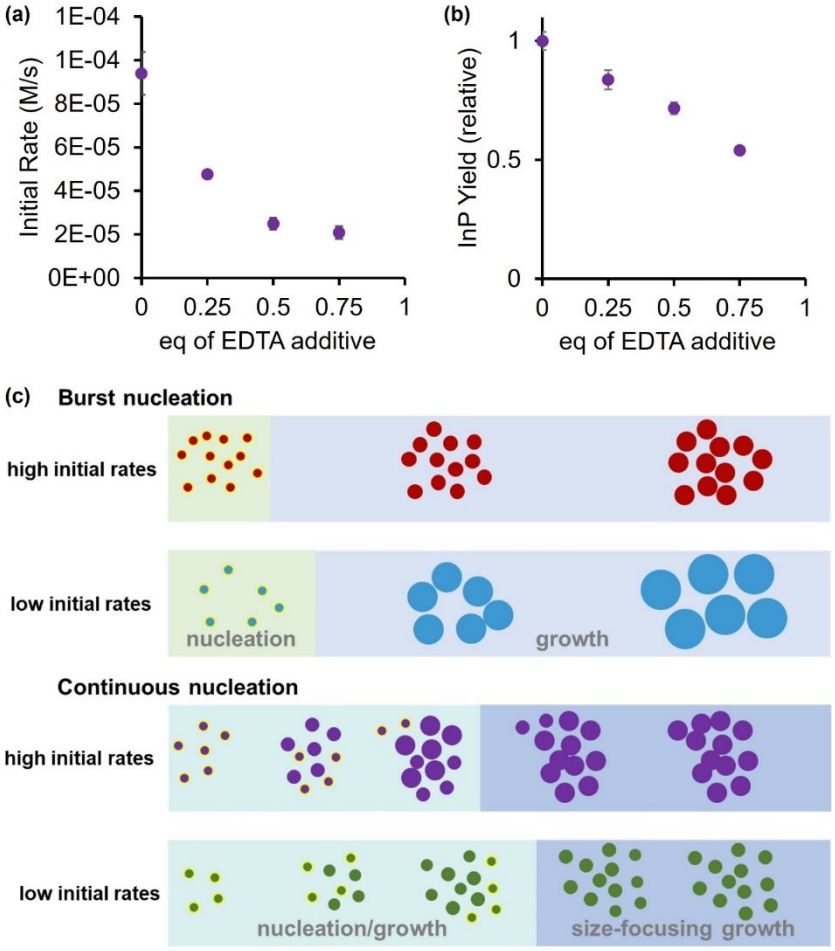


Figure 3.2 Nucleation and growth data and interpretation. Initial rates of InP growth (**a**) and InP yield (**b**) for InP QDs made using varying equivalents of EDTA. (**c**) Scheme showing size dependence on initial rates during burst nucleation compared to continuous nucleation scenarios.

Due to its strong chelation to metal ions, it is possible that EDTA is simply sequestering indium cations, and the lower concentration and molar amount of indium in solution is causing smaller QDs to form. Syntheses with a reduced $InCl_3$ stoichiometry of 0.5 and 0.25 equivalents were run as a control to compare to the 0.5 and 0.75 equivalents of EDTA experiments, respectively. Fitting the final absorbance traces shows only a ~50 nm blueshift in the LEET when equivalents of $InCl_3$ are reduced from 1 to 0.25 (**Figure 3.3**) rather than the ~200 nm blueshift

observed when using EDTA. The yields of the lower equivalents of $InCl_3$ syntheses decrease relative to the full stoichiometric equivalent as is expected for less indium (**Figure S 3.8**). The role of EDTA in the system is more complex than complete sequestration because simply less indium in solution does not provide the same magnitude of size control. The initial rates of the control $InCl_3$ series also decrease with lower molar amounts added; however, the decrease is less than is seen with the corresponding EDTA equivalents (**Figure S 3.9**). Coupled with the slight size decrease seen as the amount of $InCl_3$ decreases, this continues to point to an EDTA-specific effect on initial rates as the culprit for the observed size trend. Additionally, size control by varying the initial rates would be a kinetic effect and this can be confirmed by observing faster growth to larger QDs at higher temperatures. This was performed on the 0.75 equivalents of EDTA synthesis condition, and faster initial rates were observed as the temperature was increased up to 220 °C (**Figure 3.4**). However, the system becomes unstable above 180 °C after 1 hour (190 °C) or 20 minutes (220 °C) as evidenced by a decrease in absorbance at high energy wavelengths pointing to QD decomposition (**Figure S 3.1**). EDTA is known to undergo thermal decomposition above 180 °C in aqueous conditions.[35]

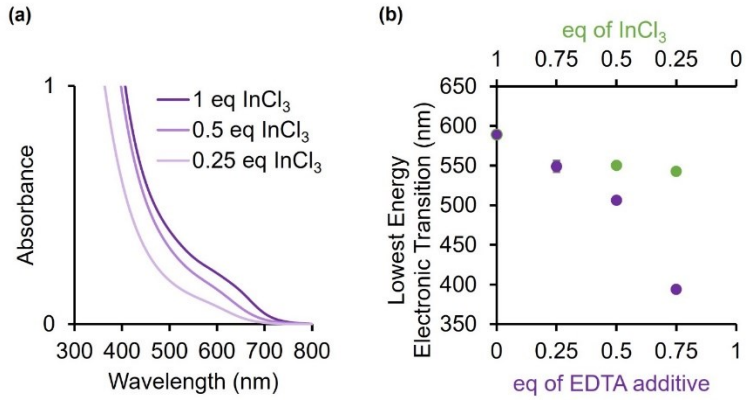


Figure 3.3 Comparing EDTA-based size control to indium stoichiometry-based size control. (**a**) Overlay of absorbance spectra of final reaction aliquots of InP QDs made using varying

concentrations of $InCl_3$. (**b**) Comparison of the lowest energy electronic transitions between lower $InCl_3$ concentration and equivalents of EDTA additive.

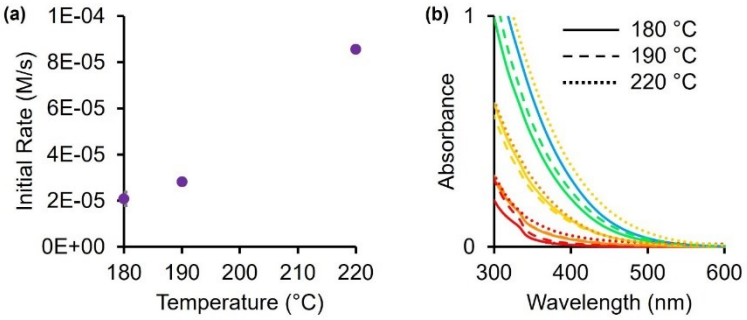


Figure 3.4 Temperature-dependent initial rate kinetics of InP QD synthesis with EDTA. (**a**) Initial rates of InP growth increase for InP QDs made using 0.75 eq. EDTA with increasing reaction temperatures of 180, 190, and 220 °C. (**b**) Absorbance spectra of initial reaction aliquots (red 30 s, orange 2 min, yellow 5 min, green 10 min, blue 15 min) across the three reaction temperatures (180 °C solid, 190 °C dashed, 220 °C dotted) for InP QDs made using 0.75 eq. EDTA.

To rule out significant influences of EDTA on the phosphorus precursor chemistry, ^{31}P NMR spectroscopy was used to track molecular phosphorus byproducts.[31] Reaction aliquots of the InP QD synthesis using 0.75 equivalents of EDTA show the active transaminated aminophosphine species disappearing over early time points (~10 minutes) as well as the tautomer species of the active transaminated aminophosphines at 14 and 11 ppm as they convert back to the more active phosphorus precursor (**Figure 3.5**). The phosphonium salt byproduct of InP bond formation (30 ppm) appears over the first 10 minutes of the reaction accompanied by an increasing amount of an additional byproduct with a resonance at 18 ppm. This peak has been observed as a minor species in previous studies, but not nearly with the intensity seen here.[31,42] The amide-forming reaction

between the carboxylic acids of EDTA and oleylamine produces water as a byproduct (observed by ^{1}H NMR in the absence of phosphorus in **Figure S 3.10**), which taken alongside the chemical shift suggests an aminophosphine oxide.[43] There is excess unincorporated phosphorus in the reaction because of the lower InP yields with higher equivalents of EDTA, and the increasing amount of aminophosphine oxide serves as a reasonable outlet. The phosphonium salt byproduct is observed in the ^{31}P NMR spectra of the crude reactions before purification throughout the EDTA series, as well as increasing amounts of the resonance attributed to an aminophosphine oxide as the equivalents of EDTA increase from 0 to 0.5 per indium (**Figure S 3.11**).

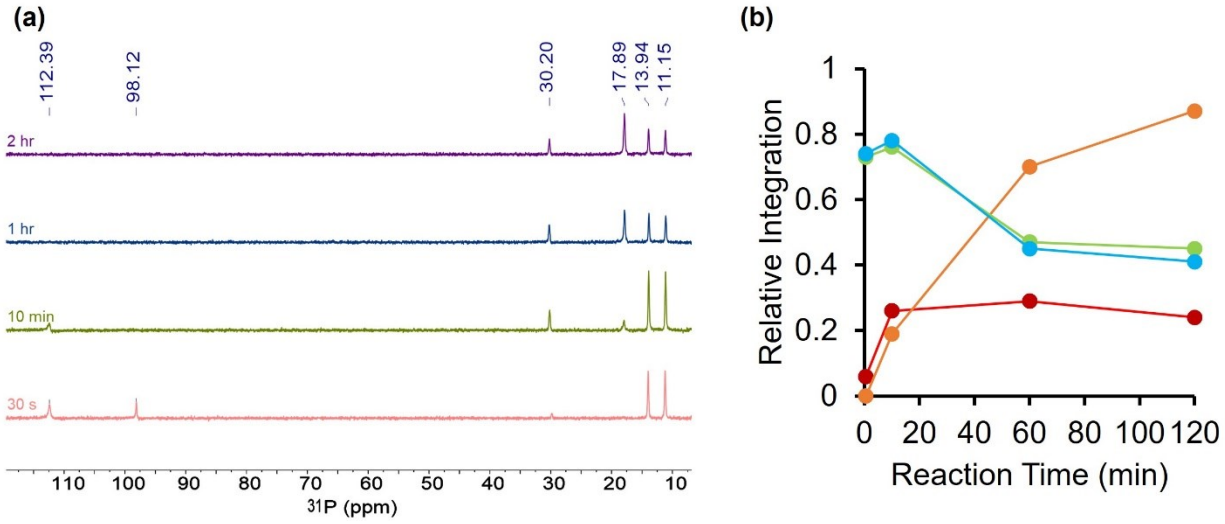


Figure 3.5 Phosphorus speciation over time of InP QD synthesis with EDTA. (**a**) ^{31}P NMR (benzene-d_6, 500 MHz, 298K) spectra of reaction aliquots of InP QDs made using 0.75 eq. EDTA. (**b**) Integrations of phosphonium salt (30 ppm, red), proposed aminophosphine oxide (18 ppm, orange), and tautomers of the active transaminated aminophosphine species (14, 11 ppm, green, blue).

3.2.3 *Formation and Study of In-EDTA Complex*

EDTA was added to the InP QD synthesis for its multiple carboxylic acid functional groups to interact with the indium cations during InP nucleation and growth. The previous work using diamines to control phosphorus availability and reactivity pointed to a competitive precursor reaction as a means to lower initial rates and lead to size control.[33] A potential competitive precursor reaction could involve partial or full binding of EDTA to indium species in the reaction. EDTA is known to form pentagonal bipyramidal complexes with In^{3+} among a plethora of other metal cations in aqueous environments with water occupying the seventh coordination site.[13] However, there are few reports describing the interactions between EDTA and indium or similar metals in organic solvents, likely due to low solubilities at room temperature. To show that EDTA can make complexes with indium chloride in aprotic solvents assisted by amines, ^{1}H NMR spectroscopy was used to track the binding of EDTA to indium. To simulate the conditions of the initial reaction mixture before phosphorus addition, indium chloride and EDTA were reacted in equimolar amounts in deuterated dimethyl sulfoxide with four equivalents of oleylamine per indium. After allowing the mixture to stir overnight, the ^{1}H NMR spectrum shows an AB quartet with coupling $J_{H\text{-}H}$ of 16 Hz at 3.1 and 2.9 ppm with integrations of 4 protons each, a singlet around 2.7 ppm overlapping with the oleylamine alpha proton triplet with an integration for 4 protons, and resonances attributed to the oleylammonium protons (**Figure 3.6**).

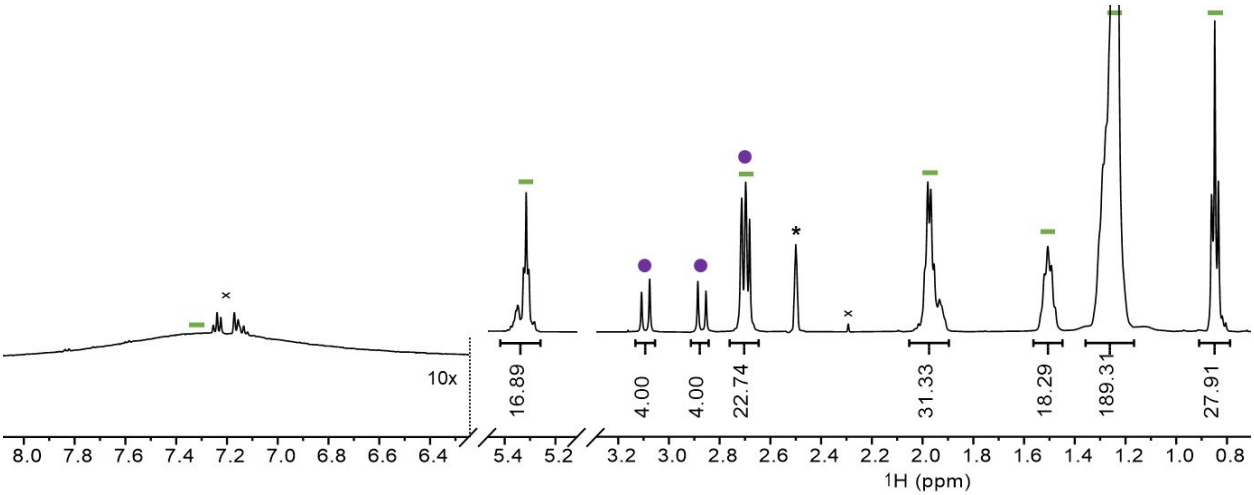
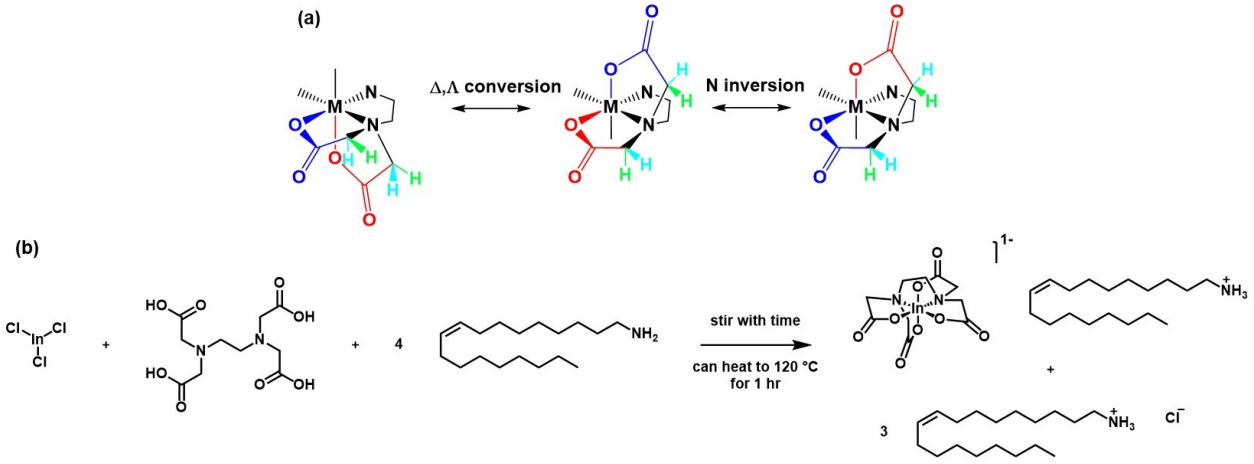


Figure 3.6 Proton NMR of the indium EDTA complex. ^{1}H NMR (DMSO-d_6, 500 MHz, 298K) spectrum of 1 eq. $InCl_3$, 1 eq. EDTA, and 4 eq. oleylamine, with integrations for the methylene peaks of EDTA at 3.09 and 2.87 ppm (J_{HH} = 16 Hz). EDTA protons are labeled with purple circles, oleylamine protons are labeled with green dashes, and residual DMSO is at 2.50 ppm (*) and toluene around 7.2 ppm and 2.3 ppm (×). The upfield spectrum portion from 6.3 to 8 ppm is magnified 10x to see the broad –N$\mathbf{H}_3^+$ resonance.

Detailed ^{1}H NMR spectroscopy studies of metal-EDTA complexes from the literature offer a framework to analyze these results. An initial study from Gennaro and coworkers describes the geminal coupling of the methylene protons in the acetyl groups of an octahedral metal-EDTA complex.[44] With four unique methylene proton environments (in- and out-of-plane, axial and equatorial), the ^{1}H NMR spectrum should exhibit two AB quartet patterns. However, variable temperature studies show that the AB quartets coalesce upon heating. This is rationalized by one or both intramolecular rearrangement processes as follows: nitrogen inversion which results in exchange of the in- and out-of-plane acetyl groups, and Δ, Λ conversion where the acetyl groups rotate coordination spots on the metal so that the protons switch in- and out-of-plane as well as

axial and equatorial environments (**Scheme 3.2a**).[45,46] The stoichiometry of the resulting octahedral indium EDTA complex requires four amines to deprotonate EDTA to form four equivalents of oleylammonium, then one charge balances the negatively charged indium EDTA octahedral complex and the other three form oleylammonium chloride salts (**Scheme 3.2b**). The shift of the amine proton signal from 2.9 ppm when oleylamine is coordinated to $InCl_3$ to a broad singlet around 7 ppm when EDTA is added supports the formation of oleylammonium (**Figure S 3.12**).[39] These control experiments indicate that a tightly chelated octahedral indium EDTA complex forms in the initial reaction mixture containing $InCl_3$, EDTA, and oleylamine before the addition of the aminophosphine.

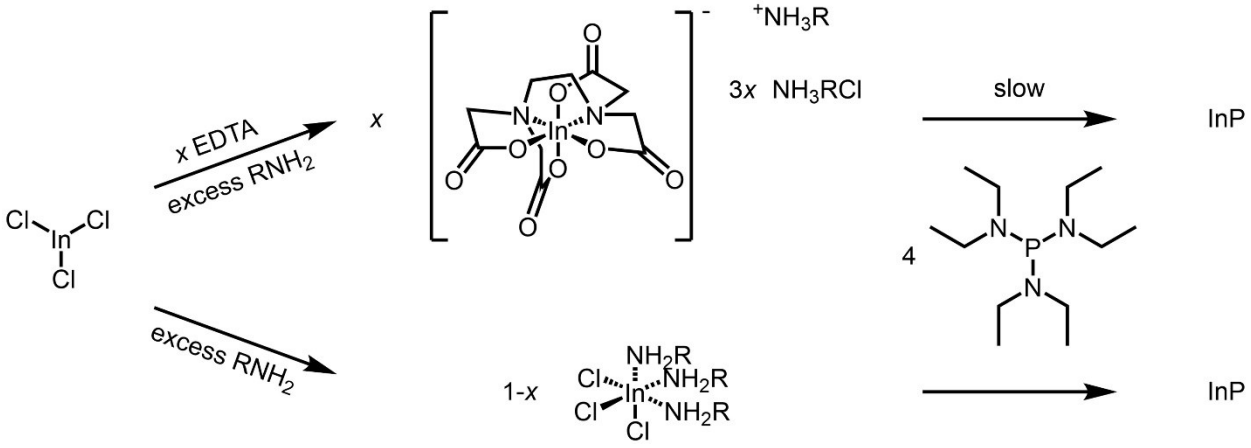


Scheme 3.2 Formation and transformation of the octahedral indium EDTA complex. (**a**) Demonstration of intramolecular rearrangement processes in an octahedral metal-EDTA complex that lead to coalescence of AB quartets in the ^{1}H NMR spectrum. In Δ, Λ conversion, the acetyl groups rotate coordination spots on the metal so the protons switch in-plane (blue) and out-of-plane (red), and axial (cyan) and equatorial (green) environments. Nitrogen inversion results in exchange of the in- and out-of-plane acetyl groups. (**b**) Proposed chemical equation for reaction mixture before addition of phosphorus.

Investigating the reactivity of the octahedral indium EDTA complex can give insights into how EDTA causes the size difference in the InP QD synthesis. First, the indium EDTA complex is stable through the initial degassing step of the synthesis, as seen through the retention of the characteristic AB quartet after heating for one hour at 120 °C (**Figure S 3.10**). After heating at the QD synthesis temperature of 180 °C, the diagnostic AB quartet persists but is accompanied by the appearance of additional byproduct resonances and the formation of water (**Figure S 3.10**). Therefore, without phosphorus present at the reaction temperature, the octahedral indium EDTA complex undergoes only partial decomposition evidenced by the AB quartet persistence and the amide/water formation.

With reasonable evidence suggesting that any EDTA added is chelating indium to form an octahedral complex at the time of phosphorus injection, it is important to determine the extent of reactivity with phosphorus of the chelated indium. When one equivalent of EDTA per indium is added to the InP QD synthesis to chelate all indium, UV-vis absorbance data shows an increase in broad, featureless absorption (**Figure S 3.13a**) relative to the equivalent reaction run in the absence of aminophosphine (**Figure S 3.14**). Despite the lack of clear InP QD formation with 1 equivalent of EDTA per indium, an initial rate can be extracted from the early reaction aliquot absorbance spectra and the result is slightly lower than the initial rate with 0.75 equivalents of EDTA per indium (**Figure S 3.13b**). Taking into account the low reactivity of the chelated indium, the molecular cause of the EDTA-dependent size control can be identified. The initial rates of InP growth decrease slightly with lower indium concentrations (**Figure S 3.9**), and the less reactive indium EDTA complex further decreases the initial InP growth rate leading to the drastic size decrease. This kinetically-informed competitive indium precursor system is summarized in **Scheme 3.3** as an explanation for the EDTA dose-dependent InP QD size decrease. The size

control is generalizable to other indium salts as InP QDs made using indium iodide instead of indium chloride also exhibit a size decrease with increasing equivalents of EDTA (**Figure S 3.15**).



Scheme 3.3 Proposed reaction scheme showing the influence of EDTA chelation on indium precursor reactivity. Increasing equivalents of EDTA lowers the initial InP growth rate. (R = $C_{18}H_{35}$, x = 0, 0.25, 0.5, 0.75).

3.3 Conclusions

In conclusion, we have explored the effects of a multidentate ligand on indium precursor reactivity and the consequences for InP QD synthesis. The aminopolycarboxylic acid EDTA chelates indium in solution by forming an indium EDTA octahedral complex using the amine solvent as a deprotonation agent and source of charge compensating counter cations. Substoichiometric amounts of EDTA per indium allow zinc blende InP QDs with low polydispersity to be grown with a diameter range of 4.5 to 2.3 nm. We propose that the balance between free indium ($InCl_3$(oleylamine)$_3$)[34] and chelated indium ($In(EDTA)^-$) as precursors in solution causes the observed lower initial InP growth rates both because of the competitive sequestration of indium by EDTA and the lower reactivity of the indium EDTA complex. The

unusual trend of smaller nanocrystals caused by lower initial growth rates is explained through the balance between nucleation and growth in a continuous nucleation scenario. The possibility of size control through surface stabilization effects was considered but discounted due to the lack of EDTA on the surface of purified QDs.

This study develops indium chelation as a synthetic handle in InP QD synthesis and shows a glimpse of the opportunities offered when metal cation reactivity and activity are controlled in QD synthesis. Analogues of synthetic control used in biomineralization, such as multidentate ligands, are sparsely used to control QD nucleation and growth but the unique regulation offered can overcome unresolved synthetic difficulties. For example, the non-ideal pre-nucleation clusters in PbS QDs were avoided by toggling lead ion reactivity using chelating ethers.[47] Continuing to apply insights from nature on QD synthesis through precise control over precursor coordination and reactivity will both expand our fundamental understanding of nucleation and growth processes and the commercial use of QDs through precise synthetic control.

3.4 Experimental Methods

3.4.1 *General Practices*

All glassware was dried in a 160 °C oven overnight prior to use. All syntheses were performed under an inert atmosphere of nitrogen using a glovebox or standard Schlenk techniques. Indium chloride (98%) and ethylenediaminetetraacetic acid (98.5%) were purchased from MilliporeSigma and dried before being stored in a nitrogen glovebox. Oleylamine (≥98%) was purchased from MilliporeSigma, dried over CaH_2, distilled, and stored over activated 3 Å molecular sieves in a nitrogen glovebox. Dimethylsulfoxide-d_6 (99.9%), benzene-d_6 (99.5%), and toluene-d_8 (99.5%) were purchased from Cambridge Isotope Laboratories and were similarly dried and stored.

Anhydrous tris(diethyl)aminophosphine (97%) and anhydrous methanol (99.8%) were purchased from MilliporeSigma and used without further purification. Toluene (high-performance liquid chromatography grade) was purchased from Fisher and used as purchased for UV-vis absorbance spectroscopy of reaction aliquots. For QD purification, toluene was purchased from MilliporeSigma, collected from a solvent still, and stored over activated 3 Å molecular sieves in a nitrogen glovebox. UV-vis spectra were collected on a Cary 5000 spectrophotometer from Agilent.

3.4.2 *Synthesis of InP QDs using $InCl_3$*

Adapted from previously optimized conditions.[31] In a nitrogen glovebox, 0.3 mmol $InCl_3$, 0, 0.075, 0.15, 0.225, or 0.3 mmol EDTA, and 5 mL anhydrous oleylamine were added to a 50 mL 3-neck flask. On the Schlenk line, the solution was then placed under vacuum at 120 °C and degassed for 1 h. The vessel was then placed under an inert atmosphere and heated to 180 °C (unless alternate reaction temperature is specified). Once the reaction temperature was reached, 0.33 mL of tris(diethyl)aminophosphine (1.2 mmol) was rapidly injected. The reaction was monitored by UV-vis absorbance spectroscopy of 20 μL reaction aliquots in 2 mL toluene. The reaction was allowed to proceed until the absorbance spectrum remained constant, observed at 2 h, or allowed to react overnight with little change in the absorbance spectrum. The flask was then cooled down to room temperature before being moved into a nitrogen glovebox for purification. The QDs were precipitated with anhydrous methanol, centrifuged for 10 min at 7830 rpm, and resuspended in toluene. This procedure was repeated 3 times to remove excess oleylamine before additional sample analysis was performed (confirmed by ^{1}H NMR spectroscopy).

3.4.3 *Synthesis of InP QDs using InI_3*

InP QDs were synthesized using the same procedure as above but instead of 0.3 mmol $InCl_3$, 0.3 mmol of InI_3 was used, and the reaction was allowed to proceed until the absorbance spectrum remained constant, observed at 30 minutes.

3.4.4 *Post-synthetic addition of EDTA to InP QDs*

In a nitrogen glovebox, 0.15 mmol of EDTA was added to 0.6 mL anhydrous oleylamine to form a slurry. InP QDs with 0 equivalents of EDTA were synthesized according to the procedure above and after 2 hours of reaction, the EDTA-oleylamine slurry was injected to the reaction mixture. The reaction was monitored by UV-vis absorbance spectroscopy of 20 μL reaction aliquots in 2 mL toluene. The reaction was allowed to proceed until the absorbance spectrum remained constant, observed at 1 hour. The QDs were purified as described above before additional sample analysis.

3.4.5 *^{1}H NMR Studies of $InCl_3$ and EDTA*

In a nitrogen glovebox, 0.03 mmol $InCl_3$, 0.03 mmol of EDTA, 0.5 mL anhydrous DMSO-d_6, and 0.12 mmol anhydrous oleylamine were added to a 20 mL scintillation vial and stirred overnight to allow for homogeneous mixing. The solution was transferred to an oven-dried airtight J. Young NMR tube and heated to 120 °C for 1 hour in a silicone oil bath, then 180 °C for 2 hours with removal for ^{1}H NMR spectroscopy as needed.

3.4.6 *Transmission electron microscopy (TEM)*

All imaging was done on a FEI Tecnai G2 F20 SuperTwin microscope operated at 200 kV using bright field imaging. Samples were prepared in a nitrogen glovebox by drop-casting 5 μL of dilute QD suspensions in toluene onto a suspended ultrathin carbon film on a lacey carbon support film,

400 mesh, copper grids purchased from Ted Pella Inc, and allowed to dry fully (10 min) then placed under vacuum overnight. TEM size analysis was performed using manual analysis in ImageJ based off images from at least two different grid locations and over 300 particle diameter measurements per sample. Due to the low contrast of InP under the electron beam, standard deviation of diameter measurements may be artificially high.

3.4.7 *Powder X-ray Diffraction (XRD)*

Powder XRD diffraction patterns were collected on solid films drop-cast onto a Si wafer using a Bruker D8 Discover diffractometer.

3.4.8 *NMR spectroscopy*

^{1}H and ^{31}P NMR spectra were recorded on 500 MHz Bruker Advance spectrometers. ^{1}H NMR spectra were collected with 10 scans, 2 dummy scans, and a delay time of 30 s for QD samples or 10 s for samples of molecular indium and EDTA species. ^{31}P NMR spectra were collected with 135 scans and a delay time of 2s for Figure S11 and 100 scans, delay time of 10s for Figure 5.

3.4.9 *Supplementary Figures*

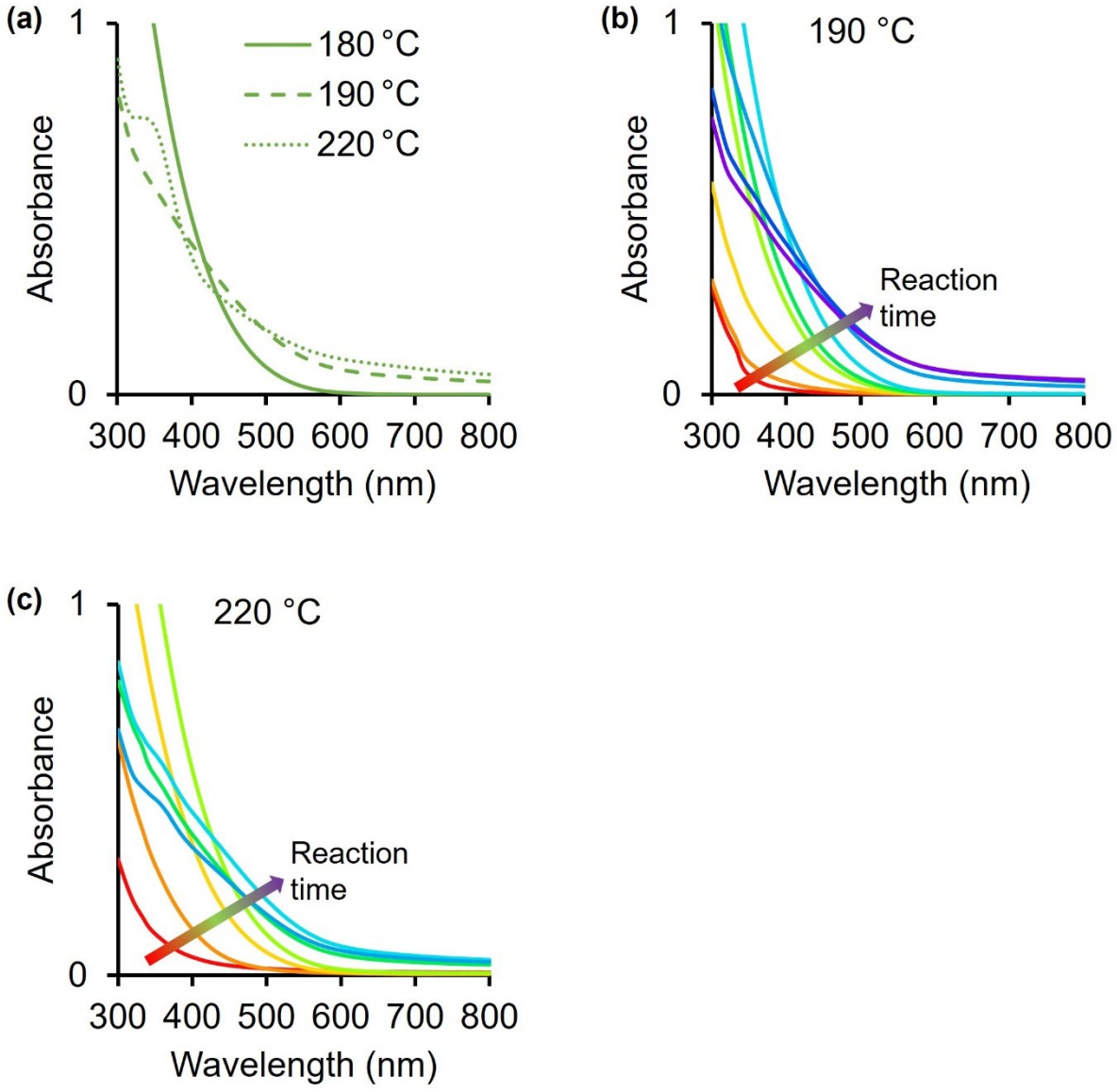


Figure S 3.1 Absorbance spectra for syntheses at 190 and 220 °C. InP QD synthesis with EDTA above 180 °C leads to decomposition shown by (**a**) comparing the final absorbance spectra of InP QDs made using 0.75 eq. of EDTA at reaction temperatures of 180, 190, and 220 °C and absorbance spectra of reaction aliquots of InP QDs made using 0.75 eq. of EDTA at (**b**) 190 °C

and (**c**) 220 °C. Note how the absorbance intensity decreases at 413 nm and there is an increase in scattering, showing a loss of colloidally stable crystalline InP.

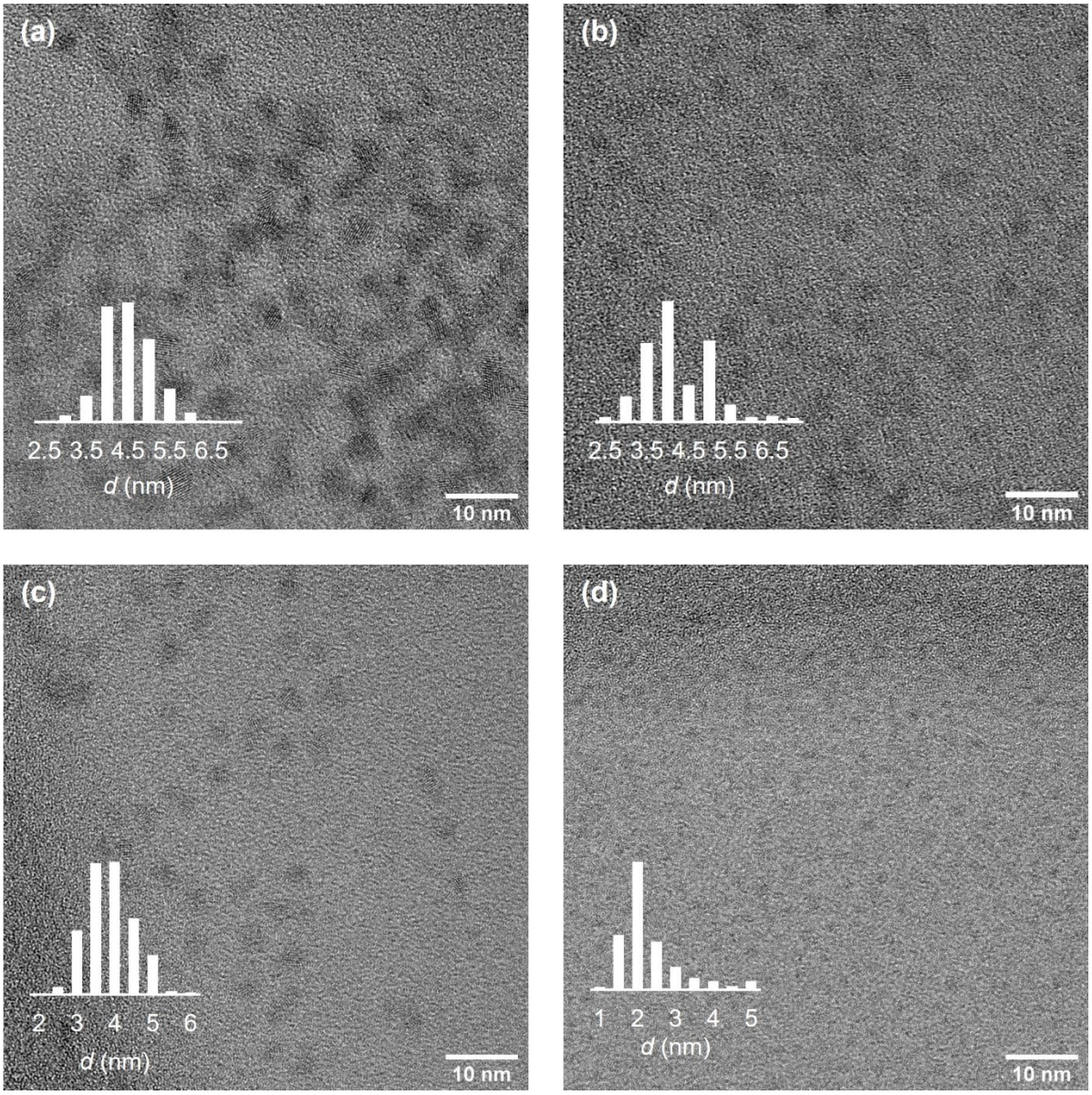


Figure S 3.2 TEM images of InP QDs made using (**a**) 0, (**b**) 0.25, (**c**) 0.5, and (**d**) 0.75 equivalents of EDTA, with diameters 4.5 ± 0.6 nm, 4.2 ± 0.8 nm, 3.9 ± 0.6 nm, and 2.3 ± 0.8 nm, respectively. Insets show histograms of QD diameter from the size analysis.

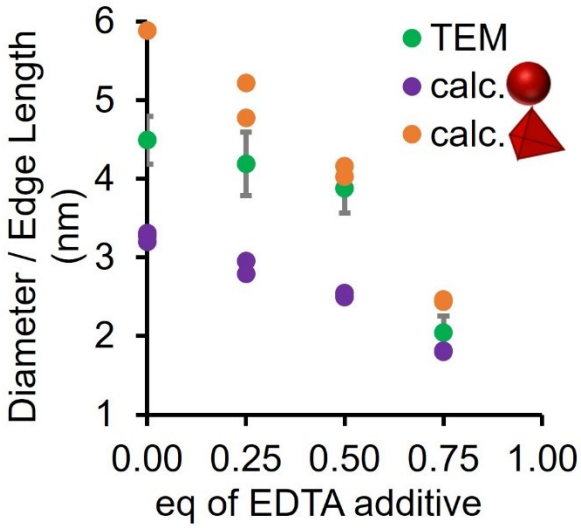


Figure S 3.3 Comparison of final InP QD size between manually measured diameter TEM images (particle count >300) and diameter calculated assuming a spherical nanocrystal shape versus edge length calculated assuming a tetrahedral nanocrystal shape from the lowest energy electronic transition extracted from fitting the final absorbance spectra.

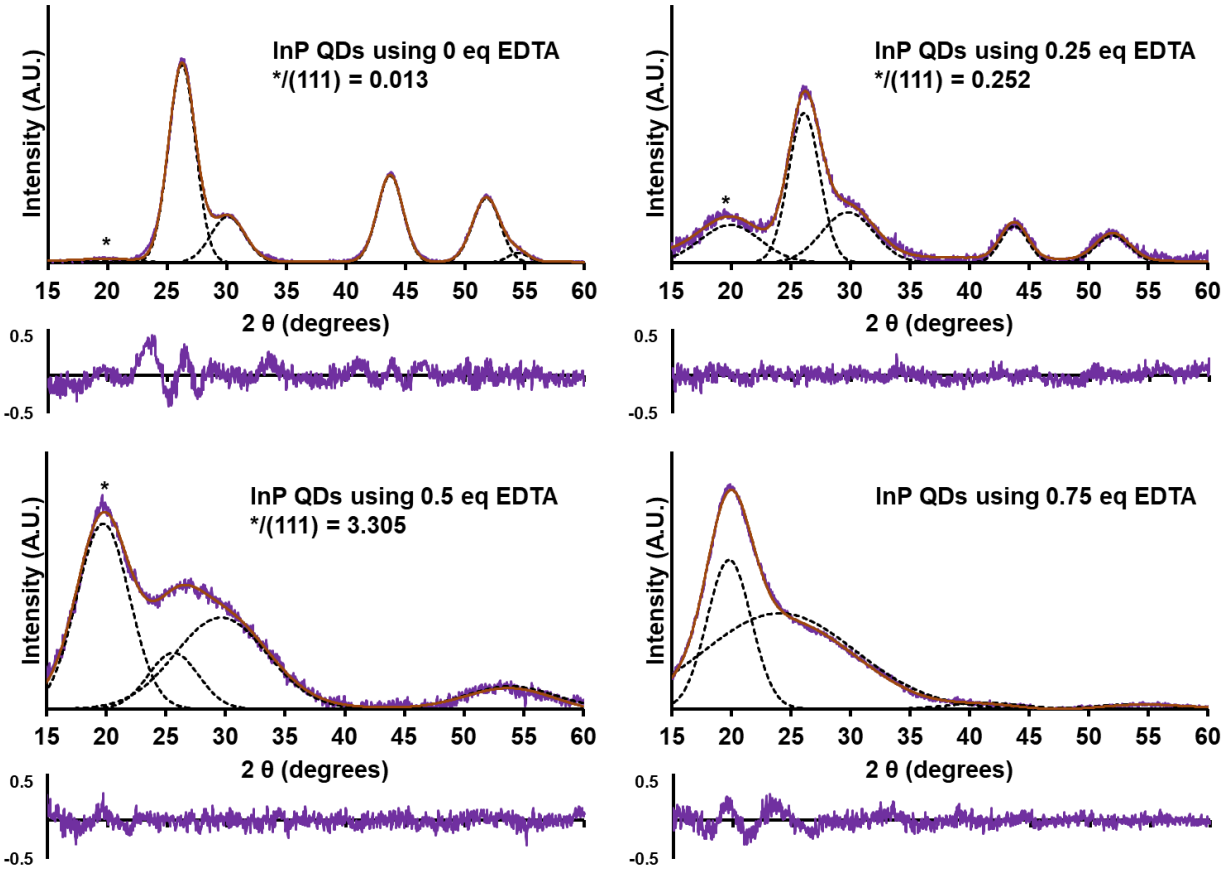


Figure S 3.4 Fits of the pXRD patterns of the EDTA series InP QDs to gaussians centered at the bulk InP zinc blende diffraction pattern. The ratio of the intensity of the peak at 20 degrees two theta attributed to ligand ordering to the (111) InP zinc blende peak decreases as the QD size decreases as is expected.

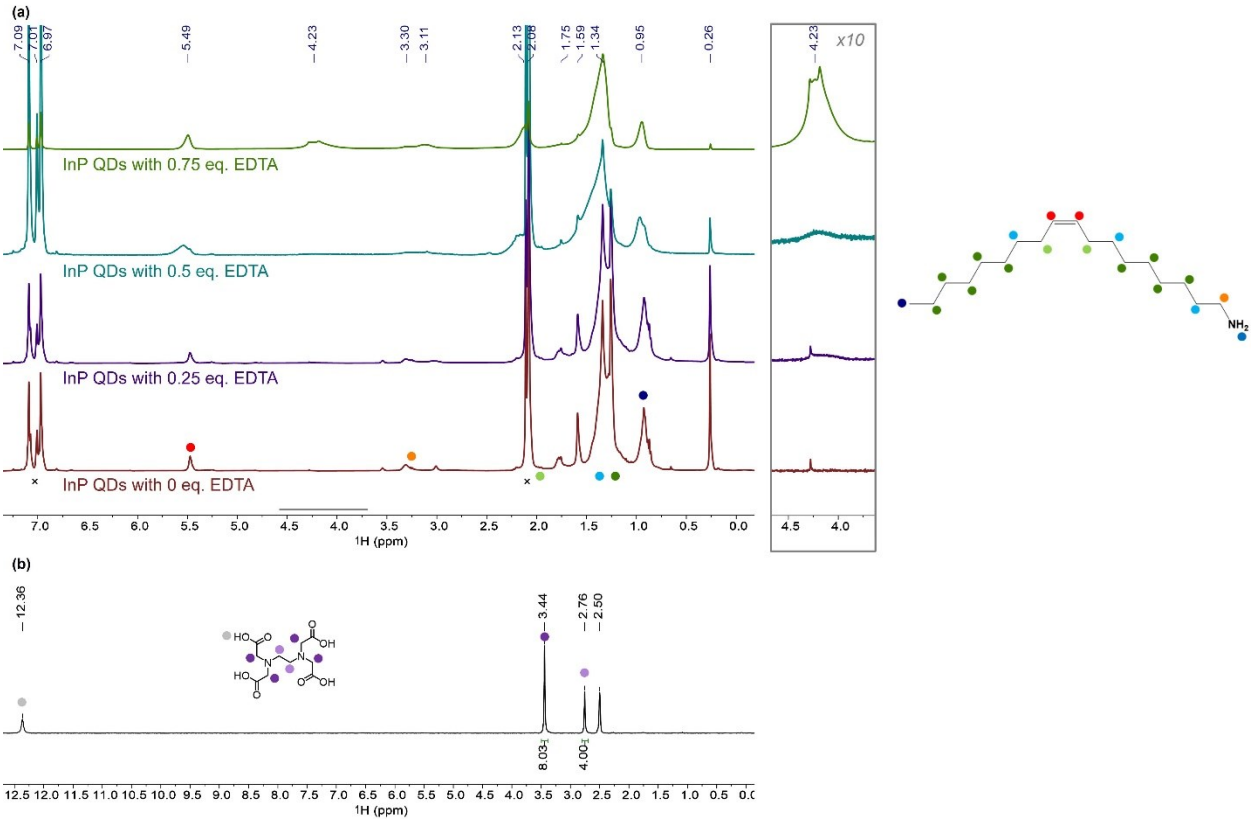


Figure S 3.5 Proton NMR spectra InP QD series and indium EDTA complex . **(a)** ^{1}H NMR (toluene-d_8, 500 MHz, 298K) spectra of purified InP QDs made with 0 – 0.75 equivalents of EDTA. Resonances attributed to oleylamine are labeled. Residual solvent labeled (×), grease impurity at 0.26 ppm, and additional byproducts from the oxidation of amines to iminium species as discussed in main text shown in magnified region to view broad peak at 4.2 ppm. **(b)** ^{1}H NMR (DMSO-d_6, 500 MHz, 298K) spectrum of EDTA for comparison, due to insolubility of EDTA in toluene. Residual solvent appears at 2.50 ppm.

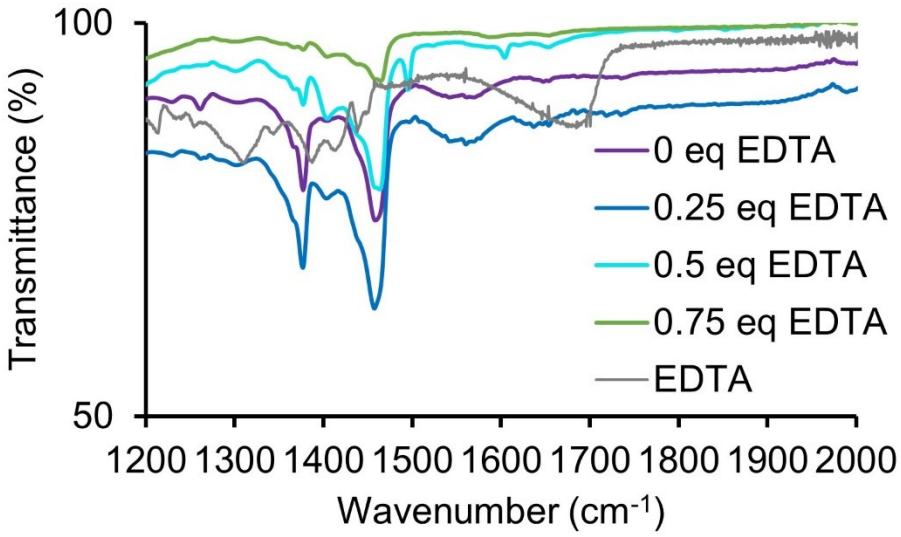


Figure S 3.6 IR spectroscopy of InP QD series. IR spectroscopy does not identify EDTA on the surface of purified InP QDs. The IR spectrum of pure EDTA is shown and C=O stretches from EDTA and sodium edetate appear at 1690 and 1590 cm^{-1} respectively. There is no identifiable trend of increasing EDTA on the surface of the InP QDs across the EDTA series.

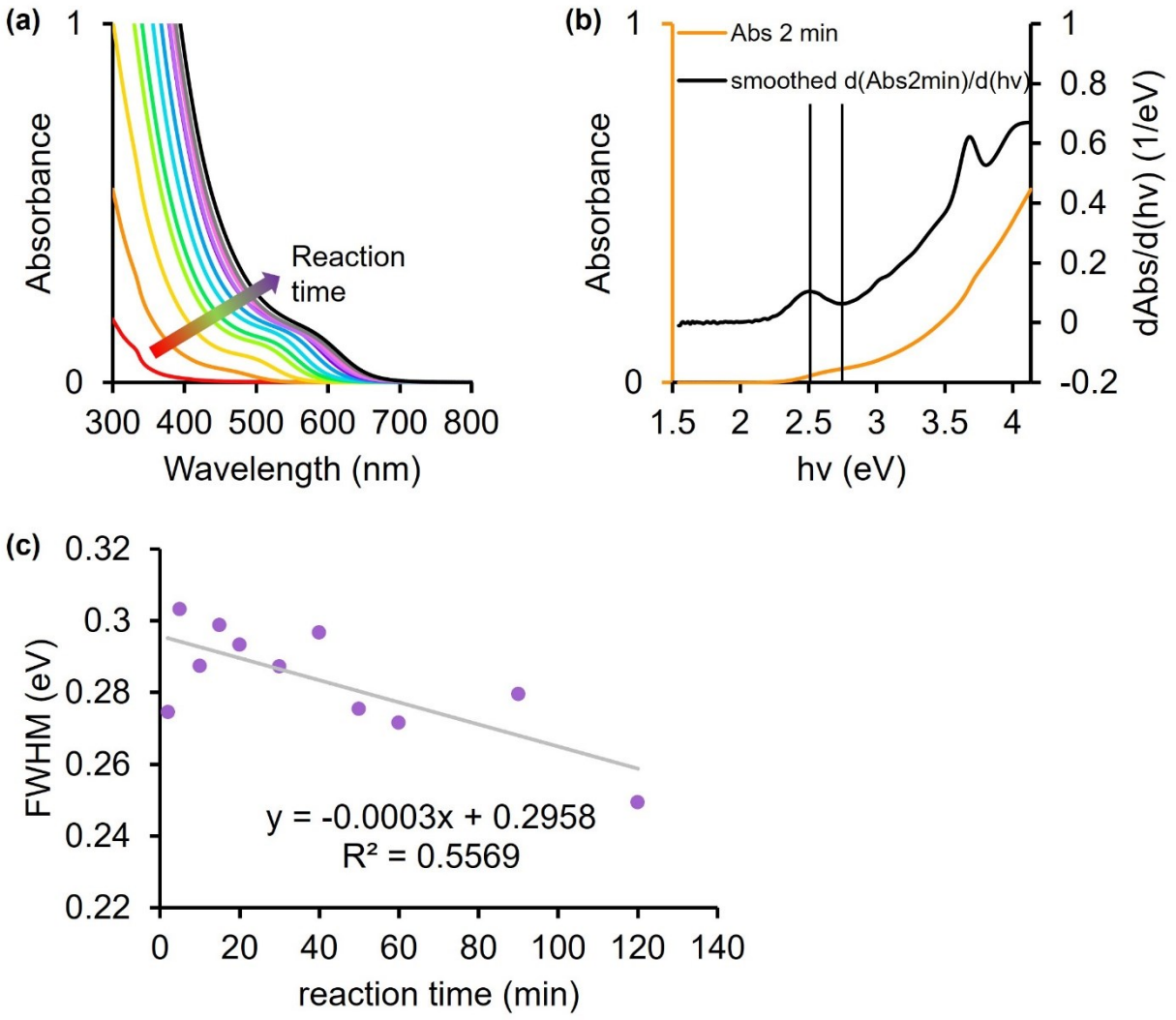


Figure S 3.7 Tracking the full width at half maximum (FWHM) of the lowest energy electronic transitions of aliquots from synthesis of InP QDs with 0.25 equivalents of EDTA. (**a**) Absorbance spectra of reaction aliquots from InP QD synthesis using 0.25 eq. EDTA, (**b**) example calculation of FWHM from an absorbance spectrum and its first derivative to find the local maximum and minimum and calculate the width of the first exciton transition (method described in reference 5).[30] (**c**) FWHM of the first exciton transition as the reaction progresses with a linear fit showing a slight lowering of the FWHM over the reaction time.

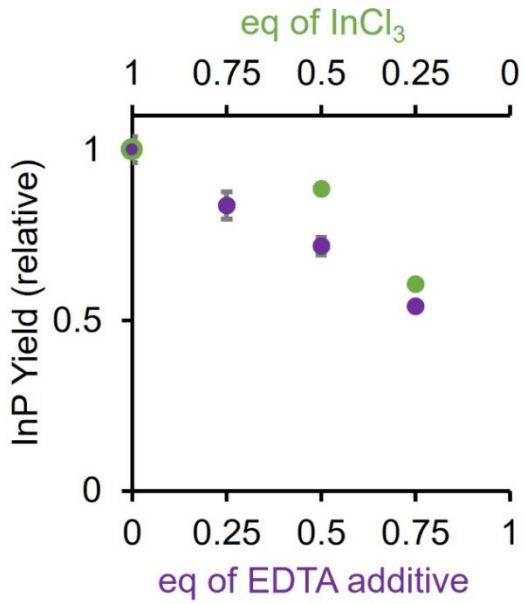


Figure S 3.8 Comparison of InP yield between lower $InCl_3$ concentration and equivalents of EDTA additive.

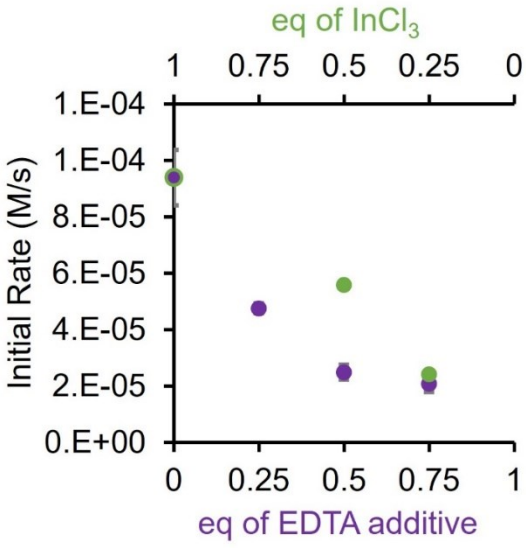


Figure S 3.9 Comparison of initial rates of InP growth between lower $InCl_3$ concentration and equivalents of EDTA additive.

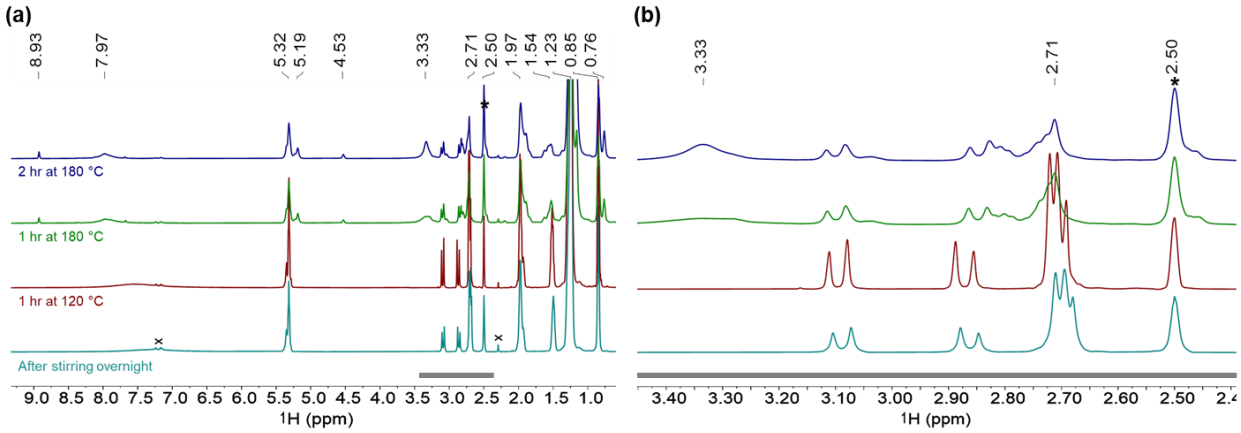


Figure S 3.10 Proton NMR spectra of heated indium-EDTA amine complex. (**a**) ^{1}H NMR (DMSO-d_6, 500 MHz, 298K) spectra of the reaction between 1 eq. $InCl_3$, 1 eq. EDTA, and 4 eq. oleylamine after stirring overnight at room temperature, then heated at 120 °C for 1 hour, then heated to 180 °C for 1 hour and a second hour. (**b**) Magnified region of the spectra in (a) to show the persistence of the diagnostic AB quartets with J_{HH} = 16 Hz signifying EDTA octahedrally coordinated to a metal. At 180 °C, J_{HH} increases to 17 Hz indicating a slight change in bonding environments. Note that after heating to 180 °C, there is decomposition and water (3.33 ppm) production (from the reaction between carboxylic acid and oleylamine). Residual solvent appears at 2.50 ppm (*), and toluene impurity appears at 2.30 and 7.25 ppm (×).

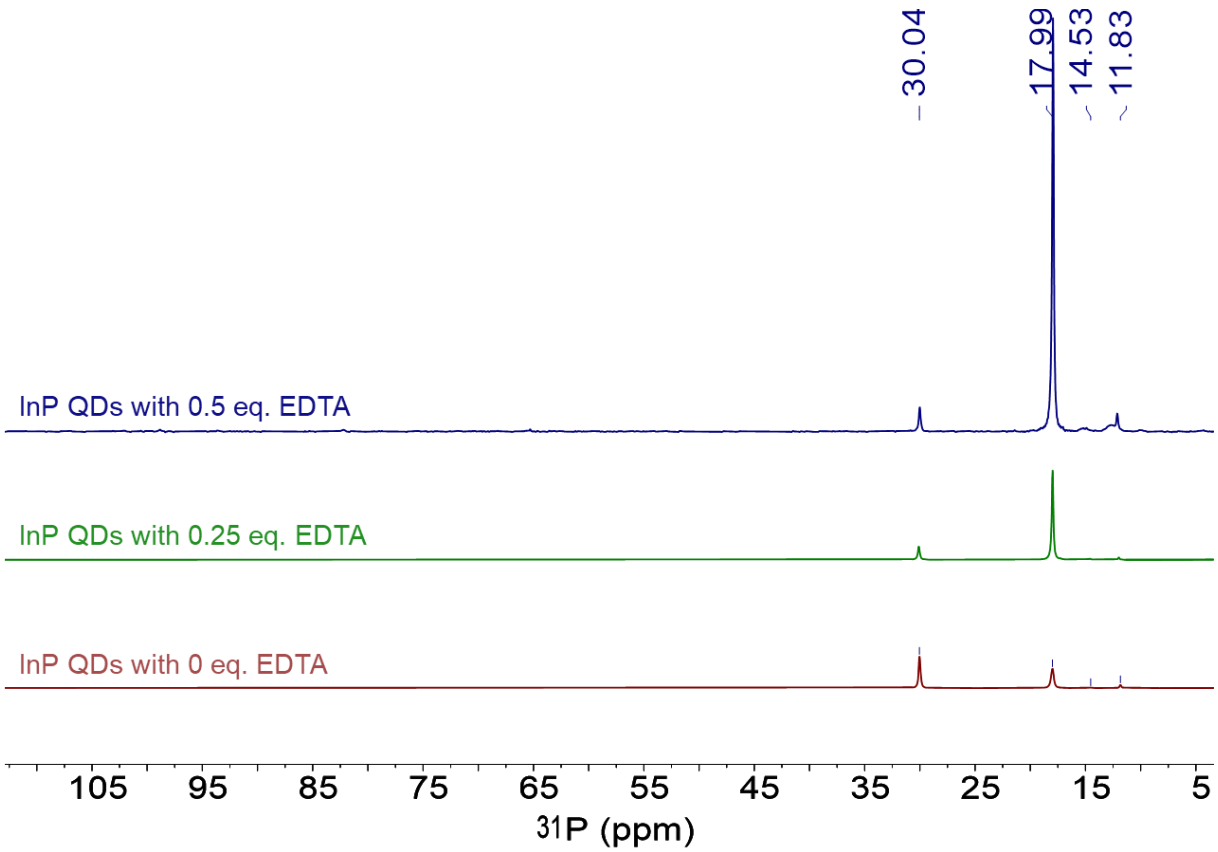


Figure S 3.11 ^{31}P NMR spectra of the crude reaction before purification of InP QDs made using 0, 0.25, and 0.5 eq. EDTA and reaction time of overnight (500 MHz, 298K). There are no observable active transaminated phosphorus species, as is expected after overnight reaction. The InP bond formation byproduct phosphonium salt is observed at 30 ppm for all three reactions, and the resonance attributed to an aminophosphine oxide (see main text) is present in increasing amounts with increasing equivalents of EDTA.

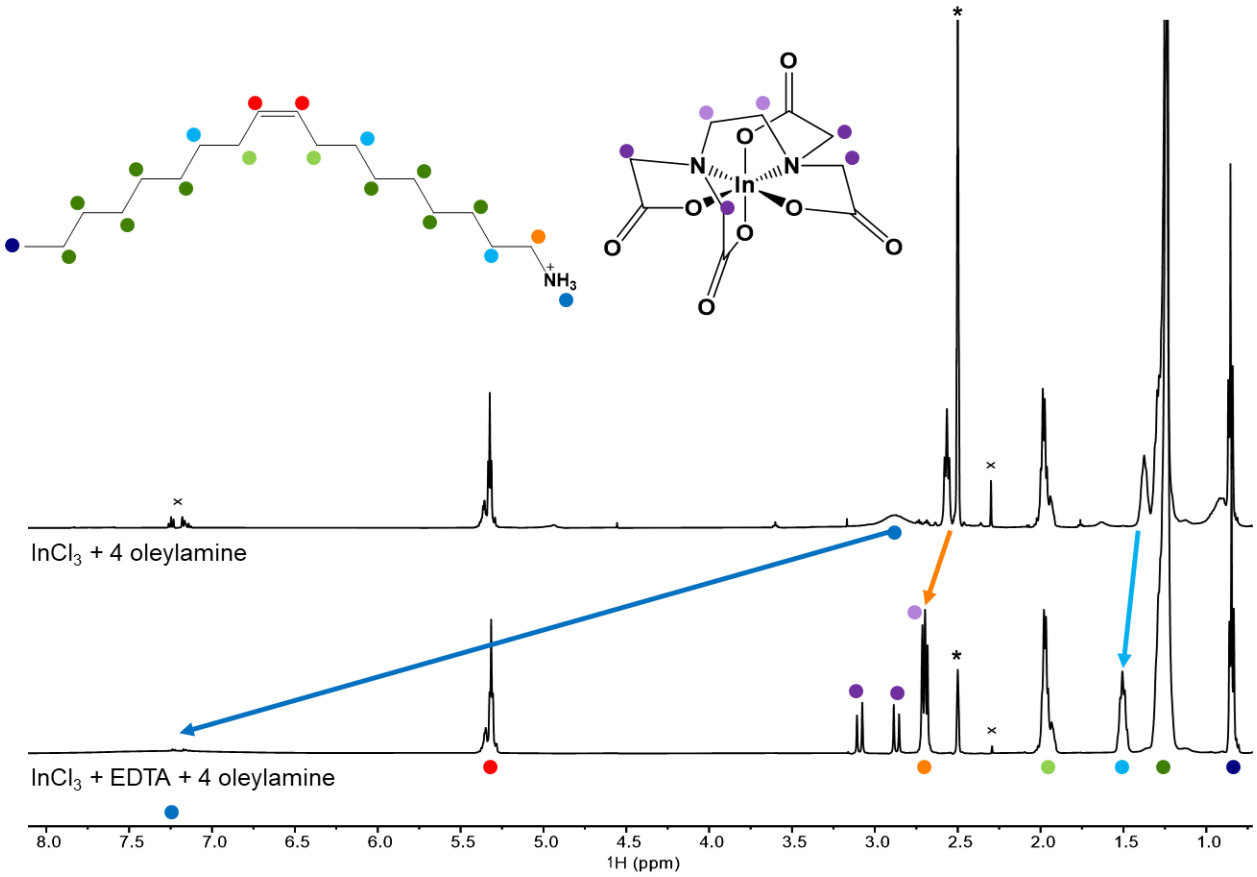


Figure S 3.12 ^{1}H NMR spectrum comparing the reaction of indium chloride with oleylamine to the reaction of $InCl_3$, EDTA, and oleylamine (DMSO-d_6, 500 MHz, 298K). Residual solvent appears at 2.50 ppm (*), and toluene impurity appears at 2.30 and 7.25 ppm (×). Light blue, orange, and dark blue arrows indicate the upfield shift of the beta, alpha, and –N**H**$_3^+$ protons respectively when oleylamine is protonated to oleylammonium by EDTA.

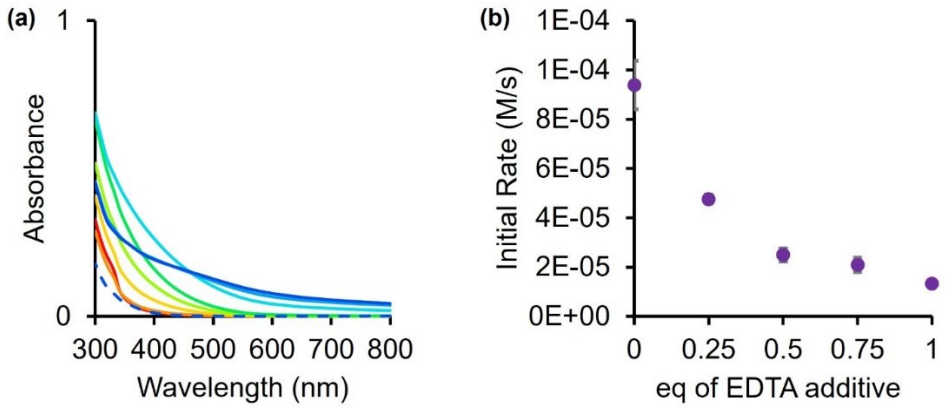


Figure S 3.13 Absorbance spectra and initial rate of InP QDs made with 1 eq. EDTA. (**a**) Absorbance spectra of aliquots (30 s red – blue 2 hr) from the reaction of the octahedral indium EDTA complex with phosphorus (i.e. InP made with 1 eq. EDTA). Dotted blue trace is from the octahedral indium EDTA complex subjected to the same conditions without the injection of phosphorus, after heating at 180 °C for two hours. (**b**) Initial rates of InP growth for InP QDs made using varying equivalents of EDTA including 1.

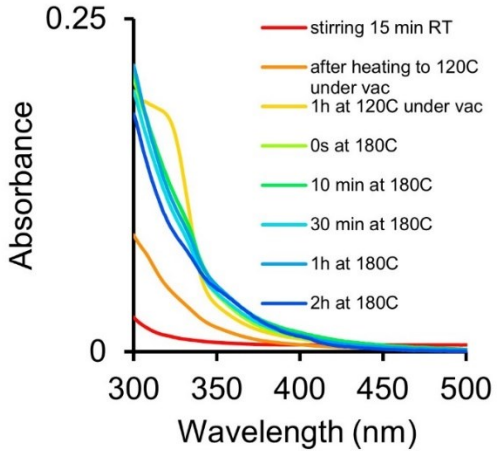


Figure S 3.14 Absorbance spectra of aliquots from the control reaction of 1eq. $InCl_3$, 1 eq. EDTA in oleylamine subjected to the InP synthesis conditions without injection of aminophosphine.

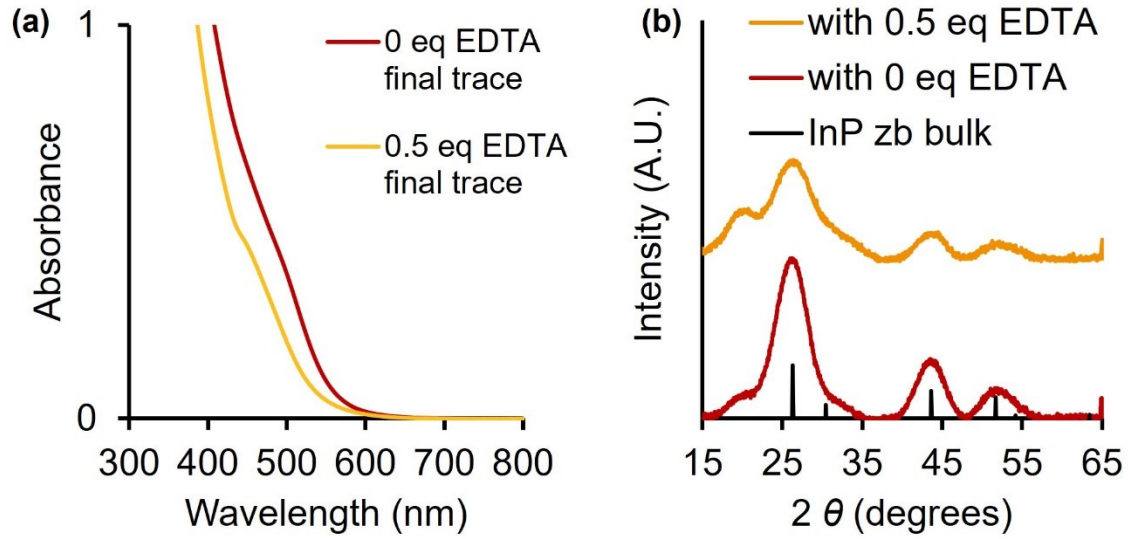


Figure S 3.15 EDTA-based size control for InP QDs made using InI_3. The size control effect of EDTA on InP QDs is generalizable to other indium halides shown by (**a**) the final absorbance spectra and (**b**) pXRD patterns of InP QDs made using indium iodide and 0 or 0.5 equivalents of EDTA at 180 °C. Scherrer analysis results in average crystallite sizes of 2.1 ± 0.3 and 1.8 ± 0.4 nm for QDs made using 0 and 0.5 equivalents of EDTA, respectively.

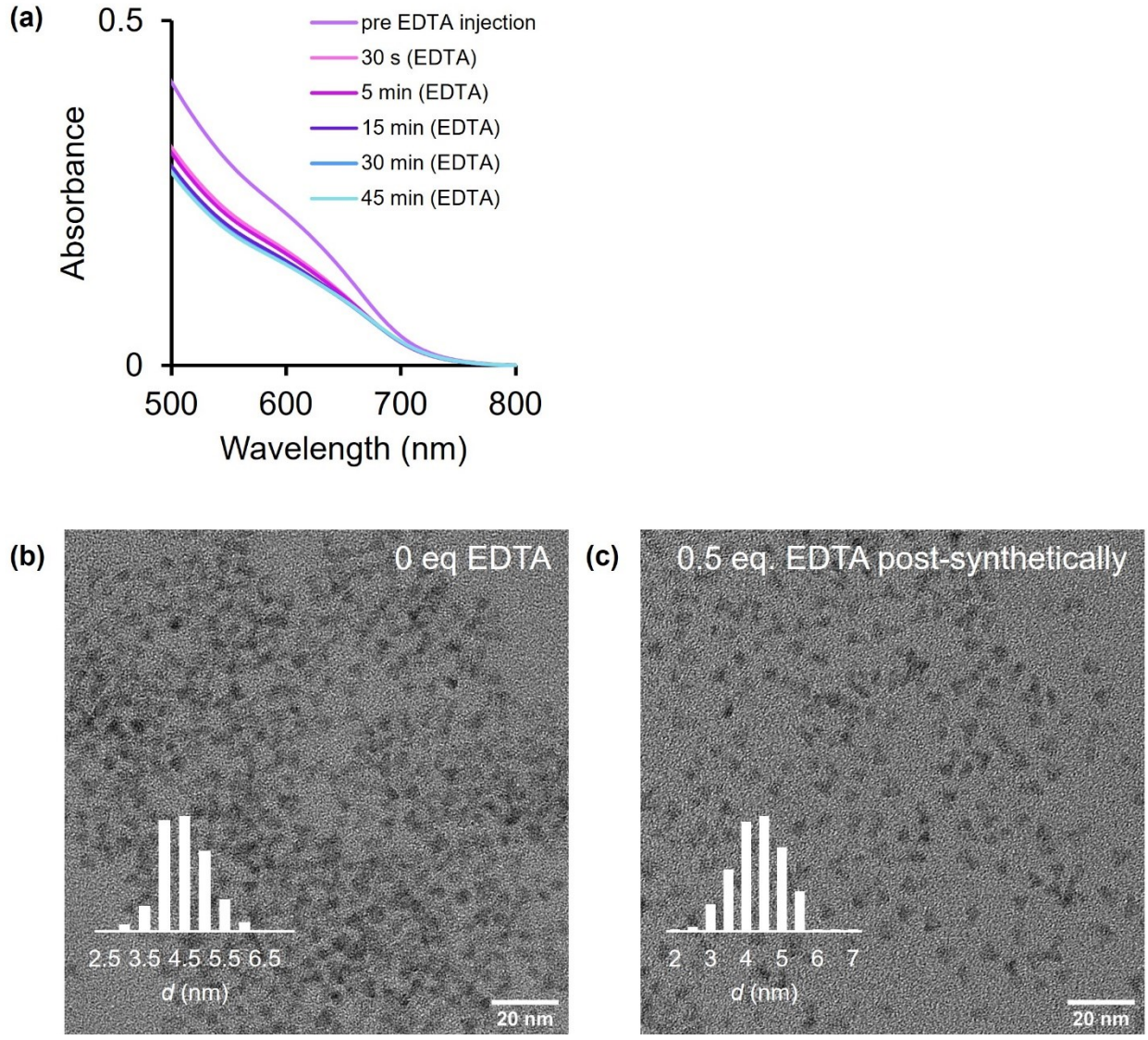


Figure S 3.16 Absorbance spectra and TEM image of QDs with a post-synthetic addition of EDTA. Adding 0.5 equivalents of EDTA to the reaction after the QDs have stopped growing (at 2 hours) does not afford the same size control as when EDTA is added with the precursors. The LEET and the TEM image size analysis do not show significant size differences when EDTA is added post-synthetically. **(a)** Absorbance spectra of InP QDs after 2 hours of reaction and then aliquots after injection of 0.5 equivalents of EDTA in oleylamine. TEM images of InP QDs made using **(b)** 0 equivalents of EDTA and **(c)** with 0.5 equivalents of EDTA added post-synthetically.

Histograms represent diameters measured of >300 particles, with diameters of 4.5 ± 0.6 nm (left) and 4.3 ± 0.7 nm (right).

3.5 REFERENCES

(1) Nudelman, F.; Sommerdijk, N. A. J. M. Biomineralization as an Inspiration for Materials Chemistry. *Angewandte Chemie International Edition* **2012**, *51* (27), 6582–6596. https://doi.org/10.1002/anie.201106715.

(2) Dorval Courchesne, N.-M.; Steiner, S. A.; Cantú, V. J.; Hammond, P. T.; Belcher, A. M. Biotemplated Silica and Silicon Materials as Building Blocks for Micro- to Nanostructures. *Chem. Mater.* **2015**, *27* (15), 5361–5370. https://doi.org/10.1021/acs.chemmater.5b01844.

(3) Nuraje, N.; Dang, X.; Qi, J.; Allen, M. A.; Lei, Y.; Belcher, A. M. Biotemplated Synthesis of Perovskite Nanomaterials for Solar Energy Conversion. *Advanced Materials* **2012**, *24* (21), 2885–2889. https://doi.org/10.1002/adma.201200114.

(4) Zhang, G.; Wei, S.; Belcher, A. M. Biotemplated Zinc Sulfide Nanofibers as Anode Materials for Sodium-Ion Batteries. *ACS Appl. Nano Mater.* **2018**, *1* (10), 5631–5639. https://doi.org/10.1021/acsanm.8b01254.

(5) Mao, C.; Flynn, C. E.; Hayhurst, A.; Sweeney, R.; Qi, J.; Georgiou, G.; Iverson, B.; Belcher, A. M. Viral Assembly of Oriented Quantum Dot Nanowires. *PNAS* **2003**, *100* (12), 6946–6951. https://doi.org/10.1073/pnas.0832310100.

(6) Braun, P. V.; Osenar, P.; Stupp, S. I. Semiconducting Superlattices Templated by Molecular Assemblies. *Nature* **1996**, *380* (6572), 325–328. https://doi.org/10.1038/380325a0.

(7) Monahan, M.; Cai, B.; Jian, T.; Zhang, S.; Zhu, G.; Chen, C.-L.; Yoreo, J. J. D.; Cossairt, B. M. Peptoid-Directed Assembly of CdSe Nanoparticles. *Nanoscale* **2021**, *13* (2), 1273–1282. https://doi.org/10.1039/D0NR07509D.

(8) Klug, M. T.; Dorval Courchesne, N.-M.; Lee, Y. E.; Yun, D. S.; Qi, J.; Heldman, N. C.; Hammond, P. T.; Fang, N. X.; Belcher, A. M. Mediated Growth of Zinc Chalcogen Shells on Gold Nanoparticles by Free-Base Amino Acids. *Chem. Mater.* **2017**, *29* (16), 6993–7001. https://doi.org/10.1021/acs.chemmater.7b02571.

(9) Singh, S.; Bozhilov, K.; Mulchandani, A.; Myung, N.; Chen, W. Biologically Programmed Synthesis of Core-Shell CdSe/ZnS Nanocrystals. *Chem. Commun.* **2010**, *46* (9), 1473–1475. https://doi.org/10.1039/B920688D.

(10) Qi, X.; Jin, B.; Cai, B.; Yan, F.; Yoreo, J. D.; Chen, C.-L.; Pfaendtner, J. Into the Facet-Selectivity of Sequenced Amphiphilic Peptoids at the Au-Water Interface. **2021**. https://doi.org/10.33774/chemrxiv-2021-77bdj.

(11) Hellner, B.; Stegmann, A. E.; Pushpavanam, K.; Bailey, M. J.; Baneyx, F. Phase Control of Nanocrystalline Inclusions in Bioprecipitated Titania with a Panel of Mutant Silica-Binding Proteins. *Langmuir* **2020**, *36* (29), 8503–8510. https://doi.org/10.1021/acs.langmuir.0c01108.

(12) Yan, F.; Liu, L.; Walsh, T. R.; Gong, Y.; El-Khoury, P. Z.; Zhang, Y.; Zhu, Z.; De Yoreo, J. J.; Engelhard, M. H.; Zhang, X.; Chen, C.-L. Controlled Synthesis of Highly-

Branched Plasmonic Gold Nanoparticles through Peptoid Engineering. *Nat Commun* **2018**, *9* (1), 2327. https://doi.org/10.1038/s41467-018-04789-2.

(13) Wadas, T. J.; Wong, E. H.; Weisman, G. R.; Anderson, C. J. Coordinating Radiometals of Copper, Gallium, Indium, Yttrium, and Zirconium for PET and SPECT Imaging of Disease. *Chem. Rev.* **2010**, *110* (5), 2858–2902. https://doi.org/10.1021/cr900325h.

(14) Sugimoto, T.; Dirige, G. E.; Muramatsu, A. Formation Mechanism of Monodisperse CdS Particles from Concentrated Solutions of Cd–EDTA Complexes. *Journal of Colloid and Interface Science* **1996**, *182* (2), 444–456. https://doi.org/10.1006/jcis.1996.0486.

(15) Zhou, L.; Wang, S.; Ma, H.; Ma, S.; Xu, D.; Guo, Y. Size-Controlled Synthesis of Copper Nanoparticles in Supercritical Water. *Chemical Engineering Research and Design* **2015**, *98*, 36–43. https://doi.org/10.1016/j.cherd.2015.04.004.

(16) Deki, S.; Kuratani, K.; Uemura, M.; Akamatsu, K.; Mizuhata, M.; Kajinami, A. Aqueous Solution-Based Synthesis of Rare Earth-Doped Metal Oxide Thin Films. *Thin Solid Films* **2004**, *460* (1), 83–86. https://doi.org/10.1016/j.tsf.2004.01.077.

(17) Wang, R.; Liu, C.; Zeng, J.; Li, K.; Wang, H. Fabrication and Morphology Control of BaWO4 Thin Films by Microwave Assisted Chemical Bath Deposition. *Journal of Solid State Chemistry* **2009**, *182* (4), 677–684. https://doi.org/10.1016/j.jssc.2008.12.014.

(18) Wang, Z.; Tao, F.; Yao, L.; Cai, W.; Li, X. Selected Synthesis of Cubic and Hexagonal NaYF4 Crystals via a Complex-Assisted Hydrothermal Route. *Journal of Crystal Growth* **2006**, *290* (1), 296–300. https://doi.org/10.1016/j.jcrysgro.2006.01.012.

(19) Yao, S.; Qi, M.; Qi, L.; Ding, Y.; Chen, M.; Wang, Y. Investigation of EDTA Concentration on the Size of Carbonated Flowerlike Hydroxyapatite Microspheres. *Royal Society Open Science 8* (3), 202148. https://doi.org/10.1098/rsos.202148.

(20) Susman, M. D.; Feldman, Y.; Vaskevich, A.; Rubinstein, I. Chemical Deposition of Cu2O Nanocrystals with Precise Morphology Control. *ACS Nano* **2014**, *8* (1), 162–174. https://doi.org/10.1021/nn405891g.

(21) Ding, M.; Yin, S.; Ni, Y.; Lu, C.; Chen, D.; Zhong, J.; Ji, Z.; Xu, Z. Controlled Synthesis of β-NaYF4:Yb3+/Er3+ Microstructures with Morphology- and Size-Dependent Upconversion Luminescence. *Ceramics International* **2015**, *41* (6), 7411–7420. https://doi.org/10.1016/j.ceramint.2015.02.054.

(22) Li, C.; Quan, Z.; Yang, J.; Yang, P.; Lin, J. Highly Uniform and Monodisperse β-NaYF4:Ln3+ (Ln = Eu, Tb, Yb/Er, and Yb/Tm) Hexagonal Microprism Crystals: Hydrothermal Synthesis and Luminescent Properties. *Inorg. Chem.* **2007**, *46* (16), 6329–6337. https://doi.org/10.1021/ic070335i.

(23) Hamachi, L. S.; Jen-La Plante, I.; Coryell, A. C.; De Roo, J.; Owen, J. S. Kinetic Control over CdS Nanocrystal Nucleation Using a Library of Thiocarbonates, Thiocarbamates, and Thioureas. *Chem. Mater.* **2017**, *29* (20), 8711–8719. https://doi.org/10.1021/acs.chemmater.7b02861.

(24) Sugimoto, T. Underlying Mechanisms in Size Control of Uniform Nanoparticles. *Journal of Colloid and Interface Science* **2007**, *309* (1), 106–118. https://doi.org/10.1016/j.jcis.2007.01.036.

(25) Gary, D. C.; Glassy, B. A.; Cossairt, B. M. Investigation of Indium Phosphide Quantum Dot Nucleation and Growth Utilizing Triarylsilylphosphine Precursors. *Chem. Mater.* **2014**, *26* (4), 1734–1744. https://doi.org/10.1021/cm500102q.

(26) Cossairt, B. M. Shining Light on Indium Phosphide Quantum Dots: Understanding the Interplay among Precursor Conversion, Nucleation, and Growth. *Chem. Mater.* **2016**, *28* (20), 7181–7189. https://doi.org/10.1021/acs.chemmater.6b03408.
(27) Tamang, S.; Lincheneau, C.; Hermans, Y.; Jeong, S.; Reiss, P. Chemistry of InP Nanocrystal Syntheses. *Chem. Mater.* **2016**, *28* (8), 2491–2506. https://doi.org/10.1021/acs.chemmater.5b05044.
(28) Kim, J. Y.; Steeves, A. H.; Kulik, H. J. Harnessing Organic Ligand Libraries for First-Principles Inorganic Discovery: Indium Phosphide Quantum Dot Precursor Design Strategies. *Chem. Mater.* **2017**, *29* (8), 3632–3643. https://doi.org/10.1021/acs.chemmater.7b00472.
(29) Li, Y.; Hou, X.; Shen, Y.; Dai, N.; Peng, X. Tuning the Reactivity of Indium Alkanoates by Tertiary Organophosphines for the Synthesis of Indium-Based Quantum Dots. *Chem. Mater.* **2021**, *33* (23), 9348–9356. https://doi.org/10.1021/acs.chemmater.1c03219.
(30) Tessier, M. D.; Dupont, D.; De Nolf, K.; De Roo, J.; Hens, Z. Economic and Size-Tunable Synthesis of InP/ZnE (E = S, Se) Colloidal Quantum Dots. *Chem. Mater.* **2015**, *27* (13), 4893–4898. https://doi.org/10.1021/acs.chemmater.5b02138.
(31) Buffard, A.; Dreyfuss, S.; Nadal, B.; Heuclin, H.; Xu, X.; Patriarche, G.; Mézailles, N.; Dubertret, B. Mechanistic Insight and Optimization of InP Nanocrystals Synthesized with Aminophosphines. *Chem. Mater.* **2016**, *28* (16), 5925–5934. https://doi.org/10.1021/acs.chemmater.6b02456.
(32) McMurtry, B. M.; Qian, K.; Teglasi, J. K.; Swarnakar, A. K.; De Roo, J.; Owen, J. S. Continuous Nucleation and Size Dependent Growth Kinetics of Indium Phosphide Nanocrystals. *Chem. Mater.* **2020**, *32* (10), 4358–4368. https://doi.org/10.1021/acs.chemmater.0c01561.
(33) Valleix, R.; Cisnetti, F.; Okuno, H.; Boutinaud, P.; Chadeyron, G.; Boyer, D. Size-Controlled Indium Phosphide Quantum Dots for Bright and Tunable Light Emission by Simple Hindered Diamine Addition. *ACS Appl. Nano Mater.* **2021**, *4* (10), 11105–11114. https://doi.org/10.1021/acsanm.1c02577.
(34) Laufersky, G.; Bradley, S.; Frécaut, E.; Lein, M.; Nann, T. Unraveling Aminophosphine Redox Mechanisms for Glovebox-Free InP Quantum Dot Syntheses. *Nanoscale* **2018**, *10* (18), 8752–8762. https://doi.org/10.1039/C8NR01286E.
(35) Chen, J.; Gao, J.; Wang, X. Thermal Decomposition of Ethylenediaminetetraacetic Acid in the Presence of 1,2-Phenylenediamine and Hydrochloric Acid. *J. Braz. Chem. Soc.* **2006**, *17*, 880–885. https://doi.org/10.1590/S0103-50532006000500010.
(36) Kim, K.; Yoo, D.; Choi, H.; Tamang, S.; Ko, J.-H.; Kim, S.; Kim, Y.-H.; Jeong, S. Halide–Amine Co-Passivated Indium Phosphide Colloidal Quantum Dots in Tetrahedral Shape. *Angewandte Chemie* **2016**, *128* (11), 3778–3782. https://doi.org/10.1002/ange.201600289.
(37) Holder, C. F.; Schaak, R. E. Tutorial on Powder X-Ray Diffraction for Characterizing Nanoscale Materials. *ACS Nano* **2019**, *13* (7), 7359–7365. https://doi.org/10.1021/acsnano.9b05157.
(38) Calvin, J. J.; Kaufman, T. M.; Sedlak, A. B.; Crook, M. F.; Alivisatos, A. P. Observation of Ordered Organic Capping Ligands on Semiconducting Quantum Dots via Powder X-Ray Diffraction. *Nat Commun* **2021**, *12* (1), 2663. https://doi.org/10.1038/s41467-021-22947-x.

(39) Dümbgen, K. C.; Leemans, J.; De Roo, V.; Minjauw, M.; Detavernier, C.; Hens, Z. Surface Chemistry of InP Quantum Dots, Amine–Halide Co-Passivation, and Binding of Z-Type Ligands. *Chem. Mater.* **2023**. https://doi.org/10.1021/acs.chemmater.2c02960.
(40) De Roo, J.; Yazdani, N.; Drijvers, E.; Lauria, A.; Maes, J.; Owen, J. S.; Van Driessche, I.; Niederberger, M.; Wood, V.; Martins, J. C.; Infante, I.; Hens, Z. Probing Solvent–Ligand Interactions in Colloidal Nanocrystals by the NMR Line Broadening. *Chem. Mater.* **2018**, *30* (15), 5485–5492. https://doi.org/10.1021/acs.chemmater.8b02523.
(41) Chen, M.; Feng, Y.-G.; Wang, X.; Li, T.-C.; Zhang, J.-Y.; Qian, D.-J. Silver Nanoparticles Capped by Oleylamine: Formation, Growth, and Self-Organization. *Langmuir* **2007**, *23* (10), 5296–5304. https://doi.org/10.1021/la700553d.
(42) Tessier, M. D.; De Nolf, K.; Dupont, D.; Sinnaeve, D.; De Roo, J.; Hens, Z. Aminophosphines: A Double Role in the Synthesis of Colloidal Indium Phosphide Quantum Dots. *J. Am. Chem. Soc.* **2016**, *138* (18), 5923–5929. https://doi.org/10.1021/jacs.6b01254.
(43) Kenny, N. P.; Rajendran, K. V.; Jennings, E. V.; Gilheany, D. G. Cleavage of P□O in the Presence of P–N: Aminophosphine Oxide Reduction with In Situ Boronation of the PIII Product. *Chemistry – A European Journal* **2013**, *19* (42), 14210–14214. https://doi.org/10.1002/chem.201302907.
(44) Gennaro, M. C.; Mirti, P.; Casalino, C. NMR Study of Intramolecular Processes in EDTA Metal Complexes. *Polyhedron* **1983**, *2* (1), 13–18. https://doi.org/10.1016/S0277-5387(00)88025-0.
(45) Ba, Y.; Han, S.; Ni, L.; Su, T.; Garcia, A. Dynamic NMR of Intramolecular Exchange Processes in EDTA Complexes of Sc3+, Y3+, and La3+. *J. Chem. Educ.* **2006**, *83* (2), 296. https://doi.org/10.1021/ed083p296.
(46) Han, S.; Ba, Y. Determination of the Concentrations of Metal Cations in Aqueous Solutions Using Proton NMR Spectral Area Integration of the EDTA Complexes. *Journal of Solution Chemistry* **2004**, *33* (3), 301–312. https://doi.org/10.1023/B:JOSL.0000035362.27111.54.
(47) Green, P. B.; Wang, Z.; Sohn, P.; Imperiale, C. J.; Voznyy, O.; Wilson, M. W. B. Glycol Ether Additives Control the Size of PbS Nanocrystals at Reaction Completion. *J. Mater. Chem. C* **2020**, *8* (35), 12068–12074. https://doi.org/10.1039/D0TC03252B.

Chapter 4. ALTERNATE INDIUM PHOSPHIDE SYNTHESIS WITH AMINOPHOSPHINES: SOLUTION-LIQUID-SOLID NANOWIRE GROWTH

Adapted with permission from the Royal Society of Chemistry. Copyright 2025 Nanoscale.

4.1 INTRODUCTION

Indium phosphide is a high-performing semiconductor found in many current and emerging technologies. The relatively large, direct bandgap of 1.34 eV and high carrier mobilities, in particular, elevate InP above other semiconductors for use in high-speed electronics, such as heterojunction bipolar transistors and high-electron-mobility transistors, and optoelectronics, such as single-photon detectors and extraterrestrial photovoltaics.[1–5] Beyond the bulk, InP nanowires are unique building blocks for electronic and optoelectronic devices due to additional properties like confined carrier transport in one dimension and a tunable band gap.[1,6,7] For example, InP nanowires have a large polarization sensitivity helpful for photodetection and are amenable to hybrid architectures, which enable complex device architectures such as avalanche photodetectors and dot-in-wire telecom emission devices.[1,8,9] Additionally, InP nanowires can be doped and assembled to build precise electronic or optoelectronic devices, as demonstrated by an electroluminescent p–n junction made of crossed InP nanowires from Lieber and coworkers.[10]

Colloidal synthesis is a potential path to scalable InP nanowire growth. Solution-phase growth is more cost-effective, uses less substrate, and operates at lower temperatures than vapor-phase nanowire manufacturing techniques.[2,11] Solution-liquid-solid (SLS) growth is a nanowire growth mechanism that achieves anisotropy by confining nucleation and growth within a colloidally dispersed liquid metal nanodroplet.[12,13] The precursors diffuse from solution into the

metal droplet, nucleate, and grow in one dimension constrained by the droplet interface. Buhro and coworkers discovered the SLS mechanism in 1995 as a solution phase analog of vapor-liquid-solid nanowire growth, which gave rise to a broad investigation of SLS nanowire growth of many compositions.[12,14] There were rapid developments in SLS-grown InP nanowires throughout the 2000s, including improvements in diameter by controlling the metal nanoparticle size,[15–18] length control by tuning precursor to metal nanoparticle ratios,[7,19,20] optical properties,[21] and self-seeded SLS.[22,23] However, the majority of SLS InP nanowire syntheses use pyrophoric, highly-toxic tris(trimethylsilyl)phosphine, with a limited number of syntheses using other phosphorus precursors such as trioctylphosphine[24] or solid hydrogen phosphide.[25] There remains a need to investigate alternate phosphorus precursors to access InP nanowire synthesis that avoids tris(trimethylsilyl)phosphine.[1,2]

Direct colloidal nucleation of anisotropic InP remains elusive.[26,27] Typical colloidal synthesis uses tris(trimethylsilyl)phosphine and an indium carboxylate, and proceeds through a kinetically stable magic-sized cluster intermediate to achieve high-quality InP quantum dots (QDs).[26,28,29] The resulting nanocrystals are quasi-spherical, with an indium-rich surface passivated by carboxylate ligands. Shapes other than spheres and tetrahedra have not been achieved.[26] Dümbgen and coworkers proposed that this is due to the inability of anionic ligands to adequately charge balance surface indium on facets such as (100), which is required for elongated nanocrystals.[27] The alternate InP chemistry based on aminophosphines, a non-pyrophoric, less hazardous phosphorus precursor, produces halide- and amine-capped tetrahedral QDs.[30–33] The aminophosphine-based synthesis has proved to be a versatile system for tuning reaction kinetics as it follows temperature-dependent continuous or burst nucleation and avoids the kinetic trap of the magic-sized cluster.[34–36] As in InP QD synthesis, aminophosphine is a great candidate for

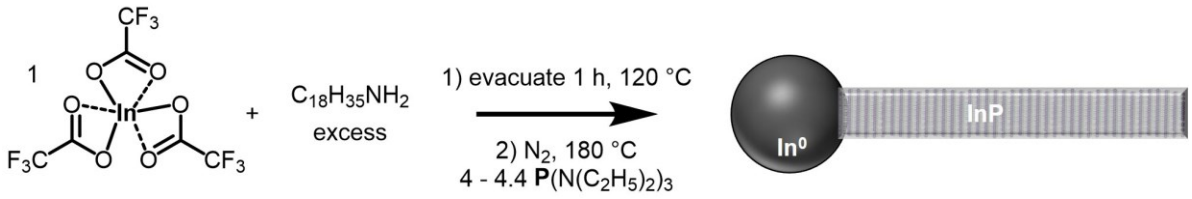
expanding the SLS phosphorus precursor chemistry. To our knowledge, the only example of InP nanowire synthesis through the SLS growth mechanism using aminophosphine is an electrically controlled nanowire synthesis using InI_3 and aminophosphine, where the metal catalyst particles were anchored to a solid electrode support.[37] Another lower toxicity phosphorus precursor, trioctylphosphine, has been used to make InP nanowires through SLS where trimethylindium decomposes into indium metal which catalyzes trioctylphosphine decomposition.[24]

In this study, we report the colloidal synthesis of approximately 11 nm diameter InP nanowires from tris(diethyl)aminophosphine and indium tris(trifluoroacetate) in oleylamine. The nanowires were characterized by transmission electron microscopy (TEM) and atomic force microscopy (AFM), revealing a flat, nanoribbon morphology. Microscopy analysis and powder X-ray diffraction (PXRD) identified indium metal on the nanowire tip, pointing toward an SLS growth mechanism. The mechanism of indium metal formation was investigated with nuclear magnetic resonance (NMR) spectroscopy and was found to depend on the interaction of aminophosphine and the indium precursor. We observed variations in the morphology of the aminophosphine-based nanowires dependent on the reaction conditions, including length control, multipod formation, and QD formation. Microns-long bulk InP nanowires were formed using an alternate indium precursor, indium tris(trifluoromethanesulfonate). We present this aminophosphine-based SLS InP nanowire synthesis as a versatile method to access colloidal anisotropic InP that does not rely on the use of tris(trimethylsilyl)phosphine.

4.2 Results and Discussion

4.2.1 *Synthesis of InP Nanowires*

InP nanowires were prepared from indium tris(trifluoroacetate) ($In(TFA)_3$) and tris(diethylamino)phosphine ($P(NEt_2)_3$). The nanowire synthesis conditions were adapted from aminophosphine-based InP QD synthesis by choosing a weakly binding indium–carboxylate pair.[31] $In(TFA)_3$ was made using a modified literature procedure by refluxing indium metal and neat trifluoroacetic acid.[38] A ^{19}F NMR spectrum containing a single peak at -75.8 ppm was obtained, and a mass spectrum was collected in methanol showing monomeric and dimeric indium-trifluoroacetate species (**Figure S 4.1**). To synthesize InP nanowires, $In(TFA)_3$ in oleylamine was heated under vacuum at 120 °C for one hour, followed by hot injection of aminophosphine at the reaction temperature of 180 °C (**Scheme 4.1**). TEM analysis revealed the main reaction product to be InP nanowires, approximately 11 nm in diameter with an average size dispersion of 50% across several replicate syntheses, with a length of hundreds of nanometers to microns (**Figure 4.1a**).



Scheme 4.1 InP nanowire synthesis from indium tris(trifluoroacetate) and tris(diethylamino)phosphine in oleylamine, proceeding through the Solution-Liquid-Solid growth mechanism.

Looking closer at some of the larger diameter nanowires with TEM, there is a stripe pattern reminiscent of the thin layer buckling of nanobelts reported in the literature (**Figure 4.1b**).[39] The fast Fourier transform of the lattice showed a single crystalline lattice, ruling out the possibility

that the stripe pattern is from stacking faults (**Figure S 4.2)**. AFM was employed to measure the height of these larger diameter (~100 nm) structures and found the height to be around 10-30 nm, with an average width-to-height ratio of 4 (**Figure 4.1e**, **Figure S 4.3**). Therefore, we can more accurately describe these nanowires as nanoribbons, a subclass of nanowires that are flat. This is interesting because anisotropy is unusual for InP nanocrystals, as discussed in the introduction. In the SLS literature for other crystal compositions, a nanoribbon morphology has been described and arises from favorable stabilization of flat facets during nanowire growth by surfactants.[40,41] With this in mind, the top facet of the nanoribbons is (110), identified as it is perpendicular to two facets observed in the TEM image, (111) and (220) (**Figure 4.1b-d**). The (110) facet is stoichiometric, unlike the cation-rich basal facets observed in cadmium chalcogenide nanoplatelets.[42–45] This makes sense as the cadmium chalcogenide nanoplatelets are synthesized with strongly coordinating acetate and fatty acids, whereas the InP nanoribbons are prepared in a bath of oleylamine with trifluoroacetate as the only potential X-type ligand. Since trifluoroacetate is a weak Lewis base, observing a stoichiometric basal plane with only L-type ligand passivation is well rationalized. Previously reported SLS-grown InP nanowire syntheses do not discuss a nanoribbon structure, although similar buckling can be noted occasionally in the published TEM images.[7,13–25,37] A (110) facet is also observed on the surface of InP nanoneedles made with trioctylphosphine as the phosphorus precursor.[24]

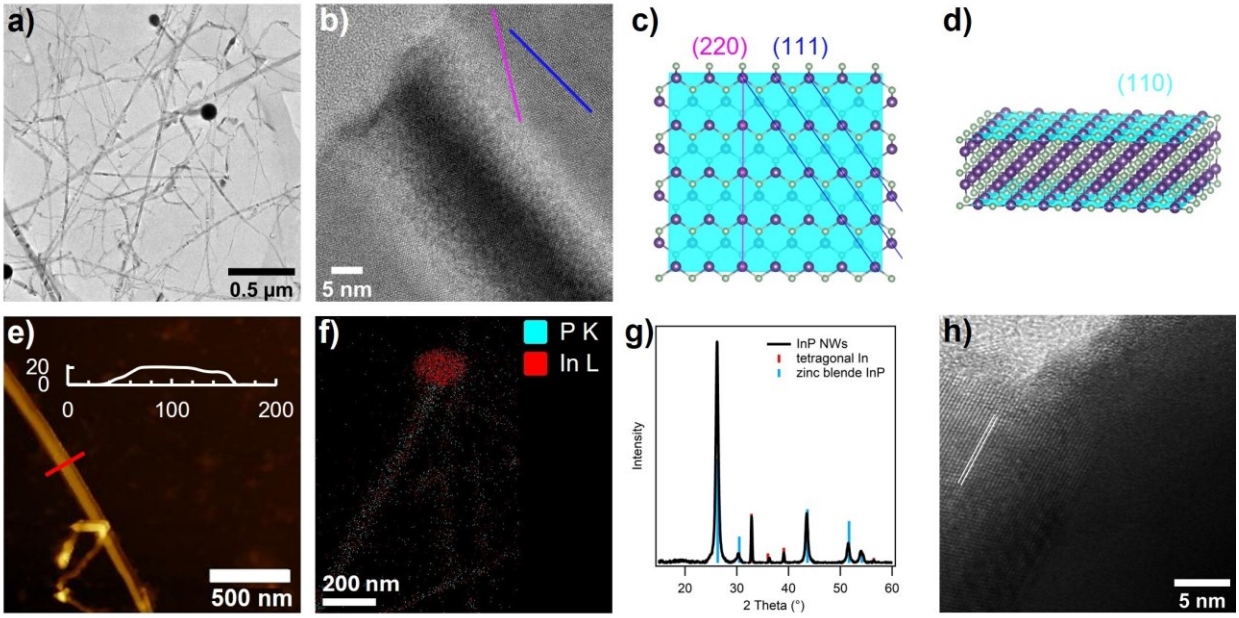


Figure 4.1 Morphological and crystallographic characterization of the InP nanowires. **a)** TEM image of InP nanowires with indium particles observed on some nanowire ends. **b)** TEM image of a nanoribbon buckling pattern in a continuous InP zincblende lattice, with the (111) (dark blue) and (220) (pink) lattice planes marked. Views of the InP zincblende lattice **(c)** matching the crystallographic orientation of b), and **d)** showing the stoichiometric (110) lattice plane in light blue. **e)** AFM image of an InP nanoribbon with the inset showing height (nm) profile along the red line. **f)** STEM EDS map showing indium located at the particle tip with both indium and phosphorus located along the nanowire. **g)** PXRD pattern of the purified reaction product revealing a zincblende InP crystallite size of 16.4 ± 1.4 nm, and large tetragonal indium metal. **h)** High-resolution TEM image of InP nanowire/In metal interface (white lines show 111 lattice planes, d = 0.34 nm).

Spherical nanoparticles of high contrast were observed on the tips of some of the nanowires by TEM. Scanning TEM Energy Dispersive X-Ray Spectroscopy (STEM-EDS) revealed that these

nanoparticle tips are primarily indium, while both indium and phosphorus are found localized on the nanowire (**Figure 4.1f**). This agrees with the PXRD pattern of the nanowires, which showed both zincblende InP with an average crystallite size of 16.6 ± 1.4 nm and tetragonal indium metal present in the isolated reaction product (**Figure 4.1g**). Zooming in on the interface between the indium nanoparticle and the InP nanowire, high-resolution TEM imaging revealed the zincblende InP lattice emerging from the indium metal, with lattice fringes showing that growth occurs along [111] (**Figure 4.1h**). The presence of indium metal nanoparticles at the tip of nanowires points toward the SLS mechanism for nanowire growth, where the indium nanoparticles are presumably formed *in situ* and then act as catalyzing 'nanoreactors' to propel the growth of the nanowires. Pre-made indium metal nanoparticles can also be used to grow InP nanowires from the aminophosphine precursor, either in addition to or instead of the indium precursor (**Figure S 4.4**).

UV-visible absorbance spectra collected over the course of the reaction initially show only a slight absorbance intensity in the high energy region, then an increase in scattering is observed around 10-15 minutes (**Figure S 4.5a**). This is attributed to initial precursor species and oleylamine, and then growth of long, less colloidally-stable nanowires. The production of indium metal nanoparticles is hypothesized to occur before the growth of the InP nanowires, as expected following the SLS mechanism.[12] Although InP nanowires with diameters around 11 nm should experience quantum confinement to absorb around 866 nm[16], clear absorbance peaks are not observed likely due to high polydispersity and scattering, and there is no observable photoluminescence (**Figure S 4.5b**). The peak around 400 nm is attributed to a plasmon resonance of the indium nanoparticles formed in the reaction.[46]

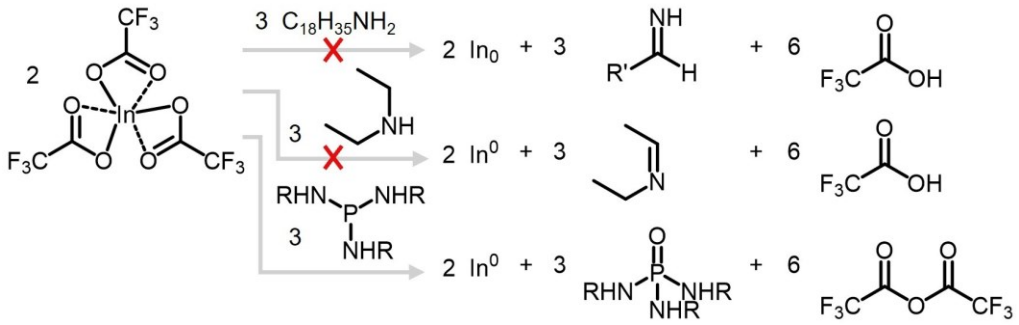
It is interesting to note the continued necessity of the evacuation step at 120 °C to synthesize nanowires. This step was previously included in aminophosphine-based InP QD

synthesis to remove water from the hydrophilic indium halide salts. To investigate this, two control syntheses without evacuation were performed. The first control held at 120 °C under nitrogen for one hour, and the second control skipped the 120 °C step and heated straight to the reaction temperature under nitrogen. The UV-vis absorbance spectra of both control syntheses showed a drastic decrease in absorbance and scattering, consistent with a very low concentration of semiconductor in solution, and the TEM images revealed sparse, low-quality indium-InP particles with a tadpole-like morphology (**Figure S 4.6**). The evacuation step appears to have a significant impact on the nanowire yield. Diffusion-ordered ^{19}F NMR spectroscopy of the reaction precursor mixture with and without the evacuation step shows a minor difference in the $In(TFA)_3$ diffusion coefficients consistent with an increase in the solubilization of the precursor (**Figure S 4.7**). Therefore, the evacuation step likely contributes to nanowire formation by increasing the concentration of $In(TFA)_3$ in solution available to form indium metal nanoparticles.

The concentration of precursors was also investigated as a synthetic parameter. A lower overall reaction concentration was initially hypothesized to improve nanowire diameter dispersity as it could limit the coalescence of the indium nanoparticles after formation and decrease the resulting polydispersity. A nanowire synthesis with 0.03 M $In(TFA)_3$ (opposed to 0.06 M for standard conditions) does produce nanowires; however, the average nanowire diameter increases to 37 nm, and the sample maintains a high dispersity of 115% (**Figure S 4.8**). Therefore, a higher indium precursor concentration is useful to access more monodisperse nanowires, potentially due to accelerated nanowire nucleation kinetics outcompeting coalescence of the indium nanoparticles.

4.2.2 *Mechanism of Indium Reduction*

The SLS mechanism of colloidal nanowire growth is well-studied in the literature,[12] and the key to accessing SLS growth is the presence of catalytic metal nanoparticles. Therefore, we investigated the production of indium metal in our synthesis by assessing potential reducing agents for $In(TFA)_3$ (**Scheme 4.2**). The most obvious candidate for the indium reducing agent was the solvent oleylamine, known to act as a reducing agent in some nanocrystal syntheses.[47–50] To test if oleylamine reduces $In(TFA)_3$ to indium metal, a control reaction was run identical to the nanowire reaction described in **Scheme 4.1** except without the aminophosphine injection. The product was nanocrystalline indium oxide by PXRD, and TEM showed a lack of the large, tens to hundreds of nanometers in diameter indium nanoparticles observed in the nanowire reaction (**Figure S 4.9**). Under these reaction conditions, oleylamine does not reduce indium to the extent seen when aminophosphine is present. This control reaction mimicked the nanowire reaction conditions until the hot injection of the aminophosphine, suggesting that $P(NEt_2)_3$ is necessary for the indium reduction. Diethylamine is released from $P(NEt_2)_3$ when it undergoes transamination with oleylamine and generally, secondary amines are stronger reducing agents than primary amines. However, a similar control reaction with the injection of aminophosphine replaced with three equivalents of diethylamine also produced indium oxide instead of indium metal (**Figure S 4.9**). Therefore, we concluded that the indium reducing agent was likely the aminophosphine itself. Aminophosphines are known to be redox active in the indium halide-based InP QD synthesis chemistry, where it reduces itself from P(III) to P(-III) through three subsequent two-electron reduction events.[30,31]



Scheme 4.2 Options for the reduction of indium. (R = $C_{18}H_{35}$, R' = $C_{17}H_{33}$)

The role of $P(NEt_2)_3$ as the indium reducing agent was investigated through analysis of the molecular byproducts of the nanowire synthesis. The ^{31}P NMR spectrum of the crude nanowire reaction solution revealed only one major phosphorus-containing molecular byproduct, at 18 ppm, which is in the chemical shift range expected for oxidized phosphorus (V) (**Figure 4.2b**).[51] A potential candidate for this byproduct is the aminophosphine oxide of the transaminated $P(NEt_2)_3$, $OP(NHR)_3$ (R = $C_{18}H_{35}$). This can be separately synthesized by adapting a literature method for tris(dimethylamino)phosphine oxide[51] and carrying out transamination with oleylamine[52,53] (**Figure S 4.10**, **Figure S 4.11**). The chemical shift of $OP(NHR)_3$ is 20.5 ppm in deuterated toluene; however, when $OP(NHR)_3$ was spiked into a sample of the crude nanowire reaction solution, there were no additional peaks observed except a slight broadening around the peak at 18 ppm (**Figure S 4.12**). This suggests that the major phosphorus-containing molecular byproduct is tris(oleyl)aminophosphine oxide, and phosphorus oxidation from (III) to (V) is likely the source of electrons to reduce In^{3+}.

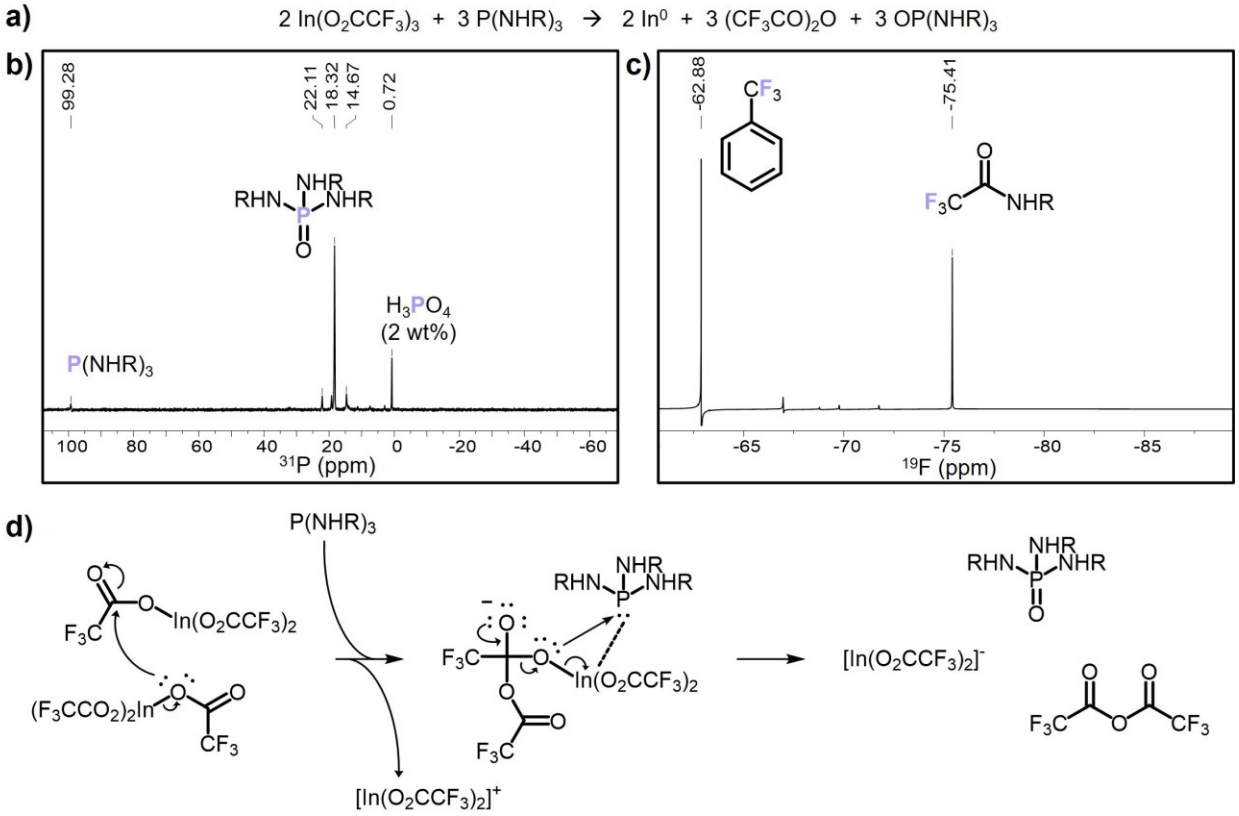


Figure 4.2 Evidence for a mechanism of indium reduction by aminophosphine. **a)** Balanced reaction equation for the reduction of $In(TFA)_3$ by transaminated aminophosphine. **b)** ^{31}P NMR spectrum of the crude nanowire reaction solution with the reaction byproduct identified as tris(oleylamino)phosphine oxide, starting material $P(NHR)_3$, and a 2 weight% H_3PO_4 capillary reference (202 MHz, toluene-d_8, DS 2, NS 40, D1 10 s). **c)** ^{19}F NMR spectrum of the crude nanowire reaction solution with the reaction byproduct identified as N-oleyltrifluoroacetamide and a trifluorotoluene capillary reference (470 MHz, toluene-d8, DS 2, NS 40, D1 10 s). **d)** Proposed mechanism for indium reduction: concerted indium reduction and sacrificial phosphorus oxidation. ($R=C_{18}H_{35}$)

The second clue to the indium reduction mechanism came from tracking the trifluoroacetate moiety of the indium precursor. The ^{19}F NMR spectrum of the crude nanowire

reaction solution contained a single peak at -75.5 ppm, indicating one major fluorine-containing molecular byproduct (**Figure 4.2c**). This is in the chemical shift region for trifluoroacetic anhydride and does not match with either $In(TFA)_3$ (-75.8 ppm) or trifluoroacetic acid (-75.9 ppm) (**Figure S 4.13**). If trifluoroacetic anhydride was produced during the indium reduction reaction, it is expected to continue to react with the solvent, oleylamine, through an aminolysis reaction to form *N*-oleyltrifluoroacetamide.[54] A separate reaction between oleylamine and trifluoroacetic anhydride at the nanowire reaction temperature of 180 °C to produce *N*-oleyltrifluoroacetamide matches the chemical shift of the observed fluorine-containing byproduct (**Figure S 4.14**). Therefore, trifluoroacetic anhydride as a byproduct of the indium reduction is reasonable, and expected from a balanced reaction equation (**Figure 4.2a**).

Considering the observed molecular byproducts of tris(oleyl)aminophosphine oxide and *N*-oleyltrifluoroacetamide, we propose that the initial step of indium reduction occurs via the mechanism shown in **Figure 4.2d**. Two equivalents of $In(TFA)_3$ participate in a nucleophilic attack between two of the trifluoroacetate moieties to begin forming the trifluoroacetic anhydride, followed by reductive elimination of the indium-oxygen bond and concerted oxygen atom transfer to the aminophosphine releasing an indium(I) bis(trifluoroacetate) complex, tris(oleyl)aminophosphine oxide, and trifluoroacetic anhydride. Further indium reduction is expected to occur via a similar pathway. In this mechanism, the electrophilicity of the carbonyl carbon in the trifluoroacetate groups drives the chemistry.

It is interesting to note that nanowires and the preceding indium metal nanoparticles have not been observed in aminophosphine-based InP QD syntheses from indium (III) halides. To confirm this, quantum dot syntheses were run with either $InCl_3$ or InI_3 as the indium precursor instead of $In(TFA)_3$, and the same purification procedure was applied as for the $In(TFA)_3$-

nanowires to isolate any large colloidally unstable nanowire or indium metal products. The PXRD pattern of the resulting product revealed small InP QDs and a large peak likely related to organics around 20 degrees two theta and no indium metal (**Figure S 4.15**). We investigated the reduction potentials of $InCl_3$, InI_3, and $In(TFA)_3$ in acetonitrile using cyclic voltammetry and observed features consistent with a nucleation loop, where there is higher current density on the reverse scan that represents electrodeposition of, in this case, indium metal (**Figure S 4.16**).[55] Both InI_3 and $InCl_3$ were easier to reduce than $In(TFA)_3$, therefore we believe that the above mechanism, which highlights the importance of the reactive carbonyl chemistry, is a better explanation for the formation of indium metal.

4.2.3 *Morphology Control*

Through modifications of the indium precursor, the phosphorus equivalents and addition rate, or the evacuation step, the aminophosphine-$In(TFA)_3$ chemistry can access a multipod morphology, lower aspect ratio nanoplates, QDs, and large, bulk InP nanowires. The multipod morphology is when multiple nanowires emerge from a single metal catalyst particle. We observed multipods as the predominant synthesis product under two conditions related to the purity of the indium precursor and the ratio of indium to phosphorus. First, multipods were observed when the $In(TFA)_3$ precursor contained excess trifluoroacetic acid (**Figure S 4.17a,b**). This is supported by a control experiment where 0.1 equivalent trifluoroacetic acid is added back into pure $In(TFA)_3$, and similar multipods and shortened nanowires were observed (**Figure S 4.17c**). Second, even with a pure $In(TFA)_3$ precursor, the standard synthesis conditions occasionally produced multipods (**Figure S 4.17d,e**). This reproducibility issue was solved by increasing the phosphorus equivalents from 4 to 4.4 per indium, which reliably produced long InP nanowires with an average diameter

of 11 nm (**Figure S 4.18**). Multiple nanowires growing from a single metal particle in SLS has been observed previously in InP nanowire literature and is attributed to either coalescence of the metallic tips of already-grown nanowires,[13,56] or differences in the solubility[57] or chemical potential[58,59] of the component atoms as they diffuse into the liquid metal. Additionally, when the metal particle is solid instead of liquid (Solution-Solid-Solid growth), it can become favorable for multiple arms to nucleate off one particle.[60,61] However, the latter case is not likely to occur in this study because the melting point of indium is well below the reaction temperature, especially considering the size-dependent melting point depression of nanoscale indium[62].

Adding additional aminophosphine is found to further control the InP morphology towards novel low aspect ratio anisotropic nanocrystals. The metal nanoparticle formation rate and the phosphorus chemical potential (in solution and dissolved in the liquid metal) affect the length of the nanowires, as found previously in SLS InP nanowire literature.[7,12,15,20] However, in this chemistry, the aminophosphine acts both as the phosphorus precursor and the indium-reducing agent, so the exact metal nanoparticle to precursor ratio cannot be easily controlled. Therefore, we investigated the effects of adding additional aminophosphine into the reaction while the nanowires formed. A slow injection at 0.02 mL/min of an additional 10 mole percent $P(NEt_2)_3$ starting 15 minutes after the initial hot injection resulted in shortening of the nanowire length and formation of rectangular nanoplate-like structures (**Figure 4.3a,b**). Increasing the amount of extra aminophosphine to 50 mole percent while maintaining the rate did not continue to shorten the aspect ratio, instead forming nanowires with wide triangular areas and irregular diameters (**Figure 4.3c,d**). Nanowire length is controlled by balancing the ratio of metal catalyst particles to precursors available for growth.[12] More catalyst nanoparticles lead to shorter nanowires while more precursors lead to a longer nanowires. Therefore, the addition of 10 mole % aminophosphine

appears to go primarily towards making indium metal because shorter, wider nanowires are observed, while the addition of 50 mole % appears to get used primarily as a nanowire precursor because longer nanowires are observed. It is interesting to find the anisotropy of the width and height in addition to the expected one-dimensional nanowire anisotropy of SLS growth. As discussed in the introduction, the surfaces of zincblende indium phosphide are not energetically favorable to take on a nanoplate or nanorod morphology.[27] SLS is a method to coax InP into anisotropic morphologies largely inaccessible by traditional colloidal nanocrystal nucleation and growth.

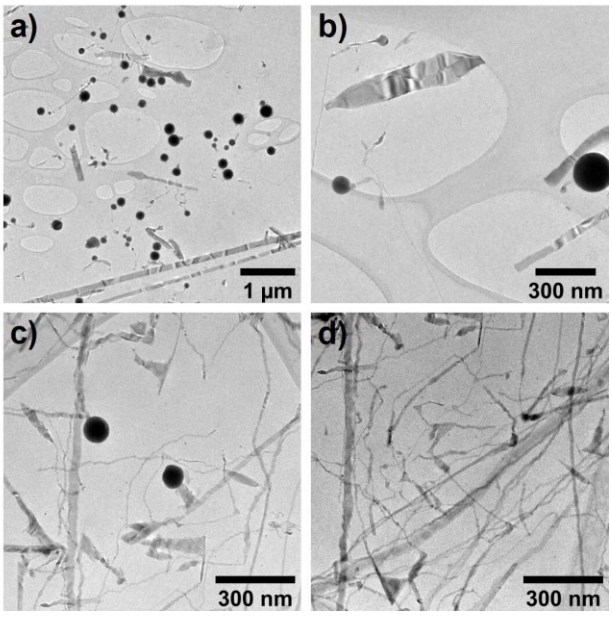


Figure 4.3 TEM images of variations on the InP nanowires with 10 **(a, b)** or 50 **(c, d)** mole % extra $P(NEt_2)_3$.

The InP nanowire synthesis using aminophosphines can be expanded to another weakly-binding indium complex, indium tris(trifluoromethanesulfonate) ($In(OTf)_3$). Trifluoromethanesulfonate was chosen to explore the extreme limit of weak indium-ligand

coordination.[63] When $In(OTf)_3$ is used as the indium precursor replacing $In(TFA)_3$, much larger bulk InP nanowires are formed, as observed with Scanning Electron Microscopy (SEM) and TEM (**Figure 4.4a,b,d,f**). These nanowires have an average diameter of 272 ± 144 nm, are 10s of microns in length, and the PXRD pattern showed bulk zincblende InP with a small amount of tetragonal indium metal (**Figure 4.4c**). A large spherical particle was observed occasionally on the end of the large nanowires which SEM-EDS confirmed contains indium and not phosphorus, which suggests a similar SLS growth mechanism to the $In(TFA)_3$-nanowires (**Figure 4.4e**).

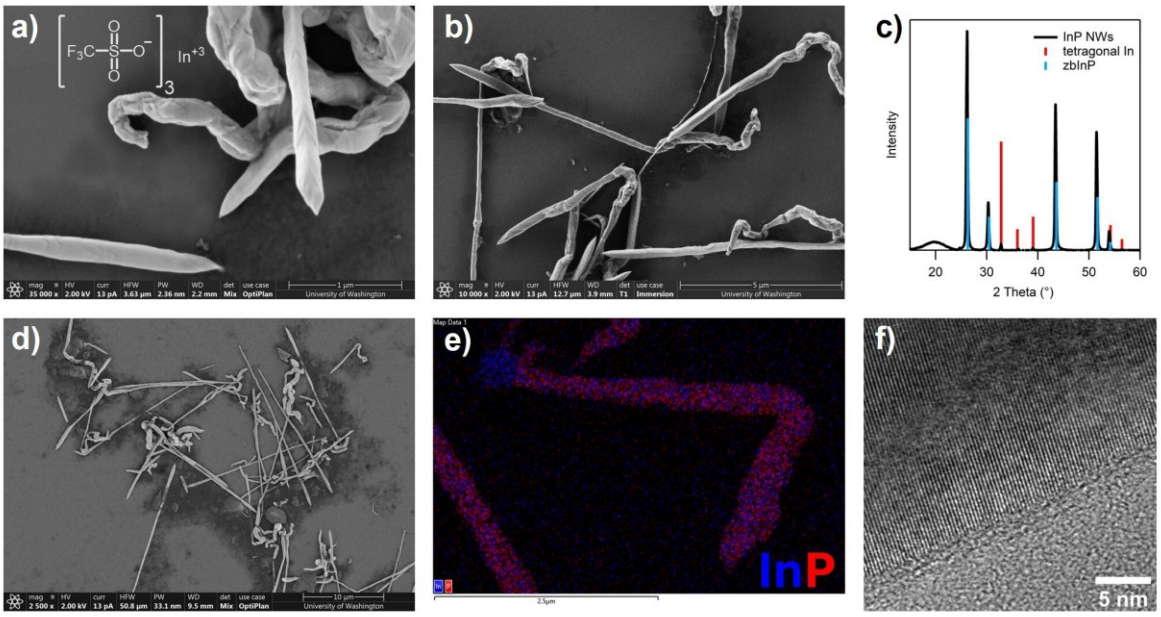


Figure 4.4 Morphological and crystallographic characterization of bulk InP nanowires synthesized using $In(OTf)_3$ including SEM images **(a, b, d)**, **c)** PXRD pattern showing bulk zincblende InP and a relatively low amount of tetragonal indium metal, **e)** SEM-EDS map showing an InP nanowire growing out of an indium particle, and **f)** high-resolution TEM image showing the (111) lattice planes of the edge of a nanowire.

In both the syntheses using either $In(TFA)_3$ or $In(OTf)_3$, InP QDs are also made as a side product. In the reported conditions for the $In(TFA)_3$-based nanowire synthesis, nanowire growth is significantly favored over QD growth, while for $In(OTf)_3$, QD growth is favored. The QDs and the nanowires are separated by centrifugation of the crude reaction solution, where the nanowires crash out and the QDs and other reaction byproducts remain in the oleylamine supernatant. After further purification to isolate the QDs, they were characterized by TEM, PXRD, and NMR spectroscopy. The InP QDs made from $In(TFA)_3$ are zincblende with a crystallite size of 2.2 ± 0.9 nm by PXRD, and have a lowest energy excitonic transition around 475 nm (**Figure S 4.19a-c**). The QDs made using $In(OTf)_3$ are small and poorly crystalline as evidenced by the broad peaks in the PXRD and the low contrast in the TEM (**Figure S 4.19d-f**). The small size of these QDs is consistent with aminophosphine-based InP reaction kinetics, where an indium halide precursor with a better leaving group produces smaller QDs.[64] The PXRD pattern of these QDs is unique from zincblende InP and is more reminiscent of a quasi-wurtzite phase also observed in InP magic-sized clusters.[29,65] Looking closer at the QD surface could explain the deviation from the expected zincblende structure. Typically, aminophosphine-based InP QDs are tetrahedra capped with halides and amines to achieve a perfect mix of X- and L-type ligand binding to passivate the 111 facet.[33] However, switching the indium halide precursor to either $In(TFA)_3$ or $In(OTf)_3$ replaces the halide with a very weakly coordinating organic anion, which is not observed in the QD sample after purification by ^{19}F NMR spectroscopy, only oleylamine is observed on the surface (**Figure S 4.20**). Additionally, by inductively coupled plasma optical emission spectroscopy, these QDs are more stoichiometric (1.1:1 In:P) than aminophosphine-based QDs made from indium chloride (1.5:1 In:P). This suggests that the QD surface is only passivated by oleylamine, and the lack of a strongly-binding X-type ligand favors the quasi-wurtzite phase over zincblende.

The QD product was favored over the nanowire product in the synthesis using $In(TFA)_3$ when the evacuation step was skipped. As discussed previously, the nanowire yield decreased with no evacuation step, resulting in more significant QD growth as noted by the prominent QD lowest energy excitonic transition in the UV-vis absorbance spectra (**Figure S 4.6d**). Another condition that favored QDs over nanowires is when the reaction was carried out using a heat-up method rather than an aminophosphine hot injection, which also does not involve the evacuation of $In(TFA)_3$ and oleylamine. Similarly, the UV-vis absorbance spectra over the reaction showed a prominent QD population and an overall low absorbance intensity compared to the hot injection synthesis (**Figure S 4.21**).

4.3 CONCLUSIONS

We developed a synthesis for InP nanowires using the non-pyrophoric, low-toxicity phosphorus precursor $P(NEt_2)_3$ and $In(TFA)_3$. The nanowires are zincblende InP, 11 nm in diameter on average, and exhibit a flat, nanoribbon morphology with the stoichiometric (110) facet exposed. These nanowires grow through the SLS mechanism, as evidenced by indium metal nanoparticles on the nanowire tips. The formation of indium nanoparticles occurs *in situ* through the reduction of $In(TFA)_3$ with aminophosphine as the reducing agent. We proposed a mechanism in which two equivalents of $In(TFA)_3$ participate in nucleophilic substitution through the reactive carbonyl, oxygen atom transfer to the aminophosphine, and reductive elimination to yield the initial two-electron reduction of indium, an oxidized aminophosphine oxide, and trifluoroacetic anhydride. We have demonstrated morphology control over the indium nanoparticle-InP nanowire system through modifications to the reactant concentration, injection amount and rate, and the evacuation step to access multipod morphologies, different nanowire lengths, and small InP QDs.

Additionally, we expanded the aminophosphine-based SLS chemistry to synthesize bulk InP nanowires from the reaction of $In(OTf)_3$ and $P(NEt_2)_3$.

This study introduces aminophosphine as a suitable phosphorus precursor for colloidal InP nanowire growth. This is important as the industrial relevance of InP and InP nanowires increases, especially while InP nanowire synthesis currently relies on the dangerous, toxic tris(trimethylsilyl)phosphine precursor.[1,66–68] In addition to technological consequence, the anisotropic growth of InP through the SLS mechanism is fundamentally significant to the nanoscale synthesis field because it is a pathway to overcome the synthetic barriers to anisotropic InP nanocrystals. Well-defined InP quantum rods and wires have been achieved through SLS as described in the literature,[7] and our work provides an example of InP nanoribbons and large, rectangular nanoplates. This shows that once the SLS mechanism steers InP into one-dimensional growth, additional width and height anisotropy can arise due to a neutral L-type amine ligand environment. Expanding the SLS mechanism for InP and this aminophosphine-based chemistry will open the possibility of achieving previously implausible anisotropic InP nanocrystals.

4.4 Experimental Methods

4.4.1 *General Practices*

All glassware was dried in a 160 °C oven overnight prior to use. All syntheses were performed under an inert atmosphere of nitrogen using a glovebox or standard Schlenk techniques. Indium chloride (98%) and indium metal pieces (99.99% trace metals basis) were purchased from MilliporeSigma and dried under vacuum before being stored in a nitrogen glovebox. Oleylamine (≥98%) and diethylamine (≥99.5%) were purchased from MilliporeSigma, dried over CaH_2, distilled, and stored over activated 3 Å molecular sieves in a nitrogen glovebox. Toluene-d_8

(99.5%) were purchased from Cambridge Isotope Laboratories and was similarly dried and stored. Anhydrous tris(diethyl)aminophosphine (97%), phosphorus(V) oxychloride (99%), trifluoroacetic acid (99%), and anhydrous methanol (99.8%) were purchased from MilliporeSigma and used without further purification. Trifluoroacetic anhydride (>98.0%) was purchased from TCI America and used without further purification. Indium(III) iodide (99.999%) and indium(III) trifluoromethanesulfonate (99%) were purchased air-free from Strem Chemicals, Inc. and used without further purification. Toluene (high-performance liquid chromatography grade) was purchased from Fisher and used as purchased for UV-vis absorbance spectroscopy of reaction aliquots. High-performance liquid chromatography grade toluene (used for purifications), dichloromethane, and tetrahydrofuran were purified and dried using a solvent still[69], and stored over activated 3 Å molecular sieves in a nitrogen glovebox. For use in electrochemistry, benzonitrile (>99.0%) was purchased from TCI and dried over phosphorous pentoxide then fractionally vacuum distilled (discarding the first and last 5%). The drying and distillation was repeated. Tetrabutylammonium hexafluorophosphate ([TBA][PF6], 98%) was purchased from VWR Scientific and recrystallized twice from ethanol. UV-vis spectra were collected on a Cary 5000 spectrophotometer from Agilent.

4.4.2 *Synthesis of In(trifluoroacetate)$_3$*

Adapted from a reported synthesis of In(TFA)$_3$.[38] In a nitrogen glovebox, 6 mmol (1 equivalent) indium metal and 9 equivalents trifluoroacetic acid were added to a 50 mL Schlenk flask equipped with a stir bar and sealed with a septum. The reaction was then placed under nitrogen on the Schlenk line with a reflux condenser and was heated until reflux and held overnight yielding a fine white powder and excess trifluoroacetic acid. The excess acid was removed under vacuum. In a

nitrogen glovebox, the white powder was washed with pentanes or hexanes and dried under vacuum. ^{19}F (470 MHz, toluene-d_8, 270 K): δ -75.81. ESI-MS *m/z*: $[[In(O_2CCF_3)_4]_2]^{2-}$ calcd for C16F24In2O16 566.8, found 566.7. $[In(O_2CCF_3)_2[HOCH_3]_2]^+$ calcd for C6H8F6In1O6 404.9, found 404.8.

4.4.3 *Synthesis of InP Nanowires using In(trifluoroacetate)$_3$*

Adapted from aminophosphine-based InP QD synthesis conditions.[31] In a nitrogen glovebox, 0.3 mmol $In(TFA)_3$ and 5 mL anhydrous oleylamine were added to a 50 mL 3-neck flask equipped with a stir bar. On the Schlenk line, the solution was placed under vacuum at 120 °C and degassed for 1 h, with 300 rpm stirring. The vessel was then placed under an inert atmosphere and heated to 180 °C. Once the reaction temperature was reached, 0.33 mL of tris(diethyl)aminophosphine (1.2 mmol) was rapidly injected. If multipods form instead of nanowires, increase the tris(diethyl)aminophosphine injection to 0.36 mL (1.32 mmol). The reaction was monitored by UV-vis absorbance spectroscopy of 20 μL reaction aliquots in 2 mL toluene. The reaction was allowed to proceed overnight for approx. 20 hr. The flask was then cooled down to room temperature before being moved into a nitrogen glovebox for purification. The nanowires were collected by centrifugation of the crude reaction solution for 10 min at 7830 rpm, and resuspended in 2-3 mL toluene. The nanowires were washed with toluene this way 3 times to remove excess oleylamine and the quantum dot coproduct before further characterization. The quantum dot product remained in the supernatant and was separately precipitated with anhydrous methanol, centrifuged for 10 min at 7830 rpm, and resuspended in toluene. This procedure was repeated 3 times to remove excess oleylamine before additional sample analysis was performed.

4.4.4 *Synthesis of InP Nanowires using In(trifluoromethanesulfonate)$_3$*

InP nanowires were synthesized using the same procedure as above but instead of 0.3 mmol $In(TFA)_3$, 0.3 mmol of $In(OTf)_3$ was used, and the reaction was allowed to proceed until the absorbance spectrum remained constant, observed after 2 hours of reaction.

4.4.5 *Synthesis of InP Nanowires using External In^0 Nanoparticles*

The indium nanoparticles were synthesized following a literature synthesis.[70,71] The synthesis of InP nanowires including indium nanoparticles in addition to $In(TFA)_3$ was ran similar to above except 0.1 mL of a 0.008 M solution of indium nanoparticles in oleylamine was injected alongside the aminophosphine.[72] The synthesis of InP nanowires including indium nanoparticles without $In(TFA)_3$ was ran as follows: 4.5 mL oleylamine was added to a 50 mL 3-neck flask under nitrogen on the Schlenk line and heated to 180 °C. Once the reaction temperature was reached, 0.33 mL of tris(diethylamino)phosphine (1.2 mmol) was rapidly injected, immediately followed by a rapid injection of a solution of 0.0449 g indium nanoparticles (0.3 mmol indium atoms) in 0.5 mL oleylamine. The reaction proceeds and was purified similar to above.

4.4.6 *Control Synthesis without Aminophosphine*

The reaction of indium tris(trifluoroacetate) and oleylamine was ran similar to the synthesis of InP nanowires using indium tris(trifluoroacetate) above, except without the hot injection of aminophosphine.

4.4.7 *Control Synthesis with Diethylamine*

The reaction of indium tris(trifluoroacetate), oleylamine, and diethylamine was ran similar to the synthesis of InP nanowires using indium tris(trifluoroacetate) above, except in a closed system to avoid rapid evaporative loss of diethylamine. In a nitrogen glovebox, 0.06 mmol $In(TFA)_3$ (0.0272 g, 1 eq.) and 1 mL oleylamine (3 mmol, 51 eq.) was added to a 15 mL 3-neck flask equipped with a t-adapter and stopper. The flask was placed under vacuum at 120 °C and degassed for 1 h. Then, the flask was placed back under nitrogen, cooled to room temperature, and brought into the glovebox. 74.4 microliters of diethylamine was added, and the solution was transferred to a J. Young tube. Heat the solution at 180 °C for 2 hours in a silicone oil bath. The reaction was then cooled down to room temperature before being moved into a nitrogen glovebox for purification similar to the nanowire synthesis.

4.4.8 *Synthesis of Tris(oleylamino)phosphine oxide*

Tris(diethylamino)phosphine oxide was synthesized by adapting a literature procedure for tris(dimethylamino)phosphine oxide by substituting dimethylamine for diethylamine.[51] ^{1}H (500 MHz, toluene-d_8); δ 2.91 (dq, $J_{H\text{-}P}$ = 14.1 Hz, $J_{H\text{-}H}$ = 7.1 Hz, 12 H), 0.91 (t, $J_{H\text{-}H}$ = 7.1 Hz, 18 H). ^{31}P {H} (202 MHz, toluene-d_8); δ 26.68. Then, the tris(diethylamino)phosphine was transaminated by adapting previous literature methods.[53,73] One equivalent of tris(diethylamino)phosphine was heated under nitrogen at 120 °C for two hours with 5 equivalents of oleylamine to produce tris(oleylamine)phosphine. ^{31}P {H} (202 MHz, toluene-d_8); δ 20.50.

4.4.9 *^{19}F NMR Study of Trifluoroacetic Anhydride*

N-oleyltrifluoroacetamide was synthesized by mixing 6.3 μL of trifluoroacetic anhydride (0.045 mmol, 1.5 eq.) and 0.5 mL oleylamine (1.52 mmol, 51 eq) in a nitrogen glovebox in an oven-dried J. Young tube. The reaction was heated to 180 °C in a silicone oil bath for 1 hour, and characterized by ^{19}F NMR spectroscopy.

4.4.10 *Synthesis of InP Quantum Dots from InI_3 or $InCl_3$*

InP QDs made from InI_3 or $InCl_3$ were synthesized as described previously in literature.[36] The insoluble reaction product was collected by centrifugation of the crude reaction solution for 10 min at 7830 rpm for characterization by PXRD.

4.4.11 *Transmission Electron Microscopy (TEM)*

All TEM imaging was done on a FEI Tecnai G2 F20 SuperTwin microscope operated at 200 kV using bright field, HAADF STEM, and Elite T EDAX EDS modes. Samples were prepared in a nitrogen glovebox by drop-casting 5 μL of dilute suspensions in toluene onto a suspended ultrathin carbon film on a lacey carbon support film, 400 mesh, copper grids purchased from Ted Pella Inc, and allowed to dry fully (10 min) then placed under vacuum overnight. TEM size analysis was performed using manual analysis in ImageJ based off images from at least two different grid locations and over 300 diameter measurements per sample.

4.4.12 *Scanning Electron Microscopy (SEM)*

All SEM imaging was done on a ThermoFisher Scientific Apreo 1 SEM.

4.4.13 *Atomic Force Microscopy (AFM)*

All AFM images were collected using ScanAsyst-Air probes (Bruker, CA) in Peakforce Tapping mode with a Dimension Icon AFM (Bruker, CA) at room temperature. Images were analyzed using Nanoscope Analysis v1.5 (Bruker, CA).

4.4.14 *Powder X-ray Diffraction (PXRD)*

Powder XRD diffraction patterns were collected on solid films drop-cast onto a Si wafer using a Bruker D8 Discover diffractometer.

4.4.15 *NMR Spectroscopy*

^{1}H, ^{19}F, and ^{31}P NMR spectra were recorded on 500 MHz Bruker Advance spectrometers. Samples prepared for ^{19}F NMR spectroscopy included a sealed capillary of 0.01 M trifluorotoluene in toluene for reference in accordance to literature.[74] Samples prepared for ^{31}P NMR spectroscopy included a sealed capillary of 2 or 80 weight % H_3PO_4 in H_2O referenced to 0.72 or 0.00 ppm, respectively. Diffusion-ordered spectra were analyzed using Bruker's TopSpin software.

4.4.16 *Mass Spectrometry*

Mass spectra were recorded on a Bruker EsquireLC – Ion Trap Mass Spectrometer.

4.4.17 *Cyclic Voltammetry*

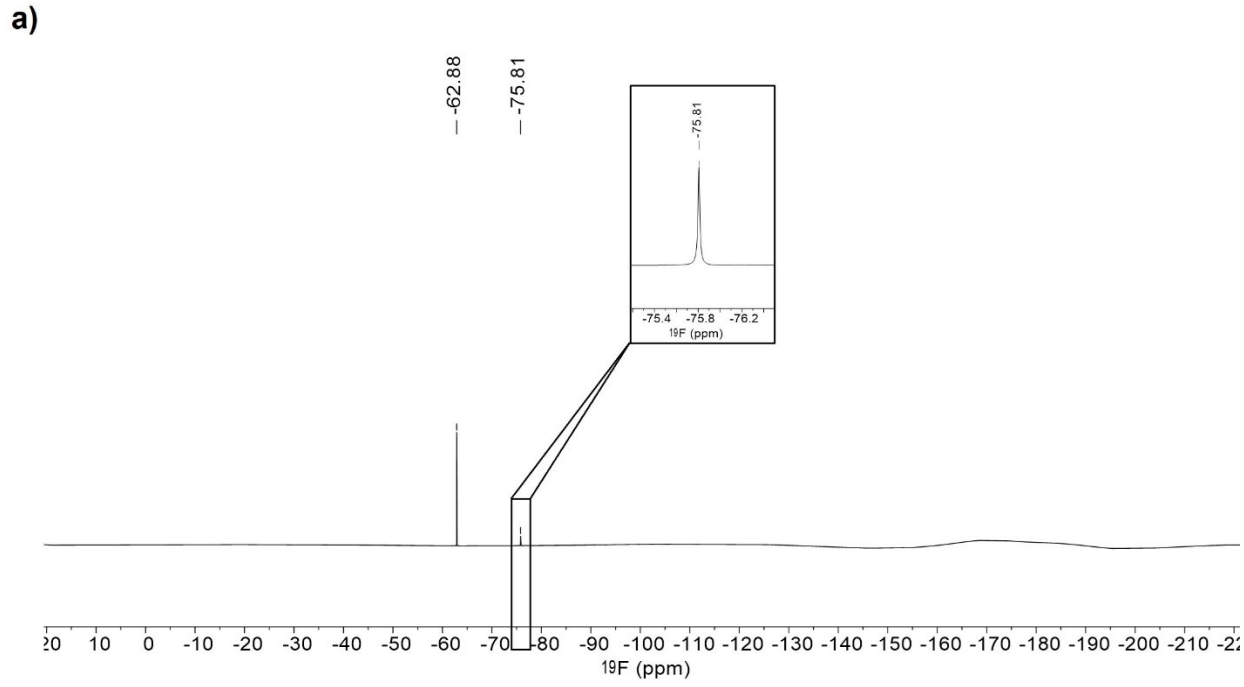
All electrochemical experiments were performed in a nitrogen-filled glove box. The potentiostat used was an EC Epsilon from BASi. Glassy carbon disk electrodes with a diameter of 3.0 mm were polished using 5, 1, and 0.1 micron polishing powder with sonication in ultrapure water

between steps. The counter electrode was a platinum wire, and the pseudoreference electrode was a silver wire in a ceramic-fritted glass tube (Pine) filled with 0.1 M [TBA][PF_6].

Inductively Coupled Plasma – Optical Emission Spectrophotometry (ICP-OES)

ICP-OES of quantum dot samples was taken on a Perkin Elmer Optima 8300. QD solids were digested with H_2O_2 and nitric acid overnight and diluted with 18 MΩ water to prepare ICP samples.

4.4.18 *Supplementary Figures*



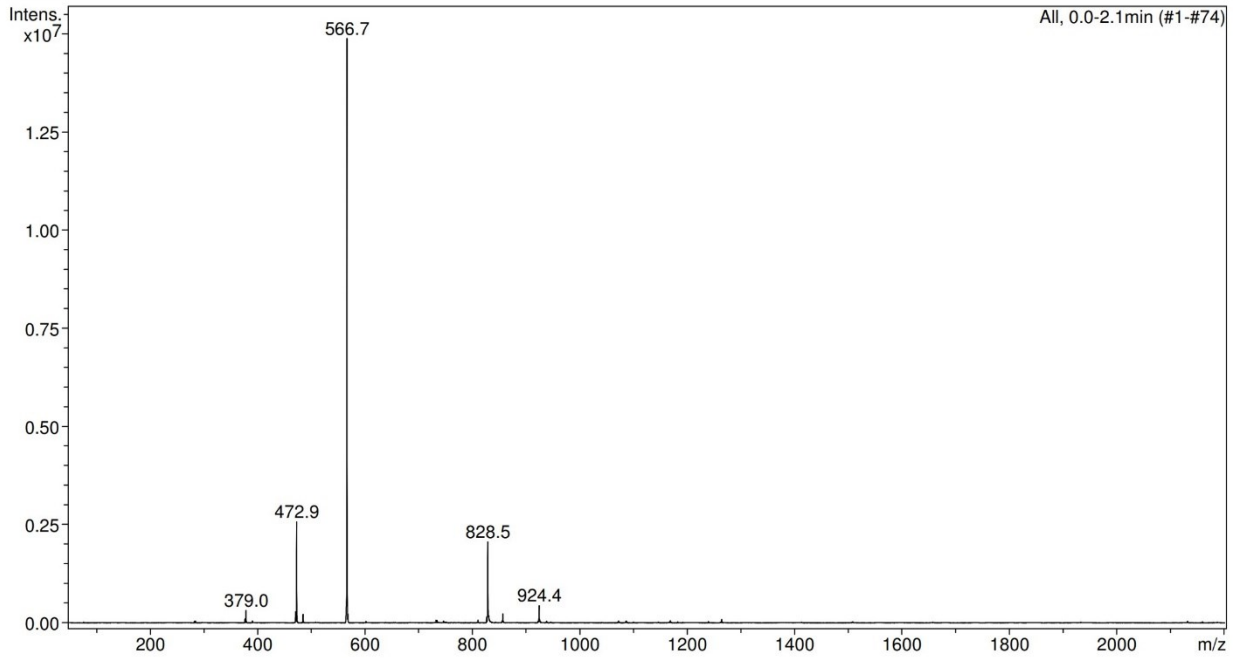
b)

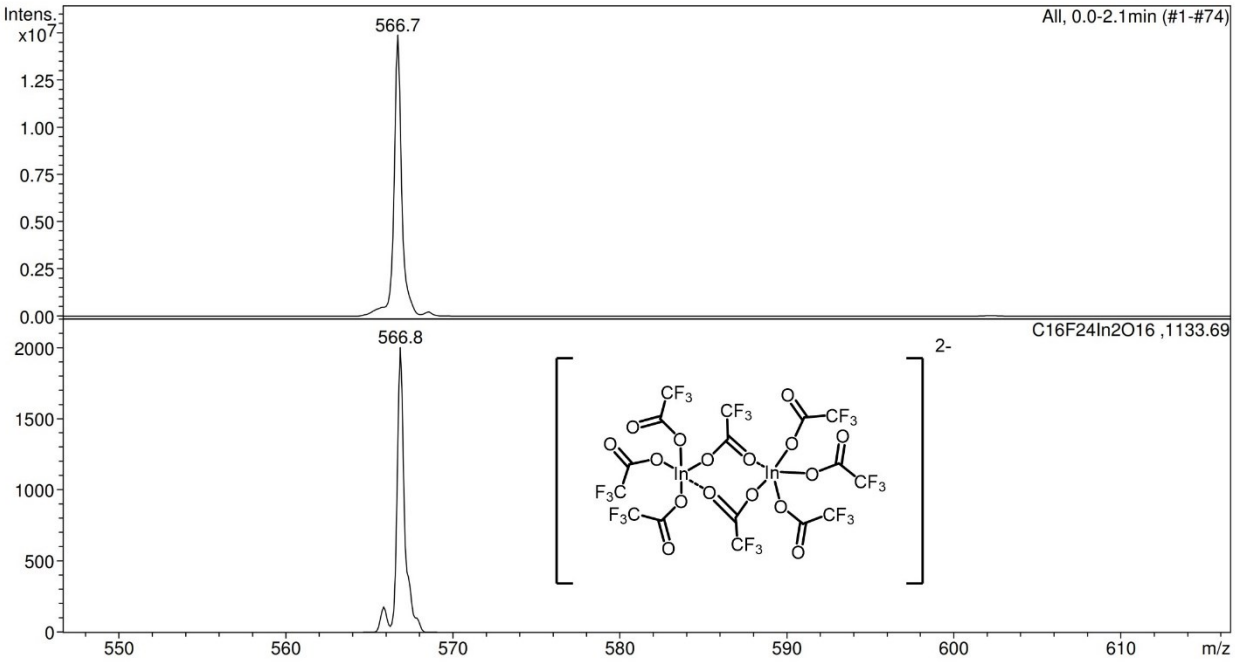
Analysis Info

Analysis Nam	HelenB07.d	Acquisition D	01/04/24 15:14:11	Operator	Administrator
Sample Nam	Default	Method	Copy of XQ Default.ms	Instrument	Esquire-LC_00066
Comment	Negative 30-70 skim voltage				

Acquisition Parameter

Ion Source Type	ESI	Mass Range	Std/Normal	Ion Polarity	Negative	Alternating Ion	n/a
Scan Begin	50.00 m/z	Mass End	2200.00 m/z	Averages	4 Spectra	Polarity	
Capillary Exit	-100.0 Volt	Skim 1	-30.0 Volt	Trap Drive	55.0	Auto MS/MS	Off





c)

Analysis Info

Analysis Nam	HelenB13.d	Acquisition D	01/04/24 15:31:00	Operator	Administrator
Sample Nam	Default	Method	Copy of XQ Default.ms	Instrument	Esquire-LC_00066
Comment	Positive 10-30 skim voltage				

Acquisition Parameter

Ion Source Type	ESI	Mass Range	Std/Normal	Ion Polarity	Positive	Alternating Ion	n/a
Scan Begin	50.00 m/z	Scan End	2200.00 m/z	Averages	4 Spectra	Rolling Time	306 µs
Capillary Exit	40.0 Volt	Skim 1	10.0 Volt	Trap Drive	55.0	Auto MS/MS	Off

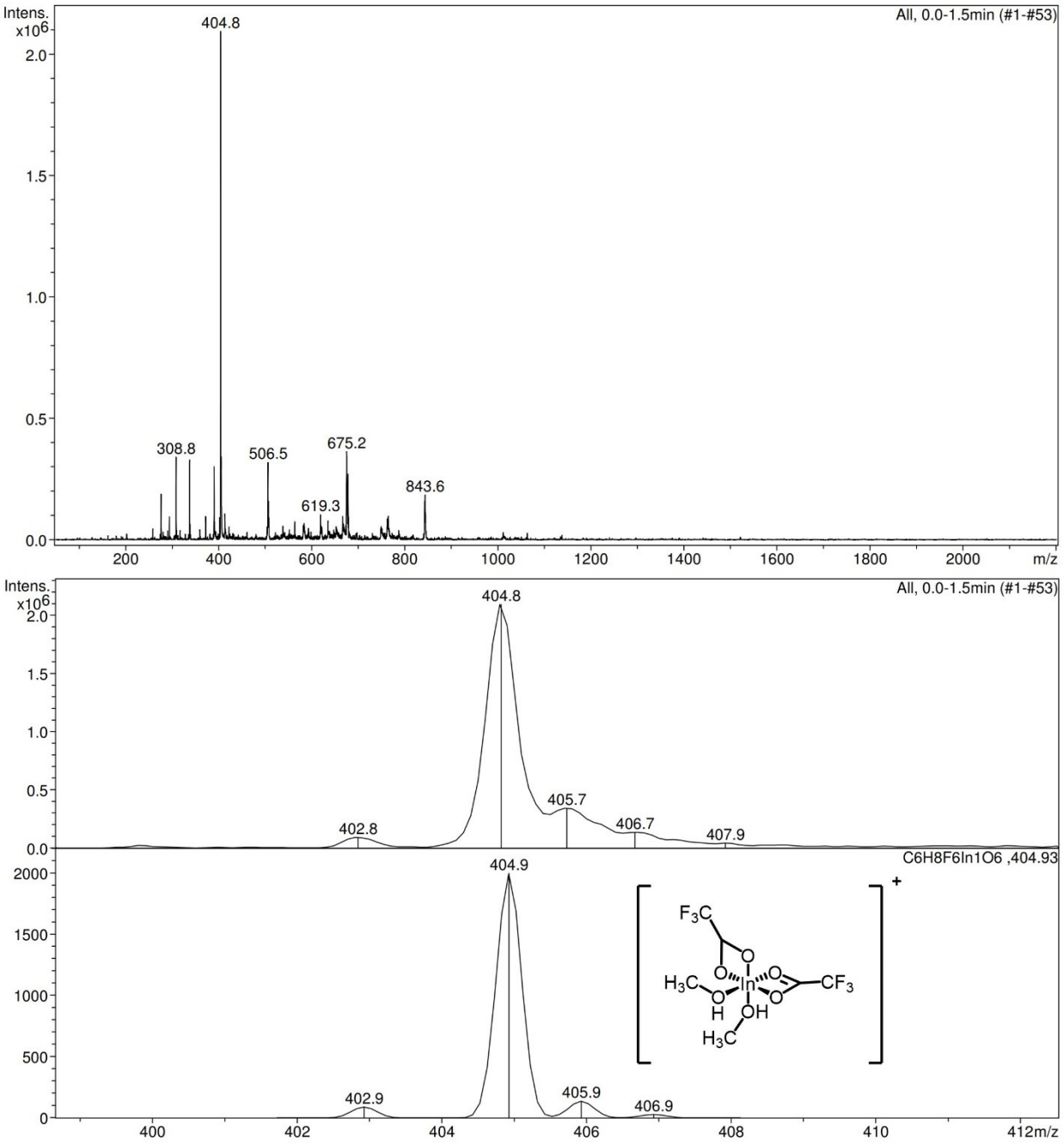


Figure S 4.1 Characterization of $In(TFA)_3$. **a)** ^{19}F NMR spectrum of $In(TFA)_3$ (470 MHz, toluene-d_8, DS 2, NS 40, D1 10 s). **b)** Negative mode mass spectrum of $In(TFA)_3$ in methanol, with the main fragment observed at 566.7 *m/z* matching the isotope pattern and molecular weight of the dimer $[[In(O_2CCF_3)_4]_2]^{2-}$, calculated for C16F24In2O16 at 566.8 *m/z*. **c)** Positive mode mass spectrum of $In(TFA)_3$ in methanol, with the main fragment at 404.8 *m/z* matching the isotope pattern and molecular weight of $[In(O_2CCF_3)_2[HOCH_3]_2]^+$, calculated for C6H8F6In1O6 at 404.9 *m/z*.

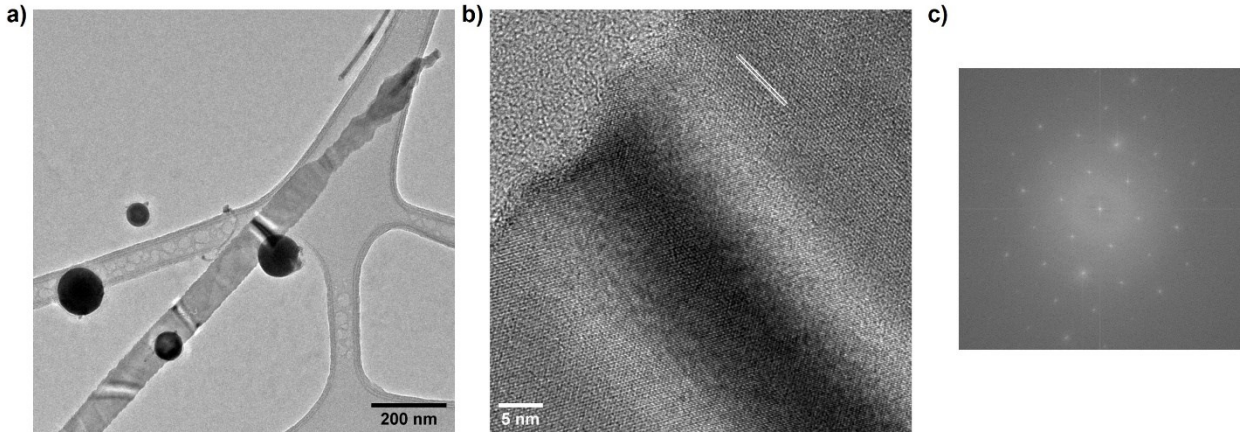


Figure S 4.2 TEM images of buckled nanoribbon **(a)** with a lower magnification image **(b)** showing a continuous InP zinc blende lattice and a stripe pattern from buckling of the nanoribbon. The white lines highlight the 111 plane with a d spacing of 0.34 nm. **c)** The FFT of (b) confirms that the lattice is single crystalline.

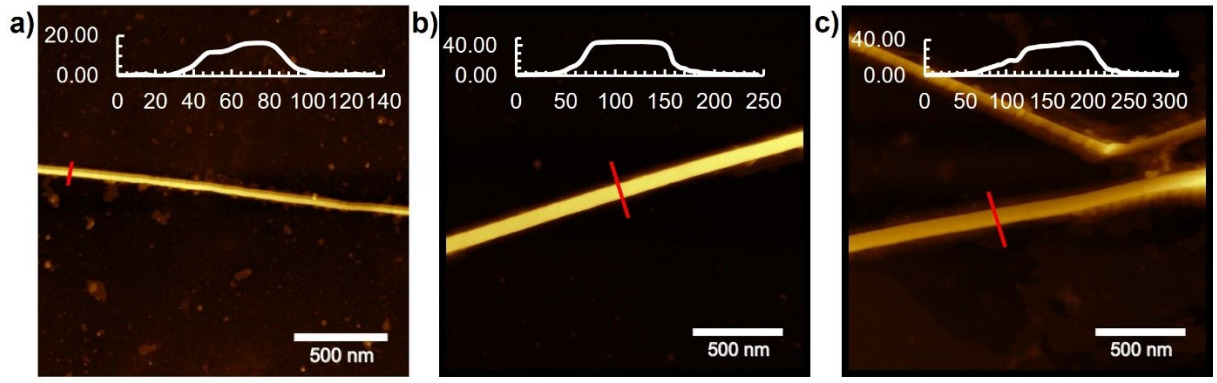


Figure S 4.3 Additional AFM of InP NWs with inset graphs of the height profiles (height (nm) vs width (nm)) along the red line.

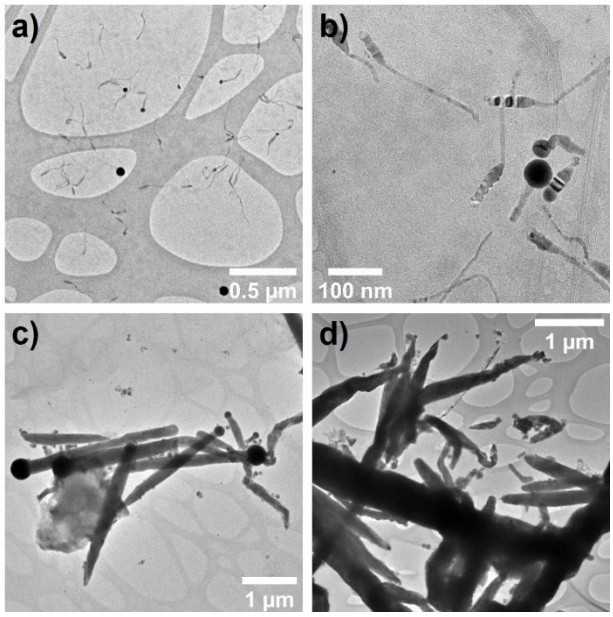


Figure S 4.4 TEM images of NWs made using pre-made indium nanoparticles, one that uses indium nanoparticles in addition to $In(TFA)_3$ **(a,b)**, and the second that uses only pre-made indium nanoparticles as an indium source **(c,d)**.

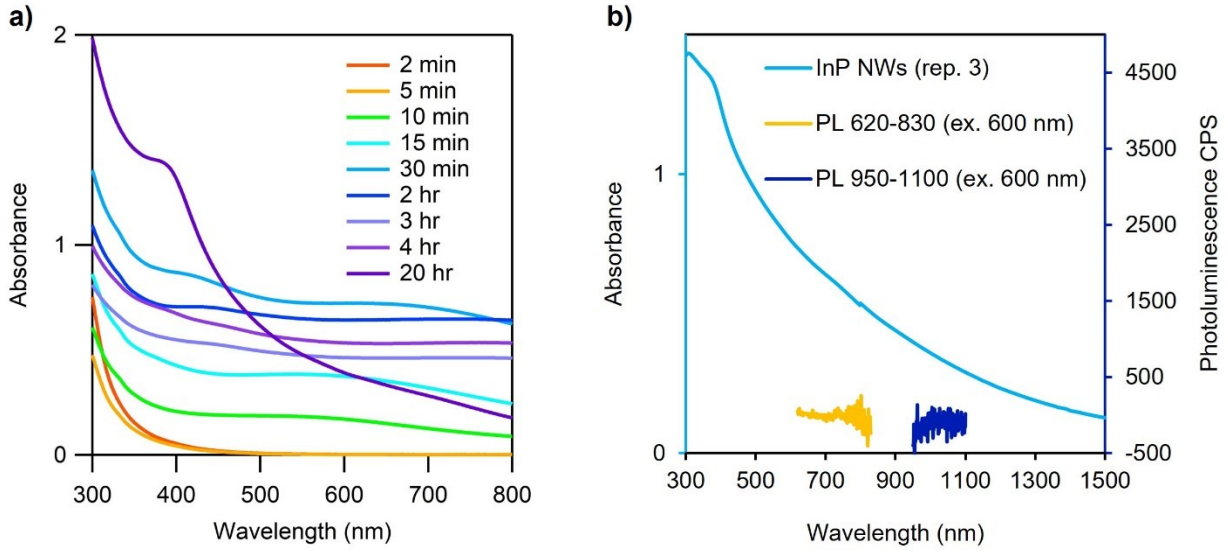


Figure S 4.5 Absorbance spectra over the course of a nanowire synthesis, and photoluminescence measurement. **a)** UV-vis absorbance spectra of aliquots taken over the course of the nanowire synthesis with 0 min at hot injection of the aminophosphine. **b)** UV-vis absorbance spectrum of purified InP nanowires from synthesis replicate 3 from 300 – 1500 nm, overlaid with photoluminescence spectra excited at 600 nm collected from 620 – 830 nm and 950 – 1100 nm. Collection between 830 and 950 is not feasible due to a detector crossover.

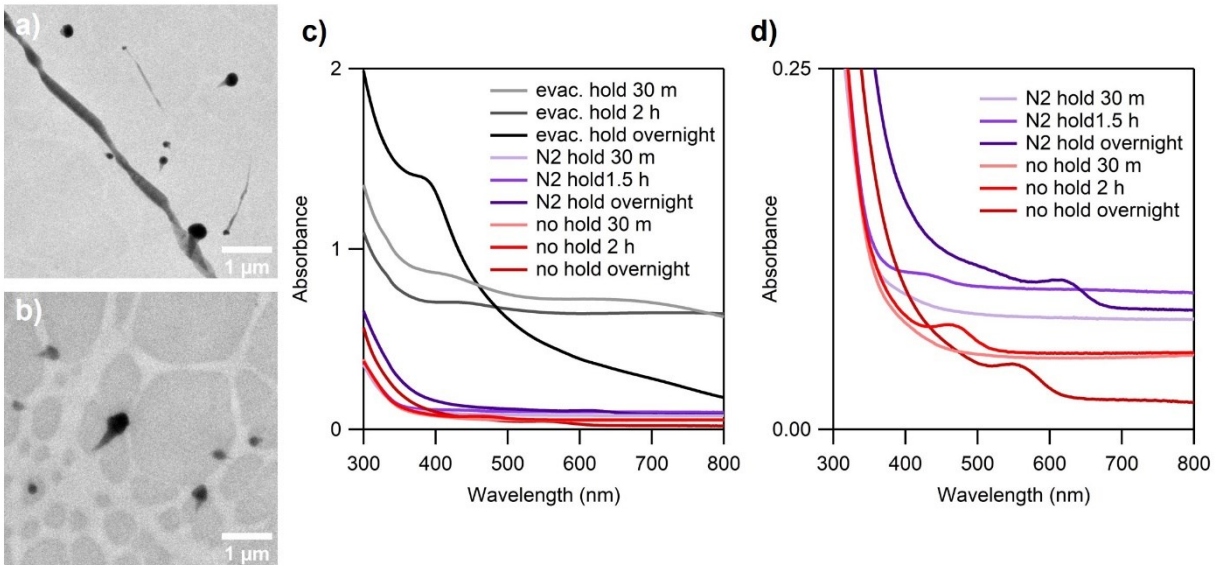
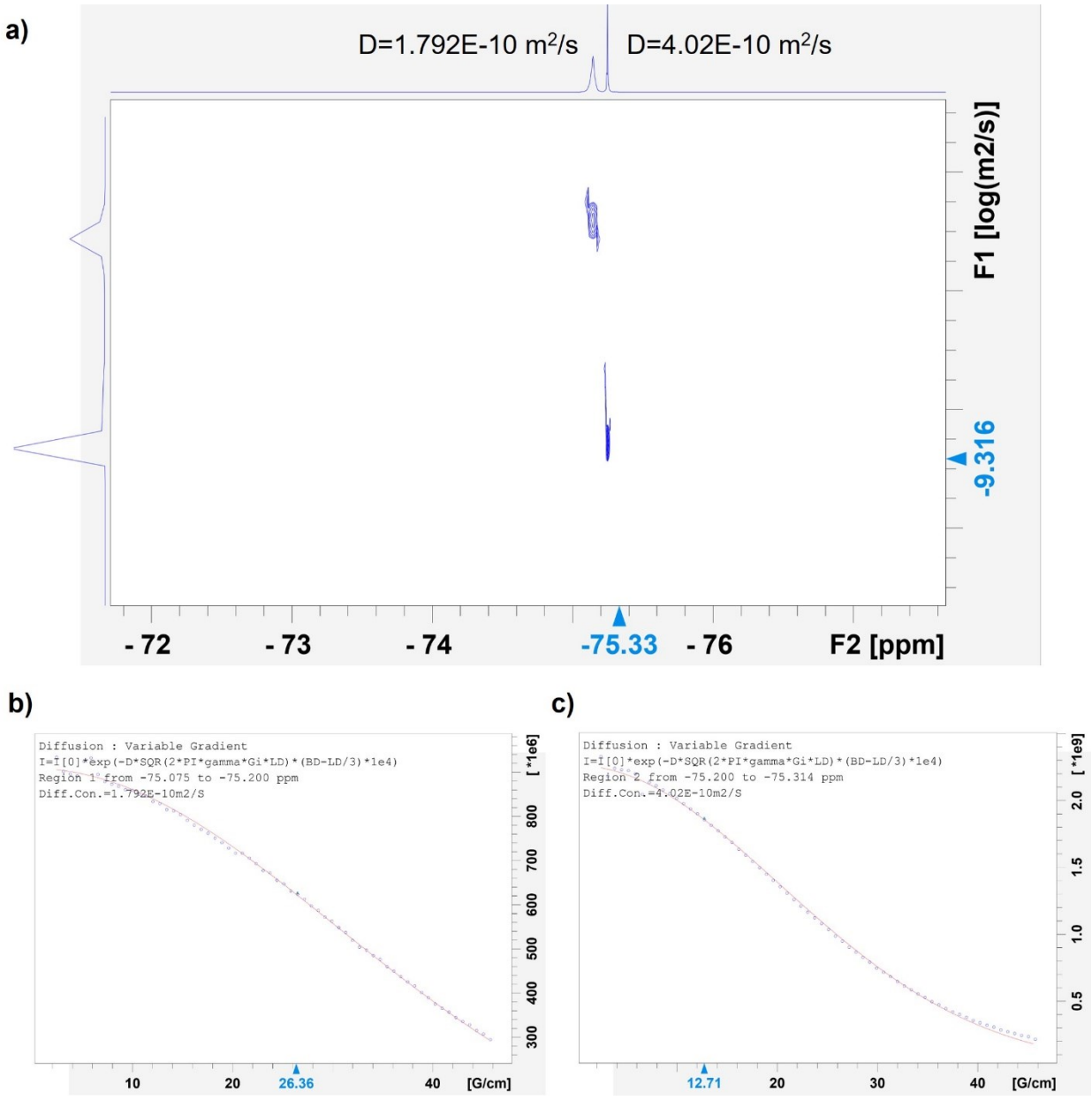


Figure S 4.6 TEM images and absorbance spectra of control syntheses varying the 120 °C evacuation step. TEM images of products from control syntheses with an hour long hold at 120 °C under nitrogen **(a)** and skipping the evacuation step at 120 °C **(b)**. **c)** UV-visible absorbance spectra comparing the standard NW synthesis conditions (with an hour long evacuation step at 120 °C) to the two control syntheses. **d)** UV-visible absorbance spectra of the two control syntheses showing growth of quantum dot product primarily and overall low semiconductor absorbance.


a)
D=1.792E-10 m²/s
D=4.02E-10 m²/s
F1 [log(m2/s)]
-9.316
- 72
- 73
- 74
-75.33
- 76
F2 [ppm]
b)
Diffusion : Variable Gradient
I=I[0]*exp(-D*SQR(2*PI*gamma*Gi*LD)*(BD-LD/3)*1e4)
Region 1 from -75.075 to -75.200 ppm
Diff.Con.=1.792E-10m2/S
[*1e6]
800
700
600
500
400
300
10
20
26.36
40
[G/cm]
c)
Diffusion : Variable Gradient
I=I[0]*exp(-D*SQR(2*PI*gamma*Gi*LD)*(BD-LD/3)*1e4)
Region 2 from -75.200 to -75.314 ppm
Diff.Con.=4.02E-10m2/S
[*1e9]
2.0
1.5
1.0
0.5
12.71
20
30
40
[G/cm]

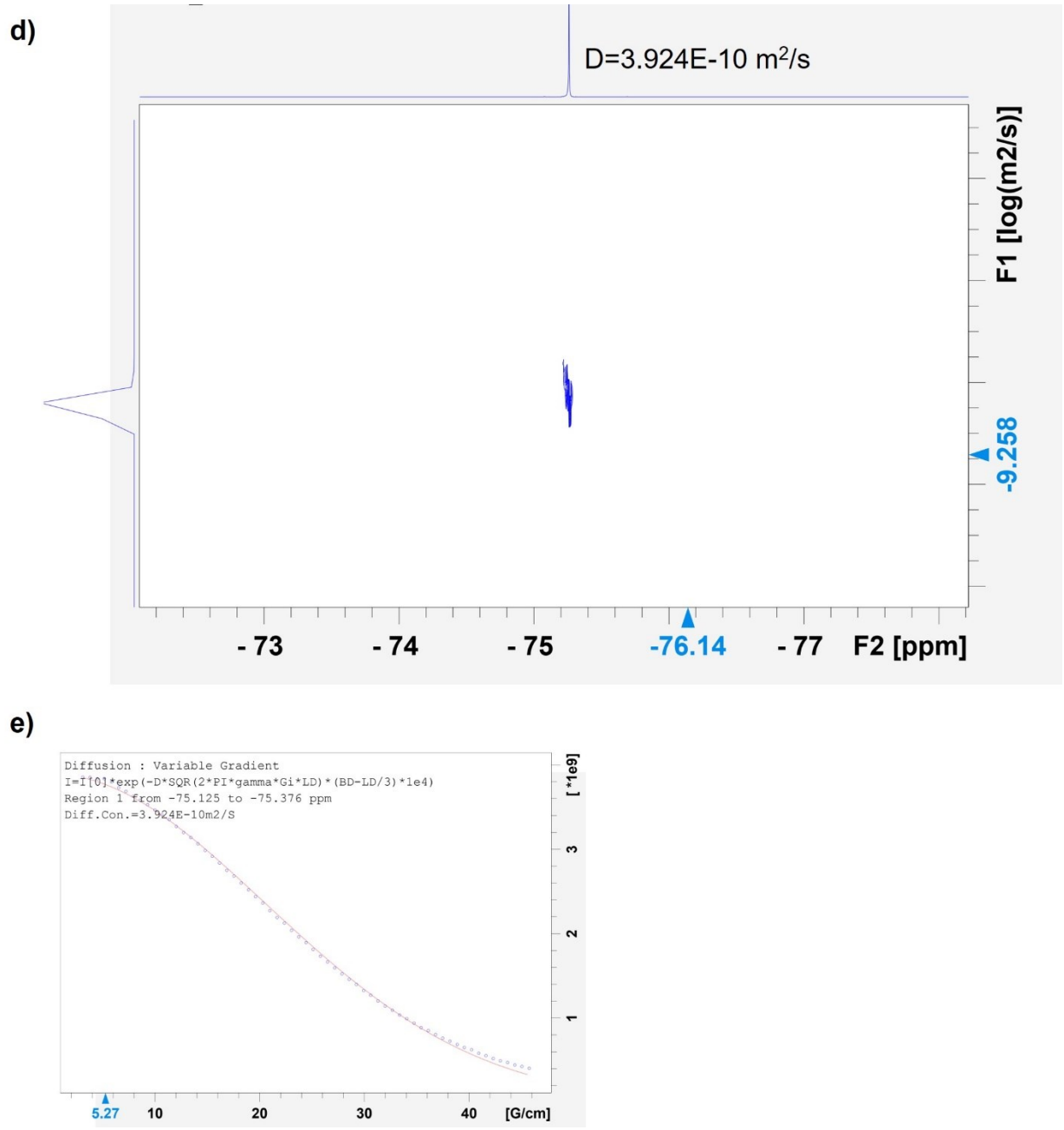


Figure S 4.7 ^{19}F Diffusion-Ordered Spectra for aliquots taken **a)** at the beginning of the evacuation step at 120 °C with fits to extract the diffusion coefficients **(b, c)** and **d)** after one hour of evacuation at 120 °C with a fit to extract the diffusion coefficient **(e)**. The two peaks before the evacuation step, one broader and with a lower diffusion coefficient than the other suggest that the indium-trifluoroacetate complex exists in two forms, one more soluble than the other. Then, after

the evacuation step is complete, only the sharper, higher diffusion coefficient peak remains implying that this step improves the solubility of the indium-trifluoroacetate complex.

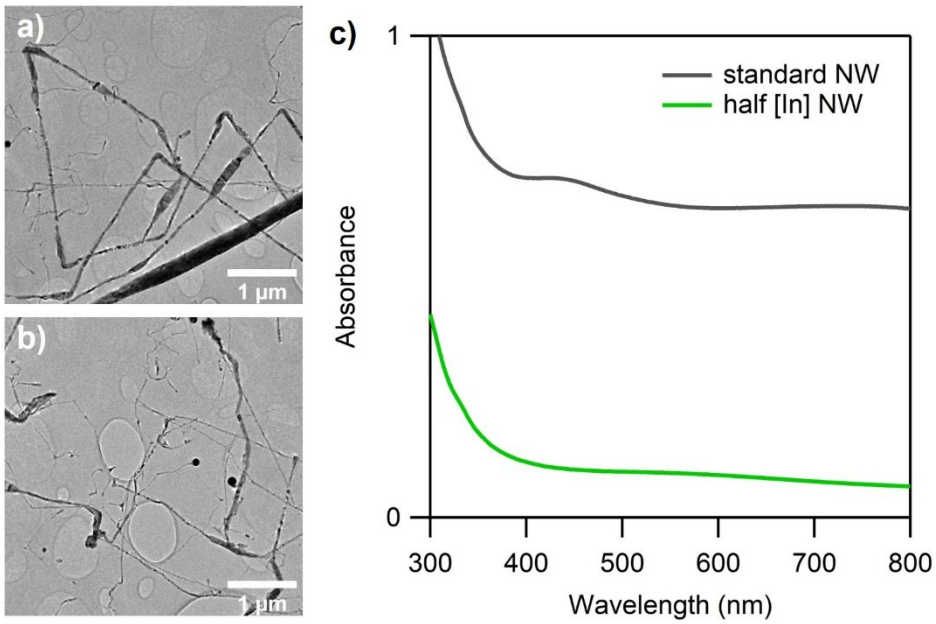


Figure S 4.8 TEM of diameter dispersity increases with lower precursor concentration ([In]=0.03 M). **a)**, **b)** TEM images showing large InP nanowires present as well as smaller expected nanowires, with overall average diameter measured as 37.1 ± 42.5 nm. **c)** UV-visible absorbance spectra comparing the standard nanowire synthesis (at 2 hr) to the lower precursor concentration condition (1 hr).

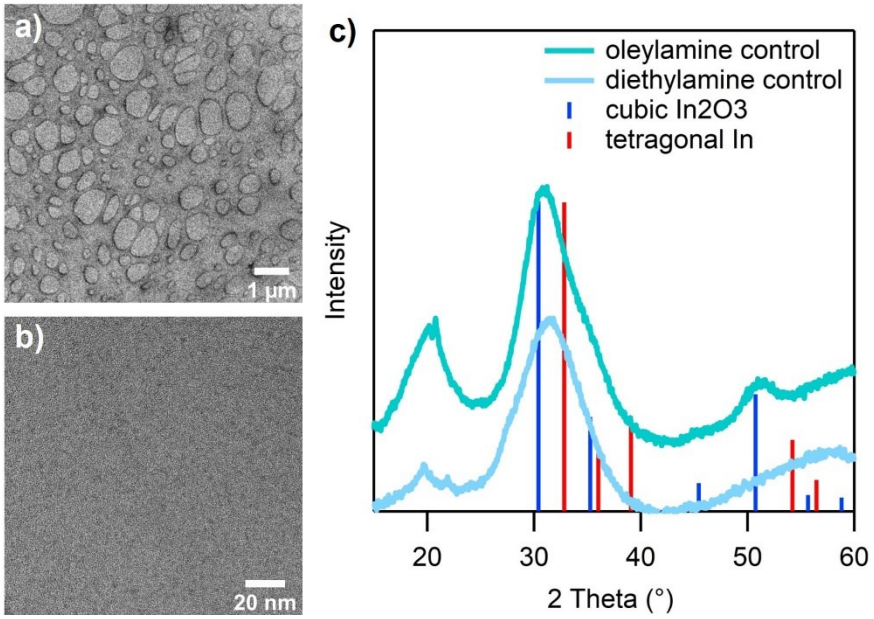


Figure S 4.9 TEM images and powder X-ray diffraction patterns of oleylamine and diethylamine control syntheses. Low **(a)** and high **(b)** magnification TEM images of $In(TFA)_3$ in oleylamine after a 1 hour hold under vacuum at 120 °C and heating to 180 °C. **c)** Powder XRD patterns of purified nanoparticles resulting from the reaction of $In(TFA)_3$ in oleylamine and the reaction of In(TFA)3 in diethylamine and oleylamine.

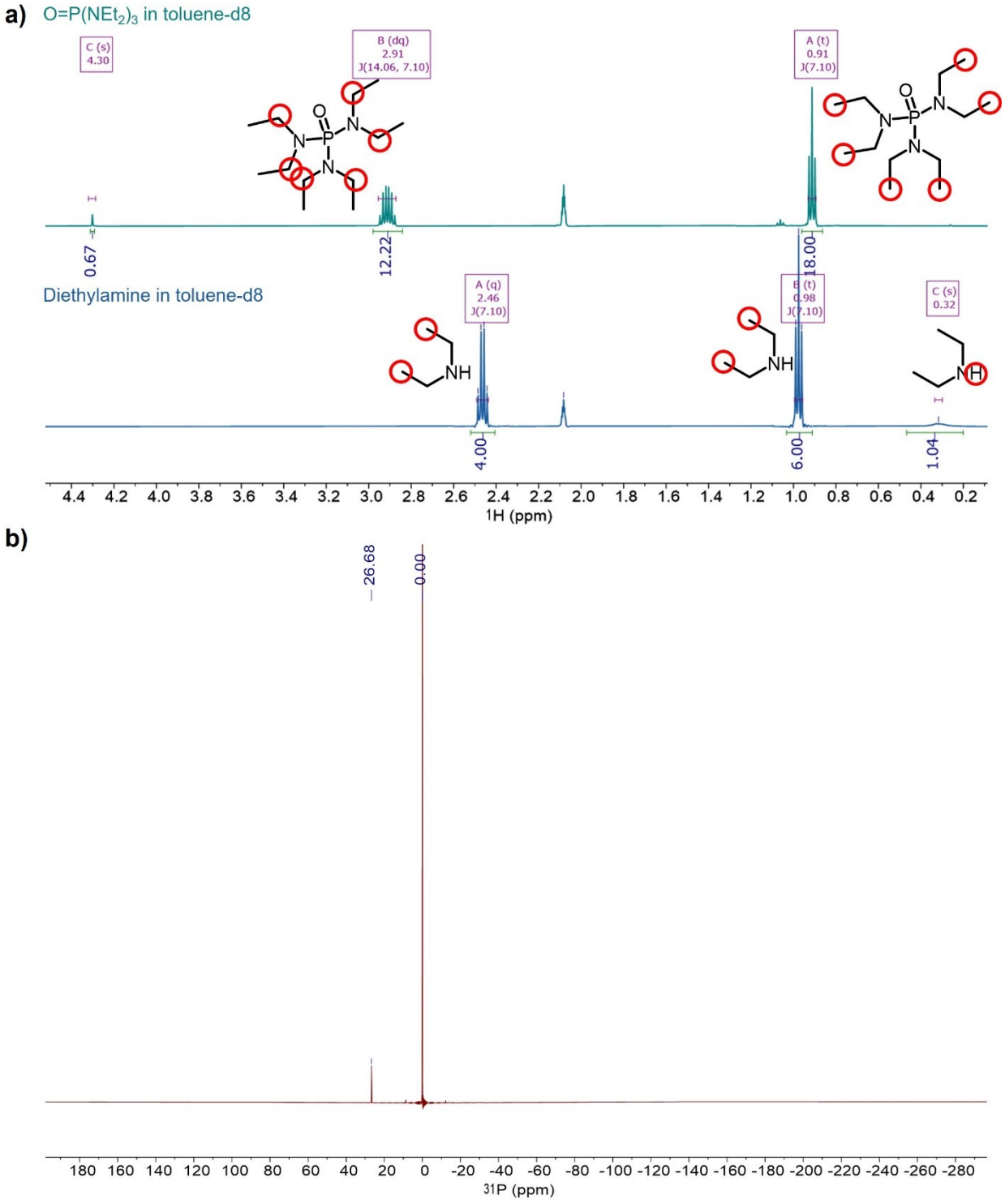


Figure S 4.10 Proton and phosphorus NMR spectra of $O=P(NEt_2)_3$. **a)** ^{1}H NMR spectra of purified $O=P(NEt_2)_3$ and diethylamine (500 MHz, toluene-d_8, DS 2, NS 10, D1 10 s). **b)** ^{31}P {H} NMR

spectrum of purified $O=P(NEt_2)_3$ with an 80 weight % H_3PO_4 standard capillary (202 MHz, toluene-d_8, DS 2, NS 40, D1 10 s). Tris(diethylamino)phosphine has a chemical shift at 118 ppm.[30] Tris(dimethylamino)phosphine oxide (also known as hexamethylphosphoramide) has a chemical shift at 20.6 ppm in $CDCl_3$.[51]

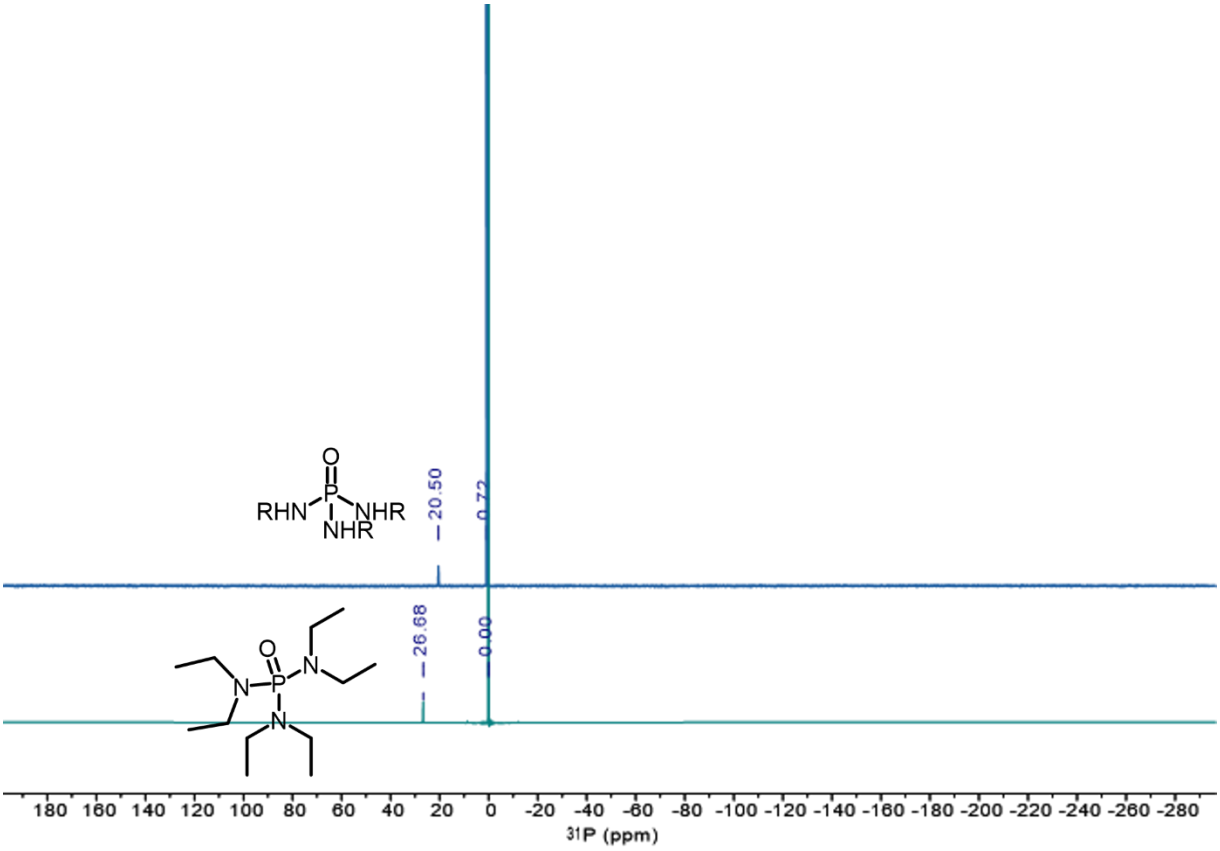


Figure S 4.11 ^{31}P NMR spectrum of transaminated $O=P(NHR)_3$ (dark blue) with an 2 weight % H_3PO_4 standard capillary which has a shift of 0.72 ppm vs an 80 weight % H_3PO_4 standard, compared to the ^{31}P NMR spectrum of purified $O=P(NEt_2)_3$ (lighter blue) with an 80 weight % H_3PO_4 standard capillary (202 MHz, toluene-d_8, DS 2, NS 40, D1 10 s). R= $C_{18}H_{35}$.

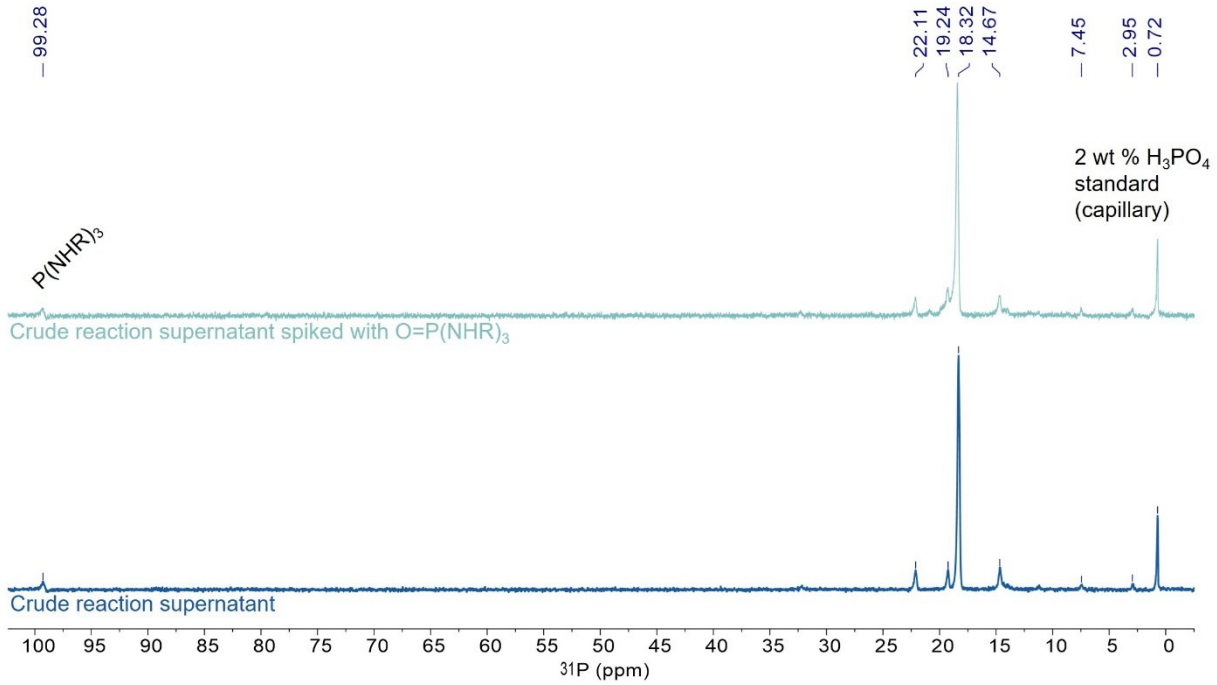


Figure S 4.12 Phosphorus NMR spectra of crude nanowire solution spiked with tris(oleylamine)phosphine oxide. ^{31}P NMR spectrum of the crude nanowire reaction solution compared with the ^{31}P NMR spectrum of the same sample spiked with separately synthesized tris(oleylamino)phosphine oxide. The spectra are referenced to the peak at 0.72 ppm which is a 2 wt % H_3PO_4 standard, added as a sealed capillary. (202 MHz, toluene-d_8, DS 2, NS 40, D1 10 s)

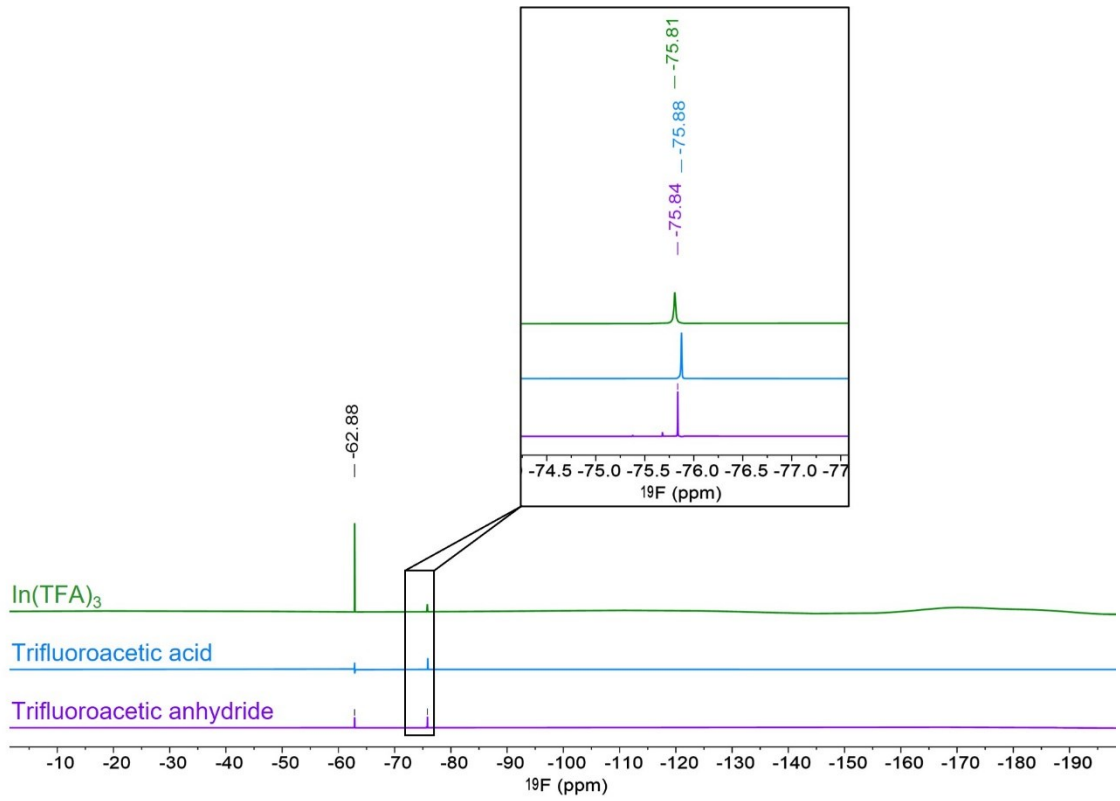


Figure S 4.13 ^{1}H NMR spectra of In(TFA)$_3$, trifluoroacetic acid, and trifluoroacetic anhydride in oleylamine. (470 MHz, toluene-d_8, DS 2, NS 40, D1 10 s)

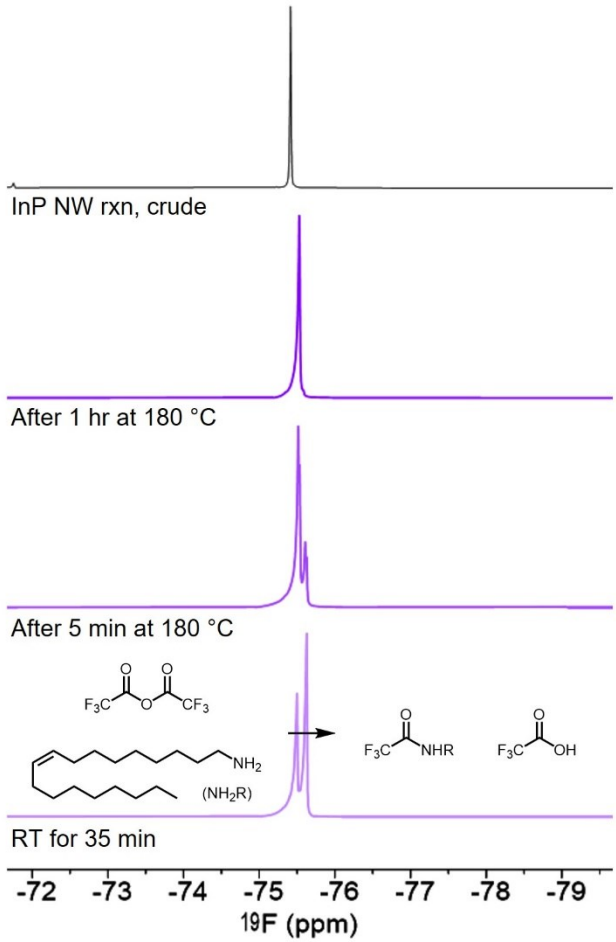


Figure S 4.14 ^{19}F NMR spectra of the crude nanowire reaction solution compared to aliquots of a control reaction between trifluoroacetic anhydride and oleylamine hypothesized to produce *N*-oleyltrifluoroacetamide. Trifluorotoluene was added as a reference. (470 MHz, toluene-d_8, DS 2, NS 40, D1 10 s)

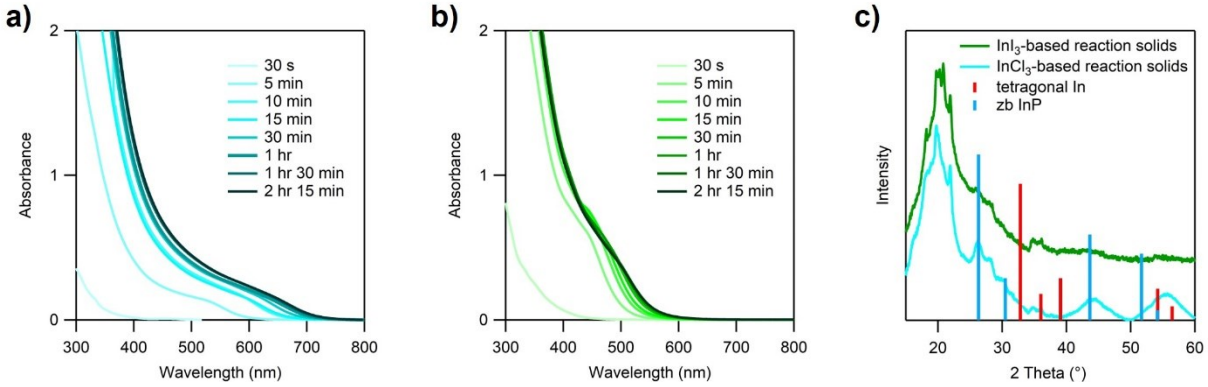


Figure S 4.15 UV-vis absorbance spectra of aliquots from control syntheses with $InCl_3$ and InI_3 (**a**, **b**, respectively). **c)** Powder X-ray diffraction patterns of the colloidally unstable fractions of both these controls to illustrate there are no InP nanowires or indium metal present.

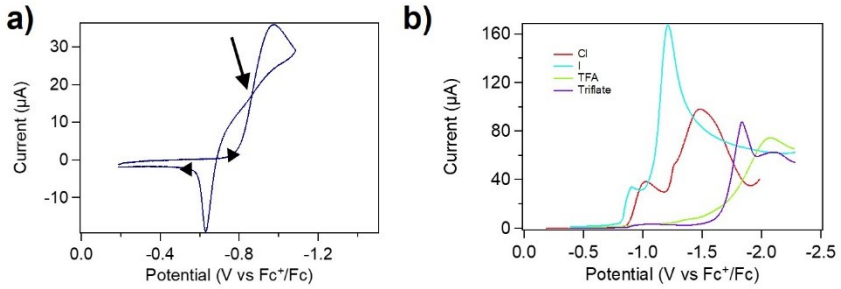


Figure S 4.16 Cyclic voltammetry data of indium salts. **a)** Cyclic voltammogram of $InCl_3$ with an arrow marking the inflection point of the indium nucleation loop reduction event. **b)** Cyclic voltammograms of the reduction events of the indium(III) salts of iodide, chloride, trifluoromethanesulfonate, and trifluoroacetate. Note how the reduction of the indium halide salts is more facile than the indium(III) trifluoromethanesulfonate or trifluoroacetate. (10 mL MeCN, 0.1 M $TBAPF_6$, glassy carbon WE, Pt wire CE, Ag pseudo reference electrode, in N_2 glovebox)

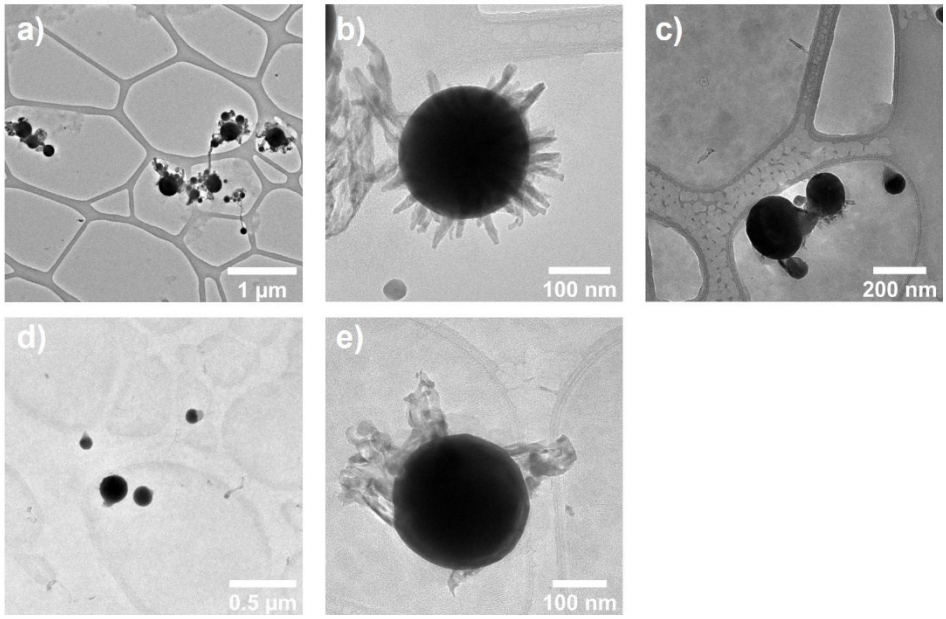


Figure S 4.17 TEM images of multipod products formed when **(a,b)** the $In(TFA)_3$ is not pure, **(c)** 0.1 equivalent of trifluoroacetic acid is added, and **(d,e)** the reaction is P starved.

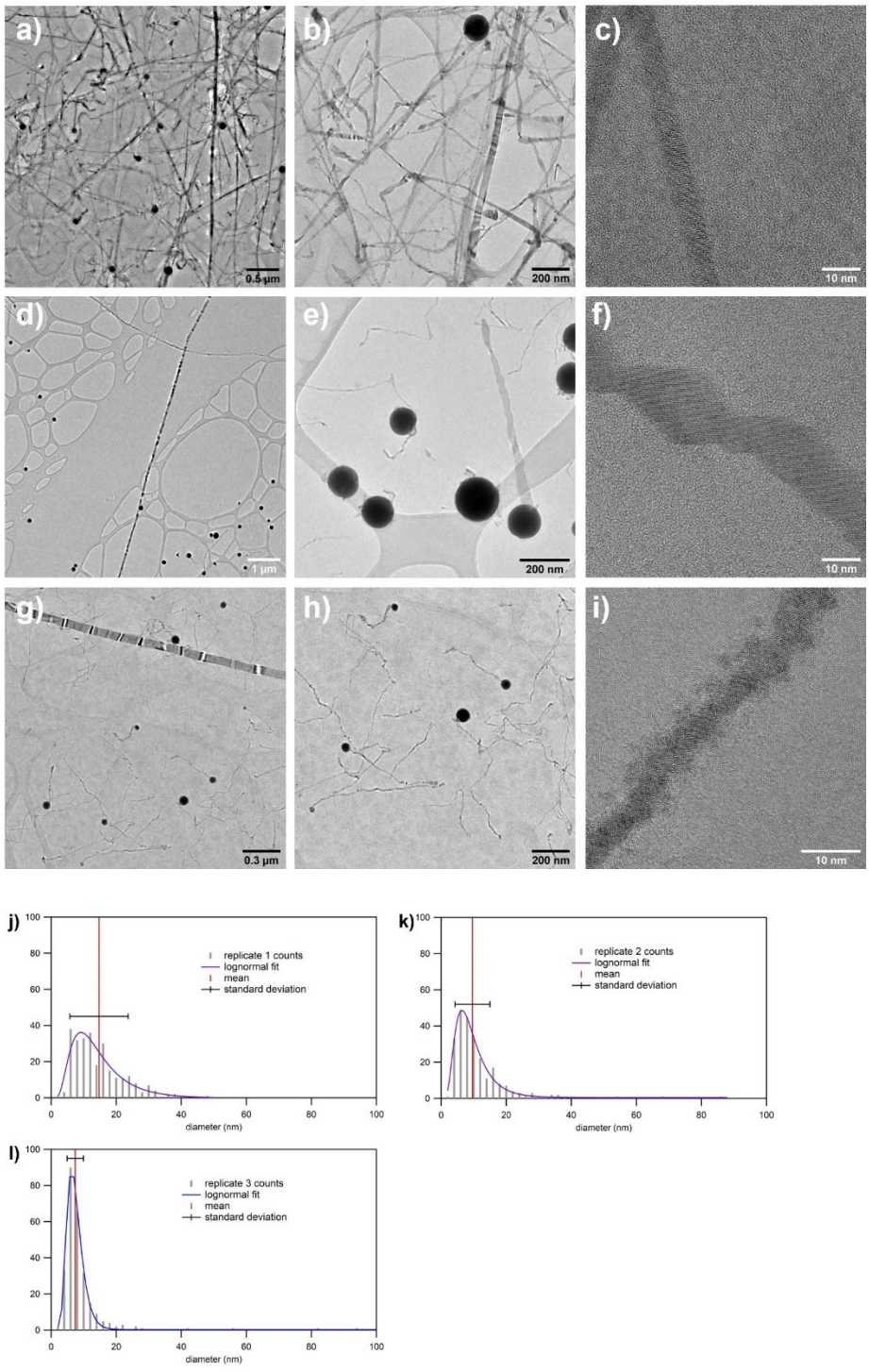


Figure S 4.18 Additional TEM images showing reproducibility over three replicate InP nanowire syntheses **(1:a-c, 2:d-f, and 3:g-i)**. The nanowire diameter distribution is described well with a lognormal distribution, giving mean diameters of **(j)** 14.7 ± 9.0, **(k)** 9.6 ± 5.4, and **(l)** 7.4 ± 2.5 nm.

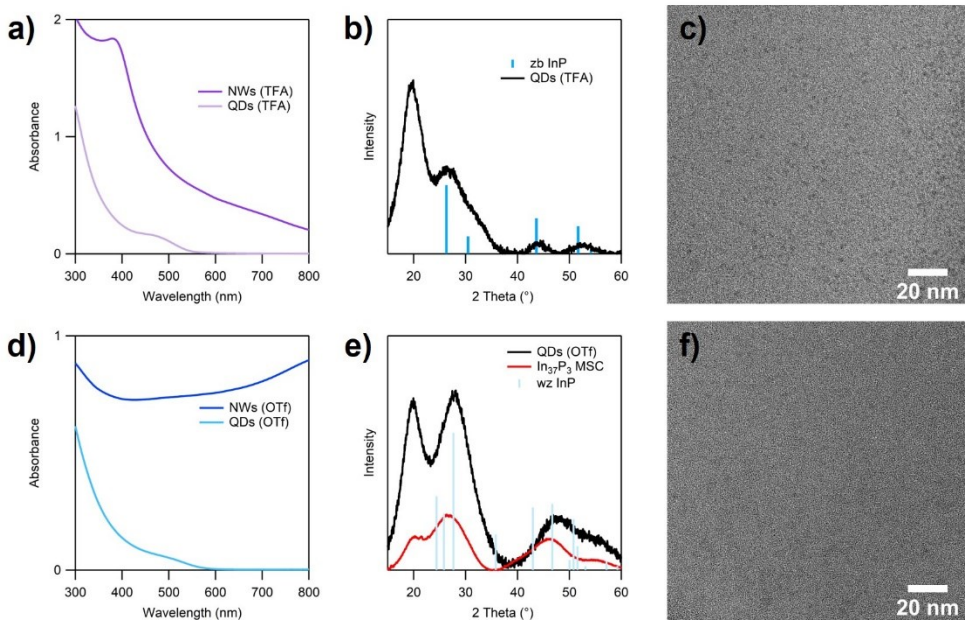


Figure S 4.19 Absorbance spectra, powder X-ray diffraction patterns, and TEM images of InP QDs made using $In(TFA)_3$ and $In(OTf)_3$. Characterization of InP QDs made using $In(TFA)_3$ including **(a)** UV-vis absorbance spectra deconvoluting the QD product from the NW product, **(b)** a pXRD pattern revealing zinc blende InP QDs with a crystallite size of 2.2 ± 0.9 nm, and **(c)** a TEM image of representative QDs. Characterization of InP QDs made using $In(OTf)_3$ including **(d)** UV-vis absorbance spectra deconvoluting the QD product from the NW product, **(e)** a pXRD pattern revealing small quasi-wurtzite InP QDs compared to the quasi-wurtzite $In_{37}P_{20}$ MSC pattern, and **(f)** a TEM image of representative QDs.

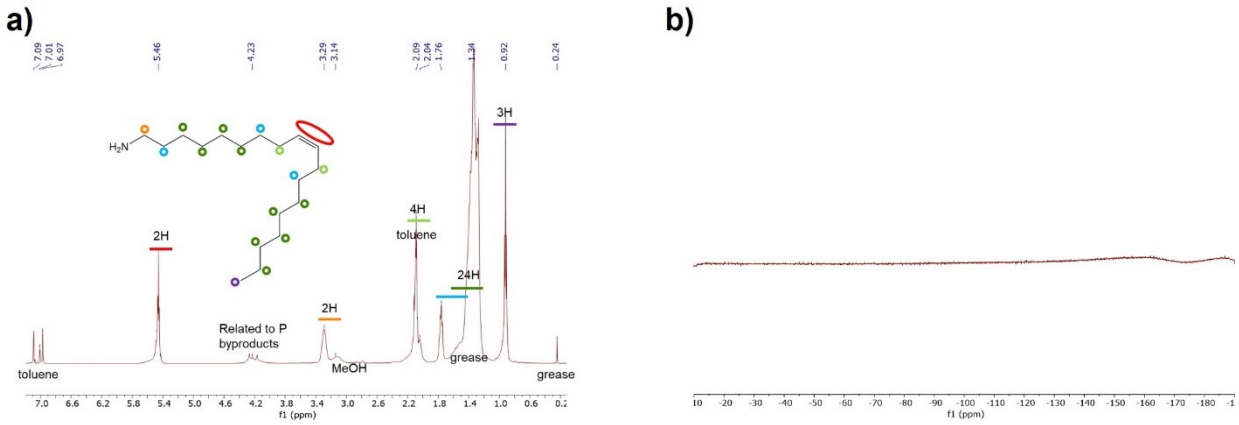


Figure S 4.20 Proton and fluorine NMR spectra of InP QDs made using $In(OTf)_3$. **a)** ^1H NMR spectrum of InP QDs made using $In(OTf)_3$ showing oleylamine both bound and free in the QD solution (500 MHz, toluene-d_8, DS 2, NS 10, D1 30 s). **b)** ^{19}F NMR spectrum of purified InP QDs made using $In(OTf)_3$ showing no triflate signal, suggesting there is no triflate found on the surface of the QDs after purification (470 MHz, toluene-d_8, DS 2, NS 40, D1 10 s).

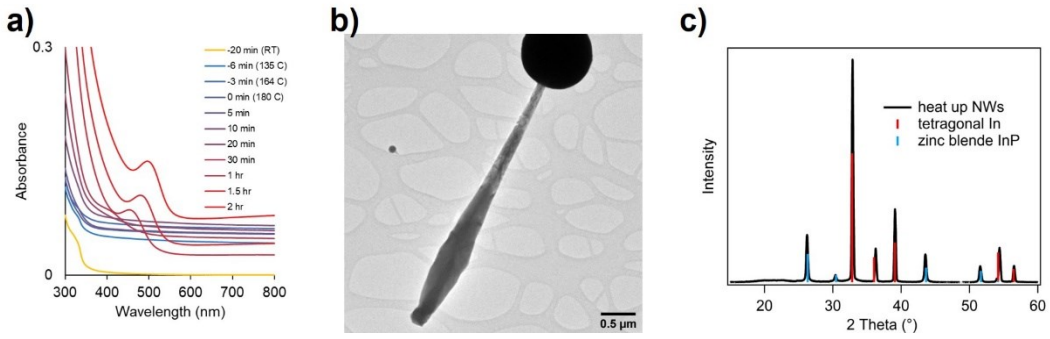


Figure S 4.21 Characterization from the heat-up nanowire synthesis from $In(TFA)_3$ and $P(NEt_2)_3$ including **a)** UV-vis absorbance spectra of aliquots throughout the reaction with 0 minutes when the reaction temperature was achieved; **b)** TEM image showing an InP nanowire with an indium particle attached; **c)** pXRD pattern of the reaction product revealing bulk-like zinc blende InP and tetragonal indium metal.

4.5 REFERENCES

(1) Yue, L.-Q.; Shi, Y.-L.; Sun, N.-F.; Qiang, S.; Qin, J.-K.; Zhen, L.; Xu, C.-Y. InP Low-Dimensional Nanomaterials for Electronic and Optoelectronic Device Applications: A Review. *Advanced Sensor Research* **2023**, *2* (10), 2200101. https://doi.org/10.1002/adsr.202200101.

(2) Zafar, F.; Iqbal, A. Indium Phosphide Nanowires and Their Applications in Optoelectronic Devices. *Proceedings of the Royal Society A: Mathematical, Physical and Engineering Sciences* **2016**, *472* (2187), 20150804. https://doi.org/10.1098/rspa.2015.0804.

(3) Mukherjee, C.; Deng, M.; Nodjiadjim, V.; Riet, M.; Mismer, C.; Guendouz, D.; Caillaud, C.; Bertin, H.; Vaissiere, N.; Luisier, M.; Wen, X.; De Matos, M.; Mounaix, P.; Maneux, C. Towards Monolithic Indium Phosphide (InP)-Based Electronic Photonic Technologies for beyond 5G Communication Systems. *Applied Sciences* **2021**, *11* (5), 2393. https://doi.org/10.3390/app11052393.

(4) Markman, B.; Schröter, M. Indium-Phosphide Transistors: A Review of Current State and Suitability for Commercial > 100-GHz Wireless Communication Systems. *IEEE Microwave Magazine* **2024**, *25* (10), 38–53. https://doi.org/10.1109/MMM.2024.3428191.

(5) Chee, A. K.-W. On Current Technology for Light Absorber Materials Used in Highly Efficient Industrial Solar Cells. *Renewable and Sustainable Energy Reviews* **2023**, *173*, 113027. https://doi.org/10.1016/j.rser.2022.113027.

(6) Mediavilla, I.; Pura, J. L.; Hinojosa, V. G.; Galiana, B.; Hrachowina, L.; Borgström, M. T.; Jimenez, J. Composition, Optical Resonances, and Doping of InP/InGaP Nanowires for Tandem Solar Cells: A Micro-Raman Analysis. *ACS Nano* **2024**, *18* (14), 10113–10123. https://doi.org/10.1021/acsnano.3c12973.

(7) Wang, F.; Buhro, W. E. Determination of the Rod−Wire Transition Length in Colloidal Indium Phosphide Quantum Rods. *J. Am. Chem. Soc.* **2007**, *129* (46), 14381–14387. https://doi.org/10.1021/ja075015c.

(8) Wang, J.; Gudiksen, M. S.; Duan, X.; Cui, Y.; Lieber, C. M. Highly Polarized Photoluminescence and Photodetection from Single Indium Phosphide Nanowires. *Science* **2001**, *293* (5534), 1455–1457. https://doi.org/10.1126/science.1062340.

(9) Bucci, G.; Zannier, V.; Rossi, F.; Musiał, A.; Boniecki, J.; Sęk, G.; Sorba, L. Zincblende InAsxP1–x/InP Quantum Dot Nanowires for Telecom Wavelength Emission. *ACS Appl. Mater. Interfaces* **2024**, *16* (20), 26491–26499. https://doi.org/10.1021/acsami.4c00615.

(10) Duan, X.; Huang, Y.; Cui, Y.; Wang, J.; Lieber, C. M. Indium Phosphide Nanowires as Building Blocks for Nanoscale Electronic and Optoelectronic Devices. *Nature* **2001**, *409* (6816), 66–69. https://doi.org/10.1038/35051047.

(11) Fang, M.; Han, N.; Wang, F.; Yang, Z.; Yip, S.; Dong, G.; Hou, J. J.; Chueh, Y.; Ho, J. C. III–V Nanowires: Synthesis, Property Manipulations, and Device Applications. *Journal of Nanomaterials* **2014**, *2014* (1), 702859. https://doi.org/10.1155/2014/702859.

(12) Wang, F.; Dong, A.; Buhro, W. E. Solution–Liquid–Solid Synthesis, Properties, and Applications of One-Dimensional Colloidal Semiconductor Nanorods and Nanowires. *Chem. Rev.* **2016**, *116* (18), 10888–10933. https://doi.org/10.1021/acs.chemrev.5b00701.

(13) Trentler, T. J.; Goel, S. C.; Hickman, K. M.; Viano, A. M.; Chiang, M. Y.; Beatty, A. M.; Gibbons, P. C.; Buhro, W. E. Solution−Liquid−Solid Growth of Indium Phosphide Fibers from Organometallic Precursors: Elucidation of Molecular and Nonmolecular Components

of the Pathway. *J. Am. Chem. Soc.* **1997**, *119* (9), 2172–2181. https://doi.org/10.1021/ja9640859.

(14) Trentler, T. J.; Hickman, K. M.; Goel, S. C.; Viano, A. M.; Gibbons, P. C.; Buhro, W. E. Solution-Liquid-Solid Growth of Crystalline III-V Semiconductors: An Analogy to Vapor-Liquid-Solid Growth. *Science* **1995**, *270* (5243), 1791–1794. https://doi.org/10.1126/science.270.5243.1791.

(15) Ahrenkiel, S. P.; Mićić, O. I.; Miedaner, A.; Curtis, C. J.; Nedeljković, J. M.; Nozik, A. J. Synthesis and Characterization of Colloidal InP Quantum Rods. *Nano Lett.* **2003**, *3* (6), 833–837. https://doi.org/10.1021/nl034152e.

(16) Yu, H.; Li, J.; Loomis, R. A.; Wang, L.-W.; Buhro, W. E. Two- versus Three-Dimensional Quantum Confinement in Indium Phosphide Wires and Dots. *Nature Mater* **2003**, *2* (8), 517–520. https://doi.org/10.1038/nmat942.

(17) Nedeljković, J. M.; Mićić, O. I.; Ahrenkiel, S. P.; Miedaner, A.; Nozik, A. J. Growth of InP Nanostructures via Reaction of Indium Droplets with Phosphide Ions: Synthesis of InP Quantum Rods and InP−TiO2 Composites. *J. Am. Chem. Soc.* **2004**, *126* (8), 2632–2639. https://doi.org/10.1021/ja039311a.

(18) Fanfair, D. D.; Korgel, B. A. Bismuth Nanocrystal-Seeded III-V Semiconductor Nanowire Synthesis. *Crystal Growth & Design* **2005**, *5* (5), 1971–1976. https://doi.org/10.1021/cg0502587.

(19) Kan, S.; Aharoni, A.; Mokari, T.; Banin, U. Shape Control of III–V Semiconductor Nanocrystals: Synthesis and Properties of InAs Quantum Rods. *Faraday Discuss.* **2003**, *125* (0), 23–38. https://doi.org/10.1039/B302898D.

(20) Shweky, I.; Aharoni, A.; Mokari, T.; Rothenberg, E.; Nadler, M.; Popov, I.; Banin, U. Seeded Growth of InP and InAs Quantum Rods Using Indium Acetate and Myristic Acid. *Materials Science and Engineering: C* **2006**, *26* (5), 788–794. https://doi.org/10.1016/j.msec.2005.09.040.

(21) Wang, F.; Yu, H.; Li, J.; Hang, Q.; Zemlyanov, D.; Gibbons, P. C.; Wang; Janes, D. B.; Buhro, W. E. Spectroscopic Properties of Colloidal Indium Phosphide Quantum Wires. *J. Am. Chem. Soc.* **2007**, *129* (46), 14327–14335. https://doi.org/10.1021/ja074049h.

(22) Banerjee, C.; L. Hughes, D.; Bochmann, M.; Nann, T. InP Nanowires from Surfactant - Free Thermolysis of Single Molecule Precursors. *Dalton Transactions* **2012**, *41* (24), 7244–7248. https://doi.org/10.1039/C2DT30283G.

(23) Liu, Z.; Sun, K.; Jian, W.-B.; Xu, D.; Lin, Y.-F.; Fang, J. Soluble InP and GaP Nanowires: Self-Seeded, Solution–Liquid–Solid Synthesis and Electrical Properties. *Chemistry – A European Journal* **2009**, *15* (18), 4546–4552. https://doi.org/10.1002/chem.200900190.

(24) Strupeit, T.; Klinke, C.; Kornowski, A.; Weller, H. Synthesis of InP Nanoneedles and Their Use as Schottky Devices. *ACS Nano* **2009**, *3* (3), 668–672. https://doi.org/10.1021/nn800846d.

(25) H. Lim, T.; Ravi, S.; W. Bumby, C.; G. Etchegoin, P.; D. Tilley, R. Synthesis, Characterization and Photoconductivity of Highly Crystalline InP Nanowires Prepared from Solid Hydrogen Phosphide. *Journal of Materials Chemistry* **2009**, *19* (27), 4852–4856. https://doi.org/10.1039/B902474C.

(26) Click, S. M.; Rosenthal, S. J. Synthesis, Surface Chemistry, and Fluorescent Properties of InP Quantum Dots. *Chem. Mater.* **2023**, *35* (3), 822–836. https://doi.org/10.1021/acs.chemmater.2c03074.

(27) Dümbgen, K. C.; Zito, J.; Infante, I.; Hens, Z. Shape, Electronic Structure, and Trap States in Indium Phosphide Quantum Dots. *Chem. Mater.* **2021**, *33* (17), 6885–6896. https://doi.org/10.1021/acs.chemmater.1c01795.
(28) Won, Y.-H.; Cho, O.; Kim, T.; Chung, D.-Y.; Kim, T.; Chung, H.; Jang, H.; Lee, J.; Kim, D.; Jang, E. Highly Efficient and Stable InP/ZnSe/ZnS Quantum Dot Light-Emitting Diodes. *Nature* **2019**, *575* (7784), 634–638. https://doi.org/10.1038/s41586-019-1771-5.
(29) Gary, D. C.; Terban, M. W.; Billinge, S. J. L.; Cossairt, B. M. Two-Step Nucleation and Growth of InP Quantum Dots via Magic-Sized Cluster Intermediates. *Chem. Mater.* **2015**, *27* (4), 1432–1441. https://doi.org/10.1021/acs.chemmater.5b00286.
(30) Tessier, M. D.; De Nolf, K.; Dupont, D.; Sinnaeve, D.; De Roo, J.; Hens, Z. Aminophosphines: A Double Role in the Synthesis of Colloidal Indium Phosphide Quantum Dots. *J. Am. Chem. Soc.* **2016**, *138* (18), 5923–5929. https://doi.org/10.1021/jacs.6b01254.
(31) Buffard, A.; Dreyfuss, S.; Nadal, B.; Heuclin, H.; Xu, X.; Patriarche, G.; Mézailles, N.; Dubertret, B. Mechanistic Insight and Optimization of InP Nanocrystals Synthesized with Aminophosphines. *Chem. Mater.* **2016**, *28* (16), 5925–5934. https://doi.org/10.1021/acs.chemmater.6b02456.
(32) Van Avermaet, H.; Schiettecatte, P.; Hinz, S.; Giordano, L.; Ferrari, F.; Nayral, C.; Delpech, F.; Maultzsch, J.; Lange, H.; Hens, Z. Full-Spectrum InP-Based Quantum Dots with Near-Unity Photoluminescence Quantum Efficiency. *ACS Nano* **2022**, *16* (6), 9701–9712. https://doi.org/10.1021/acsnano.2c03138.
(33) Kim, K.; Yoo, D.; Choi, H.; Tamang, S.; Ko, J.-H.; Kim, S.; Kim, Y.-H.; Jeong, S. Halide–Amine Co-Passivated Indium Phosphide Colloidal Quantum Dots in Tetrahedral Shape. *Angewandte Chemie* **2016**, *128* (11), 3778–3782. https://doi.org/10.1002/ange.201600289.
(34) McMurtry, B. M.; Qian, K.; Teglasi, J. K.; Swarnakar, A. K.; De Roo, J.; Owen, J. S. Continuous Nucleation and Size Dependent Growth Kinetics of Indium Phosphide Nanocrystals. *Chem. Mater.* **2020**, *32* (10), 4358–4368. https://doi.org/10.1021/acs.chemmater.0c01561.
(35) Valleix, R.; Cisnetti, F.; Okuno, H.; Boutinaud, P.; Chadeyron, G.; Boyer, D. Size-Controlled Indium Phosphide Quantum Dots for Bright and Tunable Light Emission by Simple Hindered Diamine Addition. *ACS Appl. Nano Mater.* **2021**, *4* (10), 11105–11114. https://doi.org/10.1021/acsanm.1c02577.
(36) Larson, H.; Cossairt, B. M. Indium–Poly(Carboxylic Acid) Ligand Interactions Modify InP Quantum Dot Nucleation and Growth. *Chem. Mater.* **2023**, *35* (15), 6152–6160. https://doi.org/10.1021/acs.chemmater.3c01309.
(37) Dorn, A.; Allen, P. M.; Bawendi, M. G. Electrically Controlling and Monitoring InP Nanowire Growth from Solution. *ACS Nano* **2009**, *3* (10), 3260–3265. https://doi.org/10.1021/nn900820h.
(38) Sartori, P.; Fazekas, J.; Schnackers, J. Wasserfreie trifluoracetate der hauptgruppe III. *Journal of Fluorine Chemistry* **1972**, *1* (4), 463–471. https://doi.org/10.1016/S0022-1139(00)82967-X.
(39) Massasa, E. H.; Strassberg, R.; Vurgaft, A.; Kauffmann, Y.; Cohen, N.; Bekenstein, Y. Thin Layer Buckling in Perovskite CsPbBr3 Nanobelts. *Nano Lett.* **2021**, *21* (13), 5564–5571. https://doi.org/10.1021/acs.nanolett.1c00962.

(40) Wang, F.; Buhro, W. E. Surfactant-Mediated Solution-Liquid–Solid (SLS) Growth of Phase-Pure Wurtzite CdS Quantum Wires. *Chem. Mater.* **2024**, *36* (20), 10307–10318. https://doi.org/10.1021/acs.chemmater.4c02283.
(41) Geng, X.; Liu, H.; Zhai, L.; Xiong, Z.; Hu, J.; Zou, C.; Dong, Y.; Yang, Y.; Huang, S. Colloidal Synthesis of CuGaS*x*Se2−*x* Nanoribbons Mediated by Cu1.75(SSe) Nanocrystals as Catalysts. *Journal of Alloys and Compounds* **2014**, *617*, 961–967. https://doi.org/10.1016/j.jallcom.2014.08.084.
(42) Singh, S.; Tomar, R.; ten Brinck, S.; De Roo, J.; Geiregat, P.; Martins, J. C.; Infante, I.; Hens, Z. Colloidal CdSe Nanoplatelets, A Model for Surface Chemistry/Optoelectronic Property Relations in Semiconductor Nanocrystals. *J. Am. Chem. Soc.* **2018**, *140* (41), 13292–13300. https://doi.org/10.1021/jacs.8b07566.
(43) Ithurria, S.; Tessier, M. D.; Mahler, B.; Lobo, R. P. S. M.; Dubertret, B.; Efros, A. L. Colloidal Nanoplatelets with Two-Dimensional Electronic Structure. *Nature Mater* **2011**, *10* (12), 936–941. https://doi.org/10.1038/nmat3145.
(44) van der Bok, J. C.; Prins, P. T.; Montanarella, F.; Maaskant, D. N.; Brzesowsky, F. A.; van der Sluijs, M. M.; Salzmann, B. B. V.; Rabouw, F. T.; Petukhov, A. V.; De Mello Donega, C.; Vanmaekelbergh, D.; Meijerink, A. In Situ Optical and X-Ray Spectroscopy Reveals Evolution toward Mature CdSe Nanoplatelets by Synergetic Action of Myristate and Acetate Ligands. *J. Am. Chem. Soc.* **2022**, *144* (18), 8096–8105. https://doi.org/10.1021/jacs.2c00423.
(45) Li, Z.; Peng, X. Size/Shape-Controlled Synthesis of Colloidal CdSe Quantum Disks: Ligand and Temperature Effects. *J. Am. Chem. Soc.* **2011**, *133* (17), 6578–6586. https://doi.org/10.1021/ja108145c.
(46) Chou, N. H.; Ke, X.; Schiffer, P.; Schaak, R. E. Room-Temperature Chemical Synthesis of Shape-Controlled Indium Nanoparticles. *J. Am. Chem. Soc.* **2008**, *130* (26), 8140–8141. https://doi.org/10.1021/ja801949c.
(47) Liu, Q.; Lu, W.; Ma, A.; Tang, J.; Lin, J.; Fang, J. Study of Quasi-Monodisperse In2O3 Nanocrystals: Synthesis and Optical Determination. *J. Am. Chem. Soc.* **2005**, *127* (15), 5276–5277. https://doi.org/10.1021/ja042550t.
(48) Nam, K. M.; Shim, J. H.; Ki, H.; Choi, S.-I.; Lee, G.; Jang, J. K.; Jo, Y.; Jung, M.-H.; Song, H.; Park, J. T. Single-Crystalline Hollow Face-Centered-Cubic Cobalt Nanoparticles from Solid Face-Centered-Cubic Cobalt Oxide Nanoparticles. *Angewandte Chemie International Edition* **2008**, *47* (49), 9504–9508. https://doi.org/10.1002/anie.200803048.
(49) Mourdikoudis, S.; Liz-Marzán, L. M. Oleylamine in Nanoparticle Synthesis. *Chem. Mater.* **2013**, *25* (9), 1465–1476. https://doi.org/10.1021/cm4000476.
(50) A. Airo, M.; Gqoba, S.; Otieno, F.; J. Moloto, M.; Moloto, N. Structural Modification and Band-Gap Crossover in Indium Selenide Nanosheets. *RSC Advances* **2016**, *6* (47), 40777–40784. https://doi.org/10.1039/C6RA00262E.
(51) B. Pavankumar, B.; Veerashekhar Goud, E.; Selvakumar, R.; Ashok Kumar, S. K.; Sivaramakrishna, A.; Vijayakrishna, K.; Brahmananda Rao, C. V. S.; N. Sabharwal, K.; C. Jha, P. Function of Substituents in Coordination Behaviour, Thermolysis and Ligand Crossover Reactions of Phosphine Oxides. *RSC Advances* **2015**, *5* (7), 4727–4736. https://doi.org/10.1039/C4RA13645D.
(52) Dümbgen, K. C.; Leemans, J.; De Roo, V.; Minjauw, M.; Detavernier, C.; Hens, Z. Surface Chemistry of InP Quantum Dots, Amine–Halide Co-Passivation, and Binding of Z-

Type Ligands. *Chem. Mater.* **2023**, *35* (3), 1037–1046. https://doi.org/10.1021/acs.chemmater.2c02960.
(53) Rachkov, A. G.; Schimpf, A. M. Colloidal Synthesis of Tunable Copper Phosphide Nanocrystals. *Chem. Mater.* **2021**, *33* (4), 1394–1406. https://doi.org/10.1021/acs.chemmater.0c04460.
(54) Bourne, E. J.; Henry, S. H.; Tatlow, C. E. M.; Tatlow, J. C. 767. Studies of Trifluoroacetic Acid. Part VI. Trifluoroacetyl Derivatives of Amines. *J. Chem. Soc.* **1952**, 4014–4019. https://doi.org/10.1039/JR9520004014.
(55) Hu, M.; Wang, Y.; Chen, Z.; Ning, S.; Wei, Y. Study of Indium Electrodeposition and Nucleation Mechanism in Acidic Solution Using EQCM. *Electrochimica Acta* **2023**, *443*, 141963. https://doi.org/10.1016/j.electacta.2023.141963.
(56) Karan, N. S.; Chen, Y.; Liu, Z.; Beaulac, R. Solution–Liquid–Solid Approach to Colloidal Indium Nitride Nanoparticles from Simple Alkylamide Precursors. *Chem. Mater.* **2016**, *28* (16), 5601–5605. https://doi.org/10.1021/acs.chemmater.6b02417.
(57) Kim, M.-S.; Sung, Y.-M. Successive Solution–Liquid–Solid (SLS) Growth of Heterogeneous Nanowires. *Chem. Mater.* **2013**, *25* (21), 4156–4164. https://doi.org/10.1021/cm4015018.
(58) Kapuria, N.; Imtiaz, S.; Sankaran, A.; Geaney, H.; Kennedy, T.; Singh, S.; Ryan, K. M. Multipod Bi(Cu2-xS)n Nanocrystals Formed by Dynamic Cation–Ligand Complexation and Their Use as Anodes for Potassium-Ion Batteries. *Nano Lett.* **2022**, *22* (24), 10120–10127. https://doi.org/10.1021/acs.nanolett.2c03933.
(59) Jia, G.; Du, J. Foreign Metal Ions to Control the Morphology of Solution−Liquid−Solid Reaction. *Crystal Growth & Design* **2018**, *18* (12), 7489–7495. https://doi.org/10.1021/acs.cgd.8b01289.
(60) Yong, K.-T.; Sahoo, Y.; Swihart, M. T.; Prasad, P. N. Growth of CdSe Quantum Rods and Multipods Seeded by Noble-Metal Nanoparticles. *Advanced Materials* **2006**, *18* (15), 1978–1982. https://doi.org/10.1002/adma.200600368.
(61) Wang, F.; Buhro, W. E. Crystal-Phase Control by Solution–Solid–Solid Growth of II–VI Quantum Wires. *Nano Lett.* **2016**, *16* (2), 889–894. https://doi.org/10.1021/acs.nanolett.5b03628.
(62) Zhang, M.; Efremov, M. Yu.; Schiettekatte, F.; Olson, E. A.; Kwan, A. T.; Lai, S. L.; Wisleder, T.; Greene, J. E.; Allen, L. H. Size-Dependent Melting Point Depression of Nanostructures: Nanocalorimetric Measurements. *Phys. Rev. B* **2000**, *62* (15), 10548–10557. https://doi.org/10.1103/PhysRevB.62.10548.
(63) Dixon, N. E.; Lawrance, G. A.; Lay, P. A.; Sargeson, A. M.; Taube, H. Trifluoromethanesulfonates and Trifluoromethanesulfonato-O Complexes. In *Inorganic Syntheses*; John Wiley & Sons, Ltd, 1990; pp 70–76. https://doi.org/10.1002/9780470132593.ch16.
(64) Tessier, M. D.; Dupont, D.; De Nolf, K.; De Roo, J.; Hens, Z. Economic and Size-Tunable Synthesis of InP/ZnE (E = S, Se) Colloidal Quantum Dots. *Chem. Mater.* **2015**, *27* (13), 4893–4898. https://doi.org/10.1021/acs.chemmater.5b02138.
(65) Ritchhart, A.; Cossairt, B. M. Templated Growth of InP Nanocrystals with a Polytwistane Structure. *Angewandte Chemie International Edition* **2018**, *57* (7), 1908–1912. https://doi.org/10.1002/anie.201711539.
(66) Research, S. *Indium Phosphide Wafer Market Size And Share Report, 2032*. https://straitsresearch.com/report/indium-phosphide-wafer-market (accessed 2024-11-11).

(67) Liu, J.; Nie, H.; Yan, B.; Yang, K.; Yang, H.; Khayrudinov, V.; Lipsanen, H.; Zhang, B.; He, J. Nonlinear Optical Absorption Properties of InP Nanowires and Applications as a Saturable Absorber. *Photon. Res., PRJ* **2020**, *8* (6), 1035–1041. https://doi.org/10.1364/PRJ.389669.
(68) *Targeting telecoms with nanowires - News*. Compound Semiconductor. https://compoundsemiconductor.net/article-gen/112937 (accessed 2024-11-11).
(69) Pangborn, A. B.; Giardello, M. A.; Grubbs, R. H.; Rosen, R. K.; Timmers, F. J. Safe and Convenient Procedure for Solvent Purification. *Organometallics* **1996**, *15* (5), 1518–1520. https://doi.org/10.1021/om9503712.
(70) Dreyfuss, S.; Pradel, C.; Vendier, L.; Mallet-Ladeira, S.; Mézailles, N. The Role of Water in the Synthesis of Indium Nanoparticles. *Chem. Commun.* **2016**, *52* (99), 14250–14253. https://doi.org/10.1039/C6CC08049A.
(71) Lim, T. H.; Ingham, B.; Kamarudin, K. H.; Etchegoin, P. G.; Tilley, R. D. Solution Synthesis of Monodisperse Indium Nanoparticles and Highly Faceted Indium Polyhedra. *Crystal Growth & Design* **2010**, *10* (9), 3854–3858. https://doi.org/10.1021/cg100857y.
(72) Wang, F.; Buhro, W. E. Role of Precursor-Conversion Chemistry in the Crystal-Phase Control of Catalytically Grown Colloidal Semiconductor Quantum Wires. *ACS Nano* **2017**, *11* (12), 12526–12535. https://doi.org/10.1021/acsnano.7b06639.
(73) Dümbgen, K. C.; Leemans, J.; De Roo, V.; Minjauw, M.; Detavernier, C.; Hens, Z. Surface Chemistry of InP Quantum Dots, Amine–Halide Co-Passivation, and Binding of Z-Type Ligands. *Chem. Mater.* **2023**. https://doi.org/10.1021/acs.chemmater.2c02960.
(74) Rosenau, C. P.; Jelier, B. J.; Gossert, A. D.; Togni, A. Exposing the Origins of Irreproducibility in Fluorine NMR Spectroscopy. *Angewandte Chemie International Edition* **2018**, *57* (30), 9528–9533. https://doi.org/10.1002/anie.201802620.

APPENDIX A: COLLABORATIVE EFFORTS

Transmission electron microscopy (TEM) offers unparalleled information for nanomaterial characterization. It is incredible to be able to obtain images that visualize products of a synthesis. This is not a luxury afforded to synthetic chemists making small organometallic or organic molecules. On top of morphological information gained by measuring the shape of nanoparticles and assemblies, the electron microscope can also illuminate information about nanocrystalline structure by resolving the stacks of atoms in a crystal. Fast Fourier transforms of an image with resolved lattice planes precisely determines the spacing between nanocrystal lattice planes in a high resolution TEM image, which can be compared to *d*-spacings measured by powder X-ray diffraction or to calculated crystal structures in a database. A specialized beam arrangement can also produce and capture the diffraction pattern made by the electron beam being diffracted by the nanocrystal, a technique called electron diffraction. In some instruments, electron diffraction does not have high enough spatial resolution to measure diffraction of a single >10 nm diameter nanocrystal, and in these instances analyzing the lattice planes through the FFT becomes crucial.

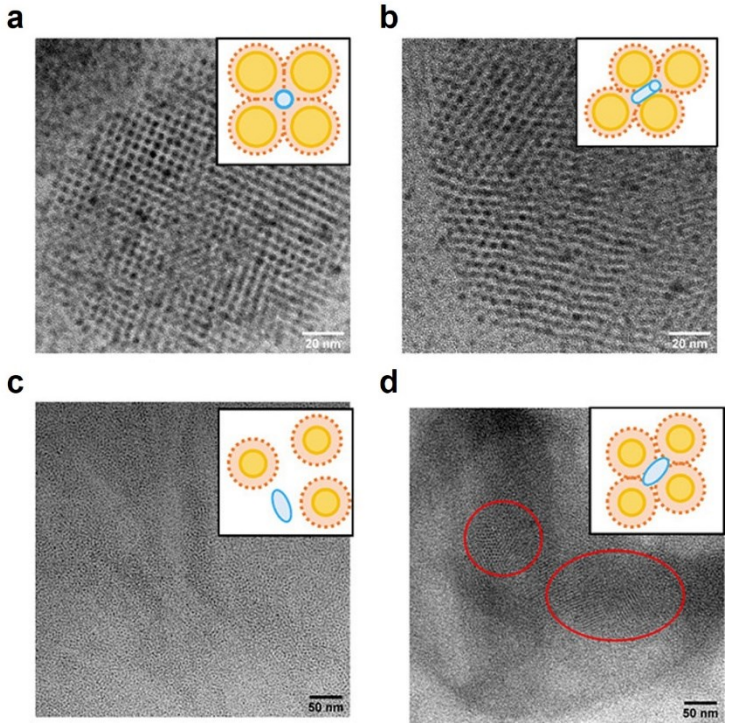
Analyzing crystal structure of single nanocrystals or regions of heterostructured nanocrystals can be paired with elemental analysis obtained with Energy-Dispersive X-Ray Spectroscopy (EDS) in scanning transmission electron microscopy (STEM). This allows microscopists to determine detailed, spatially resolved information about nanocrystalline material or phase identity and growth mechanisms of heterostructures. For example, in Chapter 4, the solution-liquid-solid nanowire growth mechanism was identified because of indium metal nanoparticles observed on the tips of indium phosphide nanowires.

Therefore, TEM is crucial to describe a nanocrystalline or hybrid nanomaterial system when taken in complement to solution phase or ensemble measurement techniques such as X-ray

diffraction or dynamic light scattering (DLS). The development of TEM imaging of cryogenic samples in particular, in concert with high resolution TEM and STEM, and DLS, is crucial to study assembly structures in their liquid state conformation through flash freezing. In the following collaborative studies, I have used TEM and related techniques to reveal and support new discoveries for novel nanocrystal synthesis techniques, characterization of nanocrystals exhibiting innovative properties, as well as hybrid assemblies of inorganic nanoparticles and biomolecules where TEM can give high resolution information of the nanoparticle component and comprehensive information about the assembly. The following data and analysis represent my contributions to works published through collaborations at the University of Washington, through the DOE EFRC Center for the Science of Synthesis Across Scales, and with other universities, along with two unpublished studies of nanocluster assembly and stability.

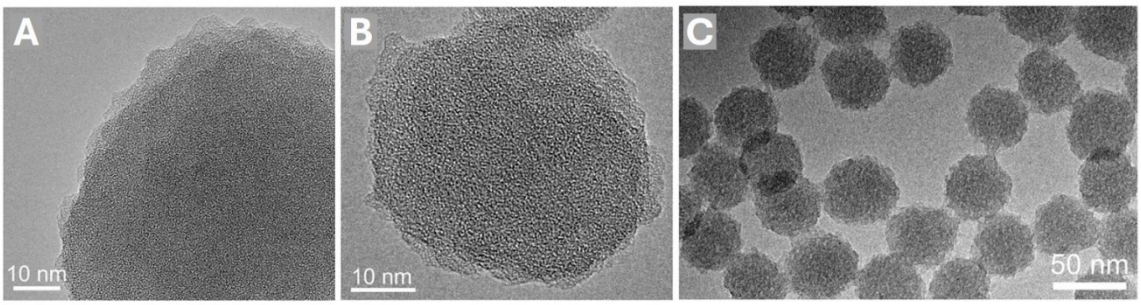
TEM studies of hybrid inorganic nanoparticle–peptide, protein, or peptoid assemblies

[1] *Towards Computation-Guided Design of Tunable Organic-Inorganic CdS Quantum Dot Binary Superlattices*[1]: bright-field TEM reveals structure of quantum dot – peptoid superlattices

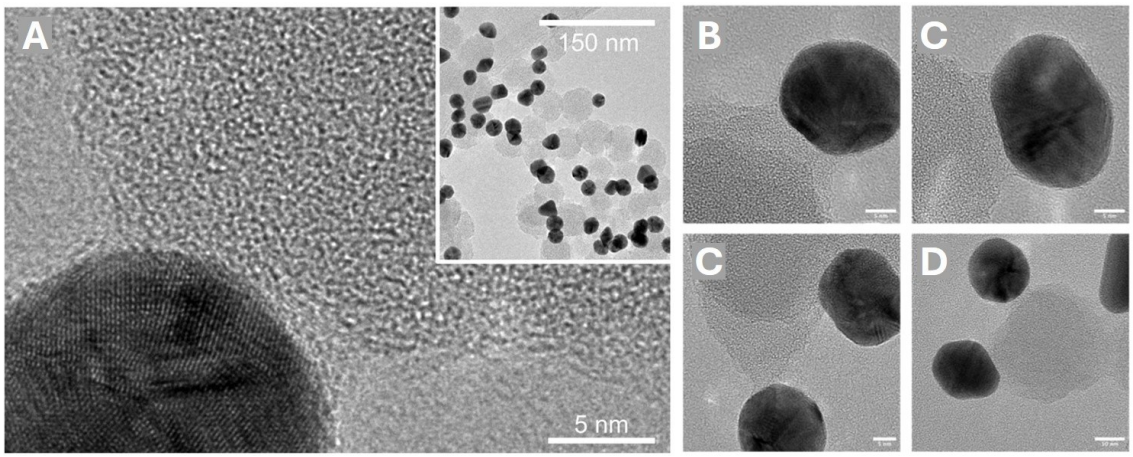


Binary superlattices or amorphous assemblies formed from cadmium sulfide quantum dots and di-block amphiphilic peptoids (Nbrpe$_x$Dig). Assemblies were formed in a chloroform solution of quantum dots and 1 equivalent of peptoid with varying length of hydrophobic segment. TEM images **a** and **b** represent square and hexagonal quantum dot packing identified for assemblies including peptoids with a shorter hydrophobic segment, Nbrpe$_4$Dig. However, for assemblies including peptoids with a longer hydrophobic segment, Nbrpe$_8$Dig, mostly amorphous deposition of quantum dots was observed by TEM (**c, d**). We hypothesize that the shape and flexibility of the peptoid drives superlattice packing and the shape and flexibility of Nbrpe$_x$Dig peptoids were predicted using molecular dynamics simulations.

[2] *Biomimetic Mineralization of Positively Charged Silica Nanoparticles Templated by Thermoresponsive Protein Micelles: Applications to Electrostatic Assembly of Hierarchical and Composite Superstructures*[2]: high-resolution TEM reveals SiO_2 and Au nanoparticle surface interactions

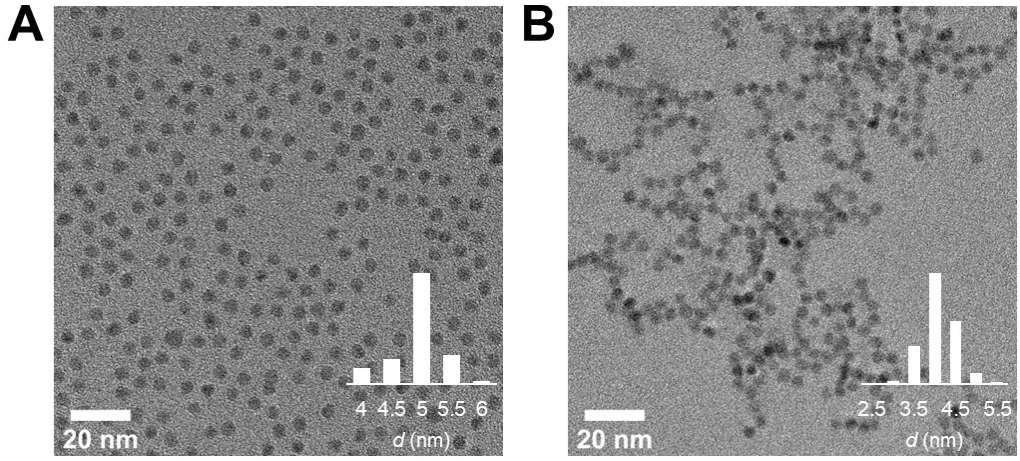


Thermoresponsive elastin-like polypeptides modified with a Car9 silica-binding peptide form 30 nm micelles that mineralize monodisperse silica nanoparticles (**a-c**). High-resolution TEM imaging supported a spherical raspberry model used for describing scattering data for the sample, where it was hypothesized that the ~ 3 nm protrusions corresponded to primary units from silica mineralization. The high-resolution TEM images were also used to support the hypothesis that the silica grows around the polypeptide mineralization template due to the lack of bulky organic features observed on the silica surface.

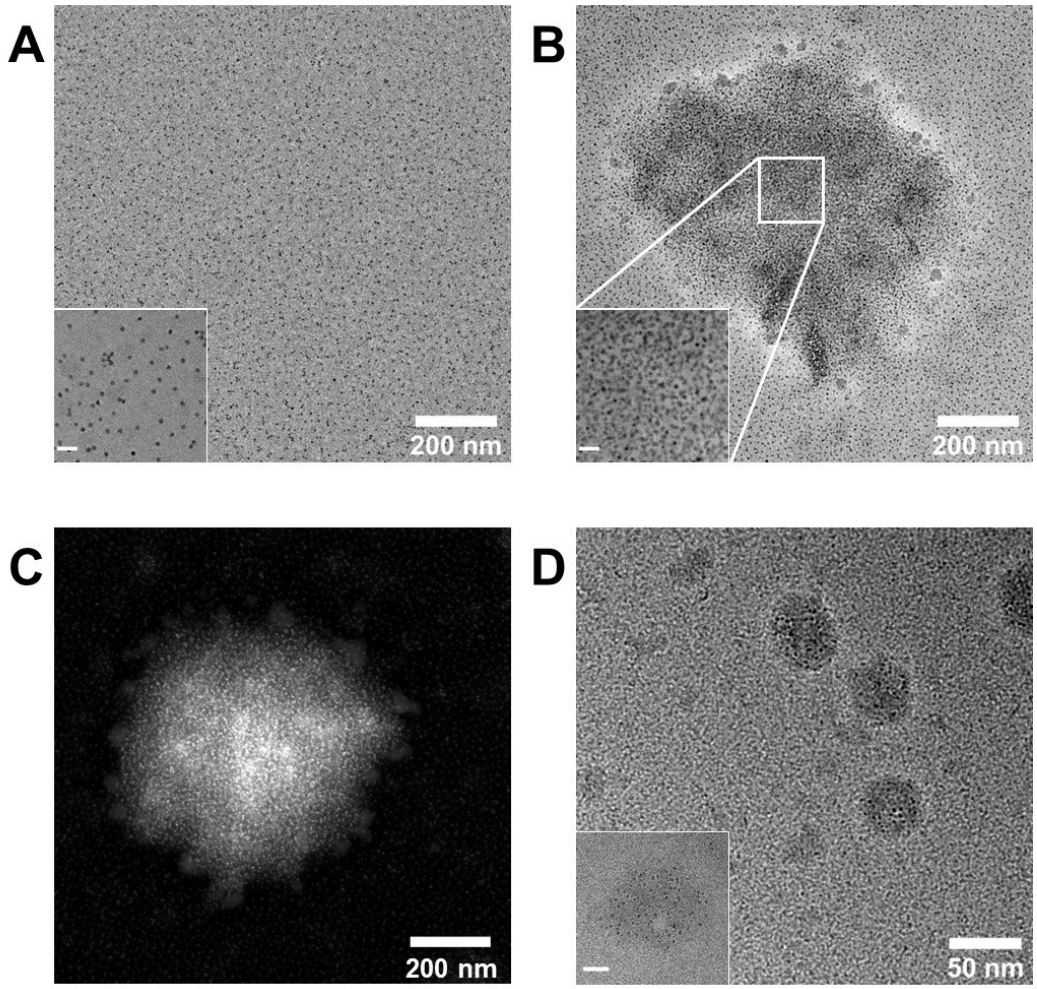


The mineralized silica was found to have a positive surface charge, unusual for silica nanoparticles. Therefore, by including negatively charged Au nanoparticles, an electrostatically-driven binary assembly forms. Bright-field and high-resolution TEM images show the structure of the binary assembly (**a inset**) and the specific intimate interaction of the Au and silica nanoparticles (**a-d**).

[3] *Induced Chirality in QDs Using Thermoresponsive Elastin-like Polypeptides*[3]: bright-field, scanning, and cryogenic TEM reveals assembly structure of quantum dots and thermoresponsive elastin-like polypeptides

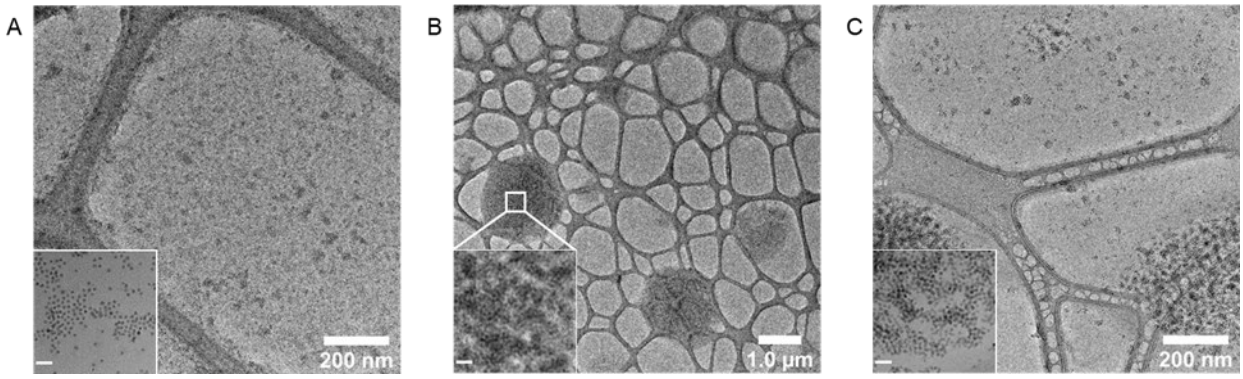


As-synthesized oleate-capped cadmium sulfide quantum dots (**a**) are 4.8 ± 0.4 nm in diameter and undergo slight etching to 4.1 ± 0.4 nm after ligand exchange with glycine for water-solubilization (**b**).



TEM images of CdS quantum dots ligated with $(VPGVG)_{54}$-Cys prepared at (**A**) 20 °C and (**B**) 45 °C. Scanning TEM (**C**) and cryogenic TEM (**D**) images of $(VPGVG)_{54}$-Cys capped quantum dots prepared at 45 °C. Higher-magnification insets have a 20 nm scale bar. The elastin-like polypeptide, $(VPGVG)_{54}$-Cys, reversibly forms coacervates when the solution temperature is above a specified transition temperature, 38 °C for $(VPGVG)_{54}$-Cys. In this study, we measured the binding of $(VPGVG)_{54}$-Cys to the surface of CdS quantum dots by measuring the induced chirality in the CdS by visible circular dichroism spectroscopy. Then, the hybrid $(VPGVG)_{54}$-Cys:CdS unit was shown to reversibly form quantum dot-dense coacervates when the solution was raised above 38 °C. The TEM samples were prepared specially to ensure the solution remained

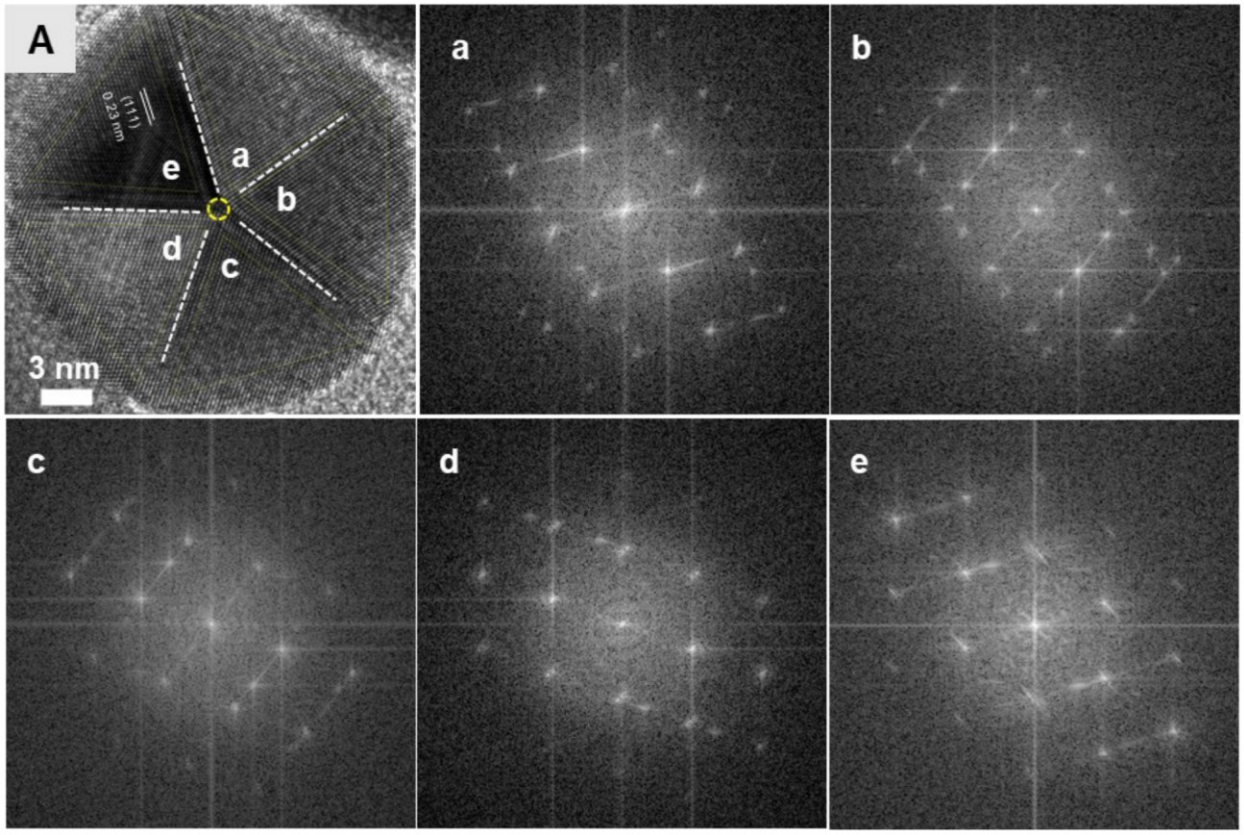
above 38 °C during deposition and drying. The cryogenic TEM images in particular revealed the structure of the $(VPGVG)_{54}$-Cys:CdS coacervates in solution by preparing the sample through plunge-freezing in liquid ethane to form vitreous ice.



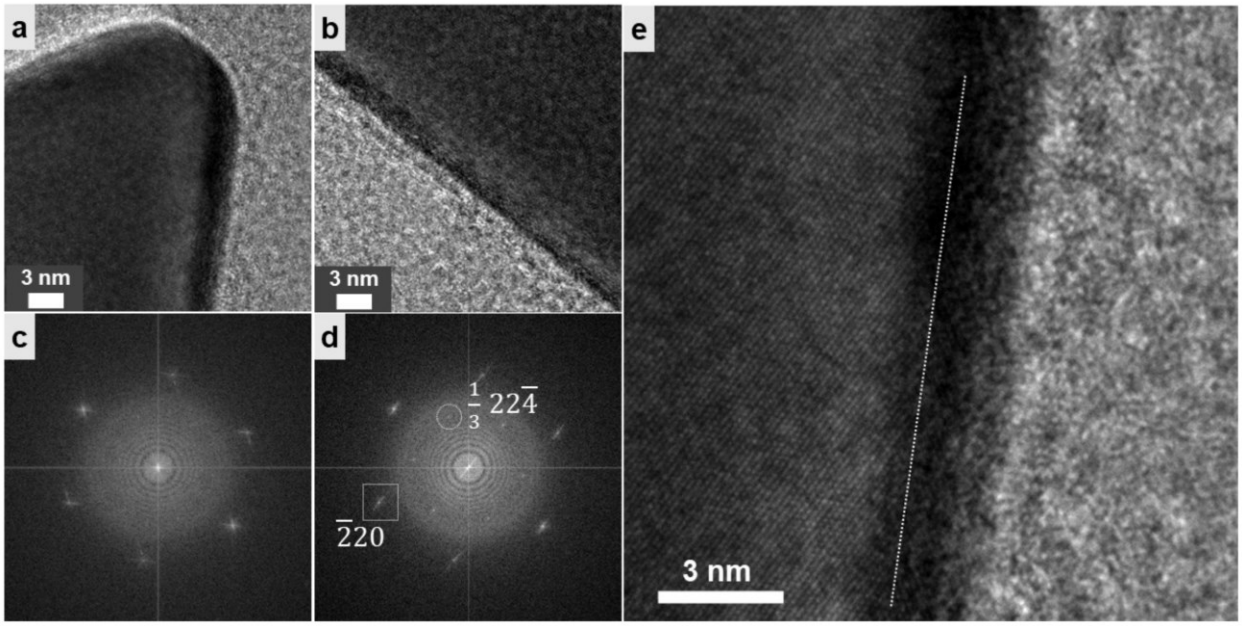
TEM images of $(VPGVG)_{96}$-Cys:CdS prepared at 20 °C (**A**) and at 40 °C (**B** and **C**), with insets of higher magnification, 20 nm scale bars. Below the transition temperature, $(VPGVG)_{96}$-Cys:CdS is observed in monolayers or small (<20 nm) aggregates. Above the transition temperature, 1-2 µm coacervates are observed with densely packed interiors (**B**). The coacervates appear to have some structuring of small aggregates (**C**) similar to those observed below the transition temperature.

TEM studies of nanocrystal morphology, size, and crystal structure

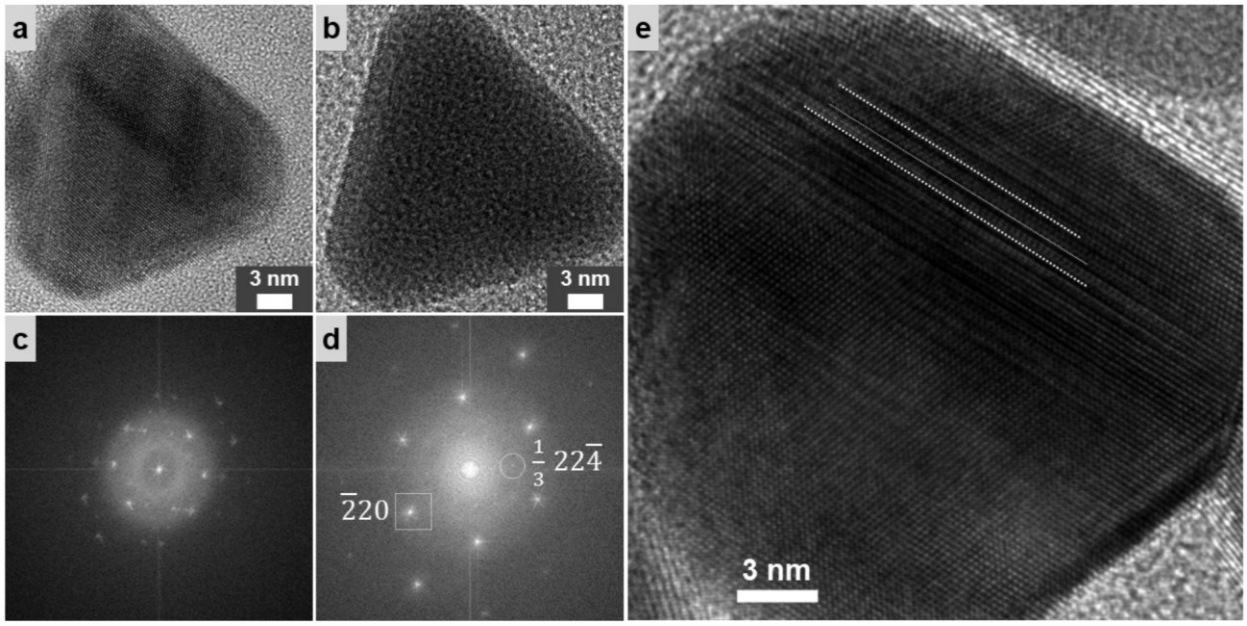
[4] *Connecting Nanoseed Defect Structure and Crystallinity with Resulting Nanoparticle Products*[4]: high-resolution TEM images with Fast Fourier Transform Analysis of lattice structure reveals Au nanoparticle defect structures



High resolution TEM image of a pentatwinned gold nanocrystal exhibiting a five-fold twinning axis (**A**). Analysis of the Fast Fourier transforms (FFTs) was performed to highlight the twin boundaries (**a-e**).

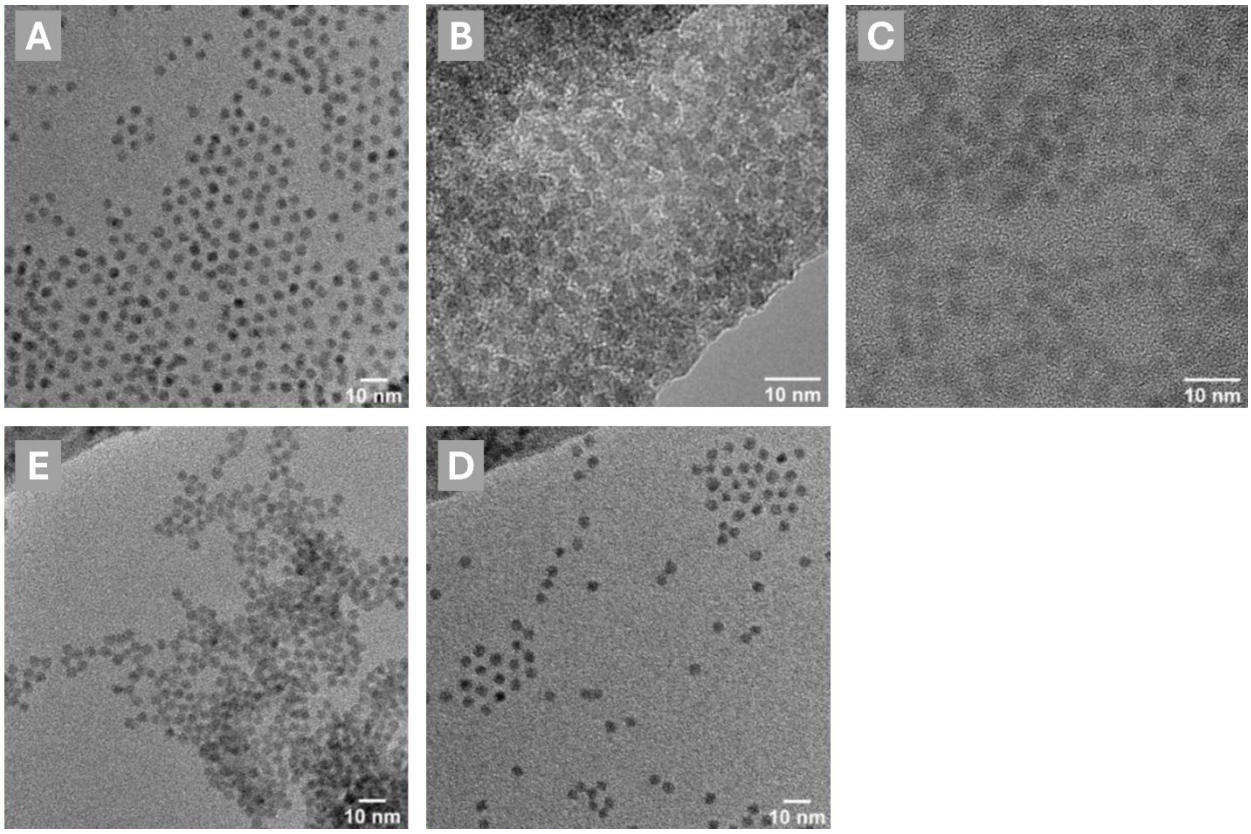


High resolution TEM images (**a, b, e**) of a representative gold truncated bitetrahedral nanocrystal allow for FFT analysis to determine twin planes (**c-e**).



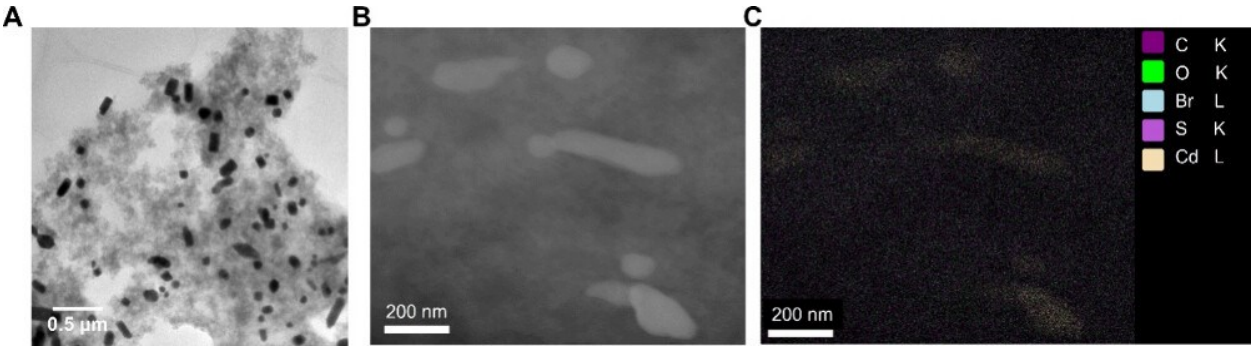
High resolution TEM images (**a, b, e**) of a representative gold triangular nanoplate allow for FFT analysis to identify the presence of stacking faults (**c-e**).

[5] *Extremely Long-Lived Charge Donor States Formed by Visible Irradiation of Quantum Dots*[5]



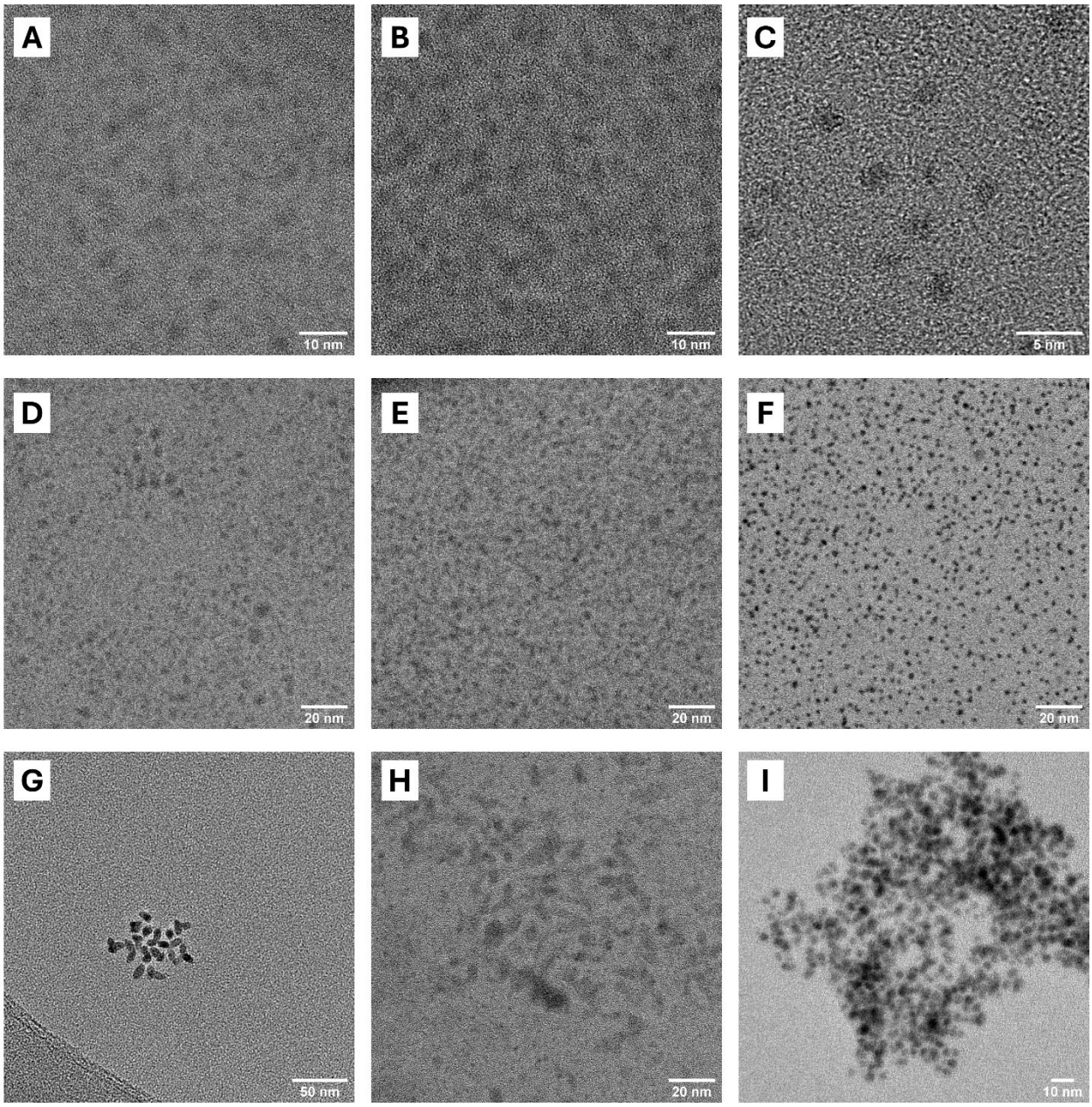
This work studied the nature of long-lived charge donor states in CdS QDs, and part of the investigation included QDs with three different surface chemistries. Bright field TEM images of QDs with native oleate ligands (**A**), the carboxylic acid 2-(2-methoxyethoxy)ethoxy acetic acid (**B**), or (2-[2-(2-methoxyethoxy)ethoxy]ethyl)phosphonic acid (**C**), along with images after etching of oleate ligands (**D**) and following exchange with 2-(2-methoxyethoxy)ethoxy acetic acid (**E**) allowed for sizing analysis to support arguments regarding the role of ligand headgroup and surface stoichiometry across similar sized particles.

[6] *Pathways of CdS Quantum Dot Degradation during Photocatalysis: Implications for Enhancing Stability and Efficiency for Organic Synthesis*[6]: Energy-dispersive X-ray Spectroscopy with Scanning Transmission Electron Microscopy reveals catalyst speciation.



(**A)** Bright-field TEM image displaying faceted microcrystals formed during catalysis. Scanning TEM image of microcrystals (**B**) alongside elemental mapping with energy-dispersive spectroscopy shows primarily cadmium colocalization on the microcrystals.

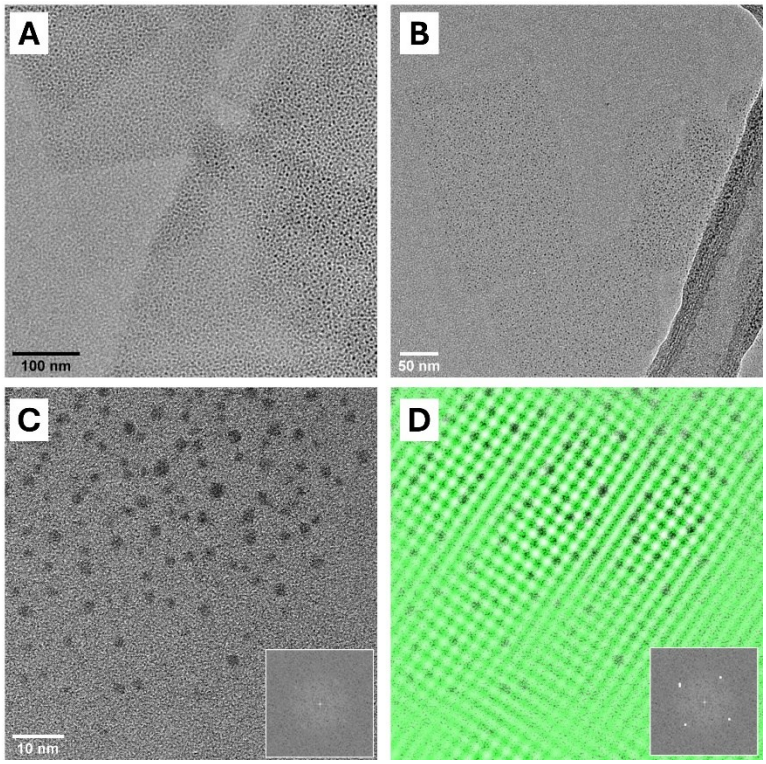
[7] *Leveraging Cation Exchange in InP Magic-Sized Clusters To Access Coinage Metal Phosphide Nanocrystals*[7]: High-resolution TEM images help characterize nanocrystals of novel compositions



High-resolution TEM was used to characterize the conversion of InP magic-sized clusters (MSCs) treated with 37 equivalents of Cu (**A, D**), Ag (**B, E**), or Au (**C, F**) and converted into coinage metal phosphide nanocrystals through hot injection (**G, H, I respectively**).

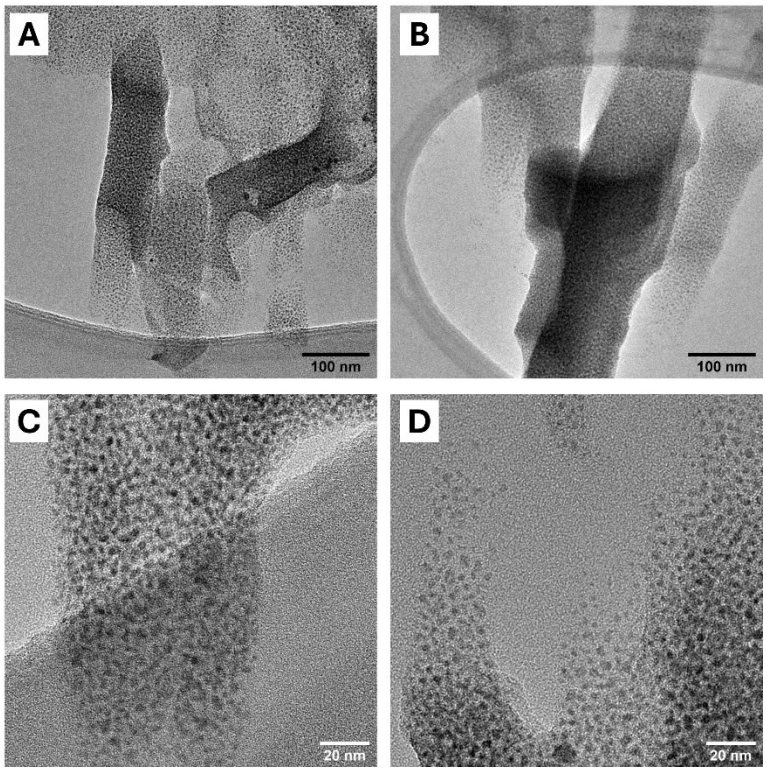
Unpublished Studies on Revealing Assembly and Stability of Nanoclusters with TEM

Ordered Sheet Formation of Cd_3P_2 Magic-Sized Clusters



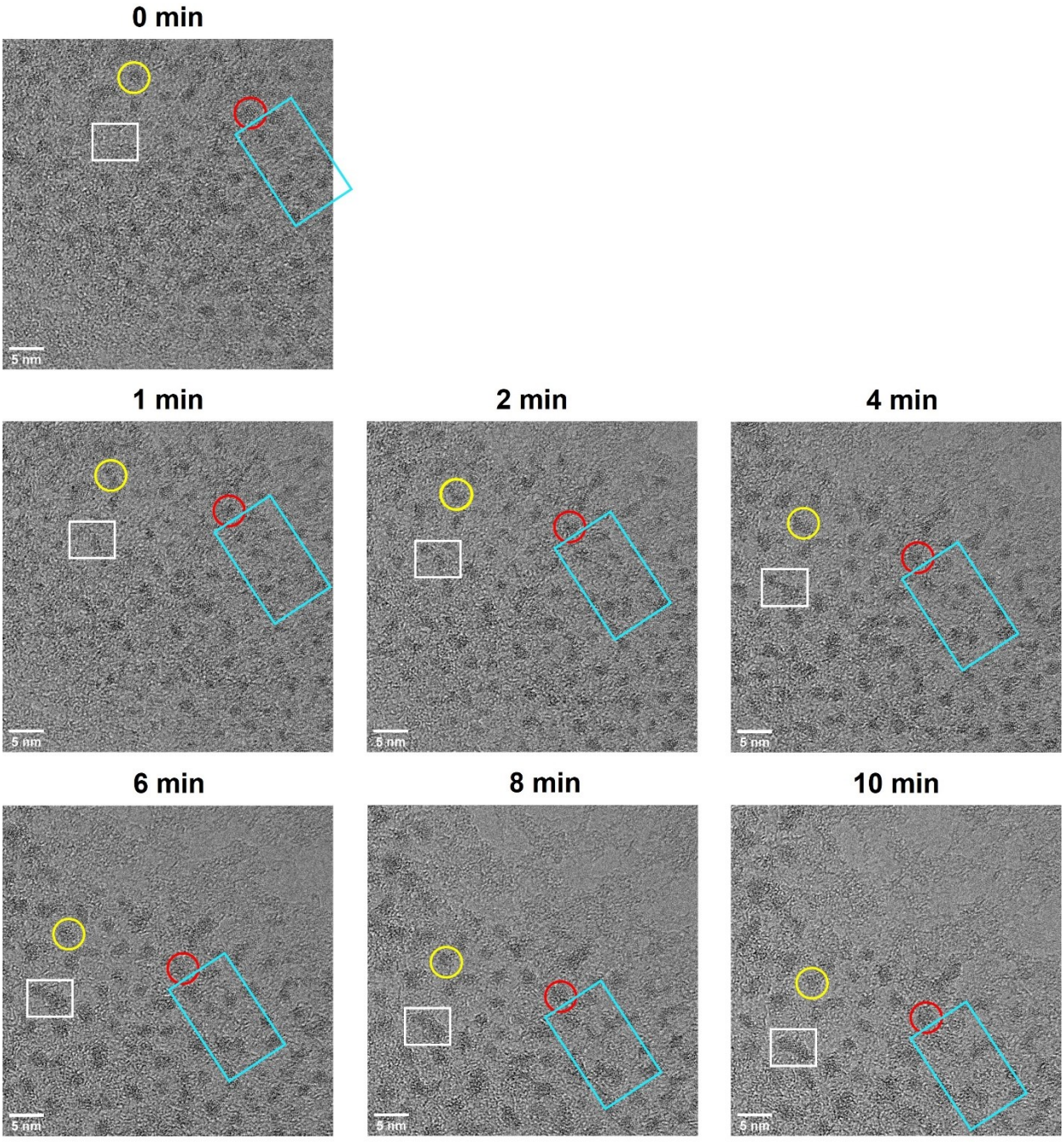
Bright-field TEM images (**A, B**) revealed thin rectangular sheets of Cd_3P_2 magic-sized clusters (MSCs). The Cd_3P_2 MSCs were capped with tert-butylphenylacetate ligands, and formed glittery suspensions in tetrahydrofuran (THF), which were diluted and dropcast on the TEM grid. Interestingly, the fast Fourier transform (FFT) of the TEM images containing the sheets showed evidence of a repeated pattern (**C, inset** – note faint white dots). By increasing the contrast of the FFT spots and performing an inverse FFT , the pattern was overlaid on a higher magnification image of the sheets (**D**) and the MSCs were observed to align with the pattern. This hints that there is a higher-order assembly process occurring that adopts a square-packing framework – also explaining the sharp edges of the nanosheets. Of the components of the system, the tert-butylphenylacetate ligands are the most likely candidate to direct the assembly, perhaps through π

– π stacking. The organic template was observed by close inspection of the nanosheets (see B), where the rectangular shape is maintained even without regular spacing of the inorganic component.



Assembled structures of Cd_3P_2 MSCs capped with phenylacetate ligands were also observed by TEM (**A-D**), and in solution where again the MSCs in THF produced a glittery solution. However, the assemblies with phenylacetate-capped MSCs were less clearly ordered in rectangular sheets, appearing to perhaps roll into tubes (**A**) or form thicker structures (**B-D**).

Investigating the Stability of Phosphonic acid-capped InP Clusters under the electron beam:



High resolution TEM images of phosphonate-capped InP clusters were taken as a time series over 10 minutes of beam exposure at 200 kV, with ‘0 min’ as the initial exposure to the beam for the particular region of particles. The red and yellow circles orient the same particles in

each image because slight drift occurred over the time series. In the white box, two clusters can be seen moving together and sintering under the electron beam. The blue box allows for multiple clusters to be tracked over the time series, and excitingly shows clusters moving around under the beam and more instances of sintering. In general, there are less defined lattice fringes after around 8 minutes (except sintered particle) although some remain in 10 minute image, indicated good stability under the electron beam. This study provides the initial framework for future studies of these clusters using high beam intensity TEM methods such as scanning TEM.

References

(1) Qi, X.; Helland, S.; Lowe, C. D.; Larson, H.; Cui, J.; Zheng, R.; Monahan, M.; Chen, C.-L.; De Yoreo, J.; Pfaendtner, J.; Cossairt, B. Toward Computation-Guided Design of Tunable Organic–Inorganic CdS Quantum Dot Binary Superlattices. *Nano Lett.* **2025**, *25* (10), 3989–3996. https://doi.org/10.1021/acs.nanolett.5c00024.

(2) Naser, N. Y.; Wixson, W. C.; Larson, H.; Cossairt, B. M.; Pozzo, L. D.; Baneyx, F. Biomimetic Mineralization of Positively Charged Silica Nanoparticles Templated by Thermoresponsive Protein Micelles: Applications to Electrostatic Assembly of Hierarchical and Composite Superstructures. *Soft Matter* **2025**, *21* (2), 166–178. https://doi.org/10.1039/D4SM00907J.

(3) Lowe, C. D.; Larson, H. C.; Cai, Y.; Chiang, H. T.; Pozzo, L. D.; Baneyx, F.; Cossairt, B. M. Induced Chirality in QDs Using Thermoresponsive Elastin-like Polypeptides. *Langmuir* **2024**. https://doi.org/10.1021/acs.langmuir.4c04339.

(4) Roy, D.; Larson, H.; Cossairt, B. M.; Moreau, L. M. Connecting Nanoseed Defect Structure and Crystallinity with Resulting Nanoparticle Products. *Nanoscale Adv.* **2025**. https://doi.org/10.1039/D5NA00418G.

(5) Homer, M. K.; Larson, H. C.; Dixon, G. J.; Miura-Stempel, E.; Armstrong, N. R.; Cossairt, B. M. Extremely Long-Lived Charge Donor States Formed by Visible Irradiation of Quantum Dots. *ACS Nano* **2024**, *18* (35), 24591–24602. https://doi.org/10.1021/acsnano.4c10526.

(6) Dou, F. Y.; Nishiwaki, E.; Larson, H.; Homer, M. K.; Zion, T.; Nguyen, H. A.; Cossairt, B. M. Pathways of CdS Quantum Dot Degradation during Photocatalysis: Implications for Enhancing Stability and Efficiency for Organic Synthesis. *ACS Appl. Nano Mater.* **2024**, *7* (13), 15781–15785. https://doi.org/10.1021/acsanm.4c02976.

(7) Eagle, F. W.; Harvey, S.; Larson, H.; Abbott, A.; Ladd, D. M.; Levine, K. R.; Toney, M. F.; Gamelin, D. R.; Cossairt, B. M. Leveraging Cation Exchange in InP Magic-Sized Clusters To Access Coinage Metal Phosphide Nanocrystals. *Chem. Mater.* **2024**, *36* (6), 2888–2897. https://doi.org/10.1021/acs.chemmater.3c03258.

VITA

Helen Larson was born and raised in Roseville, Minnesota, where she first experienced the joy of science by selectively growing populations of marigolds best suited to her shady backyard. Drawn by her love of chemistry and music, she attended St. Olaf College in Northfield, Minnesota where she researched environmentally-friendly C-H activation reactions for drug discovery with Dr. Dipannita Kalyani, and played for four years in the St. Olaf Band. After receiving her bachelors of arts in chemistry with a concentration in environmental studies at the height of a global pandemic, she moved to Seattle, Washington to pursue her PhD under the guidance of Professor Brandi Cossairt because she was enamored by the colors and exciting synthesis of quantum dots. In her free time, Helen enjoys being outside, crafting, and eating good food with friends.